UNSTEADY MODES IN THE FLOWFIELD ABOUT AN AIRFOIL WITH A LEADING-EDGE HORN-ICE SHAPE

BY

PHILLIP J. ANSELL

DISSERTATION

Submitted in partial fulfillment of the requirements
for the degree of Doctor of Philosophy in Aerospace Engineering
in the Graduate College of the
University of Illinois at Urbana-Champaign, 2013

Urbana, Illinois

Doctoral Committee:

Professor Michael B. Bragg, Chair
Professor Gregory S. Elliott
Associate Professor Michael S. Selig
Professor Kenneth T. Christensen

Abstract

An analysis of unsteady modes present in the flowfield of an airfoil with a leading-edge horn-ice shape was performed in the current study. An NACA 0012 airfoil was tested in a subsonic wind tunnel at $Re = 1.8 \times 10^6$. In addition to the clean configuration, the airfoil model was also tested with a set of boundary-layer trips, a two-dimensional extrusion of a horn-ice shape casting, and an array of simulated icing configurations created using simple geometries. Time-averaged and unsteady static pressure measurements were acquired about the airfoil surface, along with unsteady wake velocity and surface hot-film array measurements. Additionally, surface and off-body flow visualization techniques were used to visualize the airfoil flowfield. A technique was also developed to determine the unsteady shear-layer reattachment location of the ice-induced laminar separation bubble downstream of the horn-ice shape using the surface hot-film array measurements.

The maximum amount of unsteadiness in the iced-airfoil flowfield was observed to increase with increasing angle of attack. For a fixed angle of attack prior to stall, a change in the feature height of the simulated ice shape led to a change in the distribution of flowfield unsteadiness, but did not change the maximum levels of unsteadiness present in the flowfield. The iced-airfoil flowfield unsteadiness was primarily associated with three different frequencies. The first was represented by an increase in spectral energy across a broad-band frequency range, and was observed just upstream of shear-layer reattachment as well as downstream of shear-layer reattachment. This increase in spectral energy was caused by the regular mode of unsteadiness due to vortical motion in the separated shear layer and vortex shedding from the separation bubble. The average Strouhal number of this regular mode corresponded to $St_L = 0.60$, and the average vortex convection velocity was observed to be $0.45U_\infty$. These values were highly consistent with those reported elsewhere in the literature.

The other two frequencies were much lower and were observed as narrow-band peaks in the spectral content of the acquired measurements that were primarily present in the region covered by the ice-induced separation bubble. The first was attributed to the shear-layer flapping phenomenon and was particularly dominant in the upstream portion of the separation bubble. The Strouhal number associated with this shear-layer flapping mode corresponded to

$\mathrm{St}_h = 0.0185$, which was consistent with those reported in studies of separation bubbles about canonical geometries. The second frequency was lower than that of shear-layer flapping and was associated with a low-frequency mode of unsteadiness that can occur prior to static stall for airfoils of thin-airfoil stall type. This low-frequency mode was characterized by a low-frequency oscillation of the airfoil circulation, and it was clearly identified in the spectral content of the iced-airfoil lift coefficient. The resulting values of Strouhal number exhibited a dependence on the airfoil angle of attack and corresponded to a range that was consistent with the Strouhal number values reported in prior studies of the low-frequency mode in the literature.

Using the method for determining the unsteady shear-layer reattachment location, the average time-dependent relationship between the reattachment location and the lift coefficient was calculated. It was discovered that at the low-frequency mode, the lift coefficient leads the shear-layer reattachment location by a phase of $\pi/2$. This phase relationship occurred due to a feedback between the airfoil circulation and the separation bubble length. This improved understanding of the low-frequency mode in the iced-airfoil flowfield was utilized in a practical example to improve the predictive qualities of a hinge-moment-based stall prediction system. This improvement in the predictive qualities was performed by identifying the intermittent signature of the low-frequency mode in the wavelet transform of the hinge moment coefficient, which allowed the iced-airfoil stall case to be isolated from the other clean airfoil and leading-edge contamination configurations.

Acknowledgements

Throughout my academic career thus far I have had the privilege of knowing many incredible individuals. I certainly would not have had the same success in my academic development without them.

I would like to sincerely express my gratitude towards my academic advisor, Prof. Mike Bragg, who on top of providing me with opportunities to perform research also provided me with very wise and memorable discussions of working in the research environment. At times, he seemed to have more faith in my abilities than I did myself, which set me up to accomplish tasks I did not think I was capable of. I would also like to genuinely thank the rest of my doctoral committee for their helpful contributions to this work. I have immensely enjoyed the life mentoring and discussions that I have had with Prof. Greg Elliott during my time as a graduate student. I would also like to thank Prof. Michael Selig for providing me access to his vast knowledge of aeronautics and for his desire to see me succeed in the academic environment. I also owe many thanks to Prof. Ken Christensen, who supplied me with knowledge and interest in experimental techniques and signal processing which were extensively utilized in my research efforts.

I would like to also thank Dr. Mike Kerho for his patience and helpful instruction throughout the time that we've worked together. I also wish to thank Prof. Bragg's research group, including Ruben Hortensius, Jeff Diebold, Marianne Monastero, and others, for all of the laboratory assistance, insightful conversation, and encouragement that they provided. Recognition is also deserved by the friends that I have made during my time at Illinois. I would like to thank Brent Pomeroy and Tyler Naibert for their valuable friendship and constant willingness to share in conversation.

I would like to thank my lovely wife, Katie, whose encouragement has helped me through many dark days. I am so grateful for the immeasurable love and optimism that she has generously poured into my life. I'd also like to thank my family for their unwavering support. I know that wherever I find myself, I will always have a home in the love and support of my parents, along with that of my big brother and big sister.

Above all else, all praise and glory belongs to Jesus Christ. Through Him God has granted me new life. I hope to always live in gratitude of this gift that I have received.

Table of Contents

List of Figures

List of Tables

Nomenclature

a	overheat ratio
A	area
b	airfoil model span or intercept
c	chord
c_f	flap chord
C	wind tunnel test-section area or constant
C_d	drag coefficient
C_h	hinge moment coefficient
C_l	lift coefficient
C_m	quarter-chord pitching moment coefficient
C_p	pressure coefficient
C_p*	normalized pressure coefficient
D	drag
E	hot-film voltage
f	frequency
f_0	wavelet frequency scale
F	force
G	spectral density function
h	test-section height
H	hinge moment
I	intermittency function
k	feature height
K_1	solid blockage correction constant
L	lift or length
L_b	separation bubble length
L_{dB}	power ratio in decibels
m	slope
M	Mach number

M	moment
n	number of pressure taps/ports
N	number of samples
p	probability density function
P	pressure or cumulative distribution function
P_0	total pressure
P_s	airfoil surface static pressure
q	dynamic pressure
r	time lag interval
R	gas constant
R_{xy}	cross-correlation function
R_w	hot-film operating resistance
R_c	hot-film cold resistance
Re	Reynolds number
RR	range ratio
s	airfoil surface length
S	airfoil reference area
St	Strouhal number
St_h	Strouhal number based on airfoil projected height
St_L	Strouhal number based on separation bubble length
t	airfoil thickness or time
T	temperature
T_s	sensor (hot-film element) temperature
u	local velocity
U	velocity or uncertainty
U_c	convection velocity
V	voltage
V_0	zero-corrected voltage
V_m	model volume
x	chordwise direction
x_r	shear-layer reattachment location

y	chord-normal direction

Greek Symbols

α	angle of attack or temperature coefficient
γ_{CWT}	intermittency factor
Δ	change or difference
ε	correction factor
η	wavelet time scale
θ	phase angle
μ	dynamic viscosity
π	pi
ρ	Density
ρ_{xy}	correlation coefficient
σ	standard deviation
τ	time lag
τ_0	time delay
τ_s	temporal resolution
τ_w	wall shear stress
ψ_0	wavelet function

Subscripts

A	axial
amb	ambient
atm	atmospheric
avg	average
$blade$	wind tunnel fan blade
$c/4$	quarter-chord
cor	corrected
$film$	hot film
$flap$	flap
h	flap hinge

i	index or instantaneous
ind	indicated
max	maximum
min	minimum
M	moment
N	normal
offset	offset from balance center
rake	wake rake
sb	solid blockage
ss	settling section
stall	stall
struct	structural
trans	pressure transducer
ts	test section
u	uncorrected
w	wake plane
wb	wake blockage
0	total
∞	freestream

Acronyms and Abbreviations

A/D	analog to digital
CTA	constant temperature anemometer
CWT	continuous wavelet transform
dB	decibels
DFT	discrete Fourier transform
ESP	electronic pressure scanner
FFT	fast Fourier transform
GPIB	general-purpose interface bus
LDV	laser Doppler velocimetry
LES	large-eddy simulation

LWC	liquid water content
MVD	mean volumetric diameter
PCU	pressure calibration unit
PIV	particle image velocimetry
PSD	power spectral density
PSI	Pressure Systems Incorporated
QR	quarter round
RPM	rotations per minute
RTV	room temperature vulcanizing
SCXI	Signal Conditioning eXtensions for Instrumentation
SLA	stereolithography apparatus
VFD	variable frequency drive
WC	water column

Chapter 1

Introduction

Ever since the historic first flight of the Wright Flyer in 1903, the forefront of aviation technology has been swiftly advancing. While the aircraft of today become increasingly complex, the issues of increasing capability, efficiency, and safety, have remained as primary factors in modern aircraft development. In aerodynamics, most problems are approached with the assumption of a steady-state (time independent) system. However, all aerodynamic problems are, in essence, unsteady (varying with time). While the steady-state assumption that is made for many fluid flows is a valid approximation, even flows past the simplest of geometries, like a stationary cylinder, contain significant unsteady components under certain flow conditions. By addressing the changes that can occur in a flowfield due to unsteady effects, opportunities can be discovered to interact with the natural laws of fluid mechanics in new and innovative ways.

Most notably, the study of unsteady aerodynamics can lead to developments that improve aviation safety. While many factors are involved when considering aviation safety, a flight hazard that has persisted since the inception of aviation is airframe icing. Aircraft icing can occur on the ground prior to takeoff if the aircraft is exposed to freezing precipitation, but icing can also occur in flight as the aircraft flies through clouds of water droplets at sub-freezing temperatures. As the super-cooled water droplets impinge on the surface of the aircraft, they can freeze. Ice can accrete on aircraft wing and tail surfaces, along with engine components (e.g.

cowls, propellers, and inlets) and instrumentation. Extended exposure to icing conditions can cause ice to accrete on the aircraft surface in various shapes and complex profiles, depending on the aircraft configuration, flight conditions, and atmospheric conditions. The presence of these ice shapes generally disrupts the flow over the aircraft, leading to a degradation in performance. Generally, the performance penalties induced by ice shapes on an aircraft includes increases in drag, losses in lift, changes to the aerodynamic moments about the aircraft body axes, and changes in the aircraft controllability.

As a result of the vast number of studies focused on the steady-state effects of icing on an airfoil, a thorough understanding of icing effects on airfoil performance has been obtained. This understanding includes the classification of types of ice shapes, their effects on the airfoil flowfield, and the resulting effects on airfoil performance.[1] However, the current understanding of unsteady flowfield effects involved in an iced-airfoil flowfield is quite limited. As a result, the current study is being conducted in an effort to improve the state of understanding of unsteady effects in an iced-airfoil flowfield and apply this new understanding to the development of innovative aviation technology.

For example, as discussed by Bragg et al.,[1] the flowfield about an airfoil with a leading-edge horn-ice shape is dominated by a separation bubble prior to airfoil stall. As the flow about the leading-edge approaches the tip of the ice shape, the step from the tip of the horn shape to the airfoil surface induces a strong adverse pressure gradient, forcing separation to occur. If the flow reattaches to the surface of the airfoil, a separation bubble is formed. This bubble is characterized by a region of recirculating fluid constrained between the airfoil surface and the separated shear layer. Generally, the steady-state effects of this separation bubble on the airfoil performance are characterized by large increases in drag, reductions in lift, and changes to the airfoil pitching moment characteristics. However, the process of shear-layer reattachment involved in separation bubble flowfields is known to have two inherent modes of unsteadiness.

The presence of vortical motion in flowfields involving a separation bubble has been widely reported in the literature. For example, Mabey[2] presented a review of the characteristics of vortical motion involved in the flows about various geometries that produce separation bubbles. This regular mode included the presence of vortical motion in the separated shear layer and vortex shedding from the separation bubble. A second mode of unsteadiness was then later introduced by Eaton and Johnston,[3] who observed regions of high-amplitude content at low frequencies in the velocity spectra at certain locations in the separation bubble downstream of a backward-facing step. These authors attributed this low-frequency content to a vertical oscillation that was observed in the reattaching shear layer, which became known as "shear-layer flapping."

A low-frequency oscillation that can also occur prior to static stall for certain airfoils exhibiting a thin-airfoil stall type was also introduced by Zaman et al.[4] Since the thin-airfoil stall type is produced by the presence of a leading-edge separation bubble on an airfoil that grows with increasing angle of attack up to stall, this low-frequency oscillation has been thought to be directly related to the presence of the leading-edge separation bubble. This conclusion is supplemented by the observations of Bragg et al.[5] where the presence of this low-frequency oscillation was suppressed when the separation bubble was eliminated with the addition of a boundary-layer trip.

Since it is known that these unsteady modes can be present in the flowfields involving separation bubbles, it is useful to better identify how these modes are manifested in an iced-airfoil flowfield. Such knowledge could aid in the ability to detect the presence of hazardous ice accretions for aircraft in flight and provide a better understanding of potential hazards in iced-aircraft operation that are not represented in the steady-state understanding. While the unsteady modes present in an iced-airfoil flowfield were studied by Gurbacki,[6] many questions still remain about how these unsteady modes are characterized in the flowfield.

The goals of the current study are to provide a thorough understanding and characterization of the unsteady modes involved in the flowfield about an airfoil with a leading-edge horn-ice shape and to present an example of how this understanding can be applied in the development of a stall prediction system to improve flight safety. As a result, this research goal was established using the three major objectives outlined as follows:

- Characterize relevant modes of unsteadiness present in the flowfield about an airfoil with a leading-edge horn-ice shape
    - Identify the unsteady modes in measurements acquired in the flowfield about an iced airfoil.
    - Evaluate the frequency and convective characteristics of the resulting unsteady modes.

    - Provide a physical representation of the unsteady modes through visualization techniques.
- Understand the unsteady effects imposed by the low-frequency mode
    - Determine the relationship between unsteady shear-layer reattachment behavior and unsteady airfoil performance related to the low-frequency mode.
    - Identify the effect of the low-frequency mode on the time-dependent characteristics of the airfoil surface pressure.
- Improve hinge-moment-based stall prediction methodology for an airfoil with a leading-edge horn-ice shape
    - Use the improved understanding of unsteady modes in iced-airfoil flowfield towards improving stall prediction methodology.
    - Develop methods for using hinge-moment measurements for detecting changes in airfoil stall type induced by the addition of a horn-ice shape.

The current investigation was conducted using wind-tunnel experiments on an NACA 0012 airfoil under a series of clean and contaminated configurations, including a boundary-layer trip case, a geometrically-scaled two-dimensional horn-ice shape case, and several leading-edge horn-ice cases simulated using simple geometries. Several types of measurements were acquired in this investigation, including time-averaged and unsteady pressure measurements, along with unsteady surface and off-body hot-film measurements. Relevant unsteady content was identified in both on-surface and off-surface measurements. Results from these measurements were also aided with the use of surface oil flow visualization to identify the time-averaged surface flowfield characteristics, as well as smoke flow visualization to identify the unsteady characteristics of the flowfield off the airfoil surface.

Several signal processing techniques were also used in order to understand the unsteady content of the acquired measurements. These techniques included the use of spectral analysis, phase angle analysis, correlation analysis, and wavelet analysis. Relevant frequencies of unsteady modes were identified in the calculated spectral densities of measurements, and convective properties were determined using results of the phase angle analysis. Additionally, a new technique was introduced to determine the unsteady shear-layer reattachment location on the airfoil surface using measurements acquired from a series of surface hot-film array measurements. Using the resulting unsteady shear-layer reattachment locations and a conditional averaging technique, the time-dependent relationship at a low-frequency mode between the reattachment location and unsteady iced-airfoil lift coefficient was identified via correlation analysis and wavelet analysis. Additionally, the time-dependent characteristics at the low-frequency mode were identified in the unsteady airfoil surface pressures.

Finally, with the improved understanding of the unsteady modes present in the flowfield of the airfoil with the leading-edge horn-ice shape, improvements to the pre-existing hinge-moment-based stall prediction methodology[7] were made. This baseline system was shown to be effective in predicting airfoil stall for various contaminated-airfoil configurations, with the exception of a horn-ice case, which typically produced a premature stall warning. Using the intermittent signature of the low-frequency mode present in the wavelet transform of the hinge-moment measurements, the impending stall induced by the iced-airfoil could be identified prior to having a premature stall warning issued by the baseline stall prediction system. As a result, the baseline stall prediction system could be adapted in order to produce more accurate stall warnings for this particular contaminated-airfoil case.

This dissertation is divided into five chapters. This brief introduction serves as the first chapter. A more in-depth review of the literature related to icing effects on airfoils, unsteady effects associated with separation bubbles, and an introduction to aircraft performance monitoring is presented in Chapter 2. A description of the experimental facilities, data acquisition methods, post-processing techniques, and other aspects of this experimental study are presented in Chapter 3. The results obtained in this study and a discussion of various aspects of the results are presented in Chapter 4. Finally, a brief summary of the experimental investigation, review of important results, and suggestions for future investigations are presented in Chapter 5.

Chapter 2

Review of Literature

This chapter provides an overview of the literature that is relevant to the content of the current study. This summary presents results from classic and modern investigations on iced-airfoil flow physics, unsteady separation bubble flowfields, and instrumentation applicable to the current investigation.

2.1 Iced-Airfoil Flow Physics

Because of the safety concerns that airframe icing presents to air travel, numerous studies have been devoted to better understanding and characterizing the effects of icing. These studies include investigations on airfoil and aircraft performance, as well as the detailed fluid mechanics associated with certain iced-airfoil flowfield features.

2.1.1 Ice-Induced Performance Effects

Generally, an ice accretion on an airfoil alters the geometry of an airfoil, leading to a change in the airfoil performance. An iced airfoil commonly exhibits reductions of maximum lift characteristics, a reduced stall angle of attack, and large increases in drag from the clean airfoil. A thorough overview of icing aerodynamics research and types of iced-airfoil aerodynamics, including relevant flowfield features and performance effects, was presented by

Bragg et al.[1] These authors classified airfoil ice accretions by aerodynamic effect and geometry into the four categories of ice roughness, horn ice, streamwise ice, and spanwise-ridge ice. The most relevant type of ice shape from the classifications of Bragg et al.[1] to the current investigation is the horn-ice shape. An example of the horn-ice shape geometry is presented in Fig. 2.1, after Bragg et al.[1] As described by these authors, the geometry of the horn-ice shape can be described by the horn height, the angle relative to the airfoil chord line at which the horn forms, and the ice shape surface length (s/c) location on the airfoil surface.

The effects of leading-edge ice accretions on airfoil performance have been included in numerous studies. Kim and Bragg[8] used nine various sizes and shapes of simple geometries to simulate ice shapes and identify the corresponding performance effects. Each of the simulated ice shapes was positioned at six different leading-edge locations to parametrically determine the sensitivity of the iced-airfoil performance on the ice shape size and location. These authors identified that the geometric radius at the tip of the simulated horn-ice shape had little effect on the iced-airfoil performance, but that the ice-induced performance effects were highly sensitive to the horn height and location. The reductions in lift and increases in drag were greatest for the simulated horn-ice shapes with the largest height. The performance effects also increased as the ice shape location was moved downstream in the vicinity of the leading-edge region. Additionally, changes in stall type were identified, using the classifications from McCullough and Gault.[9]

An additional study by Papadakis et al.[10] identified ice-induced performance effects on an airfoil using two sizes of spoiler plates placed at the airfoil leading-edge at various angles. These authors also conducted tests at various Reynolds numbers and identified that the ice-induced performance effects were essentially insensitive to changes in Re. Use of the spoiler shapes on the airfoil leading edge resulted in reductions in maximum lift from the clean airfoil by approximately 53–76%, and increases in drag from the clean airfoil by approximately 700–1200%. Additionally, large deviations of the pitching moment characteristics from the clean airfoil were identified.

In addition to identifying the effects of simulated ice accretion on airfoil lift and drag, Lee and Bragg[11] also identified the sensitivity of hinge moments of a 25% flap on an NACA 23012 airfoil to various simulated ice shapes. Simulated ice shapes with k/c values ranging from 0.0083 to 0.0139 were tested at various locations on the airfoil surface. For the simulated shape with the greatest effect, the airfoil maximum lift coefficient was reduced from the clean value of 1.46 to the iced value of 0.27. These authors also identified that the ice shape location with the greatest effect was near the location where the greatest adverse pressure gradient was encountered on the clean airfoil. Significant changes to the flap hinge moment characteristics from the clean airfoil were also identified, and characteristics of ice-induced flow separation were studied in detail.

A later study performed by Busch et al.[12] compared performance effects due to ice shapes of varying geometric fidelity to experimentally-obtained ice accretions. When comparing the performance of an airfoil with a two-dimensional smooth ice shape casting cross-section to a simple geometry simulation, the maximum lift coefficient of the simple geometry was observed to be within 2% of that of the two-dimensional smooth casting. Additionally, the smooth two-dimensional simulation closely matched the lift and drag characteristics of the full-scale casting. These authors concluded that the horn height and location were the primary factors affecting the iced-airfoil aerodynamics, and that the roughness associated with most ice shapes serves a tertiary role in affecting the airfoil performance. As a result, this study showed that ice-induced airfoil aerodynamics can be closely simulated using simple geometries.

An investigation identifying ice-induced airfoil performance effects using high-fidelity leading-edge ice shapes on a full-scale airfoil model was also performed by Broeren et al.[13] These authors reported upon the experimental full-scale iced-airfoil performance for six different ice shapes on an NACA 23012 airfoil. Tests were conducted at ranges of $Re = 4.5 \times 10^6$ to 16.0×10^6, and $M = 0.10$ to 0.28. For the horn-ice shape at $Re = 15.9 \times 10^6$ and $M = 0.20$, the maximum lift coefficient was reduced from the clean value of 1.85 to 0.86. Also, the drag coefficients were observed to be on the order of three times higher than the clean values. A change in stall type from a leading-edge stall of the clean airfoil to a thin-airfoil stall of the airfoil with the horn-ice shape was also observed, and was consistent with observations of prior investigations.

With the continually-growing popularity of computational fluid dynamics (CFD), there has also been an increase in the contribution of computational techniques towards understanding the effects of icing on airfoil geometries. In addition to computationally predicting iced-airfoil performance, many research efforts have been conducted to computationally simulate ice accretions and ice-shape generation. Bragg[14] acquired experimental iced-airfoil performance measurements for two ice shapes – one simulated from an experimentally-obtained ice shape and one generated computationally. It was identified that at positive angles of attack, the iced-airfoil performance was similar between both shapes. Later, Bragg et al.[15] discussed the expansion of subscale aerodynamic testing to CFD application. In this study, ice accretions obtained computationally using the NASA LEWICE code[16] and ONERA ONICE code[17] were compared with experimental results from tests conducted in the NASA IRT.

2.1.2 Ice-Induced Separation Bubble

As discussed by Bragg et al.,[1] the most dominant feature of the flowfield about an airfoil with a horn-ice shape is the separation bubble that forms downstream of the horn-ice shape. This separation bubble has a structure and many similar characteristics to the long bubble on an airfoil as described by Tani.[18] This type of separation bubble typically has a global effect on the pressure distribution about the airfoil. Most notably, a long bubble tends to eliminate or reduce the suction peak near the leading edge of an airfoil and replace it with a plateau of constant pressure across the separation region. An example of the pressure plateau induced by a separation bubble is presented in Fig. 2.2, after Roberts.[19] Since the ice-induced separation bubble is so important in dictating the performance of an airfoil with a horn-ice shape, it has been a primary topic of study for airfoils with a horn-ice shape.

The structure of the horn-ice-induced separation bubble was described in detail by Gurbacki and Bragg.[20] As the tip of the horn-ice shape is approached by the air flow, the large adverse pressure gradient induced by the step from the ice shape tip to the airfoil surface causes the boundary layer to separate. A shear layer develops, forming vortices that enhance mixing, which allows the separated shear layer to gain energy and, at a sufficiently low angle of attack, reattach to the airfoil surface. This creates a separation bubble, which is characterized by a recirculation region across the forward section of the airfoil. A schematic of the ice-induced separation bubble in the airfoil flowfield is presented in Fig. 2.3, after Gurbacki and Bragg.[20]

Detailed split-film measurements in the ice-induced separation bubble were acquired by Bragg et al.[21] on an NACA 0012 airfoil. These authors identified the regions of reverse flow inside the separation bubble and estimated the location of turbulent transition in the shear layer using momentum thickness values calculated from the velocity measurements. The transition location determined using this method compared well with those determined from flow visualization and the airfoil C_p distributions.

Split-film measurements in the flowfield of an airfoil with a horn-ice shape were also obtained by Broeren et al.[22] in the NASA Langley LTPT. Data were acquired across the upper surface of an iced GLC-305 airfoil at Re = 3.5×10^6 and 6.0×10^6, with M = 0.12 and 0.21. These authors noted that the size of the separation bubble downstream of the horn-ice shape did not appear to change with Reynolds number. However, the size of the separation bubble did increase slightly as the freestream Mach number was increased. The presence of large values in the velocity RMS were also identified downstream of the shear-layer transition location.

A study by Gurbacki[6] investigated the unsteady flowfield effects produced due to the presence of a horn-ice shape. In this study, the effects of various unsteady components in the iced-airfoil flowfield structure were identified. Most notably, unsteadiness due to vortical motion (e.g. vortex pairing and shedding) and a low-frequency mode of unsteadiness were observed to affect the unsteady airfoil flowfield. Additionally, differences in the iced-airfoil flowfields between a three-dimensional ice shape casting and a two-dimensional extrusion of the ice shape casting were identified.

Following this study, the behavior of large-scale vortex shedding and the difference between the two-dimensional and three-dimensional flowfields was studied in detail by Jacobs.[23] Particle Image Velocimetry (PIV) was used to image the iced-airfoil flowfield and observe shear-layer reattachment and vortex-shedding characteristics. It was identified that the flowfield about a two-dimensional horn-ice shape produced an essentially two-dimensional separation bubble that lacked any significant spanwise variation. Conversely, a three-dimensional horn-ice shape, with variations across the span, produced streamwise vortex structures that made the flowfield notably different from that of the two-dimensional ice shape. These streamwise vortices produced three-dimensional variations to the size and shape of the separation bubble and shear layer across the span.[24] The spanwise structure associated with the three-dimensional casting led to a faster pressure recovery of the separated shear layer, and thus, a shorter mean reattachment length than the bubble associated with the two-dimensional ice shape.

2.2 Unsteady Flowfield Characteristics

Canonical geometries, like the backward-facing step, blunt flat plate, fence, or other obstacle, are oftentimes used to study separation bubbles. The separation bubble induced by a horn-ice shape in an airfoil flowfield has many fundamental similarities to the separation bubble in the flowfield about a simple geometry. As a result, many of the same unsteady flowfield characteristics present in the flowfields about simple geometries are also present in the flowfields of iced airfoils.

2.2.1 Canonical Geometries

While the canonical geometries used to study separation bubbles appear to be quite simple, the flows about them are extremely complex. Included in this complexity is the reattachment process, which has been shown to be attributed with various sources of unsteadiness. These sources of unsteadiness have been identified in measurements of local surface pressure,[25–33] shear stress,[34–37] velocity,[26,27,30–32,36–39] location of shear-layer reattachment,[31,32] and observed in flow visualization.[40,41] Additionally, unsteadiness in flows about these simple geometries have been studied using computational techniques.[42–47] While many investigations have been performed to study the flowfields about these canonical geometries, only a select number of the most relevant and seminal investigations will be discussed in detail throughout the subsequent sections.

2.2.1.1 Spectral Content Classification

There have been two main contributing sources of unsteadiness that have been identified in 2D separation bubble flowfields. The first source has been attributed to vortical motion, where large-scale vortices are regularly shed downstream of the separation bubble according to a bandwidth of frequencies. The second source of unsteadiness is represented by a low-frequency “flapping” of the shear layer, which causes large-scale unsteadiness in the separation bubble flowfield and a quasi-periodic enlargement and shrinking of the separation bubble. While both modes contribute to the unsteadiness in the separation bubble flowfield, the characteristics of these two modes are quite different.

Kiya and Sasaki[30] studied the large-scale vortex structure of the separation bubble across the surface of a blunt flat plate using unsteady velocity and surface pressure measurements. The regular mode of large-scale vortex shedding was observed to be periodic with a frequency scaling proportionally with freestream velocity and inversely with separation bubble length. These authors also identified large-scale shedding events of the separation bubble, which caused an enlargement and shrinkage of the bubble, along with a flapping motion of the shear layer near the location of separation.

Cherry et al.[26] studied the unsteady structure of the 2D separation bubble present on a blunt flat plate using a combination of pressure and velocity measurements, along with flow visualization. A point of emphasis within this study was to characterize the temporal and spatial correlation scales within various regions of the separation bubble. Additionally, changes in the spectral characteristics across the length of the separation bubble were identified. Sources of unsteadiness that were observed by these authors included shear-layer flapping near separation along with large-scale and small-scale vortex shedding near and downstream of the mean reattachment location.

Driver et al.[38] studied the primary modes of unsteadiness about the 2D separation bubble downstream of a backward-facing step using measurements of surface pressure and velocity. The directional intermittency in the velocity was measured at the surface using a thermal tuft probe, and the flowfield velocity was acquired using Laser Doppler Velocimetry (LDV). In addition to providing and discussing relevant spectral content in the measurements, these authors also discussed the impact of the shear-layer flapping process on the structure of the separation bubble and changes in shear stress in the flow. These authors acquired measurements at a freestream velocity that was significantly higher than most other investigations of flows about simple geometries. The resulting Reynolds number used in this study, based on the step height, was 37,000.

Heenan and Morrison[29] investigated the unsteady modes involved in a 2D separation bubble flowfield using unsteady pressure measurements taken on the reattachment surface downstream of a backward-facing step. Like many of the investigations prior, these authors identified a strong influence of shear-layer flapping and large-scale eddies in the reattaching flowfield. However, in addition to identifying the dominant modes in the spectral content, the influence of a permeable reattachment surface was studied along with the phase and streamwise convection characteristics of the regular and shear-layer flapping modes.

Spazzini et al.[35] developed a probe for measuring the wall skin friction in the vicinity of shear-layer reattachment downstream of a backward-facing step, and identified that the statistical characteristics of the separation bubble flow tends to scale primarily with changes in the mean reattachment length. These authors identified the influence of the regular mode and shear-layer flapping mode in the resulting spectra of the wall skin friction measurements. The changes in spectral content of the shear-layer flapping mode were also identified in the wavelet transform of the wall skin friction measurements, and an intermittent behavior in the shear-layer flapping mode was identified in the resulting wavelet transform contours. These authors conjectured that the observed cyclic nature of the shear-layer flapping mode was related to the time-dependent changes in the secondary recirculation region in the bubble observed in flow visualization.

Lee and Sung[32] used an array of microphones and hot-wire probes to evaluate the unsteady pressure, velocity, and forward-flow intermittency in the region downstream of a backward-facing step. These authors were able to determine spatio-temporal characteristics of the reattaching shear layer, including the effects of the primary modes of oscillation on the unsteady shear-layer reattachment location. Using a unique filtering approach, these authors related the periodic, low-frequency enlargement and shrinking process of the separation bubble length to fluctuations in pressure across the surface.

Hudy et al.[25] further characterized the unsteady behavior of the 2D separation bubble by studying the unsteady pressure across a splitter plate downstream of a fence geometry. In addition to discussing the two primary modes of unsteadiness, the convective trends of these modes were investigated in detail. Additionally, these authors proposed the presence of an absolute instability existing near the center of the separation bubble, which produces the shear-layer flapping phenomenon.

2.2.1.1.1 Regular Mode of Vortical Motion

In the literature, the source of the regular mode has almost unanimously been attributed to the Kelvin-Helmholtz instability, where the difference between the velocity within the recirculation region of the separation bubble and the external flow causes a roll-up and shedding of vortices in the shear layer.[31,48–50] In simple-geometry flowfields, this source of oscillation is typically associated with a Strouhal number range from 0.5 to 0.8, based on the mean length of the separation bubble and the freestream velocity.

Kiya and Sasaki[30] observed a regular, periodic shedding of vortices with dimensionless frequency ($\mathrm{St}_L = fL_r/U_\infty$) of 0.6. These large-scale vortices were observed to be spaced $0.7L_r$ to $0.8L_r$ apart, having a convection velocity near $0.5U_\infty$. Cherry et al.[26] identified the characteristic spectral content of the regular mode in the velocity spectrum taken just outside of the shear layer near reattachment, identifying a peak at a dimensionless frequency (St_L) near 0.7. Similar peaks were also identified in the pressure spectra near shear-layer reattachment and downstream of the separation bubble. In agreement with the results reported by Kiya and Sasaki,[30] Cherry et al.[26] also observed a streamwise spacing of vortices ranging from $0.6L_r$ to $0.8L_r$.

Similar values of dimensionless frequency for the regular mode have also been reported by other authors. In the velocity measurements by Driver et al.[38] at the downstream end of the separation bubble, the majority of the spectral content was identified at a dimensionless frequency (St_L) of 0.6. Hudy et al.[25] identified high-amplitude spectral content across the dimensionless frequency (St_L) range from 0.6 to 0.9 and attributed it to vortical structures in the shear layer. Other investigations observed the regular mode at slightly different frequencies. This includes Spazzini et al.[35] and Heenan and Morrison[29] where the regular mode was observed near $\mathrm{St}_L = 1.0$. A possible reason for the higher values of St_L reported in these studies will be discussed in Section 4.4.2. Additionally, Lee and Sung[32] observed the regular mode at $\mathrm{St}_h = 0.065$ ($\mathrm{St}_L = 0.48$), which was slightly lower than the typical range reported elsewhere in the literature.

2.2.1.1.2 Shear-Layer Flapping

The low-frequency oscillations associated with shear-layer flapping tend to operate across different frequency scales than those of the regular mode. In most simple-geometry flowfields, shear-layer flapping has been observed to be associated with Strouhal numbers on the order of 0.02 based on the height of the geometric feature and the freestream velocity, or on the order of 0.1 based on the mean length of the separation bubble and the freestream velocity. For example, the large-scale unsteadiness observed by Kiya and Sasaki[30] occurred at dimensionless frequencies (St_L) centered near 0.12. This unsteadiness was thought to be brought upon by an event where vortices, larger than the characteristic large-scale vortices of the regular mode, were shed periodically. As such, shear-layer flapping is representative of a large-scale shedding process of the separation bubble. Unlike the regular mode, there is not a current consensus on what causes the shear-layer flapping phenomenon to occur.

Kiya et al.[50] have theorized the existence of a feedback mechanism internal to the separation bubble that drives the low-frequency oscillations, where pressure fluctuations are generated by the impingement of large-scale vortices on the surface, which then progress upstream and affect the flowfield at the separation location. The existence of a feedback mechanism was later reinforced by Lee and Sung,[32] as these authors identified traits in the unsteady pressure that were characteristic of a standing wave at the shear-layer flapping frequency inside the separation bubble region. Conversely, Eaton and Johnston[3] considered the shear-layer flapping phenomenon to occur non-periodically due an imbalance between the rate of turbulent entrainment of fluid from the recirculation region into the separated shear layer and the rate of fluid reinjection from the reattaching shear layer into the recirculation region. Similarly, Driver et al.[38] thought it to be due to a temporary disorder of the roll-up and vortex pairing process in the shear layer.

The spectral content of the pressure measurements by Driver et al.[38] just upstream of the mean shear-layer reattachment location reveals a weak peak corresponding to shear-layer flapping at a dimensionless frequency (St_L) near 0.1. These authors commented that this peak was very weak in comparison to the peak produced by the regular mode, making it difficult to distinguish in the energy spectrum. Cherry et al.[26] also identified a spectral peak associated with shear-layer flapping at a dimensionless frequency (St_L) below 0.125 in the pressure spectra, which corresponded to characteristic frequencies below $\mathrm{St}_h = 0.025$. However, these authors discussed how the shear-layer flapping peak tended to dominate the pressure spectra within the upstream region of the separation bubble and have a decreasing effect further in the downstream direction. This is likely the reason why the low-frequency peak was difficult to discern by Driver et al.,[38] as the pressure spectra was determined by these authors from measurements near the downstream end of the separation bubble.

Shear-layer flapping was identified by Heenan and Morrison[29] at a dimensionless frequency (St_L) of 0.1 for the flow about the backward-facing step with an impermeable reattachment surface. At this frequency, pressure fluctuations were observed in the phase angle distributions to be convected in the upstream direction in the region upstream of $x/x_r = 0.4$. However, when the impermeable reattachment surface was replaced with a permeable surface, the upstream convection of the pressure waves at the shear-layer flapping frequency was no longer observed near the step and the spectral content of the shear-layer flapping frequency was significantly attenuated. As a result, the shear-layer flapping unsteadiness was thought to be regulated by a mechanism based on the upstream convection of low-frequency pressure signals across the leading-edge region of the separation bubble.

Hudy et al.[25] observed shear-layer flapping at a dimensionless frequency (St_L) range of 0.12 to 0.18. Interestingly, a non-dimensionalization of the shear-layer flapping frequency by the step height of the fence yielded a height-based Strouhal number that was not consistent with those reported in the literature for other geometries. However, when the total fence height was used as the vertical length scale, the height-based Strouhal number for shear-layer flapping corresponded to the range of St_h = 0.02–0.03, which is consistent with the literature. These authors also identified an upstream convection of the shear-layer flapping frequency at an average rate of $0.21U_\infty$ within the region upstream of $0.25x_r$.

2.2.1.2 Shear-Layer Reattachment Location

The first indications of unsteadiness in the shear-layer reattachment process downstream of a backward-facing step were reported by Abbott and Kline[40] and Kim et al.[51] It was then concluded by Eaton[52] that downstream of a backward-facing step, shear-layer reattachment occurred across a zone, rather than at a discrete location. This author was also able to identify key differences between the free shear layer and the reattaching shear layer. The presence of large-eddy structures near the mean reattachment location was also identified, and a low-frequency flapping of the shear layer reattachment location was observed.

The oscillations in the shear-layer reattachment location due to vortical motion and shear-layer flapping have also been identified in many subsequent investigations. Kiya and Sasaki[31] studied the reattaching flow about a blunt flat plate, and developed a mathematical model to describe the movement of the shear-layer reattachment location due to these various sources of flowfield unsteadiness. This model described the unsteady location of shear-layer reattachment as having contributions due to a standing wave of frequency $f_1 = 0.108U_\infty/x_r$ and amplitude $U_1 = 0.10U_\infty$, and a traveling wave of frequency $f_h = 0.65U_\infty/x_r$ and amplitude $U_h = 0.18U_\infty$. The convection speed of vortical motion was also determined to be, on average, approximately

$0.5U_\infty$. These authors also identified the structure and motion of large-scale vortex shedding in the separation bubble flowfield.

Lee and Sung[32] also identified similar classifications of spectral content in the reattaching shear layer downstream of a backward-facing step. Notably, these authors identified a sawtooth pattern in the unsteady shear-layer reattachment location when a vortex shedding event occurred. These spanwise vortical structures were observed to be convected at a speed of $0.6U_\infty$. A global bubble enlargement/shrinkage cycle was also observed to occur together with the low-pass filtered component of the pressure measurements. This allowed a time-dependent relationship between the low-frequency component of the surface pressure and reattachment location to be established. The unsteadiness in the shear-layer reattachment location in a canonical geometry flowfield has also been imaged using PIV[53] and computed using CFD.[44–47] Additionally, the sawtooth pattern associated with the regular mode was identified in the time-resolved PIV of the separation bubble on an airfoil by Burgmann and Schröder.[54]

2.2.2 Airfoil Flows

While the unsteadiness induced by separation bubbles is commonly studied about canonical geometries, the presence of a separation bubble on an airfoil flowfield can also produce both local and global unsteadiness in the flowfield about an airfoil. Various modes of unsteadiness have been identified in the flowfield produced by the ice-induced separation bubble on an airfoil, as well as the separation bubble flowfields generated on clean airfoils operating at low Reynolds numbers.

2.2.2.1 Clean Airfoil Low-Frequency Oscillation

A low-frequency flowfield oscillation can sometimes occur prior to static stall for certain types of airfoils. Investigation of this phenomenon was first pursued in great detail by Zaman et al.[4] on an LRN(1)-1007 airfoil across a Reynolds number range from 4×10^4 to 1.4×10^5. At this range of Reynolds numbers, this airfoil exhibits a mixed thin-airfoil and trailing-edge stall type. These authors identified that a high-frequency acoustic excitation of the flowfield could eliminate the leading-edge laminar separation bubble on the airfoil, which suppressed the separation-induced unsteadiness. Similar low-frequency oscillations were observed by Bragg et al.[55] for the same airfoil operating at Reynolds numbers from 3×10^5 to 1.4×10^6. The observations reported in these studies were further verified by Zaman et al.[56] who performed additional investigation into the low-frequency oscillations present in the flowfield about various airfoil geometries prior to stall at low Reynolds numbers. These authors identified that these low-frequency oscillations were an order of magnitude less than those expected for bluff body shedding, and were shown to be fundamentally different than von Kármán vortex shedding. While an appropriate length scale for non-dimensionalizing this unsteady phenomenon was not identified, these authors observed that the low-frequency oscillations tended towards a Strouhal number based on the projected height of the airfoil ($\mathrm{St}_h = fc\sin\alpha/U_\infty$) on the order of 0.02.

Bragg et al.[5] further studied the low-frequency oscillations present in the flowfield about the LRN(1)-1007 airfoil across a range of Reynolds numbers from 0.3×10^6 to 1.25×10^6 and angles of attack from 14.4° to 16.6°. While the resulting St_h appeared to increase slightly with increased Reynolds number, a much larger increase in St_h was observed with increased angle of attack. These authors attributed the low-frequency unsteadiness to the transitional separation bubble present across the leading edge of the airfoil. By tripping the leading-edge boundary layer and eliminating the separation bubble, the low-frequency oscillations were suppressed.

These low-frequency oscillations about the LRN(1)-1007 were further investigated by Broeren and Bragg,[57] who characterized the low-frequency oscillations using phase-averaged LDV and hot-wire data. A clear, periodic stalling and unstalling behavior was identified for the LRN(1)-1007 airfoil. Both the leading-edge separation bubble and the trailing-edge turbulent separation in the airfoil flowfield appeared to have an influence on this periodic stalling behavior of the airfoil.

Low-frequency oscillations were also studied in detail in a later investigation by Broeren,[58] who observed these types of oscillations in the flowfields about various airfoils operating at Reynolds numbers of 3×10^5. Six of the 12 airfoils tested in this investigation exhibited low-frequency oscillations prior to stall, all of which were classified as having either a thin-airfoil stall type or a mixed thin-airfoil and trailing-edge stall type. For the mixed thin-airfoil and trailing-edge stall type, the presence of the trailing-edge separation appeared to amplify the unsteadiness associated with the leading-edge laminar separation bubble. The low-frequency oscillations were not identified for any airfoils that were associated with a leading-edge stall type or a pure trailing-edge stall type at the Reynolds number tested.

Rinoie and Takemura[59] also identified a low-frequency oscillation in an airfoil flowfield near stall in LDV measurements taken about an NACA 0012 airfoil at a Reynolds number of 1.3×10^5. Similar to the observations of Broeren and Bragg,[57] these authors identified a similar quasi-periodic stalling and unstalling behavior of the airfoil, which was governed by the extent of the leading-edge separation region in the airfoil flowfield, which changed throughout the low-frequency oscillation cycle. The separation bubble on the airfoil surface and its effects at different phases of the oscillation cycle were also compared to the "short" and "long" bubble classifications of Tani.[18] These short bubbles can become regions of massive separation through a process known as "bursting," as described by Gaster.[60]

Similar observations were made in the LES results by Almutairi and AlQadi[61] for an NACA 0012 airfoil at a Reynolds number of 5×10^4. These authors also identified a switching from a short laminar separation bubble to a fully separated flow over the airfoil upper surface, which was brought on by a growth and bursting of the laminar separation bubble. A mechanism for this low-frequency oscillation was also proposed by these authors, where an absolute instability in the separation bubble causes the growth of the bubble and stall of the airfoil, and an interaction of the separated shear layer and the leading-edge flowfield leads to subsequent reattachment.

Sandham[62] also described the low-frequency oscillation that can occur for clean airfoils near stall. This author used a time-accurate method for computing the coupled potential flow and integral boundary-layer equations in order to calculate the unsteady pressure distribution and boundary-layer parameters. A low-frequency oscillation was observed near stall in the time-dependent lift coefficients computed for clean NACA 0012 and E374 airfoils. This oscillation was observed to be directly related to the growth, bursting, and reformation of a separation bubble. The bursting of the separation bubble was reported to be caused by a "runaway" effect, where the interaction of the displacement thickness in the separation bubble region with the potential flow leads to the bursting of the separation bubble. This bursting of the separation bubble causes the airfoil to stall, and the reduced adverse pressure gradient associated with the stalled C_p distribution allows the separation bubble to reform at the airfoil leading edge.

2.2.2.2 Iced-Airfoil Spectral Content Classification

Similar classifications of unsteadiness have also been identified in the flowfields about airfoils with a leading-edge, ice-induced separation bubble. Low-frequency oscillations in the flowfield of an airfoil with a leading-edge horn-ice shape were identified by Zaman and Potapczuk.[63] These authors observed a low-frequency oscillation in the iced-airfoil flowfield in both experimental and computational results. Hot-wire anemometry was used to measure the unsteady wake velocity downstream of the iced airfoil at three Reynolds numbers, and a dominant frequency of oscillation was identified in the wake velocity spectra. The low frequencies of oscillation at $\alpha = 8.5°$ across all three Reynolds numbers universally corresponded to a Strouhal number of 0.02. The low-frequency oscillations in the computational results were taken from the unsteady lift coefficient for the iced airfoil. These oscillations in the iced-airfoil lift coefficient at $\alpha = 9°$ and $\alpha = 10°$ corresponded to slightly lower Strouhal numbers of 0.008 and 0.011, respectively. This low frequency of oscillation was thought to be linked to the thin-airfoil stall type of the iced airfoil and were related by these authors to the low-frequency unsteadiness present in the flowfield of the LRN(1)-1007 airfoil prior to stall.

Bragg et al.[21] also identified a low-frequency oscillation in the split-film measurements acquired in the shear layer downstream of a horn-ice shape on an NACA 0012 airfoil. A peak in the spectral content of the velocity in the shear layer at $\alpha = 4°$ revealed a low-frequency peak at 11.6 Hz. This frequency corresponded to a Strouhal number ($\mathrm{St}_h = fh/U_\infty$) of 0.0185, which was similar to the Strouhal number reported in the experimental portion of Zaman and Potapczuk.[63]

The unsteady content of the iced-airfoil flowfield was further analyzed by Gurbacki[6] for an NACA 0012 airfoil with a leading-edge horn-ice shape. It was discovered that the iced-airfoil performance and distributed surface pressure had a similar classification of unsteady content as the 2D separation bubble flowfields about simple geometries. These classifications of unsteady content included a low-frequency mode and a regular mode of vortical motion. The low-frequency mode was associated with Strouhal numbers (St_h) ranging from 0.0048 to 0.0101, where the resulting Strouhal number was observed to have a dependence on airfoil angle of attack. The regular mode was associated with Strouhal numbers (St_L) ranging from 0.53 to 0.73, which was the same range as reported in the literature for simple geometries. Additionally, the convective qualities of these frequencies were analyzed, and the average convection velocity of vortices was determined to be approximately half of the freestream velocity.

2.3 Prior Use of Hot-Film Arrays

As part of the current investigation, a new technique was developed for determining the unsteady reattachment location downstream of a large flow obstacle using a surface-mounted hot-film array. This technique will be reported in Section 3.6. Development of this method was heavily influenced based on prior work with hot-film arrays discussed in the literature.[64–68] Stack et al.[68] first identified that hot-film arrays could be used to identify time-averaged flowfield features on an airfoil surface. It was observed that a location of laminar separation could be determined by identifying the location of minimum voltage output, corresponding to a minimum in the magnitude of local shear stress. These authors also identified a phenomenon where the time-averaged location of laminar separation or turbulent reattachment was observed to correspond with a location on the hot-film array exhibiting a reversal in signal phase between adjacent sensors.

The cause of this reversal in the signal phase between adjacent sensors has been attributed to the flow bifurcation that occurs at reattachment,[67] and is due to the difference in flow direction near the stagnation point at reattachment. This method was later used by Lee and Mateescu[67] to determine the mean shear-layer reattachment location downstream of a backward-facing step. Reattachment locations were determined for various Reynolds numbers and were in agreement with prior experimental and numerical investigations.

Olson and Thomas[64] developed a slightly different scheme for measuring the mean reattachment location by using a hot-film array mounted downstream of a backward-facing step. They used the relative shift in the phase spectrum between adjacent sensors to generate a "time of flight" of given Fourier modes at discrete frequencies. The sign of the calculated time of flight between two given sensors was used to determine whether that sensor interval resided upstream or downstream of the mean reattachment location, with zero time of flight corresponding to the mean reattachment location. It was also discovered in this investigation that at the location of reattachment, there was a decrease in the linear coherence between adjacent sensors over a low-frequency range.

2.4 Performance Monitoring Systems

In an effort to utilize the improved understanding of ice-induced airfoil flowfield unsteadiness from the current study, the characterization of the low-frequency mode will be applied to the development of a performance monitoring system. Stall warning on a conventional, fixed-wing aircraft is commonly provided through a simple angle-of-attack system, composed of a pivoting vane element and supporting equipment. For such systems, the angle of attack can be measured, and a stall warning can be provided when a pre-programmed threshold in angle of attack is reached. While these systems have proven to be reliable for most clean-aircraft applications, they are not fully adaptive to the state of an aircraft under adverse conditions.

For example, the time-averaged effects of icing are relatively well known, and can severely degrade the aerodynamic performance of a vehicle, as outlined in Section 2.1. This performance degradation is typically associated with a reduction in stall angle of attack. Traditional angle-of-attack systems, like those mentioned previously, compensate for the ice-induced reductions in maximum lift and stall angle of attack by reducing the angle of attack at which a stall warning would be provided when the icing protection system is turned on. While the angle-of-attack reduction is highly aircraft dependent, conventional angle-of-attack systems on business jets are programmed to reduce the angle of attack where the stall warning is provided by approximately 3–5 degrees when the icing protection system is engaged.[69] However, the aerodynamic penalties associated with some of the most severe ice shapes can lead to reductions in stall angle of attack in excess of the angle-of-attack compensation built into the angle-of-attack system and icing protection system logic.

For this reason, various forms of performance monitoring systems have been developed, which can be used in addition to the traditional angle-of-attack system. A performance monitoring system is a device or collection of equipment that can be used to provide information and awareness of the state of an aircraft to the aircraft flight crew. As such, a performance monitoring system can provide, for example, an advisory of an impending aircraft stall or departure from the normal flight envelope. While numerous systems have been developed, only some of the more established systems will be discussed here.

A method for predicting an impending stall on an aircraft wing was developed by Maris,[70] based on a series of wind tunnel tests. In this system, a hot-wire probe is used to measure the turbulence intensity at a prescribed location on the wing. A trailing-edge type stall, which is the typical stall type associated with large transport aircraft, is associated with boundary-layer separation across the trailing-edge portion of the wing before stall. As the boundary layer across the trailing-edge section edges closer towards separating, it tends to become thicker and more turbulent. As a result, when the measured turbulence intensity crosses a prescribed threshold, stall is known to be imminent.

A similar system was later introduced by Maris,[71] where the comparative turbulence intensities from sensors located at two different locations on a mast structure are used in producing the stall warning prediction. When the slope of the turbulence intensity ratio between the two sensors reaches a critical slope with respect to the DC voltage output of the forward sensor, then the system outputs an advisory of an impending stall. Additionally, this system has shown to be able to predict premature stalls due to icing and roughness.

A system that uses the aircraft as a sensor to predict ice, known as the Dynamic Icing Detection System (DIDS) was introduced by Myers et al.[72] This system uses the estimated state of the aircraft, including parameters like drag coefficient, static margin, and elevator effectiveness, to detect the presence and effects of ice on the aircraft. By estimating the effects of the ice on the aircraft performance, this system would be capable of protecting against a hazardous excursion from the flight envelope that might otherwise be unknown to the flight crew.

Similarly, Gingras et al.[73] proposed an envelope protection system for in-flight ice accretion, known as the Icing Contamination Envelope Protection (ICEPro) system, based on the concept of using the aircraft as a sensor. With the nominal aircraft performance parameters known *a priori*, the real-time state of the aircraft is compared to its nominal counterpart. Based on the residuals of this comparison, an estimation of the current envelope limits can be provided. These authors comment that since most of the required information for this system is already incorporated into the avionics of most modern aircraft, little additional implementation would be required for such a system to function.

2.4.1 Hinge Moment Based Stall Prediction for Airfoils

An alternative to these types of systems was first introduced by Gurbacki and Bragg,[74] who proposed a stall-prediction system for iced airfoils based on unsteady flap hinge moment measurements. These authors tested an NACA 23012 airfoil with a simple flap under clean and simulated glaze-ice configurations. For the iced case, as stall was approached the ice-induced separated flow in the airfoil flowfield increased the amount of unsteadiness present in the hinge moment measurements, as evaluated by the hinge moment signal RMS. This ice-induced unsteadiness was not present in the clean airfoil configuration. As a result, a correlation was discovered between the ice-induced separated flow prior to stall and the increase in unsteadiness in hinge moment measurements. Thus, it was proposed that the unsteady hinge moment measurements could be used to predict ice-induced stall.[75] This stall prediction method was also proposed to be used as a part of Smart Icing Systems.[76]

A later study by Ansell et al.[7] applied the original concept of Gurbacki and Bragg,[74] and developed a stall prediction system for airfoils in clean or contaminated configurations based solely on hinge moment measurements. These authors tested an NACA 3415 airfoil model with a simple flap under an array of simulated contaminants. A data reduction system was developed for these hinge moment measurements that provided a consistent stall prediction across most simulated contamination configurations. These authors analyzed the flap hinge moment unsteadiness using a system of three "detector functions," which operated on the unsteady hinge moment signal differently. The output of these three detector functions are presented in Fig. 2.4 as a function of angle-of-attack margin to stall ($\alpha - \alpha_{stall}$), after Ansell et al.[7] As discussed by these authors, since the detector function outputs of all of all leading-edge contamination configurations tended to collapse towards a single trend, a stall warning could be produced at a prescribed angle-of-attack margin prior to stall when a threshold is reached in the detector function outputs. The resulting error in the stall prediction results for an example margin of $\alpha - \alpha_{stall} = 2°$ is presented in Fig. 2.5, after Ansell et al.[7] This system was also effectively extended for use in predicting the sectional stall on an NACA 3415 semispan wing.[77]

Consistent stall predictions were also produced when the system of Ansell et al.[7] was used on an NACA 23012 airfoil.[78] However, the addition of a simulated horn-ice shape on the NACA 23012 model led to changes in the unsteady hinge moment behavior near stall that were distinctly different from other types of simulated leading-edge contamination configurations, which produced an outlying case. This outlying case can be observed in the detector function outputs presented in Fig. 2.6, after Ansell et al.[78] From Fig. 2.6, the trend of increasing hinge-moment unsteadiness with increasing $\alpha - \alpha_{stall}$ for the horn-ice case is inconsistent with the other contamination configurations tested by these authors. For the horn-ice case, a premature stall warning would be provided by the hinge-moment-based system, as the threshold in detector function output would be reached prior to the desired angle-of-attack margin to stall. As a result, additional understanding of the unsteadiness associated with these types of ice shapes is necessary for the continued development of a hinge-moment based stall prediction system.

2.5 Chapter 2 Figures

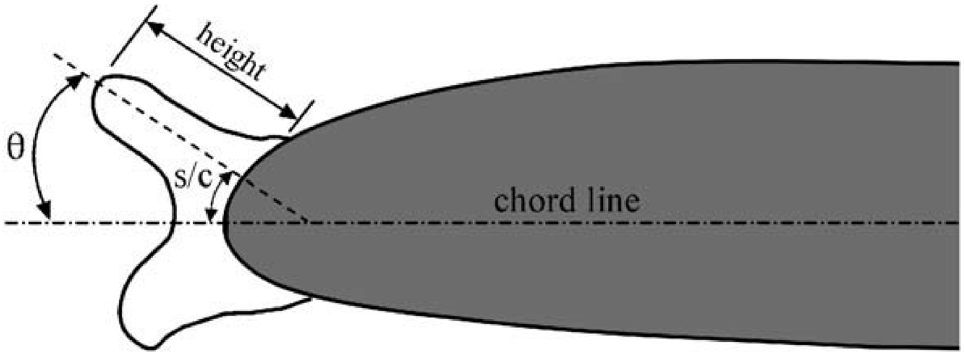

Fig. 2.1 Geometry of a horn-ice shape, after Bragg et al.[1]

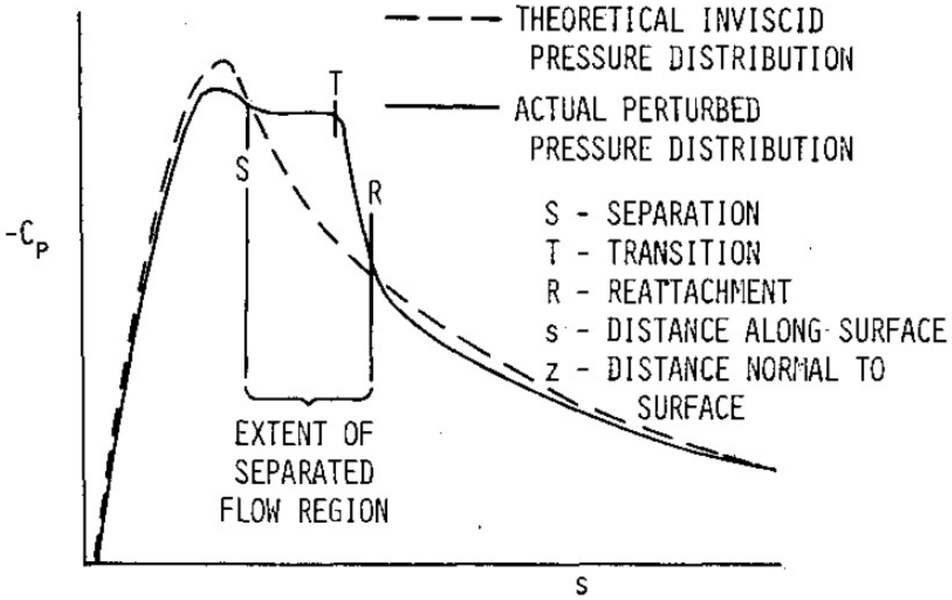

Fig. 2.2 Effect of separation bubble on airfoil C_p distribution, after Roberts.[19]

Fig. 2.3 Schematic of ice-induced separation bubble, after Gurbacki and Bragg.[20]

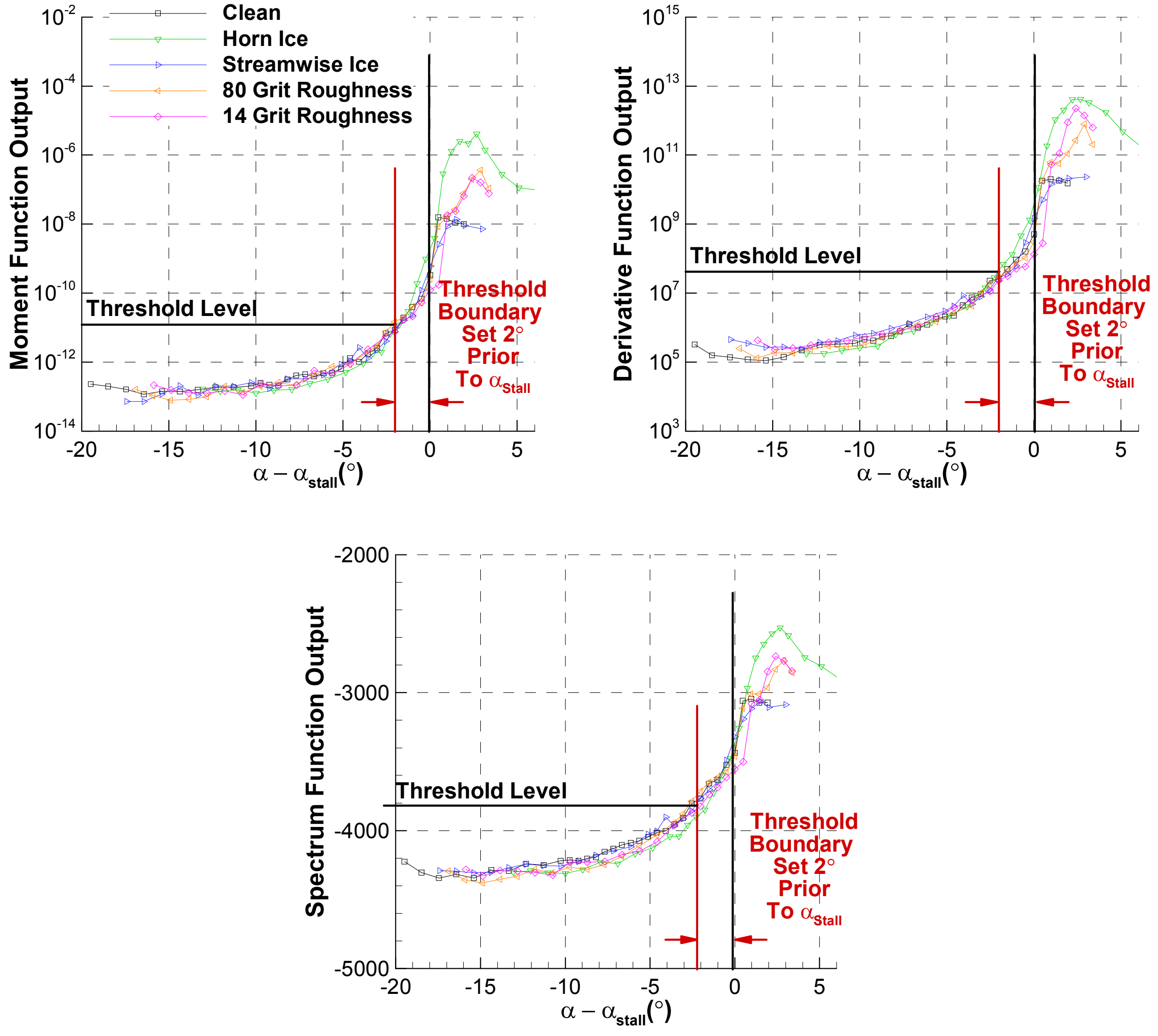

Fig. 2.4 Detector function outputs with respect to angle-of-attack margin to stall for unsteady hinge moment measurements on NACA 3415, adapted from Ansell et al.[7]

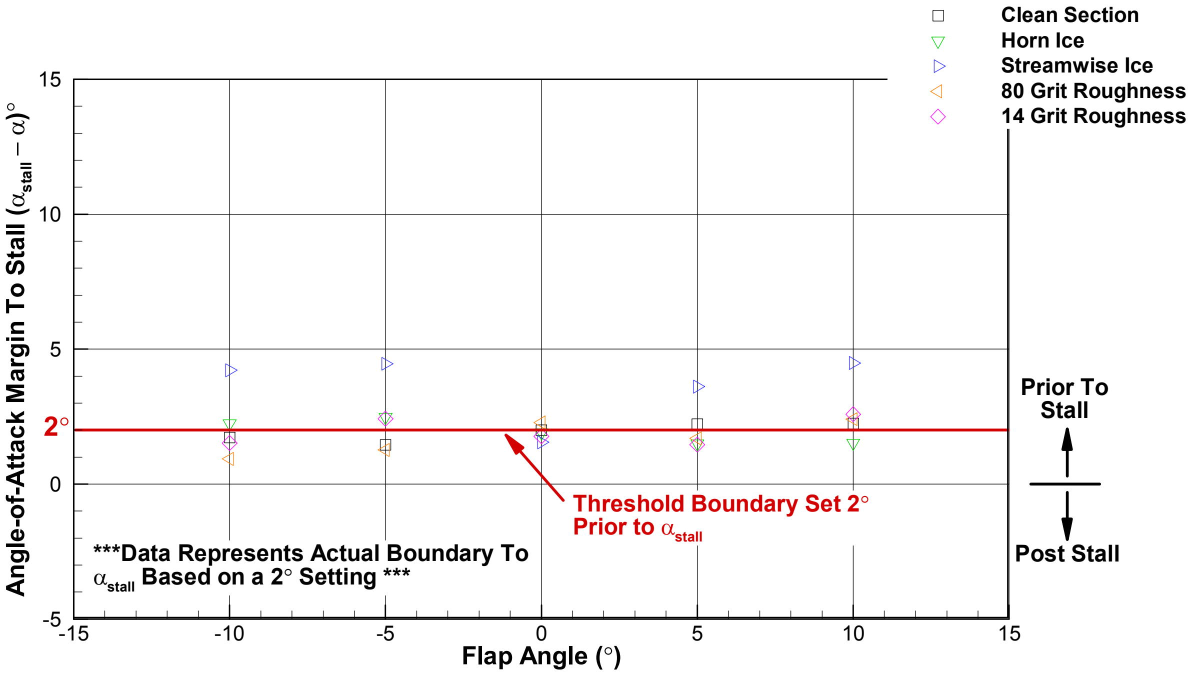

Fig. 2.5 Results for hinge-moment-based stall prediction system on NACA 3415 airfoil for $\alpha - \alpha_{stall} = 2°$, adapted from Ansell et al.[7]

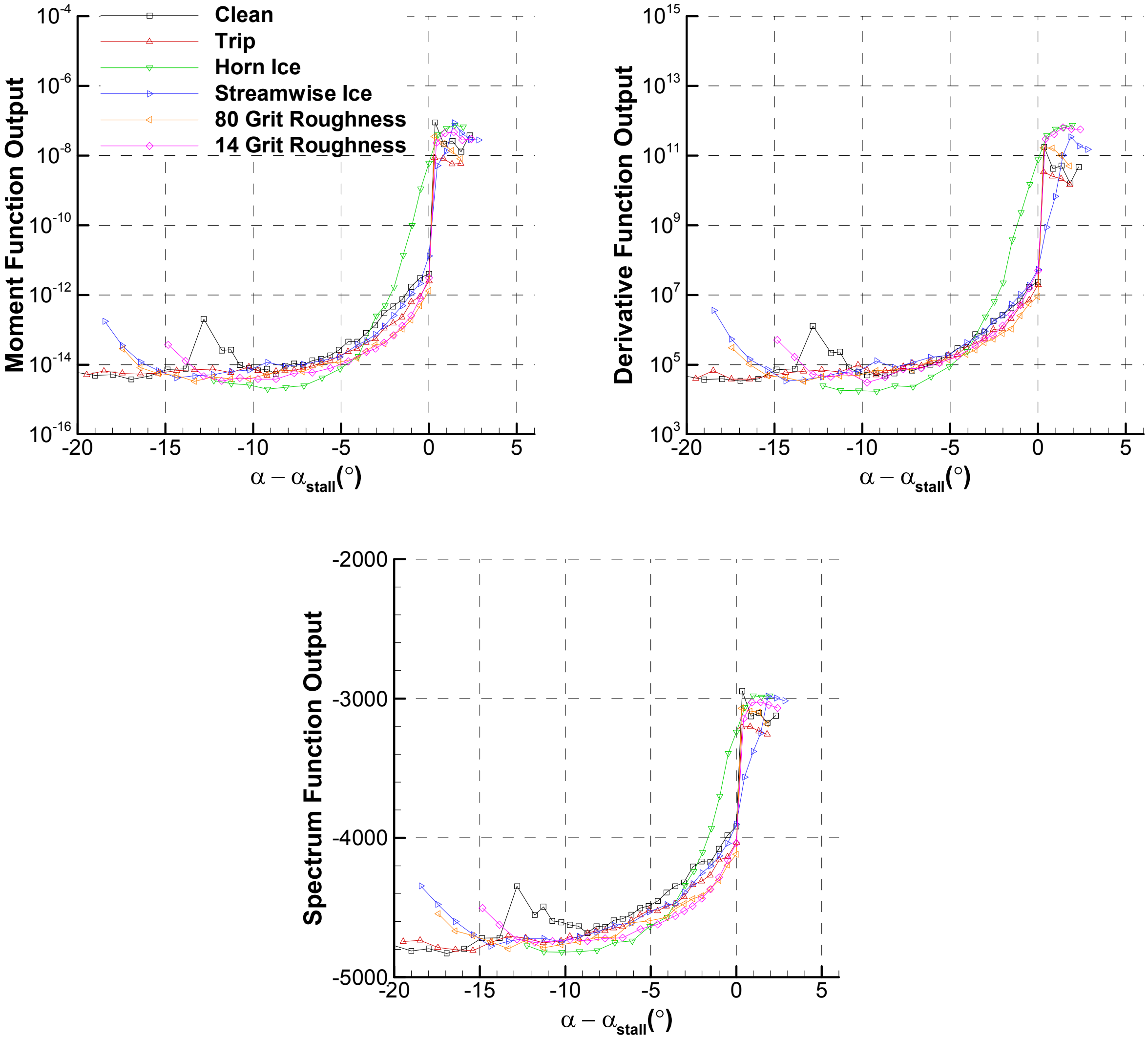

Fig. 2.6 Detector function outputs with respect to angle-of-attack margin to stall for unsteady hinge moment measurements on NACA 23012, adapted from Ansell et al.[78]

Chapter 3

Experimental Methods

This chapter describes the experimental methods and facilities used in this investigation. It provides descriptions and details of the experimental equipment, data acquisition practices, and data reduction methods that were used.

3.1 Testing Environment

All experimental aspects of this investigation were conducted at the Aerodynamics Research Laboratory at the University of Illinois at Urbana–Champaign. This laboratory is split into a control room, which is the primary location of all data acquisition equipment, and a test high bay, which houses two subsonic wind tunnels. A general layout of the Aerodynamics Research Laboratory is presented in Fig. 3.1 after Jacobs.[23]

3.1.1 Wind Tunnel

All aerodynamic testing was performed using a subsonic, low-turbulence, open-return-type wind tunnel. The test section of this wind tunnel was rectangular, measuring 2.8 ft × 4 ft, and extending a total downstream length of 8 ft. In order to account for boundary-layer growth through the test section, the downstream end of the test section was 0.5 in. wider than the upstream end. The inlet section of the wind tunnel contained a four-inch thick honeycomb flow straightener, as well as four stainless steel anti-turbulence screens. This flow conditioning configuration effectively reduced the turbulence intensity in the test section below 0.1% for all operating speeds. The contraction section of the wind tunnel reduced the sectional area from the inlet to the test section at an area ratio of 7.5:1. A schematic of the wind tunnel is presented in Fig. 3.2.

The wind tunnel was powered by an ABB ACS 800 Low Voltage AC Drive, which regulated a 125-horsepower AC motor. This electric motor was used to drive a five-bladed fan near the end of the tunnel diffuser. The maximum motor setting was approximately 1200 RPM, which resulted in a maximum empty test section speed of approximately 165 mph (242 ft/sec). This resulted in a maximum streamwise Reynolds number of 1.5×10^6 / ft. The chord-based Reynolds number of an airfoil model was calculated using,

$$\mathrm{Re} = \frac{\rho U_\infty c}{\mu} \tag{3.1}$$

where U_∞ represented the test-section freestream velocity, c represented the airfoil chord, ρ represented the air density, and μ represented the air dynamic viscosity. During wind tunnel testing, the chord-based Reynolds number was computer-controlled to within 0.50% of the set value. All commands to the ABB variable frequency drive (VFD) were sent using RS-232 communication from the data acquisition computer to a Keithley M1000 RS-232/RS-485 converter/repeater, which then routed these commands to the VFD.

The test-section freestream velocity was calculated based on the difference in static pressure (ΔP) between the inlet settling section and the test section ($P_{ss} - P_{ts}$). The value of ΔP was measured using a Setra 239 15 in. WC differential pressure transducer. A set of four pressure taps located just downstream of the anti-turbulence screens, with one tap located on each of the four tunnel walls, were connected through a single tube to the reference side of the pressure transducer. This provided an average static pressure of the inlet settling section, P_{ss}, to the transducer. Similarly, a set of four pressure taps located just upstream of the test section, with one tap located on each of the four tunnel walls, were connected through a single tube to the sensing side of the differential pressure transducer. This provided an average static pressure of the test section, P_{ts}, to the transducer. The resulting measurement by the differential pressure transducer provided the difference in static pressure across the wind tunnel inlet, ΔP.

With ΔP known, the velocity of the test section could be calculated using the well-known Venturi effect. Assuming a steady, inviscid, and incompressible flow through the tunnel, the law of conservation of mass can be expressed using Eq. 3.2. Similarly, Bernoulli's equation can be reduced to Eq. 3.3. Combining Eq. 3.2 and Eq. 3.3, the resulting test section speed could be calculated using Eq. 3.4.

$$A_{ss}U_{ss} = A_{ts}U_{ts} \tag{3.2}$$

$$\frac{1}{2}\rho U_{ts}^2 + P_{ts} = \frac{1}{2}\rho U_{ss}^2 + P_{ss} \tag{3.3}$$

$$U_{ts} = \sqrt{\frac{2\left(P_{ss} - P_{ts}\right)}{\rho_{amb}\left(1 - \left(\frac{A_{ts}}{A_{ss}}\right)^2\right)}} \tag{3.4}$$

In Eq. 3.4, the ratio of A_{ts}/A_{ss} represents the reciprocal of the contraction area ratio. Similarly, ρ_{amb} was the ambient air density. This density could be calculated using the ideal gas law,

$$\rho_{amb} = \frac{P_{amb}}{RT_{amb}} \tag{3.5}$$

where R was the ideal gas constant for air. Eq. 3.5 also required the ambient pressure (P_{amb}) and ambient temperature (T_{amb}). P_{amb} was measured using a Setra 270 absolute pressure transducer, and T_{amb} was measured using an Omega thermocouple.

3.1.2 Airfoil Model

The current study was performed using a single-element NACA 0012 airfoil model. This airfoil model was constructed from machined aluminum, and had an 18 in. chord and 33.563 in. span. The model was constructed in three separate pieces, consisting of an upper-surface section, a lower-surface section, and a leading-edge section. Additionally, the model was machined with two access panels on the lower surface. The upper-surface section and the leading-edge section were joined at the 5% chordwise location on the upper surface, and the lower-surface section and the leading-edge section were joined at the 10% chordwise location on the lower surface. One of the reasons why the airfoil model leading-edge section was constructed separately from the rest of the airfoil model was to allow for the clean NACA 0012 airfoil leading-edge contour to be replaced with that of an iced leading-edge section. The simulated leading-edge ice shapes used in this investigation will be discussed in greater detail in Section 3.1.2.1. The upper surface and lower surface were joined using 14 fasteners that ran through the lower surface section and into tapped holes on the inside of the upper surface section. These fasteners did not protrude through the upper surface of the model, retaining the high surface quality of the finished aluminum across the upper surface. The fastener holes on the lower surface were filled with modeling clay and smoothed to the airfoil contour. The NACA 0012 model was mounted vertically in the test section, spanning the tunnel floor to the tunnel ceiling, with a 0.02 in. gap at both walls. A photograph of the NACA 0012 airfoil model installed in the wind tunnel test section with the clean leading-edge section is presented in Fig. 3.3.

The NACA 0012 airfoil model was constructed with 67 surface pressure taps distributed in the chordwise direction across the airfoil upper and lower surface, which was used for acquiring time-averaged static pressure measurements. The model also had 19 taps at $x/c = 0.70$ distributed across the span to identify flow uniformity near the tunnel walls. Of the chordwise taps, 37 were distributed across the airfoil upper surface and 28 were distributed across the airfoil lower surface, with two additional taps also located at the model leading edge and trailing edge. In order to minimize the effects of bypass transition induced by one tap on the measurement from a downstream tap, the taps between the leading edge and the model mid-chord were aligned at an angle of approximately 15° from the freestream direction. Therefore, if one tap did cause bypass transition to occur, the taps downstream of this location would be outside the region of the turbulent wedge. Downstream of the model mid-chord to the model trailing edge, the taps were aligned at an angle of approximately 15° back towards the model mid-span, since natural transition would be more likely to have already occurred across these chordwise locations. The tap orifices were 0.025 in. in diameter, and were machined perpendicular to the airfoil surface. Each orifice was connected to a stainless steel tube at the tap location. Polyurethane pneumatic tubing was then connected to each of the stainless steel tubes, and these polyurethane tubes were routed out of the model through a hole in either of the two mounting spars.

The NACA 0012 model was also outfitted with a suite of ultra-miniature, high frequency response pressure transducers, which were integrated into the airfoil model surface at the model mid-span. These pressure transducers were manufactured by Kulite Semiconductor Products, Inc. under model XCS-062. All pressure transducers were configured and calibrated by the manufacturer for a ±5 psi differential maximum pressure. The pressure transducers were cylindrical, having a length of 0.375 in. and a diameter of 0.066 in. A screen was installed by the manufacturer on the sensing side of each transducer. Each transducer also had four lead wires and a reference tube, which allowed a pressure to be supplied to the reference side of the transducer. The lead wires were routed to a designated temperature compensation module for each transducer. The signal wires out of the temperature compensation modules could then be used to provide excitation to and obtain voltage measurements from the pressure transducer.

The model had a total of 37 of these pressure transducers integrated in the airfoil model surface. Of these transducers, 22 were integrated into the model upper surface and 13 were integrated into the model lower surface, with two additional pressure transducers located at the model leading edge trailing edge. Each of the reference tubes of these pressure transducers were connected to a separate polyurethane tube. All of the polyurethane tubes for the transducer references were then connected to a common pressure manifold, such that a common reference pressure would be supplied to all of the transducers. There was also an access panel machined into the model lower surface over the pressure manifold to allow easy access to the pressure manifold. The pressure manifold reference pressure supply was connected to a polyurethane tube, which was then routed out the model through the model mounting spar at the quarter-chord location. During testing, this transducer reference pressure tube was connected to the test section static pressure of the tunnel, such that the differential pressure measurements of the pressure transducers were made in reference to the freestream conditions.

3.1.2.1 Simulated Airfoil Icing

The effects of icing were simulated in this investigation using a geometrically-scaled casting of a horn-ice shape. The leading-edge ice shape used in this investigation was the same 3.5-minute glaze shape tested by Gurbacki.[6] The original ice shapes were acquired in the BFGoodrich Icing Wind Tunnel in Uniontown, OH. The original accretion was acquired on an NACA 0012 airfoil model, and was acquired with T_0 = 27.5 °F, LWC = 0.55 g/m^3, and MVD = 20 μm. Three-dimensional castings of the ice shape were acquired, and the accretion was geometrically scaled for use on an 18 in. chord NACA 0012 model. In this investigation, a two-dimensional extrusion of the ice shape was tested in order to minimize any spanwise variations in the iced-airfoil flowfield. A diagram of the contour of this ice shape is presented in

Fig. 3.4 after Gurbacki.[6] Additional details of the icing wind tunnel facilities and acquisition of the ice shapes can be found in Gurbacki.[6]

The leading edge with the horn-ice shape was constructed in three sections. The center section was 0.625 in. thick in the spanwise direction, was constructed of machined aluminum, and housed all of the instrumentation of the iced leading-edge section. The other two iced leading-edge sections were created using stereolithography (SLA) methods, and were mounted on either side of the span of the instrumented iced leading-edge section. These two iced leading-edge half-sections were joined to the airfoil model upper surface using three fasteners and two aligning pins per half-section. Like the fasteners used to join the upper and lower surface sections of the model, the fasteners used for these leading-edge sections ran through the lower surface of the iced leading-edge section and into tapped holes on the inside of the upper surface section. A picture of the NACA 0012 airfoil model with the iced leading-edge section is presented in Fig. 3.5. The instrumented portion of iced leading-edge contained 22 pressure taps and 5 unsteady, surface-integrated pressure transducers. The pressure tubes and pressure transducer wires were routed through a cavity in the main body of the airfoil model, and out the model through the quarter-chord mounting spar.

The NACA 0012 airfoil model was also tested with a series of ice shapes that were simulated using simple geometry methods. It was shown by Busch et al.[79] that using simple geometries to simulate ice shapes on an airfoil can produce effects on the airfoil performance coefficients that are consistent with high-fidelity ice shape castings. In this investigation, an ice shape was simulated using a forward-facing quarter-round geometry, which has also been used in various previous studies to simulate ice shapes.[7,11,74,77,78,80,81] This forward-facing quarter round geometry is representative of a spanwise-ridge ice shape, as described by Bragg et al.[1]

The NACA 0012 airfoil model was tested with various quarter round heights. These quarter round heights measured 1/8, 3/16, 1/4, 5/16, and 3/8 in. The quarter-round geometry was machined from steel and constructed to cover the entire span of the airfoil model. These quarter-round geometries were not instrumented with pressure taps or integrated pressure transducers. Whenever they were mounted to the airfoil model, if any pressure taps or integrated pressure transducers were covered by the simulated ice shape, the respective tap ports or transducers were not sampled during data acquisition. Separate sets of data were acquired for each quarter-round geometry mounted to the upper surface of the airfoil model at $x/c = 0.02$. A schematic of the quarter-round geometries mounted on the NACA 0012 airfoil upper surface at $x/c = 0.02$ is presented in Fig. 3.6. Additionally, the NACA 0012 airfoil was tested with the 1/4 in. quarter round placed at $x/c = 0.05$ and $x/c = 0.10$.

The quarter rounds were affixed to the airfoil model using 0.0024 in. thick removable double-sided tape on the bottom of the quarter round. Additional support was provided by adhering two separate lengths of 3M Scotch® Magic™ Tape to the quarter round on both the flat upstream side and the rounded downstream side of the shape, and adhering the other side of each length of tape to the model. These lengths of tape covered the entire span of the model. When the tape was applied to the quarter round, care was taken to ensure that the tape was applied no more than halfway up the height of the quarter round. By adhering the tape to the quarter round in this fashion, it ensured that the tape did not increase the maximum height of the quarter round.

3.1.2.2 Boundary-Layer Trip

In order to isolate the effects of boundary-layer transition on the unsteadiness in the airfoil flowfield, the airfoil model was also tested with a boundary-layer trip on the upper and lower surface. Using these boundary-layer trips ensured that certain characteristics of the unsteady airfoil flowfield could be attributed to the dynamics of the separation bubble and not solely due to turbulent fluctuations in the airfoil boundary layers. The boundary-layer trips were created by distributing glass microbeads on a 1/4 in. wide length of 0.0024 in. thick, removable double-sided tape. The boundary-layer trips were then placed on the airfoil model at a prescribed chordwise location, with the length of the trips running the full span of the airfoil model.

The boundary-layer trips were placed at $x/c = 0.01$ on the airfoil upper surface, and $x/c = 0.05$ on the airfoil lower surface. The sizes of the glass microbeads necessary for invoking a bypass-type boundary-layer transition were calculated by determining the critical roughness height that produced a Re_k of 600, as discussed by Braslow and Knox.[82] The size of the glass microbeads that were then used to create the boundary-layer trips were sized just above the roughness sizes that produced $\mathrm{Re}_k = 600$. The boundary-layer velocity profiles used to calculate Re_k were estimated using the von Kármán-Pohlhausen method,[83] where the boundary-layer external velocity was approximated using C_p data from XFOIL.[84] After calculating the critical roughness heights, the upper-surface trip was created using 60–70-grit microbeads

(k_{avg} = 0.009 in.) and the lower-surface trip was created using 40–45-grit microbeads (k_{avg} = 0.016 in.).

3.2 Data Acquisition System

All data in this investigation were acquired using routines programmed using National Instruments LabView. These programs were run on a Dell Precision T3400 computer with an Intel® Core™ Quad CPU, measuring a clock speed of 2.83 GHz, and having 4 GB RAM. The computer was run using a Windows XP 32-bit operating system. The data acquisition software incorporated a graphical user interface, where run inputs could be set and results could be sent to the user display. Commands and tasks sent by the data acquisition computer to the three-component balance, tunnel variable frequency drive controller, and IDC drive (which was used to run the wake traverse discussed in Section 3.4.1.3) were sent via RS-232 communication. Time-averaged model pressure measurements and wake surveys were acquired through a National Instruments General Purpose Interface Bus (GPIB) IEEE-488 board. Details of the time-averaged pressure measurement instrumentation and technique will be discussed in Section 3.4.1. Data acquired from the three-component balance and hot-film anemometers were converted through a National Instruments PCI-6052E 16-bit analog to digital (A/D) conversion board.

All unsteady measurements in this investigation were acquired through a National Instruments Signal Conditioning eXtensions for Instrumentation (SCXI) measurement system and a National Instruments PCI-MIO-16XE-10 A/D board. The SCXI system was composed of two SCXI-1001 chassis and associated SCXI modules. Each SCXI-1001 chassis was able to accommodate twelve SCXI modules. Each SCXI-1001 chassis was configured with three SCXI-1140 Simultaneous-Sampling Differential Amplified modules, Three SCXI-1142 Lowpass Bessel Filter modules, six SCXI-1121 Isolation Amplifier with Excitation modules, and six SCXI-1321 terminal blocks.

These modules were installed into the SCXI-1001 chassis as three groups of four modules. Each group consisted of one SCXI-1140 module, one SCXI-1142 module, two SCXI-1121 modules, and two SCXI-1321 terminal blocks. On the SCXI-1001, the SCXI-1140 modules were installed in slots 1, 5, and 9, the SCXI-1142 modules were installed in slots 2, 6, and 10, and the SCXI-1121 modules were installed in slots 3, 4, 7, 8, 11, and 12. The

SCXI-1321 terminal blocks were connected to the front panel of the SCXI-1121 modules. The signal and excitation cables from the measurement instrument were connected to the SCXI-1321 terminal block. Each SCXI-1321 was able to accommodate up to four channels of devices, and was equipped with a null-offset potentiometer. A photograph of the two SCXI-1001 chassis and associated SCXI modules is presented in Fig. 3.7.

By connecting the SCXI-1321 terminal blocks to an SCXI-1121 module, the SCXI-1121 module was able to provide electrical isolation of the instruments in case of common mode voltages, and provided excitation to the instrument if necessary. Both of the SCXI-1121 modules in a group were connected to an SCXI-1142 module using the dual ribbon cable of an SCXI-1352 Module-Cascading Cable Kit. The use of the SCXI-1142 module allowed the analog signals to be passed through a low-pass filter at the Nyquist frequency to prevent aliasing. The SCXI-1142 module was then connected to an SCXI-1140 module using the single ribbon cable of an SCXI-1352 Module-Cascading Cable Kit. The use of the SCXI-1140 module allowed the signals of all channels to be acquired simultaneously. This was accomplished using a sample-and-hold method, where the analog signal was continuously sampled by the SCXI system until a hold trigger was sent to the device. Upon receipt of the hold trigger, the voltage at that instant was stored in a capacitor. The A/D system was then able to sample the voltages stored in the capacitors successively. While the signals being acquired were not digitized simultaneously, due to the storage of the signals in the capacitors the voltages being digitized between channels were representative of the analog signals at the same instance in time. After one datum point was acquired for each channel, the sampling system went back into sampling mode until another hold trigger was received.

By configuring the SCXI modules in groups of four, a total of eight channels could be simultaneously sampled per module grouping. Since there were three groups of modules per SCXI-1001 chassis, and two SCXI-1001 chassis were used, a total of 48 channels could be simultaneously sampled. However, one of the channels of the SCXI system was faulty, so a maximum of 47 channels could actually be simultaneously sampled. Communication to the first SCXI-1001 chassis was achieved by connecting the SCXI-1001 to the PCI-MIO-16XE-10 A/D board. The first SCXI-1001 chassis was also connected to the second SCXI-1001 chassis with the use of an SCXI-1346 Shielded Multi-Chassis Adapter. A diagram displaying the full connectivity of the SCXI terminal blocks, modules, and chassis is presented in Fig. 3.8.

3.3 Force Balance Measurements

A three-component external force balance was used to obtain measurements of the model lift, drag, and quarter-chord pitching moment. The balance was manufactured by Aerotech ATE Limited, of Heathfield, U.K., and can be seen in Fig. 3.9. The airfoil model was mounted to the force plate of the balance using L-shaped mounting brackets. These brackets were clamped to the airfoil model mounting spars and fastened to the force plate. The resultant forces and moments were calculated based on measurements from three load cells. These load cells measured the forces in the normal and axial direction, and the moment about the center of the force plate.

3.3.1 Balance Measurement Acquisition

The balance signal conditioning system was configured for three different load range settings. The load range of each of the three components could be changed in order to ensure a high signal-to-noise ratio of the resulting measurement. The balance load ranges are provided in Table 3.1. For all tests in the current investigation, the high setting was used for all three balance components. The balance load cells had a full-scale output voltage of ±20 mV, which were low-pass filtered at 1 Hz and amplified to a full-scale output of ±5 V by the signal conditioning system of the balance. When balance measurements were acquired, a total of 200 samples were acquired at a sample rate of 100 Hz. These measurements were then time-averaged to produce an average voltage for the normal force, axial force, and pitching moment about the center of the force plate. The force plate of the balance was also situated on top of a turntable, which was constructed as part of the balance system. This turntable was used to regulate the model angle of attack and was controlled to within ±0.1°.

Table 3.1 Three-component balance load ranges

	HIGH RANGE	MEDIUM RANGE	LOW RANGE
NORMAL FORCE	±450 lb	±225 lb	±90 lb
AXIAL FORCE	±90 lb	±55 lb	±18 lb
PITCHING MOMENT	±45 ft-lb	±30 ft-lb	±15 ft-lb

3.3.2 Force and Moment Calculation

Balance tare measurements were acquired periodically with the wind tunnel fan off across the angle-of-attack range that would be used in the upcoming tests. These tare measurements were subtracted from the acquired measurements in order to compensate for changes in the transducer zeros. The resulting zero-corrected voltage (V_{0i}), was then multiplied by a range ratio (RR_i), which was dependent on the load range setting. By multiplying by this range ratio, the zero-corrected voltage could be scaled to appropriately account for the gain applied by the balance signal conditioning system. The scaled voltage (V_i) was calculated using

$$V_i = \left(V_{0i}\right)\left(RR_i\right) \tag{3.6}$$

A summary of the balance range ratios are provided in Table 3.2.

Table 3.2 Three-component balance range ratios

	HIGH RANGE	MEDIUM RANGE	LOW RANGE
NORMAL, RR_N	1	0.4944	0.2046
AXIAL, RR_A	1	0.6278	0.2173
MOMENT, RR_M	1	0.6755	0.3413

The resulting scaled voltages corresponding to the normal force, axial force, and pitching moment about the balance center (V_N, V_A, V_M) were multiplied by a calibration matrix in order to calculate the corresponding balance forces and moments. The balance normal force, axial force, and moment about the balance center (F_N, F_A, M) were calculated using,

$$\begin{Bmatrix} F_N \\ F_A \\ M \end{Bmatrix} = \begin{bmatrix} 37.7 & 0.03159 & -0.2095 & 0.01094 & 0 & -0.000865 \\ -0.1607 & 8.3125 & -0.01638 & 0.007084 & 0 & 0.007660 \\ -0.01299 & -0.005521 & 1.247 & -0.002122 & 0 & 0.0001497 \end{bmatrix} \begin{Bmatrix} V_N \\ V_A \\ V_M \\ V_N^2 \\ V_A^2 \\ V_M^2 \end{Bmatrix} \tag{3.7}$$

Since the resulting forces were oriented in the chord-normal and chord-axial directions, they had to be rotated by the airfoil angle of attack in order to determine the airfoil lift and drag forces. The airfoil lift and drag forces were calculated using,

$$L = F_N \cos\alpha - F_A \sin\alpha \tag{3.8}$$

$$D = F_N \sin\alpha + F_A \cos\alpha \tag{3.9}$$

where α represents the airfoil angle of attack. Similarly, the moment that was calculated using Eq. 3.7 was the pitching moment about the balance center. However, with the balance normal and axial forces known, along with the offset distance from the airfoil quarter-chord location to the balance center (x_{offset}, y_{offset}), the pitching moment about the airfoil quarter-chord could be calculated, using,

$$M_{c/4} = M - x_{offset} F_N + y_{offset} F_A \tag{3.10}$$

With the airfoil lift, drag, and quarter-chord pitching moment known, the resulting force and moment coefficients of the airfoil could be calculated. The airfoil lift coefficient (C_l), drag coefficient (C_d), and quarter-chord pitching moment coefficient (C_m) could be calculated using,

$$C_l = \frac{L}{q_\infty S} \tag{3.11}$$

$$C_d = \frac{D}{q_\infty S} \tag{3.12}$$

$$C_m = \frac{M_{c/4}}{q_\infty S c} \tag{3.13}$$

where q_∞ represents the freestream dynamic pressure, S represents the model reference area, and c represents the model chord.

While the balance was used to measure the airfoil drag, these drag measurements were used for diagnostic purposes only, and will not be reported here. The airfoil drag was also obtained using measurements from a wake survey system, which is reported in Section 3.4.1.3, which represented the profile drag of the airfoil, and was used as the primary set of drag data for this investigation. Since the airfoil model installation was associated with a small (0.02 in.) gap at both the floor and the ceiling, the drag measurements obtained by the balance included a small, but significant, induced drag component. Thus, the drag measurements obtained from the balance were slightly higher than those calculated from the wake survey system.

3.4 Pressure Measurements

Throughout this investigation, several types of pressure measurements were acquired. Generally, they can be split into time-averaged pressure measurements and unsteady pressure measurements. The time-averaged pressure measurements can also be classified into measurements of the static pressure about the airfoil surface and measurements of the total pressure in the airfoil wake. A description of the time-averaged pressure measurement acquisition and processing is described in Section 3.4.1, and the unsteady pressure measurements are described in Section 3.4.2.

3.4.1 Time-Averaged Pressure Measurements

All time-averaged pressure measurements obtained in this investigation were acquired using a Pressure Systems Incorporated (PSI) System 8400. This pressure system chassis consisted of a Central Control Unit, a 14-bit 8420 Scanner Digitizer Unit, and 1.0 and 5.0 psid Pressure Calibration Units (PCUs). Communication with the Central Control Unit was accomplished through the GPIB board discussed in Section 3.2. The System 8400 chassis also was connected to a Scanner Interface. Along with the pressure system chassis, a total of five Miniature Electrically Scanned Pressure (ESP) units were used to acquire pressure measurements. These scanners were model ESP-32HD units, with 32 ports per scanner. Each of the 32 ports could be connected to a pressure tube connecting to either a pressure tap on the airfoil model, or a total pressure probe on the wake rake. In addition to the 32 ports, each scanner also had one port for providing reference pressure when running (R_R), one port for providing reference pressure when calibrating (R_C), two manifold calibration ports (C_1 and C_2), and one calibration pressure port (Cal).

Each of the scanners had one of three different ranges. A ±5.0 psid scanner (denoted J_1) was connected to the pressure taps across the leading-edge region of the model, where the highest magnitudes of the measured pressure differentials were expected. Two ±1.0 psid scanners (denoted J_2 and J_3) were connected to the remaining pressure taps on the airfoil model. Finally, two ±0.35 psid (±10.0 in. WC) scanners (denoted J_4 and J_5) were connected to the total pressure probes on the wake rake. The three scanners used for measuring airfoil surface static pressures (J_1, J_2, and J_3) were supplied with the test section static pressure (P_{ts}) as the run reference pressure. Referencing the J_1, J_2, and J_3 scanners to P_{ts} allowed the static pressure difference between the model surface and the freestream flow to be measured. The two pressure scanners that measured the wake pressures (J_4 and J_5) were supplied with the ambient pressure from inside the control room, which was assumed to be approximately equivalent to the freestream total pressure. The reasons for configuring the wake rake scanners in this fashion will be described in greater detail in Section 3.4.1.3

The scanners were routinely calibrated during testing, with the assistance of the LabView data acquisition program discussed in Section 3.2. The calibration routine was able to switch the PSI system between run mode and calibration mode by applying 100 psi of nitrogen (from a nitrogen gas tank), for approximately 20 seconds, to the C_1 or C_2 port on the scanners. This application of pressure shifted a manifold in the pressure scanners such that all transducers in the ESP scanners would sense the supplied calibration reference pressure. In order to proceed with the calibration, a vacuum pump, a nitrogen gas tank, and the PSI chassis PCUs were used to supply the calibration pressures to the Cal port. The 5 psi PCU was used to regulate the calibration pressures to J_1, J_2, and J_3, while the 1 psi PCU was used to regulate the calibration pressures to J_4 and J_5. Each port on all five scanners simultaneously underwent a five-point calibration, which allowed for each port to have an independent, fourth-order calibration curve. Measurements acquired by the PSI system were taken at a rate of 50 Hz for two seconds.

3.4.1.1 Model Pressures and C_p Distributions

In addition to acquiring model surface static pressures, a pressure port on the J_3 scanner was reserved for measuring ($P_{ss} - P_{ts}$) in order to calculate the dynamic pressure of the freestream flow. While the Setra 239 pressure transducer was used to calculate the freestream velocity, as outlined in Section 3.1.1, the pressure measurements from the PSI system were associated with greater accuracy. Therefore, the measurements from the Setra 239 pressure transducer were only used to set the tunnel speed. The dynamic pressure which was calculated from the PSI system was used in calculating the pressure and airfoil performance coefficients when reducing acquired data. The dynamic pressure of the freestream flow (q_∞) was calculated using,

$$q_\infty = \frac{1}{2}\rho_\infty U_\infty^2 \tag{3.14}$$

Using the expression for freestream (test-section) velocity in Eq. 3.4, Eq. 3.14 becomes,

$$q_\infty = \frac{1}{2}\rho_\infty U_{ts}^2 = \frac{P_{ss} - P_{ts}}{1 - \left(\dfrac{A_{ts}}{A_{ss}}\right)^2} \tag{3.15}$$

where ρ_∞ represents the density of the freestream air. This density is assumed to be the same ambient density (ρ_{amb}) used in Eq. 3.4.

With the freestream dynamic pressure known, the pressure coefficient (C_p) of a given location on the airfoil could be calculated using the corresponding surface static pressure (P_s). The conventional definition of C_p is,

$$C_p = \frac{P_s - P_\infty}{q_\infty} \tag{3.16}$$

In the current study, the freestream static pressure was assumed to be the same as the test-section static pressure. Since the flow through the wind tunnel was assumed to be incompressible (i.e. $M_\infty \leq 0.3$), reductions of the static pressure throughout the wind tunnel for a given set of test conditions would be primarily due to a change in flow velocity via Bernoulli's equation (Eq. 3.3). Since the effective cross-sectional area of the test section was constant up to the airfoil model (boundary-layer growth was accounted for), the flow did not significantly accelerate between the test-section inlet and the location of the airfoil model. The static pressure of the test section was measured upstream of the airfoil model, and without any flow acceleration the static pressure of the incoming freestream flow encountered by the airfoil model could be assumed to have the same static pressure. Thus, the pressure difference measured by the PSI system about the airfoil ($P_s - P_{ts}$) could simply be divided by q_∞ to obtain C_p.

3.4.1.2 Airfoil Performance Coefficients from Pressure Measurements

With the distribution of static pressure about the airfoil known, the lift and pitching moment coefficients of the airfoil could be calculated. This calculation was completed by considering the airfoil surface to be split into a series of panels, where each panel was constrained by two adjacent pressure tap locations on the model. The pressure acting on each panel was assumed to be the average of the two pressures measured through the pressure taps at both ends of the panel. It was assumed that this average pressure was then uniform across the length of the corresponding panel. Since the pressure acted in a direction normal to the panel surface, the sectional force across each panel could be split into chord-normal and chord-axial components with the panel orientation known with respect to the airfoil chordline. The chord-normal sectional force and chord-axial sectional force across each panel ($\Delta F_N'$ and $\Delta F_A'$) were calculated using Eq. 3.17 and Eq. 3.18, respectively. A detailed explanation of this calculation process can also be found in Anderson.[85]

$$\Delta F_N' = \frac{P_i + P_{i+1}}{2}\left(x_{i+1} - x_i\right) \tag{3.17}$$

$$\Delta F_A' = -\frac{P_i + P_{i+1}}{2}\left(y_{i+1} - y_i\right) \tag{3.18}$$

Since the sectional force across each panel represented a contribution to the total forces acting on the airfoil, the net airfoil normal and axial sectional forces could be calculated by summing the effects of all panels. Thus, the airfoil chord-normal sectional force and chord-axial sectional force (F_N' and F_A') could be calculated using,

$$F_N' = \sum_{i=1}^{n-1} \Delta F_N' \tag{3.19}$$

$$F_A' = \sum_{i=1}^{n-1} \Delta F_A' \tag{3.20}$$

where n represents the total number of chordwise pressure taps on the airfoil model. Using these calculated normal and axial sectional forces, the airfoil sectional lift could be calculated using,

$$L' = F_N' \cos\alpha - F_A' \sin\alpha \tag{3.21}$$

Similarly, the effect of the normal and axial sectional forces on each panel contributed to the net pitching moment about the airfoil quarter-chord location. Thus, in order to calculate the effects of the normal and axial sectional forces of a given panel on the airfoil quarter-chord sectional pitching moment, the forces were multiplied by the corresponding moment arm to the airfoil quarter-chord,

$$\Delta M'_{c/4_i} = \Delta F_N'\left(x_{c/4} - \frac{x_i + x_{i+1}}{2}\right) + \Delta F_A'\left(\frac{y_i + y_{i+1}}{2}\right) \tag{3.22}$$

By summing the contributions of each panel to the sectional quarter-chord pitching moment, the total airfoil sectional quarter-chord pitching moment could be calculated,

$$M'_{c/4} = \sum_{i=1}^{n-1} \Delta M'_{c/4_i} \tag{3.23}$$

While the NACA 0012 airfoil model tested in this investigation was not constructed with a trailing-edge flap, the hinge moment that would be induced about a prescribed hinge location of a flap could be estimated from the airfoil pressure distribution. The calculation of this hinge moment is similar to that of the quarter-chord pitching moment with two important distinctions. First, since the moment being calculated is about the location of the flap hinge, the moment arm used in calculating the contribution of a panel to the hinge moment would run from the hinge location to the panel center. Second, only the surface pressures across the flapped section would contribute to the hinge moment, so only the sections that would constitute the trailing-edge flap were used in the hinge moment calculation. The resulting contribution of a given panel to the sectional hinge moment ($\Delta H'$) could be calculated using,

$$\Delta H' = \Delta F_N' \left(x_h - \frac{x_i + x_{i+1}}{2} \right) - \Delta F_A' \left(y_h - \frac{y_i + y_{i+1}}{2} \right) \tag{3.24}$$

where x_h and y_h represent the x and y locations of the flap hinge, respectively. The net sectional hinge moment for the airfoil could then be calculated by summing the contributions of each panel across the flap using,

$$H' = \sum_{i=1}^{n_{flap}-1} \Delta H'_i \tag{3.25}$$

where n_{flap} represents the number of chordwise pressure taps on the flapped section of the airfoil. Since it was desirable in this investigation to observe the hinge moment characteristics of a trailing-edge flap, a simulated hinge line was prescribed at $x/c = 0.70$ and $y/c = 0.0$. Thus, the hinge moment results reported in this investigation estimate that of a 30%-chord trailing-edge flap.

Using the sectional lift, quarter-chord pitching moment, and hinge moment from Eqs. 3.21, 3.23, and 3.25, the coefficient forms of these forces and moments could be calculated.

The resulting airfoil lift coefficient (C_l), quarter-chord pitching moment coefficient (C_m), and hinge moment coefficient (C_h) were calculated using,

$$C_l = \frac{L'}{q_\infty c} \tag{3.26}$$

$$C_m = \frac{M'_{c/4}}{q_\infty c^2} \tag{3.27}$$

$$C_h = \frac{H'}{q_\infty c_f^2} \tag{3.28}$$

where c_f represents the chord length of the trailing-edge flap.

3.4.1.3 Wake Survey System

A wake survey system was used to obtain measurements from which the airfoil profile drag was calculated. These wake survey drag results were used as the primary means for evaluating the airfoil drag. The wake survey system was composed of a traversable wake rake and a two-axis traverse system. The wake rake was constructed with 59 total pressure probes, which were made from straight, stainless steel, thin-walled tubing. These total pressure probes all had an outer diameter of 0.04 in. The total pressure probes were aligned horizontally along the wake rake, which allowed for total pressure profiles of the airfoil wake to be acquired downstream of the vertically-oriented airfoil model. The wake rake spanned 9.75 in., with 0.135 in. spacing between probes in the center of the wake rake and 0.27 in. spacing between the last six total pressure probes on either end of the wake rake. Wake profiles were acquired approximately 1.17 chord lengths downstream of the airfoil model. As noted previously, the PSI System 8400 and two ±0.35 psid ESP scanners were used to acquire the wake total pressure measurements. The wake rake was also equipped with two static pressure probes above the total pressure probes. However, these static pressure probes were not used in this investigation. A photograph of the wake rake installed in the test section downstream of the airfoil model is presented in Fig. 3.10.

The wake rake was capable of being traversed in the vertical (spanwise) and horizontal directions with the use of a two-axis traverse system. The two Lintech traverse axes were controlled by an IDC S6962 Stepper Motor Drive. This traverse system was mounted above the wind tunnel, such that the wake rake supporting structure entered the wind tunnel from the ceiling. A pressure box was installed around the traverse system in an effort to minimize air leakage into the tunnel. This box was constructed from wood and sealed the traverse system from the external atmosphere.

The span of the wake rake was large enough to capture the entire wake of the clean airfoil model at low to moderate angles of attack where the flowfield remained attached and the airfoil wakes were small. At larger angles of attack, and as the leading-edge ice shape was added to the model, the size of the wakes became much larger, and multiple wake rake measurements were required to capture the full wake deficit region downstream of the airfoil model. For this reason, when wake measurements were acquired, the wake rake was traversed in the horizontal direction and wake pressure measurements were acquired until the tails of the wake profile were sufficiently captured. This process was automated as a part of the LabView interface discussed in Section 3.2. Once the size of the wake was determined, the program located the center of the wake by identifying the location of minimum pressure. The program then calculated the total number of rake spans necessary to capture the entire wake and proceeded to take the pressure measurements to capture the entire wake, moving in the horizontal direction as necessary. Wakes could be acquired at various stations across the span. For the results reported in this investigation, the airfoil drag was calculated using the averaged drag from three wake stations across the airfoil model span.

3.4.1.4 Drag Calculation from Wake Pressures

The standard momentum deficit method found in Jones[86] and Schlichting[83] was used to calculate the drag from the wake pressures. The method uses a hypothetical flow throughout the wake downstream of the airfoil represented by the schematic shown in Fig. 3.11. This method assumes that there exists a theoretical plane (denoted with subscript 1) far downstream from the wind tunnel test section where the model wake has been spread such that the static pressure in the wake of this plane (P_1) is equal to the static pressure in the freestream (P_∞). Using this assumption, the drag per unit span could be calculated using

$$D' = \rho \int u_1 \left(U_\infty - u_1 \right) dy_1 \tag{3.29}$$

However, the form of Eq. 3.29 is not particularly useful for practically determining drag, as u_1 represents a theoretical wake velocity deficit and is not actually measured. As a result, it is then assumed that there exists a second plane between the freestream and plane 1. On this plane is where the wake rake pressure measurements were acquired, and all parameters pertaining to this plane will be denoted with subscript *w*. By assuming a streamtube that runs through plane *w* and plane 1, the incompressible form of the conservation of mass takes the form,

$$u_1 dy_1 = u_w dy \tag{3.30}$$

Substituting Eq. 3.30 into the previous relation for the sectional drag, this results in,

$$D' = \rho \int u_w \left(U_\infty - u_1 \right) dy \tag{3.31}$$

By applying Bernoulli's equation to the freestream plane, plane 1, and plane *w*, the total pressure across these planes can be expressed using Eqs. 3.32, 3.33, and 3.34, accordingly.

$$P_\infty + \frac{1}{2}\rho U_\infty^2 = P_{0,\infty} \tag{3.32}$$

$$P_1 + \frac{1}{2}\rho u_1^2 = P_{0,1} \tag{3.33}$$

$$P_w + \frac{1}{2}\rho u_w^2 = P_{0,w} \tag{3.34}$$

The velocity terms in Eqs. 3.32, 3.33, and 3.34 are solved for in terms of total and static pressure, and the pressure terms are substituted into Eq. 3.31, which results in,

$$D' = 2\int \sqrt{P_{0,w} - P_w}\left(\sqrt{P_{0,\infty} - P_\infty} - \sqrt{P_{0,1} - P_1} \right) dy \tag{3.35}$$

It is assumed that there are no losses in total pressure between plane 1 and plane *w*, so $P_{0,1} = P_{0,w}$. It was also assumed previously that $P_1 = P_\infty$. By substituting these relations into Eq. 3.35, the expression for the sectional drag becomes,

$$D' = 2\int \sqrt{P_{0,w} - P_w}\left(\sqrt{P_{0,\infty} - P_\infty} - \sqrt{P_{0,w} - P_\infty} \right) dy \tag{3.36}$$

It was assumed that the pressure losses in the wake could be attributed to the wake velocity deficit, and as such it was assumed that $P_w = P_\infty$. Using this relation and combining Eqs. 3.32 and 3.34 resulted in an expression for the dynamic pressure in the wake of,

$$q_w = q_\infty - \left(P_{0,\infty} - P_{0,w}\right) \tag{3.37}$$

As suggested by Lee,[87] Eq. 3.36 was rearranged in terms of dynamic pressure. As such, the relation from Eq. 3.37 was substituted into Eq. 3.36, such that the expression for sectional drag became,

$$D' = 2\int \sqrt{q_\infty - (P_{0,\infty} - P_{0,w})}\left(\sqrt{q_\infty} - \sqrt{q_\infty - (P_{0,\infty} - P_{0,w})}\right)dy \tag{3.38}$$

Since the dynamic pressure of the freestream was known, the expression for sectional drag in Eq. 3.38 was very useful, as the difference in total pressure between the wake and the freestream ($P_{0,\infty} - P_{0,w}$) could be directly measured in the wake surveys. This current method was employed, as it prevented the need for an extra probe to be installed in order to acquire the freestream total pressure. However, the ESP scanners that were used for acquiring the wake pressures were referenced to a stable source of atmospheric pressure in the control room. As a result, ($P_{0,\infty} - P_{0,w}$) was not measured directly, but could be easily calculated from the pressures acquired in the wake survey.

Because of the reference to atmospheric pressure, the wake survey system measured the pressure difference of ($P_{0,w} - P_{atm}$) in the wake of the airfoil model. At the edges of the wake, it was assumed that the total pressure was equivalent to the freestream total pressure. As a result, the wake survey system measured the pressure difference of ($P_{0,\infty} - P_{atm}$) outside of the wake of the airfoil model. Thus, the pressure difference ($P_{0,\infty} - P_{0,w}$) could be calculated by,

$$P_{0,\infty} - P_{0,w} = \left(P_{0,\infty} - P_{atm}\right) - \left(P_{0,w} - P_{atm}\right) \tag{3.39}$$

The calculated pressure difference ($P_{0,\infty} - P_{0,w}$) could be substituted into Eq. 3.38, along with q_∞, to calculate the sectional drag for the airfoil. The integral in Eq. 3.38 was numerically solved using the trapezoidal method. The contribution of the region between two total pressure probes on the wake rake to the net sectional drag of the airfoil could be calculated using,

$$\begin{aligned}\Delta D' = \Big[&\sqrt{q_\infty - (P_{0,\infty} - P_{0,w_i})}\left(\sqrt{q_\infty} - \sqrt{q_\infty - (P_{0,\infty} - P_{0,w_i})}\right) + \\ &\sqrt{q_\infty - (P_{0,\infty} - P_{0,w_{i+1}})}\left(\sqrt{q_\infty} - \sqrt{q_\infty - (P_{0,\infty} - P_{0,w_{i+1}})}\right)\Big]\left(y_i - y_{i+1}\right)\end{aligned} \tag{3.40}$$

In order to determine the total sectional drag of the airfoil, the contributions to the sectional drag were summed across the span of the acquired wake profile using,

$$D' = \sum_{i=1}^{n_{rake}-1} \Delta D'_i \tag{3.41}$$

where n_{rake} represented the total number of probes used to measure the wake. It should be noted that all contributions outside of the wake deficit region were ignored in Eq. 3.41, as they did not contribute to the calculation of sectional drag. The boundaries of the wake were determined by identifying the locations where the absolute value of the slope of the wake pressure in the y-direction was less than 0.01 psi/in. across the upper-surface and lower-surface wake tails. The wake pressure measurements acquired across the region between these two boundaries were then used to calculate the airfoil sectional drag. Using the sectional drag from Eq. 3.41, the drag coefficient of the airfoil was calculated using,

$$C_d = \frac{D'}{q_\infty c} \tag{3.42}$$

3.4.2 Unsteady Pressure Measurements

Unsteady pressure measurements were obtained using the XCS-062 pressure transducers that were integrated into the airfoil model, as discussed in Section 3.1.2. An excitation of 10 V was provided to each transducer using the SCXI system discussed in Section 3.2. The voltage output of these pressure transducers varied linearly with pressure. The calibration slope and intercept associated with each transducer was determined by the manufacturer through a five-point calibration at pressures between ±1 psid at room temperature. The manufacturer then applied a linear least-squares fit to the five data points to obtain the calibration slope that was unique to a given pressure transducer. As a result, the difference in pressure between the sensing side and the reference side of a transducer (ΔP_{trans}) could be calculated using,

$$\Delta P_{trans} = mV_{trans} + b \tag{3.43}$$

where m represents the calibration slope, b represents the intercept of the calibration, and V_{trans} represents the output voltage of the transducer. Since the zero-pressure voltage in the pressure transducers tended to drift with changes in temperature, zeroes were taken prior to each run when the wind tunnel fan was not running. As a result, when the transducers were re-zeroed, the difference in pressure between the sensing side and the reference side of the transducers was zero, and the resulting zero-pressure voltage was subtracted from the acquired voltage during the run. By zero-correcting the acquired voltages from the pressure transducers, Eq. 3.43 was simplified to,

$$\Delta P_{trans} = m V_{0,trans} \tag{3.44}$$

where $V_{0,trans}$ was the transducer zero-corrected voltage. Data from these integrated pressure transducers were acquired using the SCXI system described in Section 3.2.

3.4.2.1 Unsteady Model Pressures and C_p Distributions

As discussed in Section 3.1.2, the reference side of all of the integrated pressure transducers was connected to the test section static pressure. As discussed in Section 3.4.1, the ESP scanners used to measure the time-averaged airfoil surface static pressures were also referenced to the test section static pressure. Since the screens of the integrated pressure transducers were installed flush with the airfoil surface, the sensing side of the pressure transducer measured the local airfoil surface static pressure. Thus, the quantity being measured by each of the integrated pressure transducers was the difference between the instantaneous local surface static pressure and the test section static pressure ($P_{s,i} - P_{ts}$). As a result, Eq. 3.16 could also be applied to calculate the instantaneous pressure coefficient ($C_{p,i}$) of a given location on the airfoil using,

$$C_{p,i} = \frac{P_{s,i} - P_{\infty}}{q_{\infty}} \tag{3.45}$$

The freestream dynamic pressure in Eq. 3.45 was calculated using the PSI system. As was discussed in Section 3.4.1.1, the test-section static pressure was assumed to be equivalent to the freestream pressure. Thus, $C_{p,i}$ could be calculated by dividing the measured pressure difference of $P_{s,i} - P_{ts}$ by q_{∞}.

In order to determine the mean pressure coefficient ($\overline{C}_p$) measured by the integrated pressure transducers, a time average could be taken using,

$$\overline{C}_p = \frac{1}{N}\sum_{i=1}^{N} C_{p,i} \tag{3.46}$$

where N represents the number of instantaneous pressure samples acquired. An estimate of the unsteady content present in the C_p signal was also determined by calculating the standard deviation of the unsteady C_p signal (σ_{C_p}), which was calculated using,

$$\sigma_{Cp} = \sqrt{\frac{1}{N}\sum_{i=1}^{N}\left(C_{p,i} - \overline{C}_p\right)^2} \tag{3.47}$$

3.4.2.2 Unsteady Airfoil Performance Coefficients from Pressure Measurements

The instantaneous airfoil lift, quarter-chord pitching moment, and hinge moment coefficients ($C_{l,i}$, $C_{m,i}$, and $C_{h,i}$) were calculated by integrating the instantaneous airfoil surface static pressures using the same method outlined in Section 3.4.1.2 for the time-averaged airfoil pressure measurements. However, due to the coarse distribution of the integrated pressure transducers across the airfoil contour, the fidelity of the time-averaged performance coefficients determined from the unsteady pressure transducers was low. While the integrated pressure transducers do effectively measure $\overline{C}_p$ and capture local instantaneous fluctuations in pressure, the low resolution in locations where $C_{p,i}$ was measured causes the time-average of the instantaneous airfoil performance coefficients to be slightly off the actual value. As a result, the time-average and standard deviations of the instantaneous airfoil performance coefficients will not be presented here.

However, the fluctuations present in the unsteady airfoil performance coefficients are still valuable for characterizing unsteadiness present in the global flowfield about the airfoil. If an oscillation occurs at only one location local to a single pressure transducer, such an oscillation can be expected to be best observed by studying characteristics of the $C_{p,i}$ for that transducer, and the effects of this oscillation would be reduced in the unsteady airfoil performance coefficients. Conversely, if an oscillation occurs in the global flowfield, it can be expected that it may be observed in each $C_{p,i}$ about the airfoil, making it clearly visible in the unsteady airfoil performance coefficients as well. Thus, the unsteady airfoil performance coefficients will be used in this investigation to observe unsteady effects present in the airfoil flowfield. This will be accomplished by performing various operations on these unsteady airfoil performance signals to characterize the unsteady content through observations of spectral characteristics and temporal relationships.

3.5 Hot-Film Measurements

This investigation also used two different types of hot-film anemometry techniques to characterize the unsteady content of the airfoil flowfield. These two types of hot-film anemometry included surface hot-film array measurements and wake hot-film measurements.

3.5.1 Surface Hot-Film Array Measurements

The first type of hot-film anemometry used in this investigation involved the acquisition of measurements from a surface-mounted hot-film array. The hot-film array used in this investigation was a Senflex SF9501 hot-film array manufactured by Tao Systems. Surface-mounted hot-film arrays are typically used to measure a “quasi-wall-shear-stress” quantity. Since traditional hot-film anemometry measures velocity, and since the velocity quantity being measured by a surface-mounted hot-film probe is directly adjacent to a wall, the velocity in the near-wall region is being measured by the hot-film probe. It is well known that in a wall-bounded flow the local wall shear stress (τ_w) can be calculated using,

$$\tau_w = \mu \left. \frac{\partial u}{\partial y} \right|_{y=w_0} \tag{3.48}$$

where $\partial u/\partial y$ is the streamwise velocity derivative in the wall-normal direction and w_0 represents the y-coordinate of the wall. Since the flow velocity at the wall must be zero due to the no-slip condition, the level of convective cooling to the hot-film probe by the flow will be dependent on the velocity distribution in the near-wall region, averaged across a small distance in the wall-normal direction. While this quantity is not exactly τ_w, it represents something similar to $\partial u/\partial y$ evaluated at the wall.

The hot-film array consisted of 32 elements and covered a chordwise length from $x/c = 0.39$ to $x/c = 0.57$. Each sensor element on the array was made of nickel, and was electron-beam deposited onto a 0.002 in. thick polyimide film substrate by the manufacturer. The probe elements were approximately 0.004 in. wide in the streamwise direction, 0.057 in. long in the spanwise direction, and 0.20 μm thick. The probe elements were spaced 0.1 in. apart in the streamwise direction. Each probe element on the substrate was also connected to a designated pair of copper leads. These leads had a streamwise width of 0.030 in., a spanwise length of 2 in.

from the edge of the substrate to the center of the film elements, and a thickness of 0.0005 in. A diagram of the hot-film array used on the NACA 0012 model is shown in Fig. 3.12, after Ref. 88.

3.5.1.1 Hot-Film Array Installation and Configuration

Prior to installing the hot-film array, the solid test-section ceiling was replaced with a ceiling with a turntable. This ceiling was constructed from an aluminum sheet with a circular cutout, and had a ledge cut out along the circumference of the circular cutout. A circular turntable, which was constructed from Plexiglass, was placed to rest on the inside ledge of the circular cutout in the aluminum ceiling. The outside circumference of the Plexiglass turntable also had a ledge cut out in the outside circumference so that, when inserted into the ceiling, the turntable remained flush inside the test section with the aluminum ceiling. The contact surface between the aluminum ceiling and Plexiglass turntable was sealed with Teflon to prevent leakage into the test section and to provide a low-friction surface for the turntable to rotate. An aluminum rectangular insert was placed inside a slot in the Plexiglass turntable, and a fastener was placed through the insert and into a socket in the airfoil model. By tightening the fastener, the airfoil model became pinned at the ceiling. Since the model was already fastened to the balance, pinning the model to the ceiling assisted in reducing the vibrations in the airfoil model during testing. Additional tests were performed to ensure that the use of the turntable ceiling did not alter the airfoil aerodynamics from the validated configuration.

The hot-film array was mounted onto the NACA 0012 model upper surface using 0.0024 in. thick removable double-sided tape. A strand of PVC-insulated 28 AWG hook-up wire was carefully soldered to each of the copper leads on the hot-film array. These leads were then fed through the aluminum insert in the Plexiglass ceiling turntable, and the other end was soldered to a 24 AWG signal cable. The opening where the hook-up wire was fed through the ceiling was then sealed using RTV silicone. The length of hook-up wires that ran across the model span was taped to the airfoil model using book repair tape. This ensured that the aerodynamic loads imparted on the hook-up wires would not cause them to move and disturb the quality of the signal, or detach from the copper leads on the hot-film array. The hook-up wires were neatly aligned in the surface-tangent direction in order to minimize the height induced by the wires and the chordwise distance covered by the leads. A photograph of the upper surface of the NACA 0012 airfoil model with the horn-ice shape and the hot-film array installed is shown in Fig. 3.13.

After connecting the hook-up wires to the signal cable, the signal cable was then routed to a distribution of channels on a patch terminal board. This patch terminal board was used to organize the large number of signal cables and to simplify the diagnostic of problematic signals. The other ends of the channels on the patch terminal board were connected to another set of signal cables, which were then run to a set of three constant-temperature anemometer (CTA) banks. These CTA banks were manufactured by Rolling Hills Research Corporation, and each bank was capable of regulating twelve channels of hot-film probes. Since three banks were used, this system was capable simultaneously of regulating all 32 hot-film probes on the array. A photograph of the CTA banks used in this investigation is presented in Fig. 3.14.

The setup procedures for the anemometer channels were completed as follows. Throughout the setup, the probe voltages were monitored using a digital voltmeter. Beginning with the probe power supply turned off, the cable compensation was set to zero and the overheat control resistance was set below the desired value. The channel to be calibrated was selected on the anemometer channel selector, and the power switch for that channel was turned to the ON position. The probe power was then increased until the probe voltage was just below the desired voltage. The overheat control resistance was then adjusted until the desired probe voltage was reached.

The average cold resistance of the probe elements was 9.70 Ω, with a standard deviation of 0.132 Ω. The overheat control resistance was configured such that the overheat ratio (*a*) of each probe was set to 1.21. The overheat ratio of a given probe could be calculated using,

$$a = \frac{R_w - R_c}{R_c} \tag{3.49}$$

where R_w represents the wire resistance in the operating condition and R_c represents the probe cold resistance at the time of CTA configuration. The overheat ratio settings that resulted after tuning the anemometers are shown in Fig. 3.15. At these overheat settings, there was a slight amount of thermal crosstalk between sensors when the wind tunnel fan was not running, which was evident by adjusting the operating voltage of a probe element and observing a change in output voltage of an adjacent probe element. This thermal crosstalk between sensors was not observed, however, when the wind tunnel fan was running during the final balancing of the signal conditioning of each channel or as data were being acquired.

The channel cable compensation was set next, and the resulting frequency response was evaluated. This was accomplished using a standard square wave frequency response test. A square wave signal was sent through the anemometer, and the square wave signal and output voltage was monitored on an oscilloscope. The channel frequency response was tuned by adjusting the cable compensation of the anemometer. Care was taken to ensure that the cable compensation was not set too high and that the circuit did not oscillate. As discussed by Fingerson and Freymuth,[89] the response of a hot-film anemometer circuit to an electronic step voltage, like the square wave, can be represented by a voltage output similar to that shown in Fig. 3.16. In Fig. 3.16, the voltage output should be represented by a high-amplitude peak, followed by a local minimum and a tail proportional to $1/\sqrt{t}$. This tail is a characteristic of the step response of a hot-film probe, and would not be observed for a hot-wire probe. As discussed by Fingerson and Freymuth,[89] the amplitude of the resonance following the high-amplitude peak should be approximately 28% of the amplitude of the peak. The temporal resolution of the hot-film probe (τ_s) is the time interval between the crossing of this 28% amplitude level and the initial peak, as represented by the quantity Δx in Fig. 3.16. The frequency response of the anemometer circuit (f_s) can then be calculated simply using,

$$f_s = \frac{1}{\tau_s} \tag{3.50}$$

In the current study, the operating frequency response of all hot-film array elements was above 4 kHz.

After setting the cable compensation and calculating the frequency response of the anemometer circuit, the output sensitivity of the channel was adjusted. By ensuring that the output voltages of all channels exhibited the same magnitude of response to the square wave input, it ensured that the level of sensitivity was uniform for all channels. Since the anemometer limited the output voltage between 0 and 5 V, the offset level of the anemometer channel was also adjusted to ensure that there would be no clipping of the unsteady hot-film array signals during data acquisition. This setup and configuration process was repeated for all channels on the hot-film array.

All measurements obtained for the hot-film array were acquired using the SCXI system described in Section 3.2. The hot-film array was tested without being calibrated. As discussed by Mangalam and Moes,[65] calibration is not required for detecting flowfield features using hot-film array measurements, as data reduction methods involving hot-film arrays are not necessarily dependent on absolute values of surface shear stress. This was also the case for the current investigation, where the unsteady reattachment location was determined without requiring the absolute distribution of surface shear stress across the hot-film array. Instead, the unsteady reattachment location was determined in this investigation by comparison of unsteady fluctuations in the voltage outputs between channels on the hot-film array. The reduction method of these hot-film array measurements will be discussed in detail in Section 3.6.

3.5.2 Wake Hot-Film Measurements

Hot-film measurements were also acquired in the wake of the airfoil model using a single-element hot-film probe. All wake hot-film measurements were acquired using a TSI Model 1201 Disposable Probe, with a TSI IFA-100 Constant-Temperature Anemometer. When wake hot-film measurements were acquired, the wake rake, which was discussed in Section 3.4.1.3, was removed from the Lintech traverse system. The hot-film support structure was then fastened to the two-axis Lintech traverse. Like the wake rake measurements, the wake hot-film measurements were acquired approximately 1.17 chord lengths downstream of the airfoil model. Use of the Lintech traverse system allowed hot-film measurements to be acquired at any location across the wake plane downstream of the airfoil model. The hot-film support structure was composed of two struts made from streamline tubing and one mounting block at the bottom of the support structure. The mounting block had two cylindrical holes where probes could be installed. A single-element hot-film probe support was installed in the lower mounting hole, and a pitot-static probe was installed in the upper mounting hole. The pitot-static probe was used for measuring the freestream velocity during calibration, and had a beveled tip and four static ports downstream of the total pressure port. A photograph of the wake hot-film assembly, installed in the wind tunnel downstream of the NACA 0012 airfoil model, is presented in Fig. 3.17.

3.5.2.1 Wake Hot-Film Probe Configuration and Calibration

The wake hot-film probe and circuit was configured according to the TSI IFA-100 manual, using the following steps. The cable resistance of the anemometer circuit was first measured. This was accomplished by inserting a shunt probe into the probe support, and zeroing the anemometer circuit resistance. The resistance required to zero the anemometer circuit represented the approximate cable resistance. The cold resistance of the hot-film probe was then measured. This was accomplished by removing the shunt probe, inserting the hot-film probe, and zeroing the cable-compensated anemometer circuit resistance. This was performed when the anemometer was not running. The hot-film probe cold resistance was then recorded for use in later calculations.

The operating resistance was then set either to an operating resistance recommended by the manufacturer, or in order to achieve a desired overheat ratio. In this investigation, the probe operating resistance was set to the operating resistance suggested on the documentation corresponding to the probe serial number. For the hot-film probe used in this investigation, the manufacturer-recommended operating resistance was 9.621 Ω. This consistently resulted in an overheat ratio just over $a = 1.5$. In order to set the operating resistance to the desired value, the resistance of the anemometer circuit was adjusted until the desired resistance value was achieved. The bridge compensation was set to 115, which is the value recommended by the manufacturer for this type of hot-film probe. At this point, the anemometer was set to run mode. The cable compensation for the anemometer circuit was adjusted in order to tune the frequency response of the hot-film probe using the same square-wave impulse test described in Section 3.5.1.1. The resulting frequency response of the wake hot-film setup was well above 5 kHz.

After the anemometer circuit was fully configured, the hot-wire anemometry system was calibrated. This was accomplished by first moving the hot-film support structure close to the horizontal edge of the wake plane using the Lintech traverse system. At this location, the pitot-static probe and the hot-film probe were outside of the influence of the airfoil model and were far enough from the wind tunnel walls such that the wall interference on the local velocity was negligible. Thus, at this location, it was assumed that the local flow velocity encountered at the measurement location was the freestream velocity.

The hot-film calibration was conducted by measuring the local freestream velocity and the voltage output of the hot-film anemometer. The local freestream velocity was determined from the pressure measurements obtained with the pitot-static probe. The total pressure port and the static pressure port on the pitot-static probe were connected to two different ports on the J_4

scanner of the PSI 8400 system, which was described in detail in Section 3.4.1. Since the total pressure and static pressure were known at this location, the incompressible form of Bernoulli's equation was used to determine the local freestream velocity using,

$$U_\infty = \sqrt{\frac{2\left(P_{0,\infty} - P_\infty\right)}{\rho_\infty}} \tag{3.51}$$

The hot-film output voltage was then acquired at this velocity using the NI PCI-6052E A/D system described in Section 3.2.

The calibration was performed for a total of 23 different velocity settings, ranging from near-zero test-section velocity to full speed. At each calibration point, the ambient temperature and density were also recorded and were used later during correction of the acquired hot-film measurements. Details of the corrections applied to the wake hot-film voltage and velocity data will be discussed in detail in Section 3.9.2. As discussed by Bruun,[90] the relation of the hot-film output voltage and velocity can be expressed using a polynomial curve fit of the form,

$$U = C_0 + C_1E + C_2E^2 + C_3E^3 + \ldots \tag{3.52}$$

where C_0, C_1, C_2, C_3, …, represent the calibration coefficients and E represents the hot-film output voltage. A fifth-order least-squares fit was applied to the set of calibration points, and the five calibration coefficients were recorded. These calibration coefficients were then used during testing to convert the acquired unsteady wake hot-film measurements to unsteady velocity measurements. An example of the calibration points and calibration coefficients acquired during this investigation is presented in Fig. 3.18.

3.6 Unsteady Reattachment Location Reduction Using Hot-Film Array

Using the hot-film array measurements acquired on the NACA 0012 airfoil with the horn-ice shape, the unsteady shear-layer reattachment location associated with the ice-induced separation bubble could be determined. The subsequent subsections describe in detail the theory behind the method and the procedure used to reduce the unsteady reattachment location from the hot-film array measurements.

3.6.1 Theory of Method

As discussed in Section 2.3, measurements from hot-film arrays can be used to determine the location of flowfield features through a phase-reversal phenomenon that occurs between adjacent sensors on a hot-film array. While previously used in the literature to determine the time-averaged shear-layer reattachment location of a laminar separation bubble on an airfoil or downstream of a flow obstacle, a new method has been developed in the current study that uses this phase-reversal phenomenon to determine the unsteady shear-layer reattachment location.

As previously discussed in Section 2.3, the phase-reversal phenomenon arises due to the flow bifurcation that occurs at reattachment. When the flow reattaches, both upstream and downstream fluid paths develop, similar to the bifurcation of a planar jet impinging on a flat plate. This causes any flow structures and fluctuations that are being convected by the flow to follow either an upstream or a downstream path. This is shown schematically in Fig. 3.19. These structures are observed successively as they pass elements of the hot-film array further along the streamline. As a result, there exists a reversal in phase (shift by 180°) between adjacent sensors at the location where the flow reattachment occurs. In the schematic presented in Fig. 3.19, the reattaching shear layer would cause there to be a reversal in signal phase between sensors 2 and 3.

The phase between two measurements is typically determined by calculating a phase spectrum, which provides the relative phase angle of one signal to another across a distribution of frequencies. However, determining the relative phase between two signals using this method can be difficult to perform reliably across a small time window, since the phase information must be binned into a distribution of frequencies. This makes it unfit for determining the unsteady shear-layer reattachment location. For example, if calculating a phase spectrum for the signals between two adjacent sensors, oftentimes many averages would be required in order to reliably determine the relative phase distribution. Rather than explicitly identifying the location of phase reversal between adjacent sensors using a phase spectrum, the current method identified regions of strong anti-correlation between adjacent sensors near zero time lag. When a phase reversal occurs between two signals, the local maxima of one signal correspond to the local minima of the other signal at the same instance in time. By taking the cross-correlation between these two signals, the cross-correlation coefficient at zero time lag between signals will exhibit a negative value. By translating this phase-reversal phenomenon of a reattaching shear layer into a strong anti-correlation concept, a more appropriate method for determining the unsteady shear-layer reattachment location can be developed.

The theory behind this strong anti-correlation method can also be thought of intuitively by considering the bifurcation of the flow at reattachment. As the flow bifurcates at reattachment, the flow structures are convected along streamlines of opposite streamwise direction. As a flow structure passes a given sensor, it can be expected that the same structure would be observed by the adjacent sensor in the streamwise direction after a very short time lag, since the structures are convected at a fraction of the freestream velocity and the streamwise distance between adjacent sensors is very small. As a result, if calculating the cross-correlation between adjacent sensors that reside on the same side (i.e. upstream or downstream) of the instantaneous reattachment location, it is expected that near a time lag of zero seconds, a strong positive correlation coefficient would result. However, if the reattachment location occurs between two adjacent sensors, the flow structures observed by one sensor would be different than the flow structures observed by the adjacent sensor. As a result, near a time lag of zero seconds, the cross-correlation coefficient between these adjacent sensors would exhibit strong levels of anti-correlation. An example of this is presented in Fig. 3.20, using the sensor numbers shown in the schematic in Fig. 3.19.

By calculating the cross-correlation coefficients across all adjacent sensors within a short time window, the near-instantaneous shear-layer reattachment location could be determined as the location corresponding to the strong anti-correlation between adjacent sensors. By using a sliding window to extract these locations of strong anti-correlation from the acquired hot-film array data, a time history of the unsteady shear-layer reattachment location could be determined.

3.6.2 Reduction Procedure

The resulting reduction of the hot-film array signals progressed as follows. The cross-correlation coefficients between hot-film sensor elements were calculated across a small time window. An example of the cross-correlation coefficients between adjacent sensors, across one small time window, is shown in the contour of Fig. 3.21. From Fig. 3.21, a clear negative peak in the correlation contour near $\tau = 0$ sec can be identified near $x/c = 0.44$. Once the location corresponding to this peak was identified, the position of the time window was then shifted by one measurement in time. This process of computing the cross-correlation coefficients and position of maximum anti-correlation was repeated across the entire time history for all pairs of adjacent sensors.

However, it was possible that some of the near-instantaneous reattachment locations were misidentified. A correlation coefficient threshold was applied to the signal processing method, where any reattachment locations that were determined from a correlation coefficient above this threshold were replaced with the second choice in reattachment location. For these instances, the maximum anti-correlation occurred slightly farther from zero time lag, but exhibited a correlation coefficient below the threshold. In the current example, a threshold of -0.2 was used. Using this threshold, most minimum correlation coefficients were identified within ±0.5 ms from $\tau = 0$ sec, and all instances were identified within ±1.5 ms from $\tau = 0$ sec. In order to further minimize the influence of outlying points, a short-time moving average of the reattachment location was also taken.

As the size of the moving average across the reattachment time history was increased, more of the high-frequency content within the reattachment time history was averaged out. In signal processing, a moving average takes the form of a very simple low-pass filter with finite impulse response.[91] For example, the hot-film data acquired for the NACA 0012 model were sampled at a rate of 2 kHz, so using a moving average of ten samples would have a similar effect as applying a low-pass filter to the data with a cutoff frequency of 200 Hz. As a result, different sizes of the moving average window could be used to highlight different temporal characteristics in the reattachment time history.

Since it was also desirable in this study to identify the time-dependent relationship between the unsteady shear-layer reattachment location and other unsteady quantities that were acquired simultaneously with the hot-film array measurements (e.g. surface pressure), the unsteady reattachment location time history had to be re-aligned with the other measured quantities. Knowing the size of the sliding window used to calculate the cross-correlation coefficients and the size of the moving average window, the quantities acquired with the hot-film array measurements could be aligned with the near-instantaneous shear-layer reattachment location simply by truncating a number of data points at the beginning and end of the respective record length.

3.7 Setup Frequency Modes

Since much of this study was focused on characterizing the frequency content of the iced-airfoil flowfield, it was important to ensure that the frequencies of the relevant aerodynamic phenomenon were distinct from the frequency modes produced by the experimental setup and testing environment. Such experimental setup frequencies included the structural modes of the airfoil model (f_{struct}) and wind tunnel fan blade passing frequencies (f_{blade}).

3.7.1 Wind Tunnel Fan Blade Frequencies

When the wind tunnel was running with a constant test-section speed during the data acquisition, this speed was produced by the fan motor operating at a given RPM. Since the fan was used as the means of moving the freestream air through the wind tunnel test section, the pressure difference induced by a passing of a fan blade could be periodically sensed inside the test section. Knowing the fan RPM during data acquisition, the fan blade passing frequencies to be expected in a test could be determined. Beginning with the fan RPM setting and using simple dimensional analysis, the time required (in seconds) for one full revolution of the fan could be calculated by dividing 60 sec/min by the RPM of the fan. However, since there were five blades on the wind tunnel fan, the time between each individual fan blade passing was 1/5 of the time required for a full revolution of the wind tunnel fan. Finally, since the frequency of the fan blade passing was simply the inverse of the time between the periodic fan blade passing, f_{blade} could be calculated using

$$f_{blade} = 5\frac{RPM}{60} \tag{3.53}$$

Most of the data acquisition in this study was performed at a chord-based Reynolds number of 1.8×10^6. While the RPM required to achieve this Reynolds number changed slightly depending on wind tunnel blockage, atmospheric conditions, etc., this Reynolds number was typically achieved for a fan setting around 1100 RPM. At this RPM setting, the first harmonic of f_{blade} would correspond to a frequency of 91.67 Hz. It can also be expected that higher harmonics of f_{blade} would also occur in multiples of the first harmonic (e.g. 183.3 Hz, 275 Hz, …).

3.7.2 Airfoil Model Structural Modes

The structural modes of the model represent the natural frequencies of the airfoil model construction and associated components that vibrate or resonate when excited. Since the unsteadiness in the unsteady airfoil performance coefficients was characteristic of unsteadiness about the global airfoil flowfield, it was particularly useful to analyze the frequencies of the structural modes through the unsteady performance coefficients. Additionally, since the individual and integrated effects of the surface-integrated pressure transducers were used to determine the frequency content present in the flowfield and are reported extensively in this study, it was appropriate to determine the structural modes through these same means. The structural modes were determined through a simple impulse-response test. An external impulse was applied to the airfoil model and the resulting response of the pressure transducers was acquired using the prescribed data acquisition techniques of Section 3.2. After integrating these pressure measurements to obtain the unsteady airfoil performance coefficients, the power spectral density (PSD) functions of the airfoil performance coefficients were calculated using the methods that will be described in Section 3.10.1. The resulting PSDs of this impulse response test are shown in Fig. 3.22. In Fig. 3.22 the structural peaks identified in C_l and C_m are marked with a vertical dashed line, and correspond to f_{struct} = 90 Hz, 150 Hz, 245 Hz, and 390 Hz. Identification of these structural frequencies is important for analyzing data to ensure that the frequency peaks of interest are due to aerodynamic phenomena and not structural vibration.

3.8 Flow Visualization Methods

In this investigation, multiple methods of flow visualization were used in order to identify various features of the clean-airfoil and iced-airfoil flowfields. These techniques allowed for the visualization of both on-surface and off-surface flowfield characteristics. A fluorescent oil surface flow visualization method was used to provide a time-averaged image of the airfoil surface flowfield. Two variations of smoke flow visualization were used to identify unsteady features of the off-surface airfoil flowfield. The smoke flow visualization methods included the use of a fog generator visualization technique, and a smoke wire visualization technique.

3.8.1 Fluorescent Oil Surface Flow Visualization

Visualization of the airfoil surface flowfield was accomplished using a fluorescent oil surface flow visualization technique. Use of this technique allowed for the identification of key features in the time-averaged flowfield, including regions of separated flow and mean shear-layer reattachment. The fluorescent oil surface flow visualization method used in the current study was the same as that reported by Ansell[92] and by Busch.[93] Fluorescent oil surface flow visualization was completed on both the clean airfoil and the airfoil with simulated leading-edge ice shapes at various angles of attack. Surface flowfield images were acquired for $Re = 1.8 \times 10^6$, which was the Reynolds number at which airfoil data were acquired. The fluorescent oil flow visualization was completed using the following method.

First the airfoil model was wrapped in black contact paper, providing a high contrast with the fluorescent dye which increased the visibility of the oil flow patterns. Use of the contact paper also covered up the pressure taps and integrated pressure transducers, which prevented them from being contaminated by the oil used in this flow visualization method. The contact paper was manufactured by Kittrich Corporation, and had a mild adhesive on one side and a smooth surface on the other. On top of the contact paper, two strips of yellow electrical tape were applied to the model, approximately 7.5 in. from the test section floor and ceiling. The electrical tape was marked with the airfoil x/c coordinates in 5% increments.

A thin layer of 5W-30 motor oil was applied to the airfoil surface. Excess oil was removed by lightly wiping the surface with a precision wipe in the streamwise direction. A mixture of mineral oil and an oil-based fluorescent leak detector dye was then applied to the airfoil surface in a fine spray using an airbrush. The airbrush was connected to a nitrogen gas tank, which was regulated at 30 psi, in order to achieve the desired back pressure for distributing the fluorescent oil mixture. Use of the airbrush was necessary, as the spray had to be fine enough not to generate large droplets, which were susceptible to running down the model span due to gravity. Black lights were used to fluoresce the oil mixture on the model to ensure complete coverage of the surface.

After the application of the fluorescent oil mixture was complete, the airfoil model angle of attack was set to the desired value, and the wind tunnel fan was ramped up to speed. The wind tunnel was run at the desired Reynolds number for a total of four minutes. After this time, the wind tunnel was turned off and the model was rotated to $\alpha = 0°$ for photographing. It was ensured that the wind tunnel fan had stopped before rotating the model for photographing, as rotation of the model while the wind tunnel fan was ramping down could adversely alter the time-averaged flowfield image at the desired angle of attack. The overhead lights in the laboratory were then turned off and the fluorescent oil mixture was again excited using black lights. The ultraviolet wavelength from the black lights excited the leak detector dye in the oil mixture, causing it to fluoresce a green color. Images of the airfoil model upper surface were then documented using a Nikon D3100 digital SLR camera mounted on a tripod, using various extended exposure times. These images were transferred to a computer, and were checked to ensure all important flowfield features were captured. The model was then wiped clean with precision wipes and glass cleaner, and the flow-visualization process was repeated for the next desired case.

3.8.2 Smoke Flow Visualization

The use of smoke flow visualization allowed for the off-surface unsteady flowfield to be imaged and recorded. Due to certain limiting factors in the visualization techniques, the smoke flow visualization methods had to be conducted at test-section speeds reduced from those at which airfoil performance data were acquired. Like the fluorescent oil surface flow visualization method, before conducting either method of smoke flow visualization the airfoil model was wrapped in black contact paper, as described in Section 3.8.1. The test section floor was also covered in a layer of black contact paper to provide a high-contrast background for the smoke used in these visualization methods. The test-section ceiling was replaced with a Plexiglass ceiling, so that the smoke patterns in the airfoil flowfield could be seen. A Nikon D3100 digital SLR camera was mounted to a tripod located above the test-section ceiling, and was used for video recording of the smoke flow visualization. Three halogen work lamps were used to provide direct lighting in the wind tunnel test section for the smoke patterns to be observed. For both flow visualization methods, videos of the airfoil flowfields were acquired for the clean and simulated horn-ice shape configurations at α = 5°, 6°, and 7°.

3.8.2.1 Fog Generator Smoke Flow Visualization

The fog generator smoke flow visualization was conducted using a 400 Watt fog machine. An attachment was constructed and attached to the outlet nozzle of the fog generator to distribute the fog into five streamtubes at one spanwise location on the airfoil model. This attachment was T-shaped and made with connecting PVC tubing. The downstream end of the attachment had five holes which were equally spaced horizontally across the length of the PVC tube. A photograph of the fog machine with the PVC attachment is presented in Fig. 3.23. The downstream end of the PVC attachment was positioned against the wind tunnel inlet at the position where the middle streamtube in the flowfield would stagnate at the airfoil leading edge.

During testing, the airfoil model was rotated to the desired angle of attack, and the wind tunnel fan was turned on. When using the fog generator smoke flow visualization method, the wind tunnel was run at test-section speeds reduced from those used in data acquisition. This was necessary, as the fog streams that the fog machine produced were not clearly visible at higher speeds. As a result, the fog generator smoke flow visualization was conducted at $Re = 0.5 \times 10^6$. A video of the smoke flow visualization was then recorded and stored on a computer for further post-processing and analysis. A typical video length for the fog generator smoke flow visualization method was approximately two minutes.

3.8.2.2 Smoke Wire Flow Visualization

The smoke wire flow visualization method was also conducted to image the off-surface airfoil flowfield. The smoke wire flow visualization technique produced a sheet of thin smoke streamlines across one spanwise section of the airfoil model. While this method did not produce as much smoke as the fog generator method, the greater distribution of smoke streamlines produced much clearer images of the global airfoil flowfield. The smoke wire flow visualization was conducted using a wire support structure, a Nichrome wire, a smoke fluid mixture, and a high-voltage power supply. The wire support structure was constructed from angled sections of streamline tubing, and was mounted upstream of the wind tunnel model. The support structure was fastened to the inside of a wooden pressure box above the wind tunnel, which aided in sealing the smoke wire support structure from the environment outside of the wind tunnel. A length of Nichrome wire was mounted to the support structure at the two ends inside the wind tunnel. A Nichrome wire was used, as it has high resistivity which causes it to become very hot when an electrical current is passed through it. The Nichrome wire that was used in this investigation had a diameter of 0.006 in. (36 gauge). The length of Nichrome wire was tensioned before testing in order to prevent it from sagging after thermal expansion. A photograph of the wire support structure and accompanying Nichrome wire installed in the wind tunnel is presented in Fig. 3.24.

Two lengths of 16 AWG hook-up wire were connected to the two ends of the Nichrome wire and run through the streamline tubing of the support structure and out of the pressure box. These hook-up wires were then connected to positive (+) and negative (-) terminals of a power supply. The power supply that was used was a Kepco Model ABC 125-1DM and was rated for an output of 0–125 V at 0–1 A. This power output was used to heat the Nichrome wire and burn off a smoke mixture on the Nichrome wire to produce the smoke sheet. In this investigation, the smoke mixture was created by mixing a glycerin-based train smoke fluid with a small amount of xanthan gum. Since the train smoke fluid was not very viscous, only very small quantities could be deposited onto the Nichrome wire at one time. This would produce very short intervals of smoke wire flow visualization, as the small quantity of train smoke fluid would quickly burn up. By adding the xanthan gum, the viscosity of the train smoke fluid was increased, and greater quantities of the smoke mixture could be deposited onto the Nichrome wire. This resulted in longer intervals at which the smoke wire flow visualization could be continuously conducted.

While other types of fluids (e.g. mineral oil) are commonly used in smoke wire flow visualization, the train smoke fluid and xanthan gum mixture was used in the current study primarily for two reasons. First, the train smoke fluid produces a brilliant white smoke with high visibility. The smoke produced by some of the other fluids that were tested did not produce smoke that was as visible as the train smoke fluid. Second, the train smoke fluid burns at a lower temperature than the other smoke wire fluids tested. This was important, as higher test-section speeds led to greater convective cooling of the Nichrome wire, which offset some of the temperature increases of the wire imposed by the electric current. As a result, one of the major limiting factors to the test-section speed for the smoke wire flow visualization technique was the convective cooling effect from the freestream velocity. Thus, by having a smoke fluid that burned at a lower temperature, this allowed for the smoke wire flow visualization to be conducted at higher test-section speeds, as not as much power output would be required from the power supply in order to heat the wire to a lower temperature. Due to these considerations, the smoke wire flow visualization technique was completed at $Re = 0.1 \times 10^6$. At the corresponding test-section speed, the current in the wire was great enough to burn enough smoke mixture for visualization purposes, despite decreases in temperature due to convective cooling.

After all of the smoke wire equipment was installed, the smoke mixture was brushed onto the Nichrome wire. The airfoil model was then rotated to the desired angle of attack and the test-section speed was set to reach the desired Reynolds number. The power supply output was then turned on, which caused the smoke mixture on the Nichrome wire to burn. As the smoke mixture burned, a smoke sheet was produced in the wind tunnel test section for approximately ten seconds. A video of the smoke flow visualization was recorded across this entire time interval. A series of these videos were obtained and were stored on a computer for further post-processing and analysis. After the smoke mixture had burned off, the power supply output was turned off and a new coat of the smoke mixture could be brushed onto the Nichrome wire for the next desired test.

3.9 Wind Tunnel Corrections

The wind tunnel testing environment was designed to simulate the flowfield of an airfoil in an essentially unbounded, fixed-condition freestream. However, since the wind tunnel testing environment was constrained with finite wall boundaries, several corrections to the acquired data were necessary in order to compensate for the resulting wall effects. For example, since the presence of the airfoil model reduces the effective cross-sectional area of the wind tunnel test section, in order for continuity to be upheld the flow around the airfoil model must increase. Corrections for these types of effects were made to the airfoil performance measurements, and are described in Section 3.9.1. Separate corrections were made to the acquired wake hot-film measurements in order to compensate for the differences in freestream conditions between calibration and data acquisition. For example, since hot-film anemometry relies on principles of heat transfer in order to produce a given measurement, the acquired voltage is sensitive to changes in the temperature of the freestream air. These corrections that were applied to the wake hot-film data are described in Section 3.9.2.

3.9.1 Wind Tunnel Wall Corrections

The wind tunnel wall corrections that were performed in this investigation followed the standard data corrections described by Barlow et al.[94] for 2D, low-Reynolds number wind tunnel testing. Corrections were applied to the acquired airfoil performance data for three wind tunnel effects. These three effects included solid blockage, wake blockage, and streamline curvature. It should be noted that these corrections are based on the assumption of an incompressible flow and would not be valid in applications of compressible flow, unless changes in the air density were properly accounted for.

The solid blockage effect is caused by an effective reduction in the test-section cross-sectional area by the presence of the airfoil model. Since continuity must be enforced through the wind tunnel, if the cross-sectional area of the test section where the airfoil model is located is slightly lower than the cross-sectional area of the upstream end of the test section, the airspeed at the model location will be slightly higher than that of the freestream entering the test section. Generally, this solid blockage effect is a function of model thickness and angle of attack. Following the method of Barlow et al.[94] the effects of this velocity increase can be corrected using the solid-blockage velocity increment, ε_{sb}, which can be estimated by,

$$\varepsilon_{sb} = \frac{K_1 V_m}{C^{3/2}} \tag{3.54}$$

where K_1 is a constant parameter based on the airfoil configuration, C is the empty test-section area, and V_m is the airfoil model volume. From Barlow et al.[94] K_1 takes a value of 0.52 for airfoil models spanning the test-section height. The model volume was estimated using,

$$V_m = \frac{3}{4} tcb \tag{3.55}$$

where t is the airfoil (dimensional) thickness and b is the span of the airfoil model.

The wake blockage effect is similar to the solid blockage effect in that it causes the test-section velocity to increase at the airfoil model location, but it is not due to a reduction in the cross-sectional area of the test section. Instead, the increase in test-section velocity occurs due to local reductions in velocity in the wake of the airfoil model. Since the velocity in the wake of the airfoil decreases, the velocity outside of the wake must increase for the mass flow rate to remain constant through the test section. Since the extent of the wake velocity deficit can be directly related to the profile drag of the airfoil, the change in the velocity outside of the wake can be expected to scale proportional to the airfoil drag. Thus, the increase in the freestream velocity in the test section at the airfoil model can be compensated for using a wake-blockage velocity increment, ε_{wb}, which can be calculated by,

$$\varepsilon_{wb} = \frac{1}{2}\frac{c}{h}C_{d,u} \tag{3.56}$$

where h is the test-section height and $C_{d,u}$ is the uncorrected value of the airfoil drag coefficient. The total velocity increment, ε, was calculated simply by adding the solid-blockage velocity increment and the wake-blockage velocity increment,

$$\varepsilon = \varepsilon_{sb} + \varepsilon_{wb} \tag{3.57}$$

Streamline curvature is represented by a distortion of the streamlines from that of an airfoil in an unbounded freestream. As such, the wind tunnel walls impose a finite constraint on the formation of the streamlines, causing the airfoil in a closed wind tunnel to appear to have more camber than it actually has. This leads to increases in lift and changes in the quarter-chord pitching moment above what would occur in an unbounded environment. The streamline curvature effect can be compensated using the variable σ, which can be calculated using,

$$\sigma = \frac{\pi^2}{48}\left(\frac{c}{h}\right)^2 \tag{3.58}$$

The correction factors calculated in Eqs. 3.54, 3.56, and 3.58 were used to calculate the corrected values of the airfoil angle of attack and acquired airfoil performance measurements. The angle of attack, lift coefficient, drag coefficient, quarter-chord pitching moment coefficient, and pressure coefficient were corrected using Eqs. 3.59–3.63, respectively.

$$\alpha_{cor} = \alpha_u + \frac{57.3\sigma}{2\pi}\left(C_{l,u} + 4C_{m,u}\right) \tag{3.59}$$

$$C_{l,cor} = C_{l,u}\left(1 - \sigma - 2\varepsilon\right) \tag{3.60}$$

$$C_{d,cor} = C_{d,u}\left(1 - 3\varepsilon_{sb} - 2\varepsilon_{wb}\right) \tag{3.61}$$

$$C_{m,cor} = C_{m,u}\left(1 - 2\varepsilon\right) + \frac{1}{4}\sigma C_{l,u} \tag{3.62}$$

$$C_{p,cor} = \frac{C_{p,u}}{(1+\varepsilon)^2} \tag{3.63}$$

Unsteady C_p measurements were also corrected using Eq. 3.63 point-by-point across all acquired data points, using the time-averaged $C_{d,u}$ to calculate ε_{wb}.

3.9.2 Wake Hot-Film Measurement Corrections

Corrections were made to the wake hot-film measurements in order to compensate for differences in freestream conditions between calibration and data acquisition. The first correction that was made to the acquired wake hot-film measurements was used to correct for small changes in temperature at calibration and at data acquisition. Since the hot-film voltage is dependent on the heat transfer between the probe and the freestream, when the temperature of the freestream changes, the heat transfer characteristics will also change. As a result, the hot-film voltage acquired during data acquisition was corrected before applying the calibration using the method outlined by Tropea et al.,[95]

$$E_{cor} = E\sqrt{\frac{T_{film} - T_{ref}}{T_{film} - T_{amb}}} \tag{3.64}$$

In Eq. 3.64, E_{cor} represents the temperature-corrected hot-film voltage, T_{ref} is the ambient temperature during calibration, T_{amb} is the ambient temperature during data acquisition, and T_{film} is the temperature of the hot-film probe.

An additional correction was also made for changes in density between calibration and data acquisition. Since the calibration curve actually represented a calibration of the mass flow rate with respect to hot-film voltage, changes in ambient density could introduce small deviations from the calibrated velocity conditions. This correction followed the method discussed by Spring.[96] Once the calibration had been applied to the corrected hot-film voltage to get the velocity, the density correction was applied. If the ambient density was the same between calibration and data acquisition, the velocity remained unchanged from the calibration. The density correction was performed using,

$$U_{cor} = \frac{\rho_{cal} U_{ind}}{\rho_{amb}} \tag{3.65}$$

where U_{cor} is the corrected velocity, U_{ind} is the velocity indicated from the calibration, and ρ_{cal} is the ambient density during calibration.

3.10 Unsteady Data Analysis Procedures

In order to determine the characteristics of the unsteady flowfield, the unsteady measurements were analyzed using a variety of signal processing techniques. These methods included the fast Fourier transform, phase angle analysis, conditional averaging, correlation analysis, and wavelet analysis. The following subsections describe the theory and practice of these unsteady data analysis methods.

3.10.1 Power Spectral Density (PSD) and Spectral Content

In order to classify the relevant frequency scales of a given unsteady measurement, the distribution of energy in the frequency domain was analyzed. This was accomplished using standard fast Fourier transform (FFT) methods. An FFT is an algorithm that can be used to compute the discrete Fourier transform (DFT) of a signal at much greater speed than a standard DFT calculation. FFT analysis is common in data analysis, and provides estimates of spectral density functions of a signal.[97] The DFT of a signal can be described using,

$$X_k = \sum_{n=0}^{N-1} x_n e^{-i2\pi k \frac{n}{N}} \qquad k = 0,1,2,...,N-1 \tag{3.66}$$

In Eq. 3.66, X_k is the transformed signal, x_0, …, x_{N-1} are complex numbers, N is the number of data points in the DFT, and k represents the discrete frequency values such that,

$$f_k = \frac{k}{N\Delta t} \qquad k = 0,1,2,...,N-1 \tag{3.67}$$

where Δt is the temporal spacing of data points.

The resulting Fourier transform can be expressed in the form of a power spectral density function. In this investigation, the one-sided power spectral density function (G_{xx}) was used. This quantity can be calculated from a signal Fourier transform, using,[97]

$$G_{xx}(f) = 2\lim_{T\to\infty}\frac{1}{T}E\left[\left|X_k(f,T)\right|^2\right] \tag{3.68}$$

where E represents the expected value of the bracketed term. Using this method, the distribution of power could be observed across the frequency spectrum ranging from $f = 0$ Hz to the Nyquist frequency (i.e. half of the sampling frequency).

When analyzing a PSD, it is sometimes useful to observe the amplitude in decibel (dB) format, which is a logarithmic ratio of units of power. The conversion from power to decibel can be calculated using,

$$L_{dB} = 10\log_{10}\left(\frac{P_1}{P_0}\right) \tag{3.69}$$

where L_{dB} represents the power ratio in dB, P_1 represents the measured power of a signal, and P_0 represents a reference power level. In this investigation, the amplitudes of all PSDs shown in dB format were calculated with a P_0 reference level of unity in the same units of P_1.

Ensemble averaging of PSDs is commonly performed in order to reduce the influence of random occurrences, making the trends in the spectral content of a signal easier to observe. In the current study, PSDs were calculated using 500,000 data points for a given measured quantity and test condition, except when otherwise indicated. These data points were split between 20 identical runs of 25,000 samples. Each of these runs could also be split into multiple ensembles, increasing the number of ensembles used in the PSD average, but decreasing the frequency resolution of the resulting PSD.

In order to utilize the self-similarity that is exhibited in fluid mechanics, the Strouhal number is commonly used to non-dimensionalize the frequency of unsteady, periodic aerodynamic phenomena. Thus, when a phenomena of interest is observed at a certain frequency in the PSD, the corresponding Strouhal number can be calculated. The Strouhal number (St) is commonly defined as,

$$\mathrm{St} = \frac{fL}{U_0} \tag{3.70}$$

where f is the frequency, L is the reference length scale, and U_0 is the reference velocity scale. In the current study, all Strouhal numbers will be referenced to the freestream velocity. However, different reference length scales will be used to better classify different aerodynamic phenomena. In this study, a Strouhal number based on the separation bubble length (St_L) and a Strouhal number based on the airfoil projected height (St_h) are used. These Strouhal numbers are calculated using,

$$\mathrm{St}_L = \frac{fL_b}{U_\infty} \tag{3.71}$$

$$\mathrm{St}_h = \frac{f(c\sin\alpha)}{U_\infty} \tag{3.72}$$

where L_b represents the length of the separation bubble.

3.10.2 Phase Angle Analysis

While the FFT is useful for identifying the frequency content of a given signal, it can also be used to determine the phase relationships between two different signals across a frequency spectrum. To aid in this comparison, the one-sided cross-spectral density function (G_{xy}) can be calculated using,[97]

$$G_{xy}(f) = 2\lim_{T\to\infty}\frac{1}{T}E\left[X_k^*(f,T)Y_k(f,T)\right] \tag{3.73}$$

where X_k^* represents the complex conjugate of the Fourier transform of one signal and Y_k represents the Fourier transform of the other signal. Since G_{xy} is complex-valued, it can be expressed in complex polar notation as,

$$G_{xy}(f) = \left|G_{xy}(f)\right|e^{-i\theta_{xy}(f)} \tag{3.74}$$

where θ_{xy} is the phase angle spectrum.

As discussed in Bendat and Piersol,[97] G_{xy} can be expressed using contributions from the coincident spectral density function (C_{xy}), which represents the real contribution to G_{xy}, and the quadrature spectral density function (Q_{xy}), which represents the imaginary contribution to G_{xy}. The resulting phase angle spectrum can be calculated using,

$$\theta_{xy}(f) = \tan^{-1}\left(-\frac{Q_{xy}(f)}{C_{xy}(f)}\right) \tag{3.75}$$

Using the phase angle spectrum, the relative phase angle between two signals can be observed as a function of frequency. Thus, for particular frequency of interest, the angular phase (within $\pm\pi$) could be determined between two measurements.

A given shift in phase angle between two known locations is commonly used to determine the time delay of a given Fourier mode between these two locations. In the current example, the time delay represents the average time of convection or progression of a given Fourier mode between two locations. This method has been shown by Piersol[98] to be capable of rendering time delay estimates with accuracy comparable to other conventional methods of estimating time delay. The time delay (τ_0) associated with a given phase angle between two measurements can be calculated by,

$$\tau_0 = \frac{\theta_{xy}(f)}{2\pi f} \tag{3.76}$$

With the time delay and the distance between two locations known, the average convection velocity of a given Fourier mode can be calculated. In this way, the slope of the phase angle distribution can be used to calculate the average propagation velocity of a given frequency using,

$$U_c = \frac{2\pi f c}{m} \tag{3.77}$$

where U_c represents the convection velocity and m represents the slope of θ with respect to x/c.

3.10.3 Conditional Averaging

For certain non-periodic or quasi-periodic processes, determining a strict time-dependent relationship between measurements can sometimes be difficult. For this reason, conditional averaging is sometimes used to determine the average relationship between measurements with respect to a conditional occurrence or event. In the current investigation, conditional averaging was used to identify the average time-dependent relationship between the unsteady shear-layer reattachment location and the airfoil performance coefficients corresponding to a low-frequency mode. In order to perform the conditional average, the low-frequency mode of the unsteady shear-layer reattachment location was calculated, and the end of the shrinking phase of the separation bubble was used to specify which segments of the signal time histories would be extracted for use in the conditional averaging scheme.

When the low-frequency component of the instantaneous shear-layer reattachment location reached a peak below a certain threshold, a number of samples before and after this peak were extracted. The extractions of time histories from the total record length were selected such that there was no overlap between any segments of the extracted time histories. After an ensemble of these time history segments were extracted, they were averaged. The time histories for the unsteady airfoil performance coefficients and C_p were also processed in the same way, using the same time intervals as the unsteady shear-layer reattachment location. This conditional averaging procedure resulted in the mean responses of the iced-airfoil performance and C_p signals during the low-frequency oscillation of the shear-layer reattachment location.

Once the conditional averaging scheme was completed, aspects of the average relationship between the shear-layer reattachment location and the airfoil pressure and performance coefficients could be determined. These relationships were identified through the use of additional signal processing techniques on the conditionally-averaged signals.

3.10.4 Correlation Analysis

The first signal processing method that was used to determine the time-dependent relationship between the shear-layer reattachment location and the airfoil performance was the cross-correlation coefficient. The cross-correlation coefficient can be used to describe the average time lag between similar features observed in two signals. The cross-correlation coefficient was calculated based on an estimation of the cross-correlation function, which when computed directly can be calculated by,[97]

$$R_{xy}(r\Delta t) = \frac{1}{N-r}\sum_{n=1}^{N-r} x_n y_{n+r} \tag{3.78}$$

where N represents the number of data samples, $r = 0, 1, 2, \ldots, m$ represents the given time lag interval (with $m < N$), and x and y represent the quantities for which the cross-correlation is being computed. It should be noted that for this investigation, Δt was known to be the inverse of the sample rate, thus making the quantity $r\Delta t$ the time lag, τ, between points n and $n + r$. Using the calculated cross-correlation function, the cross-correlation coefficient, ρ_{xy}, was estimated using,

$$\rho_{xy}(\tau)=\frac{R_{xy}}{\sigma_x\sigma_y} \tag{3.79}$$

where σ represents the standard deviation of the sample.

3.10.5 Wavelet Analysis

In addition to the observations that can be made to the spectral content of a signal using FFT methods, it can also be beneficial to identify changes in spectral content in a signal over time. Identifying the time-dependent spectral content of signals was particularly useful in the current study after using the conditional averaging scheme, as regions of high spectral activity could be identified in a signal at a time relative to a given event (e.g. end of the shrinking phase of the shear-layer reattachment location). This was accomplished by performing a wavelet transform on the conditionally-averaged signals.

While a simplified discussion of continuous wavelet transforms will be discussed here, a more in-depth discussion of wavelet analysis and its use in signal processing can be found in several seminal texts.[91,99,100] A continuous wavelet transform is accomplished by taking a basic wavelet function (sometimes called a "mother" wavelet) and from it creating a family of wavelets. This family of wavelets corresponds to the full frequency spectrum of a signal, via dilation (scaling) of the basic wavelet function, and the full temporal length of a signal, via translation of the wavelet function. The resulting wavelet transform then represents the amount of energy contained in the signal at a given frequency and at a given instance in time.

The Morlet wavelet was used to calculate the continuous wavelet transform (CWT) of the conditionally-averaged reattachment location, airfoil performance coefficients, and airfoil pressure distribution. As discussed by Torrence and Compo,[100] the Morlet wavelet is defined as a sine wave multiplied by a Gaussian envelope and can be expressed using the wavelet function (ψ_0) of,

$$\psi_0(\eta)=\pi^{-1/4}e^{if_0\eta}e^{-\eta^2/2} \tag{3.80}$$

where η represents a dimensionless time parameter and f_0 represents a dimensionless frequency parameter.

The Morlet wavelet was used in the current study for various reasons. One of which is that it has a complex-valued wavelet function, which is typically better for identifying oscillatory behaviors in a signal.[100] Another advantage of using the Morlet wavelet is that it has a wavelet scale that is approximately equivalent to the corresponding Fourier scale. This allows the content of the wavelet transform at a given wavelet frequency scaling to be easily translated to the corresponding Fourier frequency. This is particularly useful for the current investigation where knowledge of the dimensional frequency content is important, as specific aerodynamic phenomena occur at distinguished Fourier modes. A diagram of the Morlet wavelet function and associated Fourier transform are shown in Fig. 3.25 after Torrence and Compo.[100] From Fig. 3.25, it can be seen that the Morlet wavelet function with frequency of 1 corresponds to a central frequency in the Fourier transform of 1.

3.11 Uncertainty Analysis

Like with all experimental investigations, the results obtained in the current study were associated with a given level of uncertainty. As described by Kline and McClintock,[101] experimental uncertainty represents “a possible value the error might have.” As discussed by Moffat,[102] sources of errors in an experiment can be attributed to bias or precision errors. Bias errors typically occur due to uncertainty in the measurement capabilities of an instrument or accuracy of a calibration, and are accompanied with a consistent and repeatable offset. Conversely, precision errors behave randomly with zero mean. The sum of these two sources of error represents the total error of a measurement. In the current study, the potential bias errors will be estimated using the methods of Kline and McClintock[101] and Coleman and Steel.[103] The precision error of a measurement mean value will be estimated as being two standard deviations of the sample from the mean, which is then divided by the square root of the number of samples, assuming that the samples represent a Gaussian distribution. As discussed by Moffat,[102] this method supplies a 95% confidence interval (20:1 odds) that the true mean value exists within the experimental uncertainty provided.

The premises of the bias uncertainty calculation of Coleman and Steel[103] presumes that a result (R) is determined using several independently measured variables (x_i), such that:

$$R = R(x_1, x_2, ..., x_n) \tag{3.81}$$

By assuming that the uncertainties of each measured variable were independent of each other, the uncertainty associated with a resulting quantity (U_R) can be calculated as the square root of the sum of the squares of each uncertainty component produced by each variable,

$$U_R = \sqrt{\left(\frac{\partial R}{\partial x_1} U_{x_1}\right)^2 + \left(\frac{\partial R}{\partial x_2} U_{x_2}\right)^2 + \ldots + \left(\frac{\partial R}{\partial x_n} U_{x_n}\right)^2} \tag{3.82}$$

Using this method, the resulting uncertainties were calculated as described in the following sections. These calculations were similar to those carried out by Ansell[92] and by Busch.[93] A summary of representative example uncertainties from this can be found in Section 3.11.7.

3.11.1 Uncertainty in Flow Condition Results

The first set of quantities that the experimental uncertainties were estimated for included the flow conditions at which the experiments were run. These results included the freestream dynamic pressure, atmospheric density, dynamic viscosity, freestream velocity, and Reynolds number setting. Some example uncertainties of the flow conditions at a reference condition are presented in Table 3.4.

3.11.1.1 Dynamic Pressure

As discussed in Section 3.4.1.1, the freestream dynamic pressure was calculated using Eq. 3.15, where the difference in pressure between the settling section and the test section was divided a quantity involving the contraction ratio across the tunnel inlet. Since the inlet contraction ratio was constant and the uncertainty in the area ratio was assumed to be very low, the uncertainty in the inlet contraction ratio was assumed to be negligible. As a result, the contribution of the pressure difference in Eq. 3.15 was assumed to be the only factor included in determining the uncertainty of the freestream dynamic pressure. Following Eq. 3.82, the resulting uncertainty in the dynamic pressure was calculated using,

$$U_{q_\infty} = \sqrt{\left(\frac{\partial q_\infty}{\partial\left(P_{ss} - P_{ts}\right)} U_{(P_{ss}-P_{ts})}\right)^2} \tag{3.83}$$

Additionally, it was assumed that the uncertainty of the measured pressure difference between the settling section and the test section was constant. As a result, Eq. 3.83 could be expressed using,

$$U_{q_\infty} = \frac{\partial q_\infty}{\partial (P_{ss} - P_{ts})} U_{(P_{ss}-P_{ts})} = \frac{1}{1 - \left(\frac{A_{ts}}{A_{ss}} \right)^2} U_{(P_{ss}-P_{ts})} \tag{3.84}$$

The uncertainty of the pressure measurement for the PSI module used to measure this pressure difference in Eq. 3.84 was 0.0014 psid. More details of the uncertainties of the PSI system measurements will be presented in Section 3.11.3. The Setra 239 was also used to measure the pressure difference when setting the wind tunnel Reynolds number. The uncertainty of the Setra pressure transducer was quoted by the manufacturer to be 0.14% of the full-scale, which was 15 in. WC (0.541 psid). As a result, the uncertainty in the pressure difference measurement by the Setra 239 transducer was 0.000757 psid. Using an inlet area ratio of 7.5:1, the resulting uncertainty in the freestream dynamic pressure was U_{q_∞} = ±0.001425 psid for the PSI system and U_{q_∞} = ±0.000771 psid for the Setra 239 transducer.

3.11.1.2 Atmospheric Density

The atmospheric density was calculated using the ideal gas law, presented in Eq. 3.5. It was known that the gas constant of air, R, had a constant value of 1716 ft-lb/slug-°R. As a result, it did not contribute to the uncertainty of the resulting density. However, P_{amb} and T_{amb} were both measured quantities and did have a contribution to the uncertainty of ρ_{amb}. As a result, the uncertainty in the atmospheric density could be calculated using,

$$U_{\rho_{amb}} = \sqrt{\left(\frac{\partial \rho_{amb}}{\partial P_{amb}} U_{P_{amb}} \right)^2 + \left(\frac{\partial \rho_{amb}}{\partial T_{amb}} U_{T_{amb}} \right)^2} \tag{3.85}$$

where

$$\frac{\partial \rho_{amb}}{\partial P_{amb}} = \frac{1}{R T_{amb}} \tag{3.86}$$

$$\frac{\partial \rho_{amb}}{\partial T_{amb}} = -\frac{P_{amb}}{R T_{amb}^2} \tag{3.87}$$

The values of uncertainty provided by the manufacturer for the Setra 270 pressure transducer and the Omega thermocouple used to obtain the ambient pressure and temperature measurements were 0.008 psi and 1.8 °R, respectively.

3.11.1.3 Dynamic Viscosity

The dynamic viscosity was used in order to calculate the Reynolds number in Eq. 3.1. The dynamic viscosity was calculated using Sutherland's formula,

$$\mu_{amb} = \mu_0 \frac{T_0 + C}{T_{amb} + C} \left(\frac{T_{amb}}{T_0} \right)^{3/2} \tag{3.88}$$

where μ_0, T_0, and C are known constants having values of 3.58404×10^{-7} slug/ft-sec, 491.6 °R, and 199.8 °R, respectively. Since the only variable in Eq. 3.88 is the ambient temperature, it provides the only contribution to the uncertainty in the dynamic viscosity. As a result, the uncertainty of the dynamic viscosity can be calculated using,

$$U_{\mu_{amb}} = \sqrt{\left(\frac{\partial \mu_{amb}}{\partial T_{amb}} U_{T_{amb}} \right)^2} \tag{3.89}$$

where

$$\frac{\partial \mu_{amb}}{\partial T_{amb}} = \frac{3}{2} \mu_0 \sqrt{\frac{T_{amb}}{T_0}} \frac{T_0 + C}{T_0 \left(T_{amb} + C \right)} - \mu_0 \left(\frac{T_{amb}}{T_0} \right)^{3/2} \frac{T_0 + C}{\left(T_{amb} + C \right)^2} \tag{3.90}$$

3.11.1.4 Freestream Velocity

Since the dynamic pressure in an incompressible flow is defined as $q_\infty = \frac{1}{2}\rho U_\infty^2$, the uncertainty in U_∞ can alternatively be calculated using,

$$U_\infty = \sqrt{\frac{2 q_\infty}{\rho_{amb}}} \tag{3.91}$$

The resulting uncertainty of the freestream velocity could then be calculated using,

$$U_{U_\infty} = \sqrt{\left(\frac{\partial U_\infty}{\partial q_\infty} U_{q_\infty} \right)^2 + \left(\frac{\partial U_\infty}{\partial \rho_{amb}} U_{\rho_{amb}} \right)^2} \tag{3.92}$$

where

$$\frac{\partial U_\infty}{\partial q_\infty}=\frac{1}{\sqrt{2q_\infty \rho_{amb}}} \tag{3.93}$$

$$\frac{\partial U_\infty}{\partial \rho_{amb}}=-\frac{1}{\rho_{amb}}\sqrt{\frac{q_\infty}{2\rho_{amb}}} \tag{3.94}$$

Since U_{q_∞} and $U_{\rho_{amb}}$ were calculated in Sections 3.11.1.1 and 3.11.1.2, respectively, they could be used in Eq. 3.92.

3.11.1.5 Reynolds Number

Since the Reynolds number was calculated using Eq. 3.1, its uncertainty had contributions from the freestream velocity, dynamic viscosity, density, and chord length. In this study, an average CNC machining tolerance for the model construction was assumed to be 0.005 in. The resulting uncertainty in the Reynolds number setting could then be calculated using,

$$U_{\mathrm{Re}}=\sqrt{\left(\frac{\partial \mathrm{Re}}{\partial U_\infty}U_{U_\infty}\right)^2+\left(\frac{\partial \mathrm{Re}}{\partial \rho_{amb}}U_{\rho_{amb}}\right)^2+\left(\frac{\partial \mathrm{Re}}{\partial \mu_{amb}}U_{\mu_{amb}}\right)^2+\left(\frac{\partial \mathrm{Re}}{\partial c}U_c\right)^2} \tag{3.95}$$

where

$$\frac{\partial \mathrm{Re}}{\partial U_\infty}=\frac{\rho_{amb}c}{\mu_{amb}} \tag{3.96}$$

$$\frac{\partial \mathrm{Re}}{\partial \rho_{amb}}=\frac{U_\infty c}{\mu_{amb}} \tag{3.97}$$

$$\frac{\partial \mathrm{Re}}{\partial \mu_{amb}}=-\frac{\rho_{amb}U_\infty c}{\mu_{amb}^2} \tag{3.98}$$

$$\frac{\partial \mathrm{Re}}{\partial c}=\frac{\rho_{amb}U_\infty}{\mu_{amb}} \tag{3.99}$$

3.11.2 Uncertainty in Force Balance Measurements

While measurements were acquired for the three-component floor balance discussed in Section 3.3, they were only used for diagnostic purposes and are not presented here. Furthermore, for portions of the current study the balance measurements were interfered with by pinning the model to the ceiling in order to reduce model vibrations. For these reasons, the uncertainty of the balance forces and moments were not calculated. However, since the balance turntable was used to rotate the airfoil angle of attack, it should be noted here that the uncertainty in the angle of attack position was ±0.02°.

3.11.3 Uncertainty in Time-Averaged Pressure Measurements

Since the PSI system discussed in Section 3.4.1 was used in acquiring the time-averaged pressure measurements, it was important to assess the uncertainties associated with this equipment. The uncertainties associated with the ESP modules of the PSI system are presented in Table 3.3, and were provided by the manufacturer. The ESP module uncertainties were quoted as being 0.07% of the full-scale range for the ±5.0 psid module, and 0.10% of the full-scale range for the ±1.0 psid and ±0.35 psid modules. The calibration uncertainty was estimated from the uncertainty of the PCUs that were used to calibrate the ESP modules. The uncertainties of both PCUs were within 0.02% of the full-scale calibration range. The total uncertainty of each ESP module measurement was then estimated to be the square root of the sum of the squares. Using the uncertainties of these PSI system measurements, the uncertainties of the results obtained using the PSI system could be evaluated. A set of example uncertainties calculated for the airfoil C_p and time-averaged performance coefficients at the reference condition are presented in Table 3.5.

Table 3.3 ESP module uncertainties

ESP Module	Module Uncertainty	Calibration Uncertainty	Total Uncertainty
±5.0 psid	±0.0035 psid	±0.0010 psid	±0.0036 psid
±1.0 psid	±0.0010 psid	±0.0010 psid	±0.0014 psid
±0.35 psid	±0.00035 psid	±0.0002 psid	±0.0004 psid

3.11.3.1 Pressure Coefficient

From Eq. 3.16 and Section 3.4.1.1, the time-averaged C_p results were obtained using measurements of the pressure difference ($P_s - P_{ts}$) and the calculated dynamic pressure. As a result, the uncertainty in the time-averaged C_p could be estimated using,

$$U_{C_p} = \sqrt{\left(\frac{\partial C_p}{\partial\left(P_s - P_{ts}\right)} U_{(P_s - P_{ts})}\right)^2 + \left(\frac{\partial C_p}{\partial q_\infty} U_{q_\infty}\right)^2} \tag{3.100}$$

where

$$\frac{\partial C_p}{\partial\left(P_s - P_{ts}\right)} = \frac{1}{q_\infty} \tag{3.101}$$

$$\frac{\partial C_p}{\partial q_\infty} = -\frac{P_s - P_{ts}}{q_\infty^2} \tag{3.102}$$

3.11.3.2 Lift Coefficient

Using the calculation of the lift coefficient in Eq. 3.26, the uncertainty of the resulting lift coefficient can be estimated using,

$$U_{C_l} = \sqrt{\left(\frac{\partial C_l}{\partial L'} U_{L'}\right)^2 + \left(\frac{\partial C_l}{\partial q_\infty} U_{q_\infty}\right)^2 + \left(\frac{\partial C_l}{\partial c} U_c\right)^2} \tag{3.103}$$

where

$$\frac{\partial C_l}{\partial L'} = \frac{1}{q_\infty c} \tag{3.104}$$

$$\frac{\partial C_l}{\partial q_\infty} = -\frac{L'}{q_\infty^2 c} \tag{3.105}$$

$$\frac{\partial C_l}{\partial c} = -\frac{L'}{q_\infty c^2} \tag{3.106}$$

The uncertainty in the sectional lift, $U_{L'}$, needed to be calculated before the uncertainty in the lift coefficient could be determined. In order to calculate the sectional lift uncertainty, it was first split up into its normal and axial components. By combining and expanding Eqs. 3.19 and 3.20, the expressions for the sectional normal force and sectional axial force were calculated using Eqs. 3.107 and 3.108, respectively.

$$F_{N'} = \frac{1}{2}\left[P_1(x_2 - x_1) + \sum_{i=2}^{n-1} P_i(x_{i+1} - x_{i-1}) + P_n(x_n - x_{n-1}) \right] \tag{3.107}$$

$$F_{A'} = \frac{1}{2}\left[P_1(y_2 - y_1) + \sum_{i=2}^{n-1} P_i(y_{i+1} - y_{i-1}) + P_n(y_n - y_{n-1}) \right] \tag{3.108}$$

Using the expanded forms of the sectional normal force and sectional axial force and substituting them into Eq. 3.21, a full form of the sectional lift resulted,

$$\begin{aligned} L' = & \frac{1}{2}\cos\alpha\left[P_1(x_2 - x_1) + \sum_{i=2}^{n-1} P_i(x_{i+1} - x_{i-1}) + P_n(x_n - x_{n-1}) \right] \\ & -\frac{1}{2}\sin\alpha\left[P_1(y_2 - y_1) + \sum_{i=2}^{n-1} P_i(y_{i+1} - y_{i-1}) + P_n(y_n - y_{n-1}) \right] \end{aligned} \tag{3.109}$$

Using the expression for the sectional lift in Eq. 3.109, the uncertainty in the resulting sectional lift could be estimated using,

$$U_{L'} = \sqrt{\left(\frac{\partial L'}{\partial \alpha} U_\alpha \right)^2 + \sum_{i=1}^{n} \left(\frac{\partial L'}{\partial P_i} U_{P_i} \right)^2} \tag{3.110}$$

where

$$\begin{aligned} \frac{\partial L'}{\partial \alpha} = & -\frac{1}{2}\sin\alpha\left[P_1(x_2 - x_1) + \sum_{i=2}^{n-1} P_i(x_{i+1} - x_{i-1}) + P_n(x_n - x_{n-1}) \right] \\ & -\frac{1}{2}\cos\alpha\left[P_1(y_2 - y_1) + \sum_{i=2}^{n-1} P_i(y_{i+1} - y_{i-1}) + P_n(y_n - y_{n-1}) \right] \end{aligned} \tag{3.111}$$

$$\begin{aligned} \frac{\partial L'}{\partial P_1} &= \frac{1}{2}\cos\alpha(x_2 - x_1) - \frac{1}{2}\sin\alpha(y_1 - y_2) \\ \frac{\partial L'}{\partial P_i} &= \frac{1}{2}\cos\alpha(x_{i+1} - x_{i-1}) - \frac{1}{2}\sin\alpha(y_{i-1} - y_{i+1}); \quad i = 2, n-1 \\ \frac{\partial L'}{\partial P_n} &= \frac{1}{2}\cos\alpha(x_N - x_{N-1}) - \frac{1}{2}\sin\alpha(y_{n-1} - y_n) \end{aligned} \tag{3.112}$$

It should be noted that the uncertainty of the pressure measurement, U_{P_i}, depended upon the ESP module that the pressure tap was connected to. The taps located between $x/c = 0.18$ on the airfoil upper surface and $x/c = 0.15$ on the airfoil lower surface (including the taps at these prescribed locations) were all connected to the ±5.0 psid ESP module. All of the remaining taps on the NACA 0012 airfoil model were connected to the ±1.0 psid ESP modules.

3.11.3.3 Pitching Moment Coefficient

Assessing the uncertainty of the time-averaged quarter-chord pitching moment coefficient proceeded in a similar fashion as that for the lift coefficient described in the previous section. Using the calculation of the quarter-chord pitching moment coefficient in Eq. 3.27, the uncertainty of the resulting pitching moment coefficient can be estimated using,

$$U_{C_m} = \sqrt{\left(\frac{\partial C_m}{\partial M'_{c/4}} U_{M'_{c/4}}\right)^2 + \left(\frac{\partial C_m}{\partial q_\infty} U_{q_\infty}\right)^2 + \left(\frac{\partial C_m}{\partial c} U_c\right)^2} \tag{3.113}$$

where

$$\frac{\partial C_m}{\partial M'_{c/4}} = \frac{1}{q_\infty c^2} \tag{3.114}$$

$$\frac{\partial C_m}{\partial q_\infty} = -\frac{M'_{c/4}}{q_\infty^2 c^2} \tag{3.115}$$

$$\frac{\partial C_m}{\partial c} = -\frac{2M'_{c/4}}{q_\infty c^3} \tag{3.116}$$

Using the expanded forms of the axial and normal force in Eqs. 3.107 and 3.108, along with Eqs. 3.22 and 3.23, the expanded form of the sectional quarter-chord pitching moment could be expressed as,

$$M'_{c/4} = \frac{1}{4}\begin{bmatrix} P_1\left(x_1^2 - x_2^2 - 2x_1 x_{c/4} + 2x_2 x_{c/4} + y_1^2 - y_2^2\right) \\ + \sum_{i=2}^{n-1}\left[P_i\left(x_{i-1}^2 - x_{i+1}^2 - 2x_{i-1}x_{c/4} + 2x_{i+1}x_{c/4} + y_{i-1}^2 - y_{i+1}^2\right)\right] \\ + P_n\left(x_{n-1}^2 - x_n^2 - 2x_{n-1}x_{c/4} + 2x_n x_{c/4} + y_{n-1}^2 - y_n^2\right) \end{bmatrix} \tag{3.117}$$

The resulting uncertainty of the sectional quarter-chord pitching moment could thus be calculated using,

$$U_{M'_{c/4}} = \sqrt{\sum_{i=1}^{n}\left(\frac{\partial M'_{c/4}}{\partial P_i}U_{P_i}\right)^2} \tag{3.118}$$

where

$$\begin{aligned}
\frac{\partial M'_{c/4}}{\partial P_1} &= \frac{1}{4}\left(x_1^2 - x_2^2 - 2x_1x_{c/4} + 2x_2x_{c/4} + y_1^2 - y_2^2\right) \\
\frac{\partial M'_{c/4}}{\partial P_i} &= \frac{1}{4}\left(x_{i-1}^2 - x_{i+1}^2 - 2x_{i-1}x_{c/4} + 2x_{i+1}x_{c/4} + y_{i-1}^2 - y_{i+1}^2\right); \quad i = 2, n-1 \\
\frac{\partial M'_{c/4}}{\partial P_n} &= \frac{1}{4}\left(x_{n-1}^2 - x_n^2 - 2x_{n-1}x_{c/4} + 2x_nx_{c/4} + y_{n-1}^2 - y_n^2\right)
\end{aligned} \tag{3.119}$$

3.11.3.4 Hinge Moment Coefficient

The assessment of the hinge moment coefficient uncertainty was performed using the same method as the quarter-chord pitching moment coefficient in the previous section. The only significant difference was that only the taps over the trailing-edge portion of the airfoil model that covered the region of the simulated flap were used in the uncertainty analysis calculation. Additionally, the flap chord was used in lieu of the airfoil chord, since it was the reference length used in Eq. 3.28. Using the form of Eq. 3.82, the uncertainty of the hinge moment coefficient was estimated using,

$$U_{C_h} = \sqrt{\left(\frac{\partial C_h}{\partial H'}U_{H'}\right)^2 + \left(\frac{\partial C_h}{\partial q_\infty}U_{q_\infty}\right)^2 + \left(\frac{\partial C_h}{\partial c_f}U_{c_f}\right)^2} \tag{3.120}$$

where

$$\frac{\partial C_h}{\partial H'} = \frac{1}{q_\infty c_f^2} \tag{3.121}$$

$$\frac{\partial C_h}{\partial q_\infty} = -\frac{H'}{q_\infty^2 c_f^2} \tag{3.122}$$

$$\frac{\partial C_h}{\partial c_f} = -\frac{2H'}{q_\infty c_f^3} \tag{3.123}$$

The expanded form of hinge moment per unit span was calculated in the same fashion as the quarter-chord pitching moment per unit span calculation in Eq. 3.117. Using the expression for the sectional hinge moment in Eqs 3.24 and 3.25, and expanding the sectional axial and normal force terms according to Eqs. 3.107 and 3.108, the sectional hinge moment can be expressed using,

$$H' = \frac{1}{4}\left[\begin{array}{l} P_1\left(x_1^2 - x_2^2 - 2x_1x_h + 2x_2x_h + y_1^2 - y_2^2 - 2y_1y_h + 2y_2y_h\right) \\ + \sum_{i=2}^{n_{flap}-1}\left[P_i\left(x_{i-1}^2 - x_{i+1}^2 - 2x_{i-1}x_h + 2x_{i+1}x_h + y_{i-1}^2 - y_{i+1}^2 - 2y_{i-1}y_h + 2y_{i+1}y_h\right)\right] \\ + P_{n_{flap}}\left(x_{n_{flap}-1}^2 - x_{n_{flap}}^2 - 2x_{n_{flap}-1}x_h + 2x_{n_{flap}}x_h + y_{n_{flap}-1}^2 - y_{n_{flap}}^2 - 2y_{n_{flap}-1}y_h \right. \\ \left. + 2y_{n_{flap}}y_h\right) \end{array}\right] \tag{3.124}$$

This resulted in an uncertainty in the sectional hinge moment as,

$$U_{H'} = \sqrt{\sum_{i=1}^{n_{flap}}\left(\frac{\partial H'}{\partial P_i}U_{P_i}\right)^2} \tag{3.125}$$

where

$$\begin{aligned} \frac{\partial H'}{\partial P_1} &= \frac{1}{4}\left(x_1^2 - x_2^2 - 2x_1x_h + 2x_2x_h + y_1^2 - y_2^2 - 2y_1y_h + 2y_2y_h\right) \\ \frac{\partial H'}{\partial P_i} &= \frac{1}{4}\left(x_{i-1}^2 - x_{i+1}^2 - 2x_{i-1}x_h + 2x_{i+1}x_h + y_{i-1}^2 - y_{i+1}^2 - 2y_{i-1}y_h + 2y_{i+1}y_h\right); \quad i = 2, n-1 \\ \frac{\partial H'}{\partial P_{n_{flap}}} &= \frac{1}{4}\left(x_{n_{flap}-1}^2 - x_{n_{flap}}^2 - 2x_{n_{flap}-1}x_h + 2x_{n_{flap}}x_h + y_{n_{flap}-1}^2 - y_{n_{flap}}^2 - 2y_{n_{flap}-1}y_h + 2y_{n_{flap}}y_h\right) \end{aligned} \tag{3.126}$$

3.11.3.5 Drag Coefficient

The drag coefficient of the airfoil was calculated using Eqs. 3.40–3.42. By combining these equations, the expanded form of the drag coefficient expression of Eq. 3.42 becomes,

$$\begin{aligned} C_d = \frac{1}{q_\infty c} \sum_{i=1}^{n_{rake}-1} \Bigg(& \sqrt{q_\infty^2 - q_\infty \left(P_{0,\infty} - P_{0,w_i}\right)} + \sqrt{q_\infty^2 - q_\infty \left(P_{0,\infty} - P_{0,w_{i+1}}\right)} \\ & - 2q_\infty + 2P_{0,\infty} - P_{0,w_i} - P_{0,w_{i+1}} \Bigg)\left(y_i - y_{i+1}\right) \end{aligned} \tag{3.127}$$

Since both $P_{0,\infty}$ and $P_{0,w}$ were reference to atmospheric pressure, the atmospheric pressure terms would all cancel when the acquired wake rake pressures are inserted into Eq. 3.127. As a result, the only contributors to the drag coefficient uncertainty stem from the dynamic pressure, airfoil chord, and the measurement of the wake pressures inside the airfoil wake and the freestream total pressure measured outside the wake. Thus, the uncertainty in the drag coefficient can be expressed using,

$$U_{C_d} = \sqrt{\left(\frac{\partial C_d}{\partial q_\infty} U_{q_\infty}\right)^2 + \left(\frac{\partial C_d}{\partial c} U_c\right)^2 + \left(\frac{\partial C_d}{\partial P_{0,\infty}} U_{P_{0,\infty}}\right)^2 + \sum_{i=1}^{n_{rake}-1} \left(\frac{\partial C_d}{\partial P_{0,w}} U_{P_{0,w}}\right)^2} \tag{3.128}$$

where

$$\begin{aligned} \frac{\partial C_d}{\partial q_\infty} = -\frac{1}{q_\infty^2 c} \sum_{i=1}^{n_{rake}-1} \Bigg(& \sqrt{q_\infty^2 - q_\infty \left(P_{0,\infty} - P_{0,w_i}\right)} + \sqrt{q_\infty^2 - q_\infty \left(P_{0,\infty} - P_{0,w_{i+1}}\right)} \\ & - 2q_\infty + 2P_{0,\infty} - P_{0,w_i} - P_{0,w_{i+1}} \Bigg)\left(y_i - y_{i+1}\right) + \frac{1}{q_\infty c} \sum_{i=1}^{n_{rake}-1} \Bigg[\frac{2q_\infty - \left(P_{0,\infty} - P_{0,w_i}\right)}{2\sqrt{q_\infty^2 - q_\infty \left(P_{0,\infty} - P_{0,w_i}\right)}} \\ & + \frac{2q_\infty - \left(P_{0,\infty} - P_{0,w_{i+1}}\right)}{2\sqrt{q_\infty^2 - q_\infty \left(P_{0,\infty} - P_{0,w_{i+1}}\right)}} - 2 \Bigg]\left(y_i - y_{i+1}\right) \end{aligned} \tag{3.129}$$

$$\begin{aligned} \frac{\partial C_d}{\partial c} = -\frac{1}{q_\infty c^2} \sum_{i=1}^{n_{rake}-1} \Bigg(& \sqrt{q_\infty^2 - q_\infty \left(P_{0,\infty} - P_{0,w_i}\right)} + \sqrt{q_\infty^2 - q_\infty \left(P_{0,\infty} - P_{0,w_{i+1}}\right)} \\ & - 2q_\infty + 2P_{0,\infty} - P_{0,w_i} - P_{0,w_{i+1}} \Bigg)\left(y_i - y_{i+1}\right) \end{aligned} \tag{3.130}$$

$$\begin{aligned} \frac{\partial C_d}{\partial P_{0,\infty}} = \frac{1}{q_\infty c} \sum_{i=1}^{n_{rake}-1} \Bigg(& 2 - \frac{q_\infty}{2\sqrt{q_\infty^2 - q_\infty \left(P_{0,\infty} - P_{0,w_i}\right)}} \\ & - \frac{q_\infty}{2\sqrt{q_\infty^2 - q_\infty \left(P_{0,\infty} - P_{0,w_{i+1}}\right)}} \Bigg)\left(y_i - y_{i+1}\right) \end{aligned} \tag{3.131}$$

$$\frac{\partial C_d}{\partial P_{0,w_i}} = \frac{1}{q_\infty c}\left(\frac{q_\infty}{2\sqrt{q_\infty^2 - q_\infty\left(P_{0,\infty} - P_{0,w_i}\right)}} - 1\right)\left(y_i - y_{i+1}\right) \tag{3.132}$$

3.11.3.6 Shear-Layer Reattachment Location

The uncertainties of the time-averaged shear-layer reattachment location were determined from the surface oil flow visualization results. The uncertainty was assumed to come from two sources, being the reference chord tape placement accuracy and the visual identification of the mean reattachment location. The reference chord tape uncertainty was estimated to be ±0.01 *x*/*c*. Since the location of mean shear-layer reattachment was identified in the flow visualization results by estimating the location where the streamwise direction of the flow changes from an upstream flow in the recirculation region to a downstream flow aft of the separation bubble. These uncertainties were typically higher due to the difficulty in identifying this location, resulting in uncertainties on the order of ±0.03 *x*/*c*. For high angles of attack where the reattachment zone was large, the uncertainties of identifying the reattachment location from the flow visualization results were estimated to be higher, on the order of ±0.05 *x*/*c*.

3.11.4 Uncertainty in Time-Dependent Pressure Measurements

The uncertainties in the time-dependent measurements that were acquired in this study are evaluated in this section. The unsteady pressure measurements that were acquired in this study included the unsteady airfoil surface static pressures, which were also used to calculate the unsteady airfoil performance coefficients. The resulting uncertainties of the time-dependent airfoil C_p and airfoil performance coefficients at the reference condition are presented in Table 3.6.

3.11.4.1 Unsteady Pressure Measurements

The uncertainty in the unsteady pressure coefficients was evaluated in the same way as the time-averaged pressure coefficients in Section 3.11.3.1. However, since Kulite XCS-062 transducers were used to acquire the unsteady pressure difference between the static airfoil surface pressure and the freestream pressure, the uncertainty of these surface-integrated pressure transducers are used instead of the ESP scanners. Using Eq. 3.45, the uncertainty in the unsteady C_p can be calculated using,

$$U_{C_p} = \sqrt{\left(\frac{\partial C_p}{\partial \left(P_{s,i} - P_{ts} \right)} U_{\left(P_{s,i} - P_{ts} \right)} \right)^2 + \left(\frac{\partial C_p}{\partial q_\infty} U_{q_\infty} \right)^2} \tag{3.133}$$

where

$$\frac{\partial C_p}{\partial \left(P_{s,i} - P_{ts} \right)} = \frac{1}{q_\infty} \tag{3.134}$$

$$\frac{\partial C_p}{\partial q_\infty} = -\frac{P_{s,i} - P_{ts}}{q_\infty^2} \tag{3.135}$$

The uncertainty of the pressure measurement was quoted by the manufacturer to be within ±0.1% of the full-scale ±5 psid range. This resulted in a value of $U_{(P_{s,i} - P_{ts})}$ = ±0.005 psid. The uncertainty of the dynamic pressure was assessed in Section 3.11.1.1.

3.11.4.2 Unsteady Airfoil Performance

The uncertainty of the unsteady airfoil performance coefficients (including C_l, C_m, and C_h) were evaluated using the same method as the time-averaged counterparts, which is described in Section 3.11.3. Due to the extensive length of this derivation, it is not repeated here.

3.11.5 Uncertainty in Hot-Film Measurements

The uncertainty in the various hot-film measurements and quantities derived from these acquired measurements are addressed in this section. This includes the uncertainty in the acquired wake hot-film measurements, the surface-mounted hot-film array measured voltages, and the reduced unsteady reattachment location. A summary of some example uncertainties of these quantities is presented in Table 3.7.

3.11.5.1 Wake Hot-Film Measurements

The uncertainty in the wake hot-film measurements will be described first in this section. While there are many potential sources of uncertainty when acquiring hot-wire measurements, it will be assumed that the only significant factor is due to the hot-wire calibration. Other sources of uncertainty due to factors such as model interference, probe vibration, probe angle effects, and heat conduction effects were assumed to be negligible. These types of effects are described in detail by Whalen,[104] where flow angle effects were the most significant cause of uncertainty. However, in the current study the wake hot-wire measurements were obtained in a region of relatively low flow angularity and for this reason the uncertainty cause by flow angle effects were regarded as being insignificant.

In order to assess the uncertainty of the calibration of the wake hot-film probe, the uncertainty of the freestream velocity during calibration is imposed as a constant bias error throughout the calibration. Since a pitot-static probe was used in conjunction with a ±0.35 psid ESP module in order to determine the dynamic pressure during calibration, the relation in Eq. 3.92 can be used to determine the bias error of the calibration. However, the uncertainty of q_∞ will be due to the measured pressure difference of $P_0 - P_{ts}$. During calibration, the freestream velocity was determined using the definition of dynamic pressure given in Eq. 3.91. The uncertainty of the calibration velocity progressed in a similar fashion as in Section 3.11.1.4, except the dynamic pressure was measured using a ±0.35 psid ESP module, resulting in U_{q_∞} = ±0.0004 psid. The other component of the calibration was related to the fit of the calibration. This uncertainty was assessed by identifying the 95% confidence interval of the velocity using the normalized standard deviation between the measured velocity at calibration and the indicated velocity from the calibration voltages and the calibration coefficients. However, upon analyzing this contribution to the uncertainty in the hot-film velocity, it was identified that the component due to the fit of the calibration was negligible.

3.11.5.2 Surface-Mounted Hot-Film Array

Assessing the uncertainty of the surface-mounted hot-film array measurements was more difficult. Since the hot-film array was tested in an uncalibrated configuration, the uncertainty of the measurement only depended on the uncertainty of the acquired voltage. In the current study, it was assumed that the anemometer bridge voltage that was measured was only dependent on uncertainty induced by changes in the freestream temperature. In most thermal anemometry applications, it is reasonable to assume that,

$$\frac{E^2}{T_s - T_\infty} = const \tag{3.136}$$

where T_s is the sensor (hot-film element) temperature. Indeed, this assumption is the reason for the temperature correction presented in Eq. 3.64, as described by Tropea et al.[95] and Lemonis and Dracos.[105] By referencing between the conditions at which measurements were acquired and the conditions at which the CTA tuning was completed, the uncertainty of the hot-film array measurements were estimated. By holding Eq. 3.136 constant between these two conditions, the measured voltage can be expressed using,

$$E = E_{cal}\sqrt{\frac{T_s - T_\infty}{T_s - T_{\infty,cal}}} \tag{3.137}$$

The relation presented in Eq. 3.137 is similar to that in Eq. 3.64, except instead of correcting the acquired voltage to use the calibration conditions, the tuning conditions are being related to the data acquisition conditions. By changing the freestream temperature from the tuning conditions, a bias error in the measurement would be introduced. It is presumed that this would be the greatest contribution to the uncertainty of the hot-film array voltage measurements.

Using Eq. 3.137, the uncertainty of the voltage measurement of the hot-film array was assessed. It was assumed that the uncertainty associated with the digitization of the analog voltages under the hot-film array tuning conditions was negligible. Additionally, it was assumed that the sensor temperature remained constant with negligible deviation, since all sensors were regulated using constant temperature anemometers. As a result, the uncertainty in the acquired hot-film array voltage measurements would be due to the ambient temperature measurements under tuning and data acquisition conditions. Thus, the uncertainty of the acquired voltage can be expressed as,

$$U_E = \sqrt{\left(\frac{\partial E}{\partial T_\infty}U_{T_\infty}\right)^2 + \left(\frac{\partial E}{\partial T_{\infty,cal}}U_{T_{\infty,cal}}\right)^2} \tag{3.138}$$

where

$$\frac{\partial E}{\partial T_\infty} = \frac{E}{2(T_\infty - T_s)}\sqrt{\frac{T_s - T_\infty}{T_s - T_{\infty,cal}}} \tag{3.139}$$

$$\frac{\partial E}{\partial T_{\infty,cal}} = \frac{E}{2(T_s - T_{\infty,cal})}\sqrt{\frac{T_\infty - T_s}{T_{\infty,cal} - T_s}} \tag{3.140}$$

As noted in Section 3.11.1.2, the uncertainty of the ambient temperature measurement was 1.8 °R. This value represented the uncertainty in the freestream temperature under both tuning and data acquisition conditions. However, the sensor temperature during operation was unknown and needed to be calculated. This calculation was performed by introducing an alternative version of Eq. 3.49 for the overheat ratio, which can also be written as,

$$a = \alpha\left(T_s - T_{ref}\right) \tag{3.141}$$

where α is the temperature coefficient of resistance of the sensor and T_{ref} is the reference temperature. Since the overheat ratios were set as the anemometer circuits were being tuned, the reference temperature was prescribed as 69.6 °F, which was the ambient temperature of the anemometer tuning conditions. Since the temperature coefficient of nickel is known to be 0.00587/°C (0.00326/°F), and using the average overheat ratio of 1.21, the sensor temperature must be 371.2 °F higher than the ambient conditions. This sets the average sensor temperature at $T_s = 440.8$ °F.

3.11.5.3 Unsteady Shear-Layer Reattachment Location

Since the method for determining the unsteady shear-layer reattachment location using hot-film arrays was introduced in the current investigation, there is not a conventional method for evaluating the uncertainty. Monte Carlo simulations could possibly be used to evaluate the uncertainty of the processing method in the current study, which is similar to what is often done for evaluating the processing uncertainty of PIV results. However, this was not attempted in the current study. Instead, a simpler method will be attempted to provide an estimate of what the error in the unsteady reattachment location could be. The uncertainty in the shear-layer reattachment location determined from the data acquired using the hot-film array was assumed to have two major contributions. The first is due to the uncertainty of correctly identifying the location corresponding to minimum correlation near zero time lag in the signal processing routine. This could be caused by the propagation of the uncertainty in the hot-film array voltages, which was described in the previous section, or due to the influence of noise in the correlation coefficient estimation. It was assumed that the errors in the unsteady shear-layer reattachment location due to the uncertainty in the voltage measurements were small in comparison to those associated with the correlation processing method. The second source of uncertainty is the precision error associated with the shear-layer reattachment location when a moving average is taken.

The effects of the correlation processing method were assessed first. The significance of this contribution to the uncertainty was analyzed by assuming that the minimum correlation value and the average cross-correlation coefficient of all of the other adjacent sensor pairs formed two independent data sets that follow a bivariate normal distribution. The resulting average and standard deviation of the minimum correlation coefficient across the processed hot-film array time history was -0.579 and 0.098, respectively. The average and standard deviation of the average in the other correlation coefficients of adjacent sensor pairs at the same time lag were 0.150 and 0.200, respectively. The cross-correlation coefficient between these two sets of data was 0.141. The probability that the minimum correlation coefficient was less than the average in the other correlation coefficients was then calculated using,

$$z = \frac{E(Y-X)}{\sqrt{Var(Y-X)}} \tag{3.142}$$

where z follows a normal distribution and

$$E(Y-X) = \mu_Y - \mu_X \tag{3.143}$$

$$Var(Y-X) \approx \sigma_Y^2 - 2\sigma_Y \sigma_X \rho_{XY} + \sigma_X^2 \tag{3.144}$$

In Eqs. 3.142–3.144, the variable X represents the minimum correlation value data set and the variable Y represents the data set of the average in the remaining cross-correlation coefficients of adjacent sensor pairs at the same time lag. Based on the value of z calculated in Eq. 3.142, the minimum value of the cross-correlation coefficient between adjacent sensors was identified as being less than the other cross-correlation coefficients with 99.97% probability. As a result, the contributions of the processing method towards the uncertainty in the unsteady shear-layer reattachment location were deemed to be negligible.

The uncertainty in the precision error will be accounted for by calculating the bounds of a 95% confidence interval of the moving average used to determine the low-frequency component of the unsteady reattachment location. The standard deviation of the unsteady reattachment location prior to any averaging was 0.0517, in *x*/*c*. When a 60-point moving average was used, the resulting uncertainty in the unsteady shear-layer reattachment location was ±0.0134 in *x*/*c*.

3.11.6 Uncertainty in Strouhal Number

The uncertainty of the two representations of Strouhal numbers in Eqs. 3.71 and 3.72 were identified using the form of Eq. 3.82. The resulting expressions for the two Strouhal number calculations were,

$$U_{St_L} = \sqrt{\left(\frac{\partial St_L}{\partial U_\infty} U_{U_\infty}\right)^2 + \left(\frac{\partial St_L}{\partial f} U_f\right)^2 + \left(\frac{\partial St_L}{\partial L_R} U_{L_R}\right)^2} \tag{3.145}$$

$$U_{St_h} = \sqrt{\left(\frac{\partial St_h}{\partial U_\infty} U_{U_\infty}\right)^2 + \left(\frac{\partial St_h}{\partial f} U_f\right)^2 + \left(\frac{\partial St_h}{\partial c} U_c\right)^2 + \left(\frac{\partial St_h}{\partial \alpha} U_\alpha\right)^2} \tag{3.146}$$

where

$$\frac{\partial St_L}{\partial U_\infty} = -\frac{f L_R}{U_\infty^2} \tag{3.147}$$

$$\frac{\partial St_L}{\partial f} = \frac{L_R}{U_\infty} \tag{3.148}$$

$$\frac{\partial St_L}{\partial L_R} = \frac{f}{U_\infty} \tag{3.149}$$

and

$$\frac{\partial St_h}{\partial U_\infty} = -\frac{f c \sin\alpha}{U_\infty^2} \tag{3.150}$$

$$\frac{\partial St_h}{\partial f} = \frac{c \sin\alpha}{U_\infty} \tag{3.151}$$

$$\frac{\partial St_h}{\partial c} = \frac{f \sin\alpha}{U_\infty} \tag{3.152}$$

$$\frac{\partial St_h}{\partial \alpha} = \frac{f c \cos\alpha}{U_\infty} \tag{3.153}$$

The uncertainty associated with the frequency was assumed to be equivalent to the frequency resolution of the PSDs in which the corresponding unsteady mode was identified. The resulting uncertainties in the Strouhal numbers of the three unsteady modes at the reference conditions are presented in Table 3.8.

3.11.7 Example of Uncertainties

Example uncertainties were calculated for the quantities discussed in Sections 3.11.1–3.11.6. With the exception of the uncertainty in the unsteady shear-layer reattachment location, the uncertainties were calculated for all quantities during the same run for the airfoil with the leading-edge horn-ice shape at Re = 1.8×10^6 and $\alpha = 6°$. This angle of attack was just under the airfoil stall angle of attack and was primarily selected for the uncertainty analysis as all three modes of unsteadiness were clearly visible in the PSDs of the data acquired at this angle of attack. The unsteady shear-layer reattachment location was analyzed at Re = 1.8×10^6 and $\alpha = 5°$, as this was the angle of attack where the hot-film array data were acquired.

Table 3.4 Example uncertainties for test conditions of NACA 0012 airfoil model with leading-edge horn-ice shape at Re = 1.8×10^6 and $\alpha = 6°$

Parameter	Reference Value	Absolute Uncertainty	Relative Uncertainty (%)
c	18 in	±0.005 in	±0.0277
α	5.988°	±0.02°	±0.3340
$q_{\infty,Setra}$	0.3147 psi	±0.000771 psi	±0.2450
$q_{\infty,PSI}$	0.2988 psi	±0.001425 psi	±0.4769
P_{amb}	14.54 psi	±0.008 psi	±0.0550
T_{amb}	530.5 °R	±1.8 °R	±0.3393
ρ_{amb}	2.301×10^{-3} slugs/ft^3	$\pm 1.047 \times 10^{-5}$ slugs/ft^3	±0.4552
μ_{amb}	3.803×10^{-7} lb-s/ft^2	$\pm 9.984 \times 10^{-10}$ lb-s/ft^2	±0.2625
U_∞	198.5 ft/sec	±0.2460 ft/sec	±0.1240
Re	1800757	±9735	±0.5406

Table 3.5 Example uncertainties for airfoil time-averaged pressure and performance coefficients of NACA 0012 airfoil model with leading-edge horn-ice shape at Re = 1.8 × 10^6 and $\alpha = 6°$

Parameter	Reference Value	Absolute Uncertainty	Relative Uncertainty (%)
C_p 5 psi ($x/c = 0.10$)	-1.318	±0.01359	±1.031
C_p 1 psi ($x/c = 0.40$)	-0.9307	±0.006454	±0.6935
C_l	0.6020	±0.003311	±0.5500
C_m	-0.01991	±0.0005655	±2.840
C_h	-0.04011	±0.001457	±3.633
C_d	0.1245	±0.0008664	±0.6960
x_r	0.76 x/c	±0.051 x/c	±6.711

Table 3.6 Example uncertainties for airfoil unsteady pressure and performance coefficients of NACA 0012 airfoil model with leading-edge horn-ice shape at Re = 1.8 × 10^6 and $\alpha = 6°$

Parameter	Reference Value	Absolute Uncertainty	Relative Uncertainty (%)
$C_{p,i}$ ($x/c = 0.245$)	-1.294	±0.01784	±1.379
$C_{l,i}$	0.4926	±0.003091	±0.6276
$C_{m,i}$	-0.03845	±0.002797	±7.276
$C_{h,i}$	-0.04287	±0.002883	±6.725

Table 3.7 Example uncertainties for unsteady shear-layer reattachment location on NACA 0012 airfoil model with leading-edge horn-ice shape at Re = 1.8 × 10^6 and $\alpha = 5°$, along with example uncertainty of hot-film velocity calibration and surface-mounted hot-film array voltage

Parameter	Reference Value	Absolute Uncertainty	Relative Uncertainty (%)
$U_{\infty,Hot\ Film}$	108.0 ft/sec	±0.3417 ft/sec	±0.3164
E_{HFA}	1.539 V	±0.005280 V	±0.3429
$x_{r,i}$	0.4667 x/c	±0.01335 x/c	±2.862

Table 3.8 Example uncertainties for Strouhal numbers of unsteady modes present in the flowfield about an NACA 0012 airfoil with leading-edge horn-ice shape at Re = 1.8 × 10^6 and $\alpha = 6°$

Parameter	Reference Value	Absolute Uncertainty	Relative Uncertainty (%)
$\mathrm{St}_{L,Regular}$	0.6	±0.02472	±4.119
$\mathrm{St}_{h,Flapping}$	0.0185	±0.0002457	±1.328
$\mathrm{St}_{h,Low\text{-}Freq}$	0.006454	±0.0002376	±3.682

3.12 Chapter 3 Figures

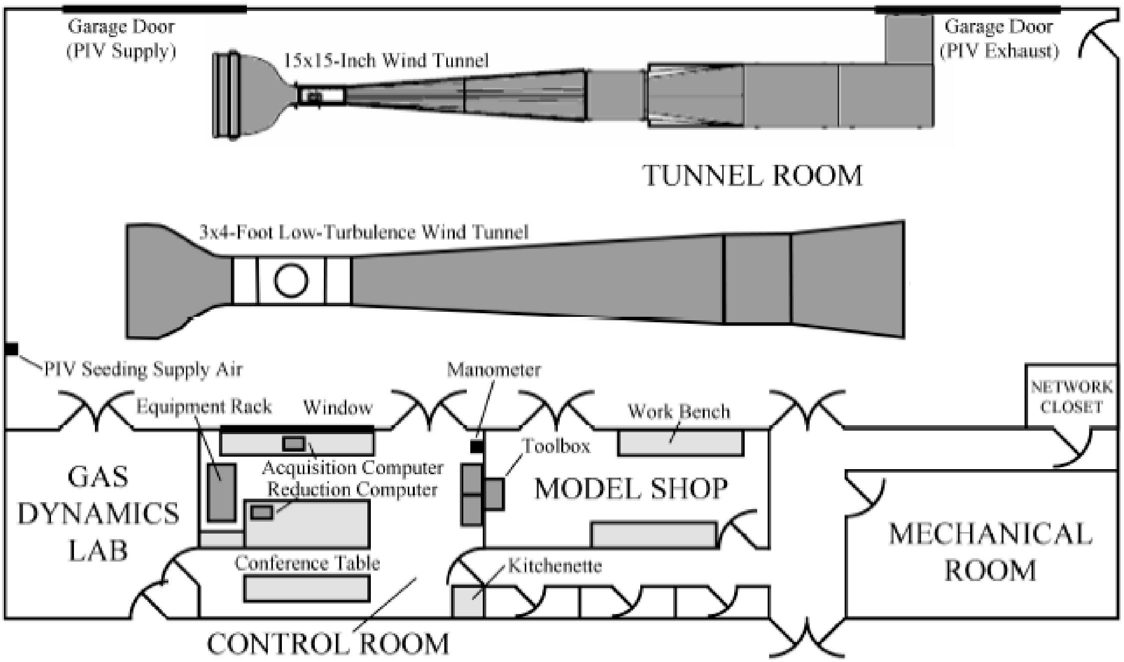

Fig. 3.1 University of Illinois Aerodynamics Research Laboratory (not to scale), after Jacobs.[23]

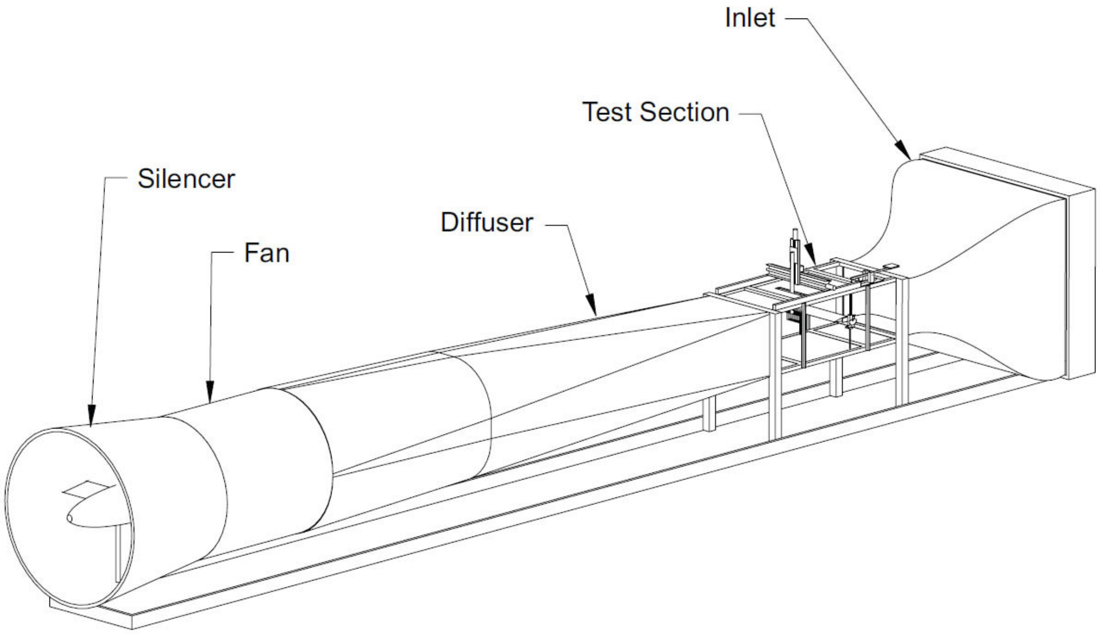

Fig. 3.2 University of Illinois low-speed, low-turbulence subsonic wind tunnel.

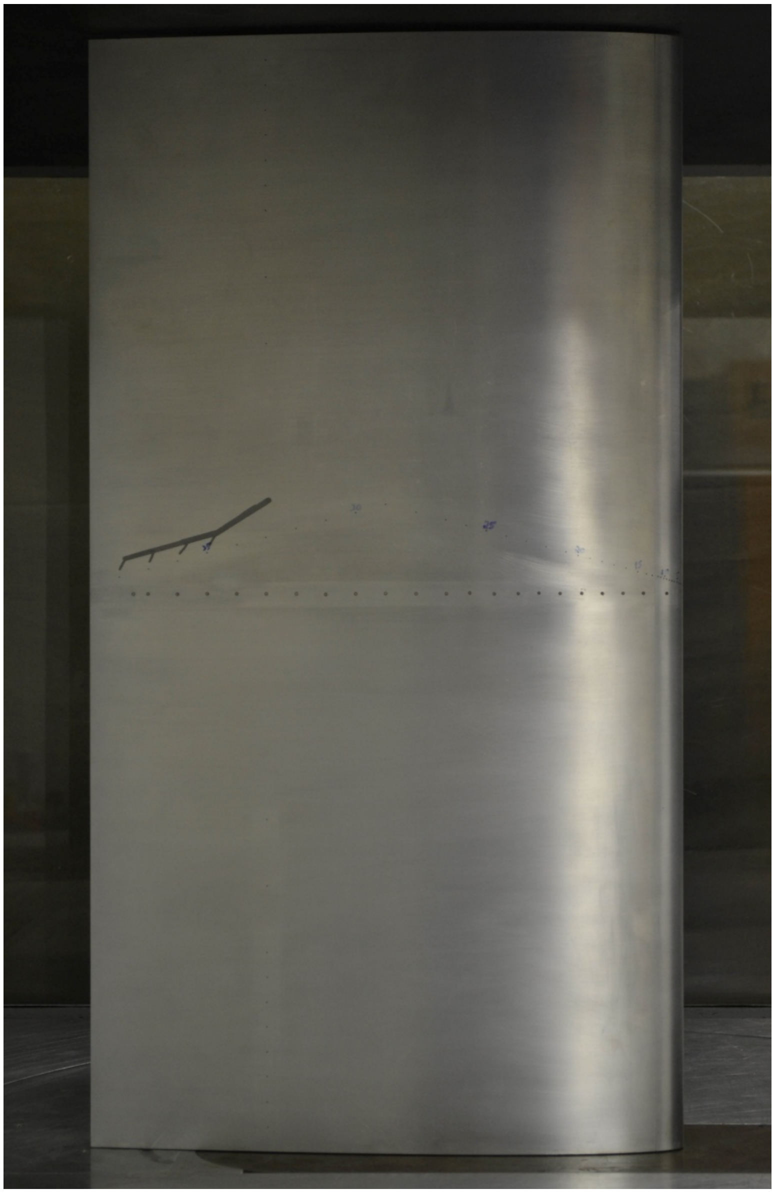

Fig. 3.3 Clean NACA 0012 airfoil model installed in the wind tunnel test section.

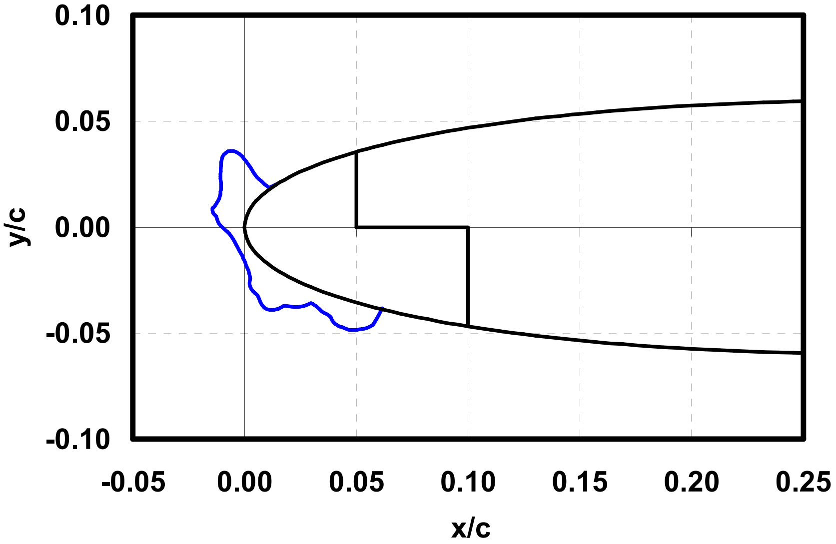

Fig. 3.4 NACA 0012 with horn-ice shape, after Gurbacki.[6]

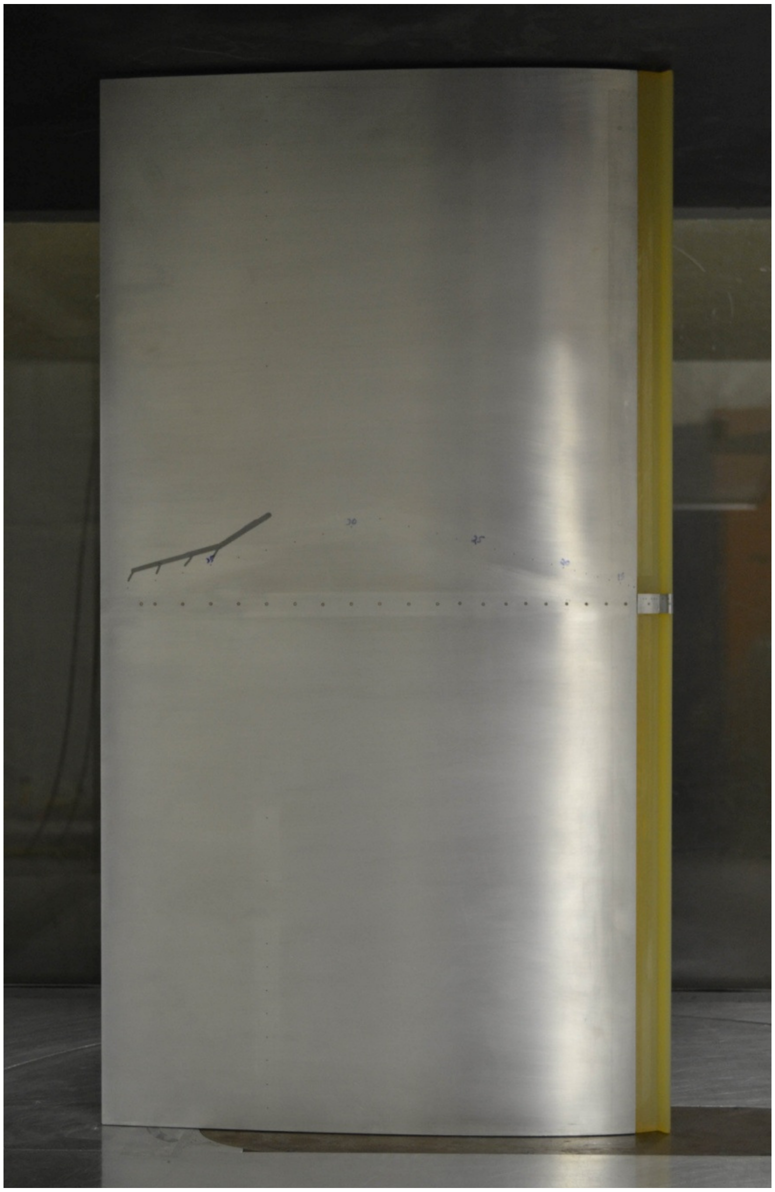

Fig. 3.5 Iced NACA 0012 airfoil model installed in the wind tunnel test section.

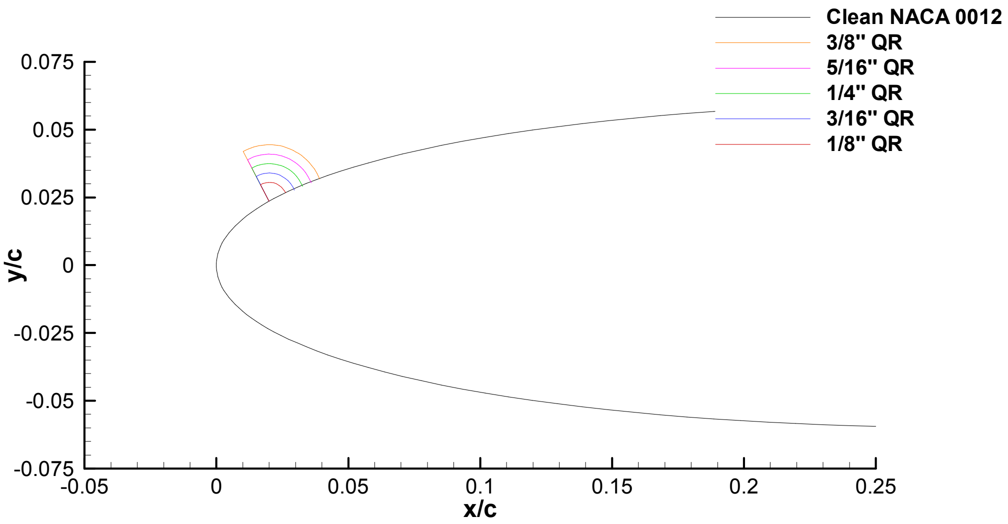

Fig. 3.6 Schematic of quarter-round simulated ice shape on NACA 0012 airfoil.

Fig. 3.7 SCXI-1001 chassis and associated SCXI modules.

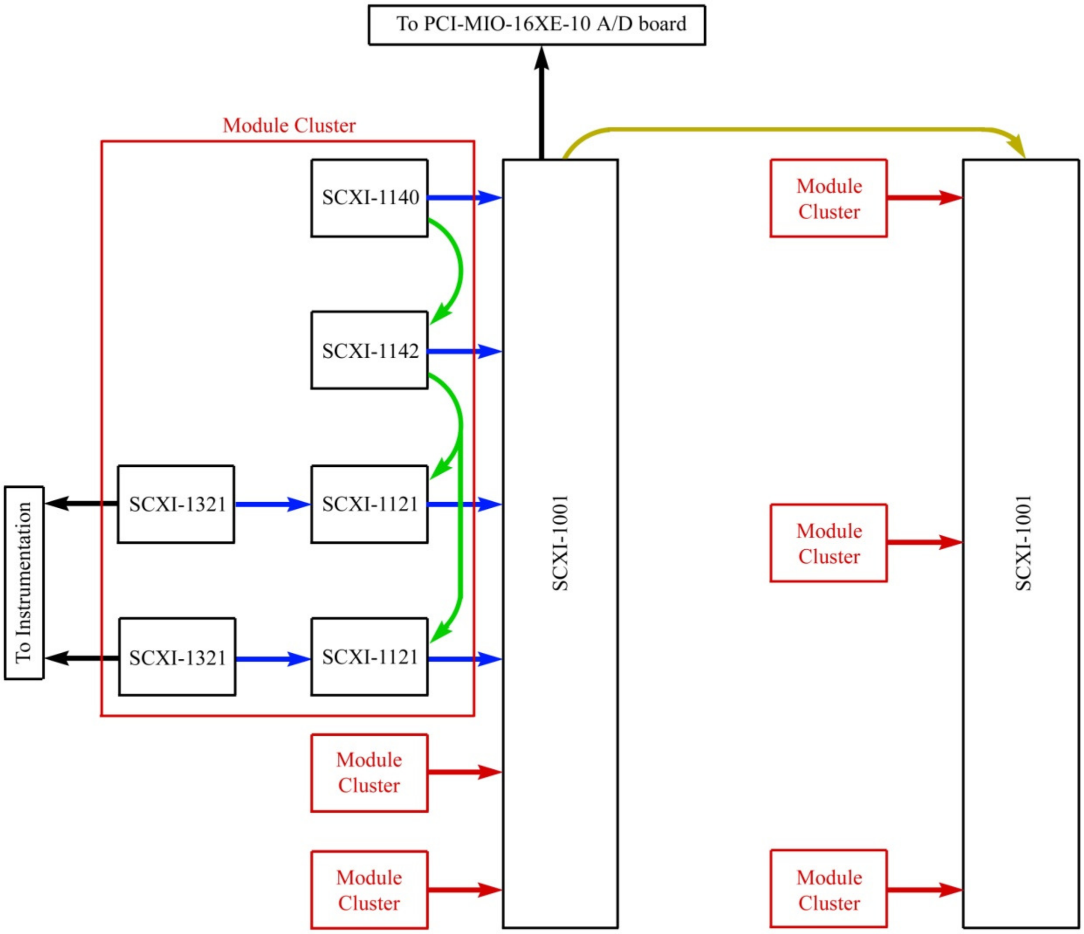

Fig. 3.8 Schematic of SCXI module and chassis connection.

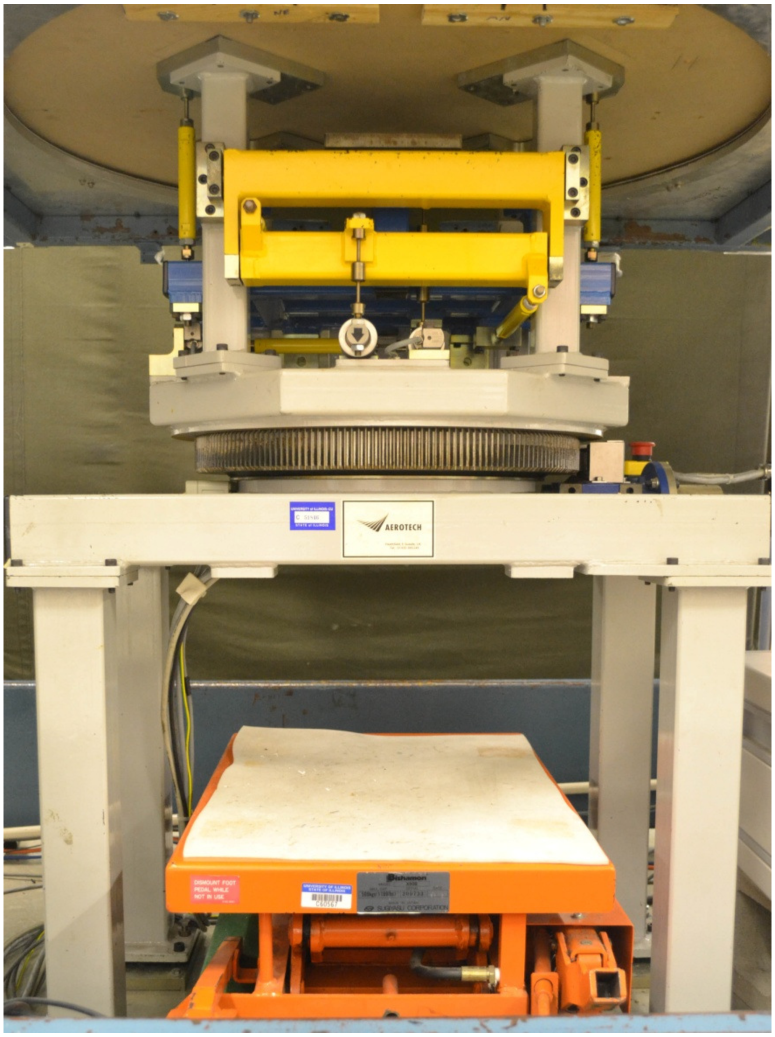

Fig. 3.9 Three-component floor balance.

Fig. 3.10 Wake rake installed in test section downstream of NACA 0012 airfoil model.

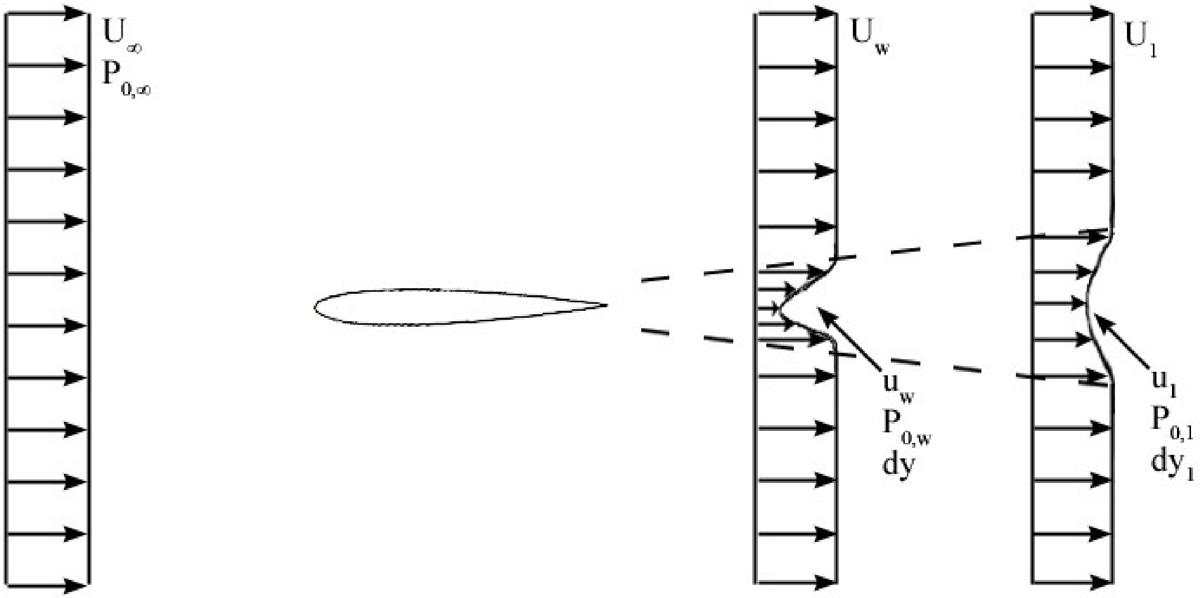

Fig. 3.11 Schematic of airfoil wake used for profile drag reduction with wake pressure measurements.

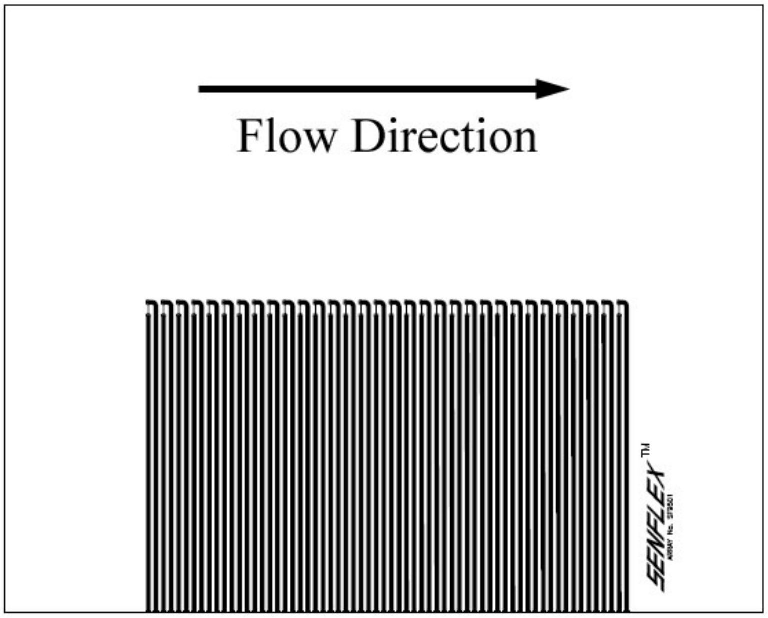

Fig. 3.12 Diagram of hot-film array used on NACA 0012 airfoil model, after Ref. 88.

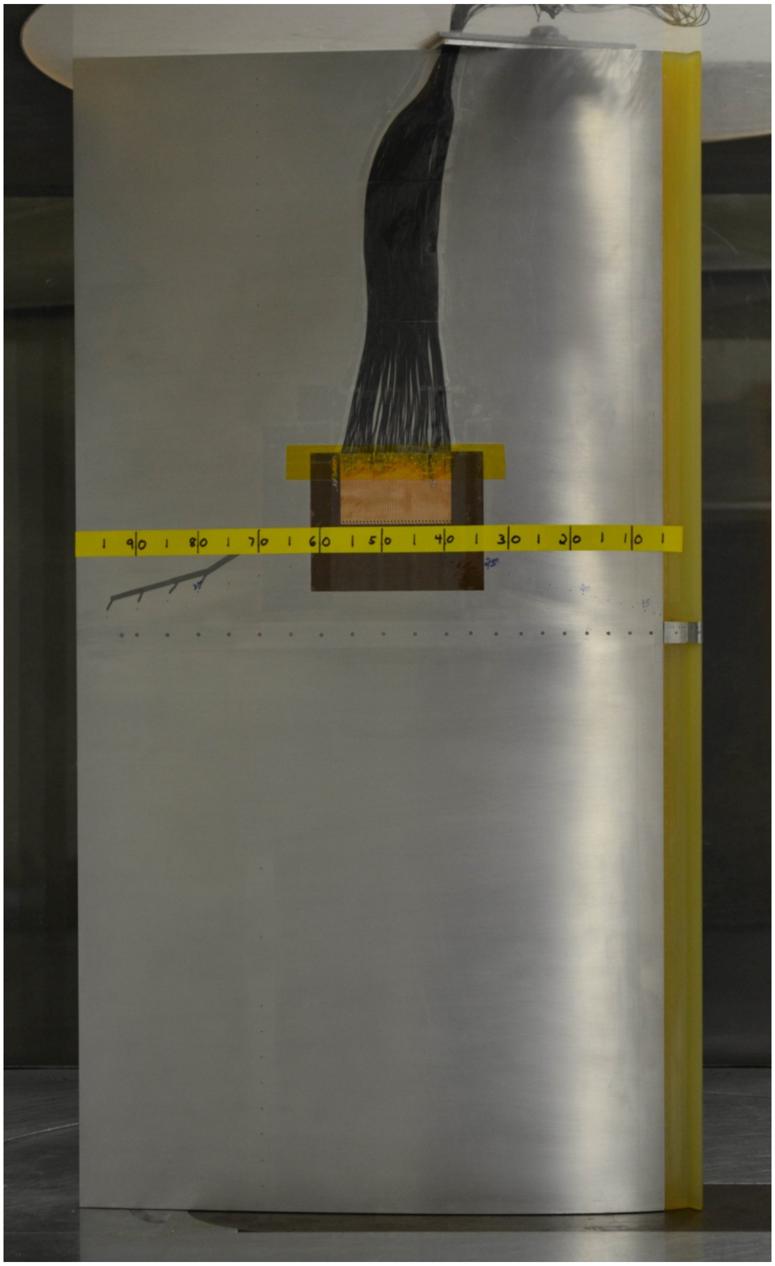

Fig. 3.13 Iced NACA 0012 airfoil model with hot-film array installed on upper surface.

Fig. 3.14 Constant temperature anemometer banks used for regulating hot-film array.

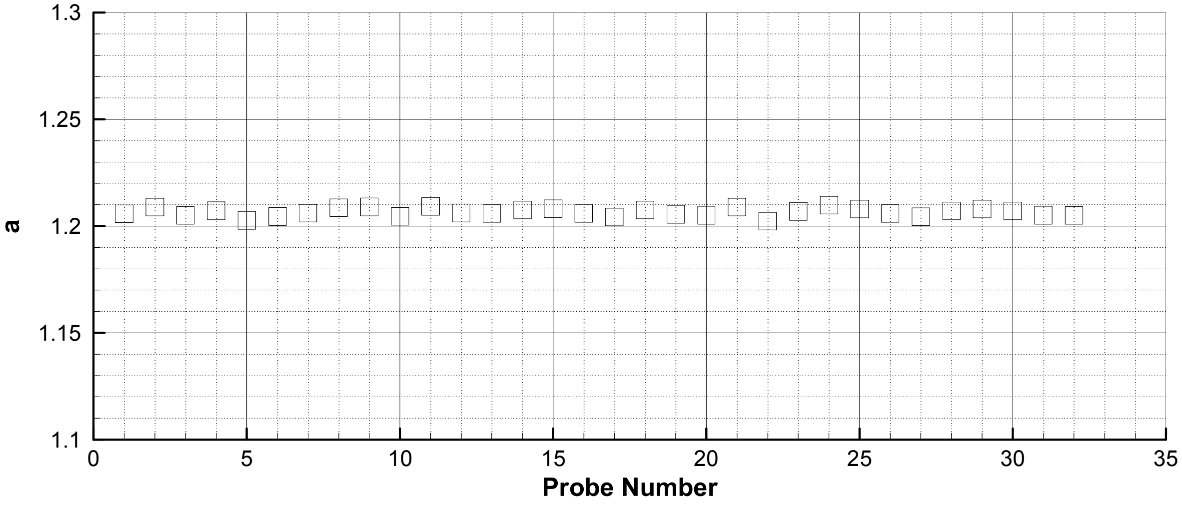

Fig. 3.15 Overheat ratio (*a*) of each probe element on hot-film array after completing configuration procedures.

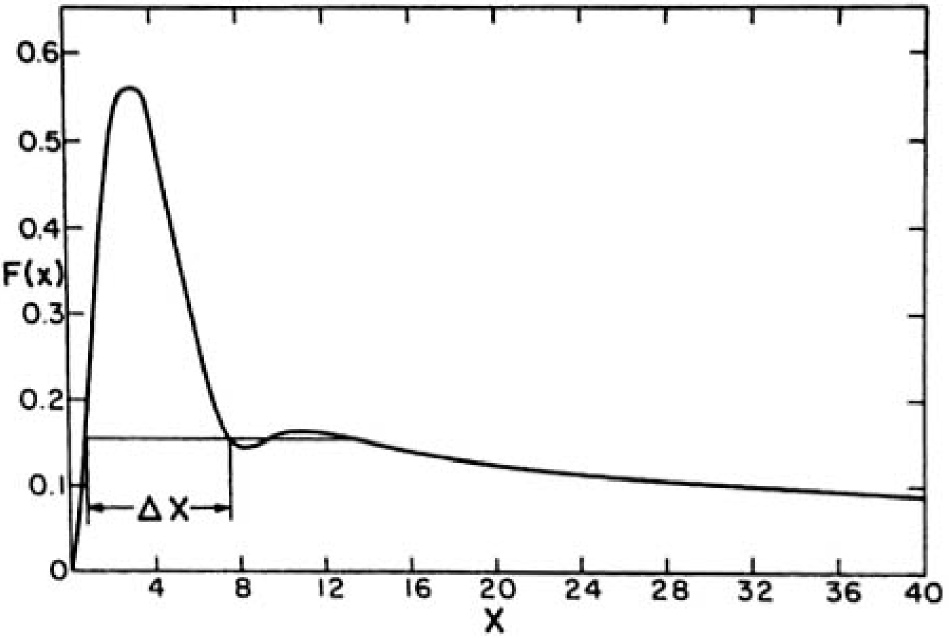

Fig. 3.16 Ideal response of a hot-film anemometer to a square wave input, after Fingerson and Freymuth.[89]

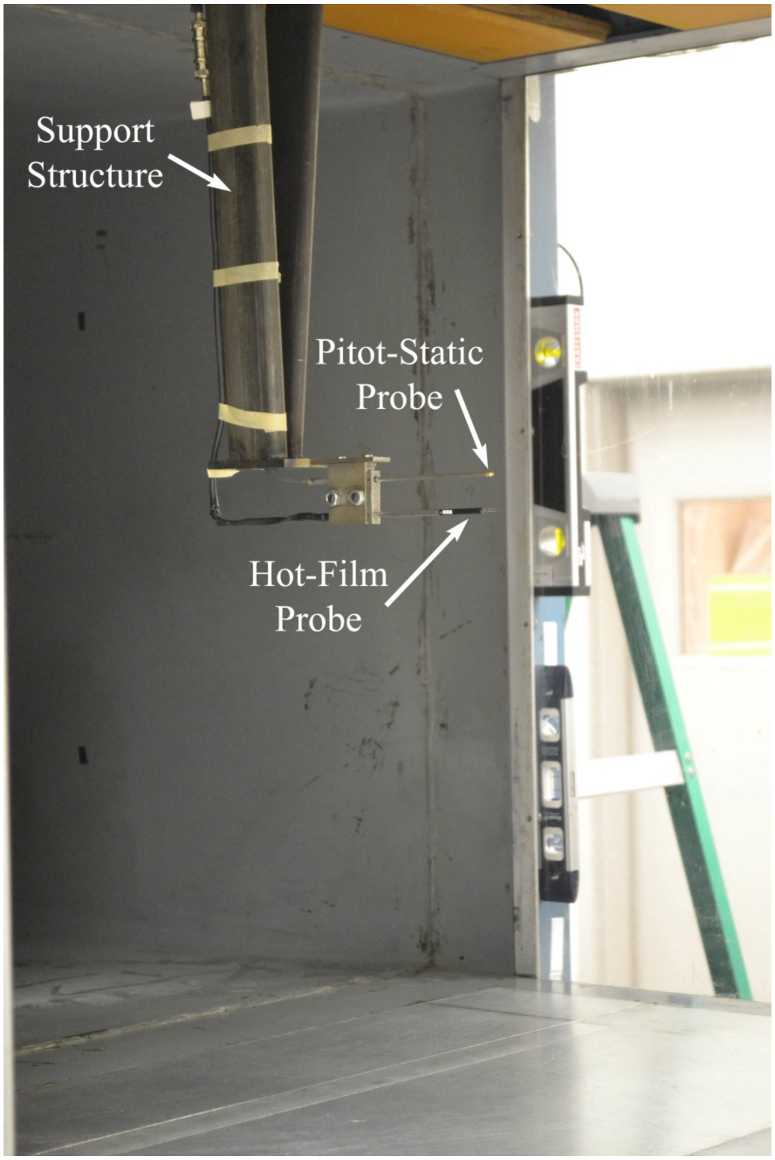

Fig. 3.17 Wake hot-film measurement assembly installed in wind tunnel, downstream of NACA 0012 airfoil model.

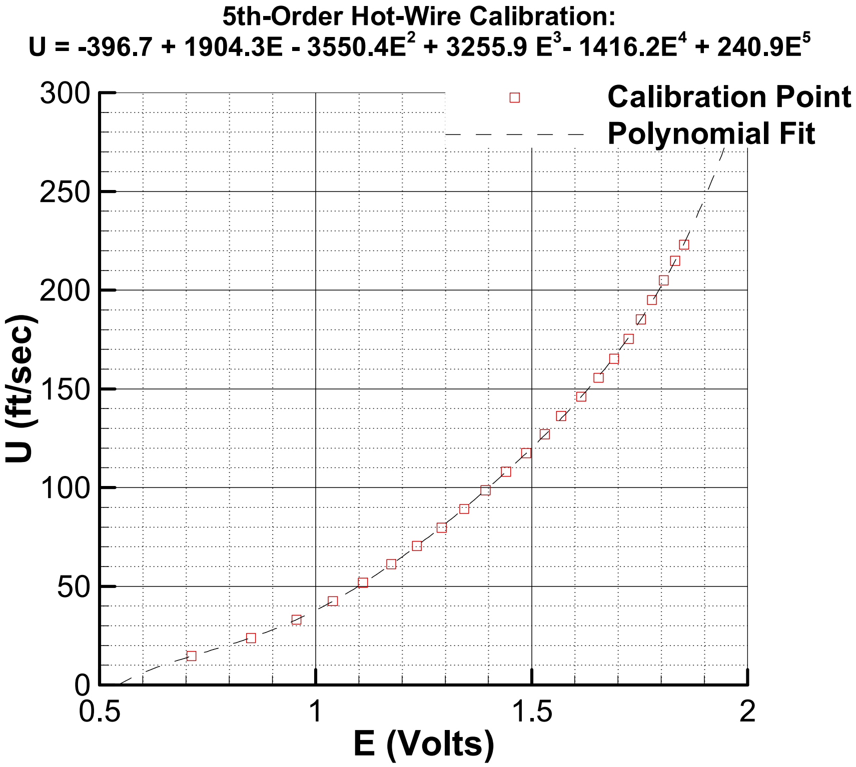

Fig. 3.18 Example hot-film calibration and resulting fifth-order calibration coefficients.

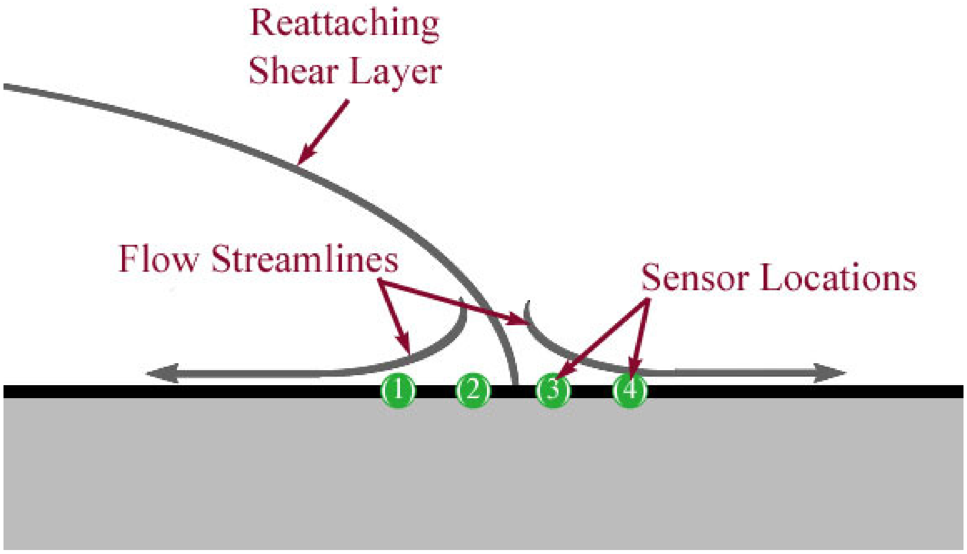

Fig. 3.19 Schematic of shear layer reattachment on airfoil surface.

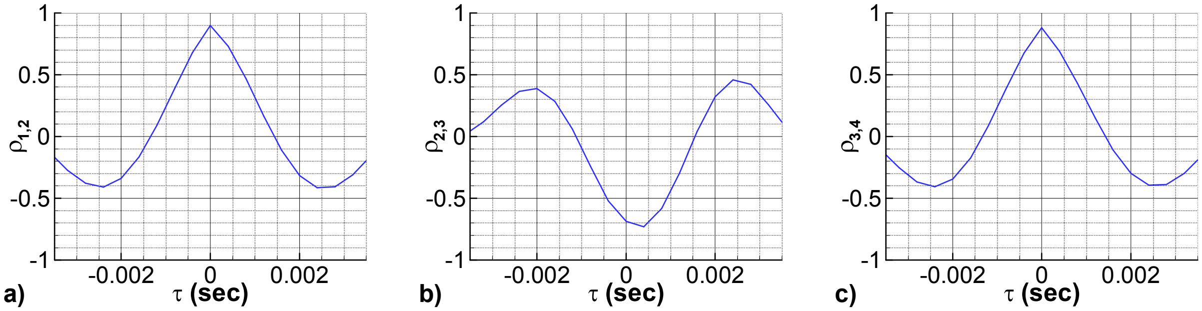

Fig. 3.20 Notional cross-correlation coefficients between adjacent sensors on hot-film array; sensor numbers shown in Fig. 3.19: a) upstream of reattachment, b) at reattachment, c) downstream of reattachment.

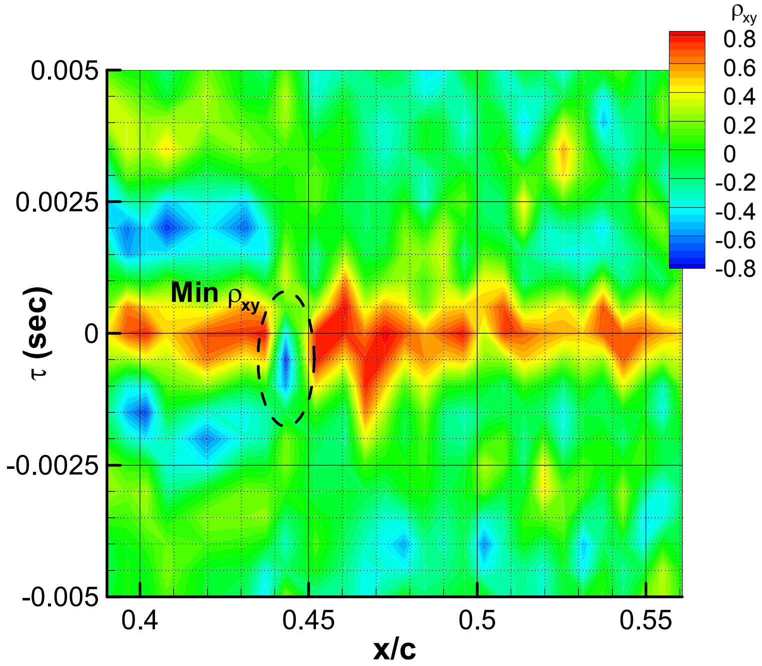

Fig. 3.21 Example cross-correlation contour of all adjacent sensor pairs for hot-film array.

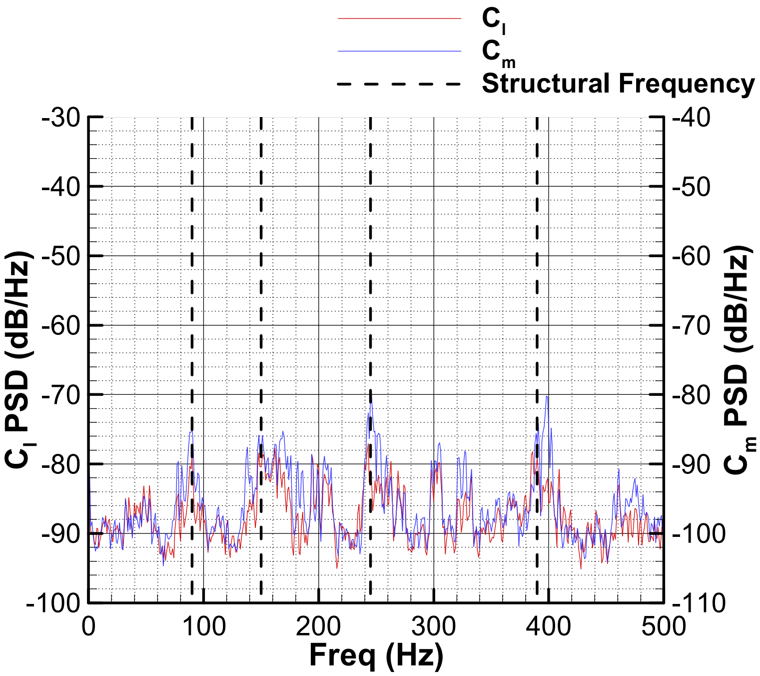

Fig. 3.22 PSD of impulse response test showing structural frequency modes.

Fig. 3.23 Fog machine with PVC attachment used for smoke flow visualization.

Fig. 3.24 Smoke wire and support structure installed upstream of airfoil model (view angled downstream).

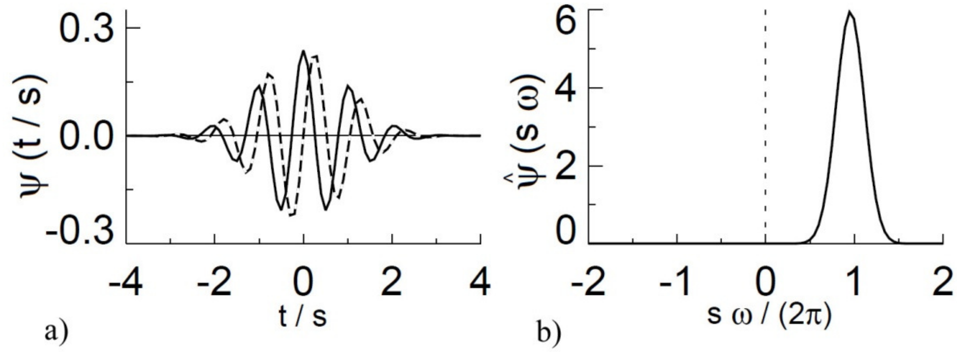
a) b)

Fig. 3.25 a) Morlet wavelet function, ψ_0 (solid curve represents real part, dashed curve represents imaginary part), b) Fourier transform of Morlet wavelet function, $\hat{\psi}_0$; after Torrence and Compo.[100]

Chapter 4

Results and Discussion

This chapter describes the results obtained from the experimental investigation and includes an analysis and discussion of these results. This section includes an improved understanding of the unsteady modes associated with iced-airfoil flowfields and an application of this improved understanding towards the development of a hinge-moment-based stall prediction system for airfoils.

4.1 Experimental Validation

Prior to analyzing the iced-airfoil flowfield, the experimental setup, data acquisition, and reduction processing was validated by comparing the clean airfoil performance coefficients and pressure distributions to those found in the literature.

4.1.1 Airfoil Performance

The installation of the airfoil model and reduction of the airfoil performance and pressure distributions were validated by comparison with prior studies. An example of the clean NACA 0012 airfoil performance from the current study is compared to those from the literature in Fig. 4.1. Included in this comparison are results reported by Gurbacki,[6] Abbott and von Doenhoff,[106] Ladson,[107] and computed using XFOIL.[84]

As shown in Fig. 4.1, the airfoil performance determined in the current investigation is consistent with those reported in the literature. The current results are closest to those determined by Gurbacki,[6] which is to be expected as the measurements were acquired using the same facilities and at the same Reynolds number as this prior study. All three performance coefficients (C_l, C_m, and C_d) are quantitatively consistent with this prior study. This includes the region near stall, which occurred in the current investigation at an angle of attack of 14.37°. The only slight difference between the data from the current investigation and the results of Gurbacki is in the airfoil drag polar at small, positive angles of attack. The results from the current investigation have slightly higher drag values for C_l between approximately 0 and 0.8. However, it is worth noting that for a symmetrical airfoil, like an NACA 0012, the drag polar is typically expected to be symmetric about $\alpha = 0°$, or $C_l = 0$, which is the case for the current investigation. In contrast, the C_d values reported by Gurbacki are somewhat lower for $0 \leq C_l \leq 0.5$ than they are for $-0.5 \leq C_l \leq 0$. Regardless, the C_d data are reasonably consistent between these two investigations and display the anticipated trends in comparison with the other results reported in the literature.

The validation data from the current investigation are also consistent with those reported by Abbott and von Doenhoff,[106] with some slight deviation occurring near stall. The stall angle of attack and $C_{l,max}$ are higher in the results reported by Abbott and von Doenhoff than they are for the current study. Additionally, the values of C_d are markedly lower than they are for the current study. This is also true when comparing the C_d results from the current study to those reported by Ladson.[107] These slight differences in $C_{l,max}$ and C_d can be explained by the difference in Reynolds number between the current study and these other two studies from the literature. It can be expected that as the Reynolds number is increased, the stall angle of attack will also increase and the drag coefficient will decrease, as reflected in the validation data of Fig. 4.1. Perhaps more significantly is the difference in C_m near stall between the data reported by Abbott and von Doenhoff and the results from the current study. Rather than having a slightly positive pitching moment induced by the leading-edge suction peak prior to stall, the C_m results of Abbott and von Doenhoff[106] appear to have a value close to zero just prior to stall. However, since the C_m results of the current study are in agreement with the other results from the literature, this discrepancy appears to be of little consequence.

Additional validation of the current study can be conducted by comparing the pressure distribution results from the current investigation to those reported in the literature. An example of the comparison of the C_p distribution determined by the current study at $\alpha = 10°$ to those reported by Gurbacki,[6] Gregory and O'Reilly,[108] and computed using XFOIL[84] is shown in Fig. 4.2. Only the upper surface C_p values were provided by Gregory and O'Reilly.[108] From Fig. 4.2, the C_p distribution from the current study is quantitatively consistent with the results from the literature. This includes the magnitude of the suction peak, which reaches a maximum in magnitude of approximately $C_p = -5.3$ in the current study, Gurbacki,[6] and Gregory and O'Reilly.[108]

Generally, the airfoil performance coefficients and pressure distributions computed using XFOIL, as presented in Fig. 4.1 and Fig. 4.2, were less consistent with the results from the current investigation and the results reported in the literature. In Fig. 4.1, the calculated C_l and C_m are in agreement with the experiments at low angles of attack, prior to stall. However, C_d is substantially lower than what is reported in the experimental data. With increasing angle of attack through stall, the discrepancy between the XFOIL-computed airfoil performance coefficients and the experimental data increases. This discrepancy is attributed in large part to the decrease in the accuracy of XFOIL predictions that generally occurs as the airfoil stall angle of attack is approached or exceeded. While an inspection of all of the experimental airfoil performance data in Fig. 4.1 seems to suggest that the NACA 0012 experiences a leading-edge stall type for $1.8 \times 10^6 \leq \text{Re} \leq 3.0 \times 10^6$, the results computed by XFOIL appear to be more consistent with a trailing-edge stall type. Additionally, in the C_p distributions presented in Fig. 4.2, the leading-edge suction peak computed by XFOIL is somewhat greater in magnitude than the experimental data at $\alpha = 10°$. Despite this difference, the C_p distribution across the remainder of the chord is fairly consistent with the experimental data.

As described in Section 3.4.1.2, the acquired pressure distribution was also used to calculate the hinge moment coefficient about a theoretical trailing-edge flap with a hinge line prescribed at $x/c = 0.70$, $y/c = 0.0$. The resulting hinge moment coefficients from the current study were compared to existing hinge moment data by Street and Ames[109] for an NACA 0009 airfoil with a 30%-chord trim tab, as well as hinge moment coefficients calculated using XFOIL[84] for an NACA 0012 airfoil with a 30%-chord flap. The resulting comparison is presented in Fig. 4.3.

From Fig. 4.3, the hinge moment coefficients from the current investigation are qualitatively consistent with those reported in the literature. The hinge moment coefficients from the current study appear to be quantitatively consistent with those reported by Street and Ames, except near $\alpha = \pm 10°$. Some differences between these two studies are to be expected, since the investigations were conducted at different Reynolds numbers on slightly different geometries. For this reason, the hinge moment coefficients computed using XFOIL prove to be particularly useful, as they display a qualitative agreement with the current results, and quantitative agreement at low angles of attack in the linear regime.

4.2 Time-Averaged Airfoil Effects of Simulated Ice

Prior to assessing the unsteady effects of icing on the performance of the NACA 0012 airfoil, the time-averaged effects of the simulated ice shapes on the airfoil performance and surface flowfield were analyzed. As discussed in Section 2.1.1, the addition of an ice shape to the contour of an airfoil generally degrades the airfoil performance by reducing maximum lift, increasing drag, and changing pitching moment characteristics. This is shown in Fig. 4.4 for the simulated horn-ice shape and the boundary-layer trip, in Fig. 4.5 for the quarter-round geometries at $x/c = 0.02$, and in Fig. 4.6 for the 1/4 in. quarter round at various locations across the airfoil upper surface. The resulting effects of the simulated ice shapes and boundary-layer trips on the airfoil maximum lift, stall angle of attack, and drag coefficient at zero lift are summarized in Table 4.1. Details related to each of these configurations will be discussed in the subsequent sections.

Table 4.1 Summary of performance effects of leading-edge contaminants

Configuration	$C_{l,max}$	$\Delta C_{l,max}$ **(%)**	α_{stall} **(°)**	$\Delta\alpha_{stall}$ **(%)**	$C_{d,zl}$	$\Delta C_{d,zl}$ **(%)**
Clean	1.336	—	14.37	—	0.0076	—
Trip	1.229	-7.99	13.34	-7.15	0.0119	56.27
Horn Ice	0.529	-60.37	6.61	-54.02	0.0261	243.20
1/8” QR $x/c = 0.02$	0.601	-54.97	8.12	-43.52	0.0164	116.20
3/16” QR $x/c = 0.02$	0.526	-60.59	7.09	-50.66	0.0199	161.52
1/4” QR $x/c = 0.02$	0.443	-66.82	6.05	-57.87	0.0237	211.35
5/16” QR $x/c = 0.02$	0.401	-69.97	5.55	-61.39	0.0266	249.34
3/8” QR $x/c = 0.02$	0.360	-73.08	5.03	-64.97	0.0313	311.83
1/4” QR $x/c = 0.05$	0.504	-62.25	7.56	-47.36	0.0292	284.35
1/4” QR $x/c = 0.10$	0.356	-73.34	6.01	-58.21	0.0356	367.49

4.2.1 Clean Airfoil

From Fig. 4.4, the clean NACA 0012 airfoil is associated with a leading-edge type stall at Re = 1.8×10^6 and M = 0.18. This is evident by inspection of the C_l vs. α and C_m vs. α characteristics of the clean model. For the clean case, the C_l vs. α curve remains mostly linear up until the stall angle of attack, though there is a very slight break and change in slope as stall is approached. However, with the onset of stall, the flow separates at the leading edge of the airfoil and fails to reattach to the surface, leading to a sharp decrease in C_l, as observed in Fig. 4.4 after $\alpha = 14.37°$ is exceeded. Similarly, the C_m vs. α curve remains approximately linear up until stall. As the flow separates at the airfoil leading edge, the positive contribution to the pitching moment from the suction peak decreases, and the decreased pressure over the airfoil trailing edge leads to a strong negative contribution to the airfoil C_m. As such, the C_m vs. α curve experiences a sharp decrease upon stall, indicating a leading-edge stall type.

Additional characteristics of the clean NACA 0012 airfoil can also be determined by analyzing the surface C_p distribution for the clean NACA 0012, which is presented in Fig. 4.7. From Fig. 4.7, the pressure distribution consists primarily of a leading-edge suction peak and a pressure recovery region. As the airfoil angle of attack is increased from $\alpha = 0°$ to $\alpha = 14°$, the strength of the leading-edge suction peak increases. From Fig. 4.7 b), the leading-edge stall type of the clean NACA 0012 airfoil is evident in the surface pressure distribution. At the angle of attack of maximum lift ($\alpha = 14°$), there is no evidence of any significant amount of trailing-edge separation. Upon increasing the angle of attack past $\alpha = 14°$, the flow separates at the leading-edge of the airfoil and fails to reattach. The effect of this leading-edge separation on the distribution of surface pressures can be seen in Fig. 4.7 b) for $\alpha = 16°$.

Using surface oil flow visualization, additional traits of the airfoil surface flowfield can also be determined. A summary of the flowfield features extracted from surface oil flow visualization on the clean NACA 0012 airfoil model is presented in Fig. 4.8. At low angles of attack, the flow over the airfoil upper surface is fully attached. The transition location is estimated by determining the location where the surface shear stress experiences a sudden increase, causing the oil droplets to be scrubbed away faster in the streamwise direction. An example of this is presented in the surface oil flow visualization at $\alpha = 0°$ presented in Fig. 4.9. From Fig. 4.9, the increase in surface shear stress is evident at approximately $x/c = 0.45$.

As also indicated in Fig. 4.8, a laminar separation bubble forms near the leading edge of the airfoil upper surface across the angle-of-attack range from α = 8° to α = 14°. The laminar separation bubble was identified using patterns that were formed in the surface oil flow visualization. An example of this is shown in the flow visualization at α = 8° presented in Fig. 4.10. The location of boundary-layer separation is associated with a pooling of the fluorescent oil, as the oil in the region upstream of the separation location is scrubbed downstream until the location of zero surface shear stress is reached. The time-averaged reattachment location is identified as the location just downstream of separation where the oil has been scrubbed away due to the increased surface shear stress of the reattached turbulent boundary layer. These features in the surface oil flow visualization created by the leading-edge separation bubble can also be seen in the close-up image of the leading-edge region in Fig. 4.11. As the stall angle of attack is exceeded, the upper surface flowfield is fully separated.

4.2.2 Boundary-Layer Trip

From Table 4.1 and Fig. 4.4, the addition of the boundary-layer trips resulted in the least amount of performance reduction of all of the contamination configurations tested. This is to be expected, as the purpose of the boundary-layer trips was only to promote boundary-layer transition with minimal additional effects to the airfoil flowfield. The slight decrease in maximum lift and increase in drag brought about by the boundary-layer trips are to be expected, as earlier boundary-layer transition leads to thicker, more turbulent boundary layers across the airfoil surface than would occur for natural transition downstream of the boundary-layer trips. The addition of the boundary-layer trips does not change the primary stall type of the airfoil.

4.2.3 Horn-Ice Shape

As shown in Fig. 4.4, the addition of the leading-edge horn-ice shape to the NACA 0012 airfoil model was associated with very significant changes to the airfoil stall characteristics, large increases in airfoil drag, and changes to the airfoil pitching moment. In addition to the reductions in maximum lift and stall angle of attack, as summarized in Table 4.1, the horn-ice configuration changed the stall type of the NACA 0012 airfoil from a leading-edge stall type to a thin-airfoil stall type. This change in stall type can be inferred by comparing the C_l vs. α and C_m vs. α characteristics of the clean and horn-ice configurations. From the horn-ice case shown in Fig. 4.4, the C_l vs. α curve is linear from approximately $-3° \leq \alpha \leq 3°$, but near α = 3° the slope of the C_l vs. α curve experiences a decrease in slope with increased α. As the airfoil angle of attack is increased up through stall, the slope of C_l vs. α smoothly decreases, forming a local maximum in C_l. The plateau that is formed in C_l across the stalled region is typically indicative of a thin-airfoil type stall.

As discussed in Section 2.1.2, the most dominant flowfield feature associated with a horn-ice or spanwise-ridge-ice shape is the separation bubble that forms on the airfoil upper surface. The growth of this ice-induced separation bubble is what causes the change in stall type of the NACA 0012 from a leading-edge type stall to a thin-airfoil type stall with the addition of the ice shape. A summary of the movement of the shear-layer reattachment location with angle of attack is shown in Fig. 4.12. The time-averaged shear-layer reattachment locations in Fig. 4.12 were determined from surface oil flow visualization.

From Fig. 4.12, the growth of the leading-edge separation bubble with increased angle of attack can be observed. Across the angle-of-attack range at which surface oil flow visualization was performed, the location of boundary-layer separation was fixed at the tip of the ice shape at $x/c = -0.0038$, due to the salient nature of the horn-ice shape. The time-averaged reattachment location was estimated using the flow bifurcation that occurs at shear-layer reattachment. As a result of this bifurcation, the oil droplets upstream of the reattachment location are scrubbed upstream and the oil droplets downstream of the reattachment location are scrubbed downstream. Thus, the time-averaged reattachment location corresponded to the location where the oil stream patterns reversed in the streamwise direction. An example of this is shown in Fig. 4.13, which represents the surface oil flow visualization completed for the airfoil with the horn-ice shape at $\alpha = 5°$.

From Fig. 4.13, the mean reattachment location for the horn-ice case at $\alpha = 5°$ corresponds to $x/c = 0.48$. Also included in Fig. 4.13 is the approximate reattachment zone, which occurred across a chordwise range from approximately $x/c = 0.42$ to $x/c = 0.53$. This reattachment zone was qualitatively determined by marking locations where the oil flow pattern appeared to change from a strong displacement in a single streamwise direction to a weaker displacement due to reductions in mean shear stress created by the influence of the flow stagnation at reattachment. It can be expected that this reattachment zone determined from the time-averaged flow visualization image is more characteristic of a standard deviation of the reattachment location from the mean value, rather than the absolute bounds of the reattachment zone since these estimated bounds were visually selected in a qualitative fashion.

It is the growth of the leading-edge separation bubble with increased angle of attack, as shown in Fig. 4.12, that leads to the change in stall classification from leading-edge stall type to thin-airfoil stall type with the addition of the ice shape to the clean airfoil model. As the separation bubble grows, it has an increasing decambering effect on the airfoil flowfield, which acts to alter the distribution of pressure about the airfoil and decrease the lift generated by the airfoil throughout the stalling process. The effect of a separation bubble on the distribution of pressure about an airfoil was discussed in detail by Tani.[18] The effect of the ice-induced separation bubble on the airfoil C_p distribution in the current study can be observed in Fig. 4.14 at $\alpha = 5°$. From Fig. 4.14, the ice-induced separation bubble at this angle of attack can be classified as a "long" bubble following the definitions of Tani.[18] As such, the separation bubble has a global effect on the airfoil pressure distribution, acting to reduce the strength of the suction peak and causing long stretches of constant pressure on the surface within the separation bubble region. Prior to a state of fully-separated flow across the airfoil surface, as the length of the separation bubble increases the effects on the C_p distribution become greater. For example, the C_p distributions for the clean and horn-ice cases at $\alpha = 6°$ are presented in Fig. 4.15. By comparing Fig. 4.14 with Fig. 4.15, the effect of a growth in the separation bubble size is associated with a further decrease in the magnitude of the clean airfoil leading-edge suction peak and a longer length of constant pressure across the airfoil upper surface.

For reference, the airfoil C_p distributions for the horn-ice case are presented in Fig. 4.16 across the angle-of-attack range from $\alpha = 0°$ to $\alpha = 9°$. The effect of the growth of the ice-induced separation bubble with increased angle of attack can further be seen in Fig. 4.16, where the chordwise length of the plateau in C_p increases with angle of attack up until stall. After stall, the C_p distribution at $\alpha = 9°$ of the iced airfoil in Fig. 4.16 b) approaches a constant pressure across the entire airfoil upper surface, which is characteristic of the separated flow about a bluff body.

4.2.4 Quarter-Round Geometry

From Fig. 4.5, the addition of the quarter-round geometry at $x/c = 0.02$ on the airfoil upper surface was associated with an effect on the performance similar to the horn-ice case. For all five heights of quarter rounds, a significant decrease in maximum lift and stall angle of attack, as well as increases in drag from the clean case, resulted. The addition of the quarter-round geometries also changed the airfoil stall from a leading-edge stall type to a thin-airfoil stall type for all quarter-round feature heights. Not surprisingly, the larger feature heights of the larger quarter-round geometries imposed a greater aerodynamic effect, which led to larger penalties in the airfoil performance coefficients. This is also reflected in the summary presented in Table 4.1. It is also interesting to note the decreasing aerodynamic penalty associated with a proportional increase in quarter-round feature height past 1/4 in.. For example, there is a larger difference in performance penalty imposed between the 1/8 in. and the 3/16 in. height than there is between the 5/16 in. and the 3/8 in. height, even though the incremental increase in the quarter-round height is the same.

The effect of the increased feature height of the quarter round on the location of shear-layer reattachment can be observed in the summary of flow visualization results for the quarter-round cases at $x/c = 0.02$, presented in Fig. 4.17. From Fig. 4.17, as one might expect, the smaller quarter-round geometries tend to be associated with smaller separation bubbles at the same angle of attack as those produced from the larger quarter-round geometries. For example, for $\alpha = 5.5°$, the reattachment location produced using the 1/8 in. quarter round was $x/c = 0.28$, while the reattachment location produced using the 1/4 in. quarter round was $x/c = 0.89$. At this same angle of attack, the flow over the airfoil upper surface with the 3/8 in. quarter round is fully separated. However, similar trends in growth of the separation bubble with increased angle of attack can be observed across the various sized quarter-round cases.

As the length of the separation bubble increased with increased angle of attack or increased feature height of the quarter round, the separation bubble had a greater effect on the airfoil C_p distribution. This is consistent with the observations made previously for the horn-ice shape. The C_p distributions for the quarter-round geometries placed at $x/c = 0.02$ on the airfoil upper surface at $\alpha = 5°$ are shown in Fig. 4.18. From Fig. 4.18, the reduction of the magnitude of the clean airfoil leading-edge suction peak is shown to increase with increased quarter-round feature height.

As the 1/4 in. quarter-round was moved to two additional locations downstream of $x/c = 0.02$, the effect was somewhat more unexpected. From Fig. 4.6, the movement of the quarter-round geometry from $x/c = 0.02$ to $x/c = 0.05$ on the airfoil upper surface resulted in slightly higher $C_{l,max}$, consistent C_m between these two cases, and an increase in C_d. When the quarter-round geometry was placed at x/c = 0.10, however, the resulting performance effects were greatest of all the locations tested, resulting in higher losses in lift and increases in drag than the other locations. Similar observations were also made by Lee[87] when determining the effect of moving the location of a forward-facing quarter-round geometry across the upper surface of a NLF 0414 airfoil and a modified NACA 23012 airfoil.

The changes in performance due to the quarter round at various locations on the airfoil surface can be further understood by analyzing the airfoil surface flowfield. A summary of the time-averaged shear-layer reattachment locations determined from surface oil flow visualization for the 1/4 in. quarter round at three locations on the airfoil upper surface is presented in Fig. 4.19. The chordwise locations of the tip of the 1/4 in. quarter-round geometry, which was assumed to be the separation locations of each of these cases, are also shown in Fig. 4.19 with a vertical dashed line in the color corresponding to the figure legend. From Fig. 4.19, the reattachment locations are relatively consistent between the x/c = 0.02 case and the x/c = 0.05 case. For the x/c = 0.10 case, reattachment occurs much farther downstream than the other two cases. This results in a greater effect on the airfoil flowfield when the quarter-round geometry is placed at x/c = 0.10 than for the other two locations of the 1/4 in. quarter round.

The effects of the separation bubbles induced by the 1/4 in. quarter round shape at different locations across the airfoil leading-edge region can also be identified in the resulting C_p distributions as shown in Fig. 4.20. From Fig. 4.20, the C_p distributions that result with the quarter-round placed at x/c = 0.02 and x/c = 0.05 are similar. However, the pressure of the plateau region in the C_p distribution was lower within the separated region when the quarter round was placed at x/c = 0.05. This helps to explain why a higher $C_{l,max}$ was reached for the case of the quarter round at x/c = 0.05 than at x/c = 0.02 in Fig. 4.6. In contrast, at α = 5°, when the quarter round was placed at x/c = 0.10, the shear layer failed to reattach to the airfoil surface. Since the entire upper surface was separated in this case, the C_p distribution was highly affected, as evident in Fig. 4.20.

4.3 Ice-Induced Flowfield Unsteadiness

The presence of elevated flowfield unsteadiness due to separation bubbles has been well documented (e.g. Gaster[60]). Using the surface-integrated pressure transducers across the airfoil surface, the unsteadiness in the C_p distribution can be estimated using the standard deviation of the unsteady pressure coefficient (σ_{C_p}). Unsteadiness in the C_p distribution can be further designated to specific frequency scales by studying the frequency spectra of the unsteady pressure distribution about the airfoil. Analyzing the unsteadiness distributed throughout the airfoil surface pressure in this way provides an initial indication to the location and classification of relevant unsteady flowfield behavior.

4.3.1 Clean Airfoil

Prior to evaluating the unsteadiness induced by the leading-edge ice shapes used in this study, the unsteadiness in the clean airfoil C_p distribution was evaluated. The distribution of σ_{C_p} across the upper surface of the clean NACA 0012 airfoil is presented in Fig. 4.21. Only the unsteadiness in the upper surface pressures is presented, as the pressure distribution across the lower surface had very little variation in the amount of measured unsteadiness when compared with the unsteadiness about the upper surface. From Fig. 4.21, prior to stall the unsteadiness measured across the airfoil upper surface was very low. This can be observed by comparing the distribution of $C_{p.StDev}$ for $\alpha = 0°$ and $\alpha = 14°$, where similar levels of magnitude in unsteadiness can be observed between these two angles of attack. It can also be observed that the greatest amount of unsteadiness in the airfoil C_p is consistently measured by the transducer at $x/c = 0.07$, which is the first transducer location downstream of the leading-edge suction peak. The σ_{C_p} distributions at these two angles of attack are also representative of the entire angle-of-attack range prior to the airfoil stall.

After the airfoil stalls, however, the unsteadiness in the pressure measurements drastically increases. This can be seen in Fig. 4.21 for $\alpha = 14.5°$, which is just after the airfoil stall. The highest levels of unsteadiness occur in the leading-edge region of the airfoil, from $x/c = 0.05$ to $x/c = 0.20$. As the angle of attack is further increased, the flowfield unsteadiness decreases. This can be seen in Fig. 4.21 from the σ_{C_p} distributions for $\alpha = 15°$, 16°, and 17°, where after stall the high levels of unsteadiness in the leading-edge region decrease, and the size of this region of high unsteadiness at the airfoil leading edge shrinks. By $\alpha = 17°$, most of the leading-edge unsteadiness is on the same order of magnitude as the rest of the unsteadiness across the remainder of the airfoil upper surface.

4.3.2 Boundary-Layer Trip

As shown in Section 4.2.2, the addition of the boundary-layer trips to the clean NACA 0012 had a minimal effect on the airfoil performance and did not appear to change the stall type classification of the airfoil. Similarly, the addition of the boundary-layer trips had a small effect on the flowfield unsteadiness about the airfoil surface. This is shown in Fig. 4.22, where the σ_{C_p} distribution across the airfoil upper surface is shown for the airfoil model with the boundary-layer trips. For reference, the distribution of σ_{C_p} for the clean airfoil upper surface at $\alpha = 0°$ and $\alpha = 14.5°$ is also shown in Fig. 4.22. From Fig. 4.22, prior to stall for the tripped airfoil model, the upper surface flowfield is associated with consistent low levels of unsteadiness, which are comparable to the pre-stall unsteadiness levels of the clean airfoil model. This can be observed in Fig. 4.22 for the tripped airfoil model at $\alpha = 0°$ and $\alpha = 13.5°$

As was the case for the clean model, however, after stall the σ_{C_p} distribution displays high levels of unsteadiness across the tripped airfoil upper surface, particularly across the leading-edge region from $x/c = 0.05$ to $x/c = 0.15$. This is shown in Fig. 4.22 for the tripped airfoil model at $\alpha = 14°$. Immediately after stall, the levels of maximum unsteadiness in the tripped airfoil surface pressure in Fig. 4.22 appear to be slightly higher than those observed for the clean airfoil in Fig. 4.21. However, in both the clean and tripped cases the unsteadiness in the pressure measurements appear to be greatest just past the stall angle of attack, so the higher levels of unsteadiness just past stall for the tripped case than the clean case could also simply be due to the fact that a finite resolution in angle of attack was used when acquiring data. Since the true angle-of-attack margin past α_{stall} could be different between the clean case at $\alpha = 14.5°$ and the tripped case at $\alpha = 14°$, it is possible that the tripped case at $\alpha = 14°$ is closer to the stall angle of attack than the clean case at $\alpha = 14.5°$.

One significant difference between the flowfield unsteadiness produced by the tripped case from the clean case is the post-stall level of unsteadiness with increasing angle of attack. From Fig. 4.22, as $\alpha = 14°$ is exceeded the level of unsteadiness in the surface pressure drastically decreases within the leading-edge region of the airfoil upper surface. This can be seen in the σ_{C_p} distribution for $\alpha = 14°$ and $\alpha = 15°$. The clean airfoil, as shown in Fig. 4.21, retains much of the unsteadiness in surface pressure within the leading-edge region of the airfoil upper surface as the angle of attack is increased in the post-stall regime. Conversely, in Fig. 4.22

at α = 15° or α = 16° the level of unsteadiness in the surface pressure across the leading-edge region of the tripped airfoil is below the level of unsteadiness at locations farther downstream.

4.3.3 Horn-Ice Shape

As discussed in Section 4.2.3, the addition of the horn-ice shape was shown to significantly alter the clean airfoil time-averaged C_p distribution and changed the airfoil stall classification from a leading-edge stall type to a thin-airfoil stall type. The addition of the horn-ice shape to the clean NACA 0012 airfoil also changed the distribution of unsteadiness in the airfoil flowfield. The upper-surface distribution of unsteadiness, as estimated by σ_{C_p}, for the horn-ice case is presented in Fig. 4.23. In Fig. 4.23, the upper-surface distribution of σ_{C_p} for the clean airfoil at α = 0° is also provided for reference. As discussed in Section 4.3.1, this distribution of σ_{C_p} for the clean airfoil is representative of the distribution of unsteadiness across the airfoil upper surface at all pre-stall angles of attack for the clean case.

From Fig. 4.23, the addition of the horn-ice shape to the clean NACA 0012 airfoil leads to increased levels of unsteadiness across the airfoil surface when compared to the pre-stalled clean airfoil case. At low angles of attack, (i.e. α = 0°, 1°, and 2°) in Fig. 4.23 a), the elevated levels of unsteadiness are primarily constrained to the leading-edge section of the airfoil from approximately x/c = 0.05 to x/c = 0.20. As the angle of attack is increased, the maximum value of σ_{C_p} reached across the upper surface increases and moves further downstream. This can be observed in Fig. 4.23 a) for α = 4° and Fig. 4.23 b) for α = 5° and α = 6°. As the airfoil begins to stall, the unsteadiness in the leading-edge region from x/c = 0.0 to x/c = 0.25 begins to increase, as seen in Fig. 4.23 b) for α = 6° and α = 7°. After the airfoil stalls, the value of maximum σ_{C_p} begins to decrease, and the distribution of unsteadiness across the airfoil flowfield moves closer to being uniform, which can be seen in Fig. 4.23 b) for α = 7°, 8°, and 9°.

By comparing Fig. 4.23 with Fig. 4.12, it is interesting to observe that the location of maximum unsteadiness in the flowfield, corresponding to the location of maximum σ_{C_p}, does not correspond to the location of mean shear-layer reattachment. This is shown in Fig. 4.24, where the C_p and σ_{C_p} distributions of the horn-ice case are presented at α = 5, along with the mean location of shear-layer reattachment. From Fig. 4.24, the location of maximum σ_{C_p} in the flowfield corresponds to $0.75x_r$ at α = 5°. This is similar to the prior observations made by Gurbacki.[6]

A comparison of the locations of maximum σ_{C_p} and time-averaged reattachment location are shown in Fig. 4.25 for an angle-of-attack range near stall. Due to the coarse distribution of surface-integrated unsteady pressure transducers, the location corresponding to the maximum σ_{C_p} was determined without great precision in Fig. 4.25. However, this comparison was still useful for qualitatively identifying that the location of maximum unsteadiness in pressure across the airfoil chord occurred upstream of the mean reattachment location. For the angle-of-attack range included in Fig. 4.25, the average location of maximum σ_{C_p} corresponded to $0.787x_r$. As can also be observed in Fig. 4.25, the location of maximum σ_{C_p} tended to reside farther upstream of reattachment at a greater percentage of the total separation bubble length with increased angle of attack until stall.

At an angle-of-attack range from $\alpha = 0°$ to $\alpha = 5°$, Gurbacki[6] identified the maximum unsteadiness in surface pressure occurring between $x = 0.60x_r$ and $x = 0.75x_r$. As discussed by Mabey,[2] the location of maximum fluctuation in pressure on a surface with reattaching flows typically occurs between $x = 0.75x_r$ and $x = 0.90x_r$. The results from the current study fall within this range. These results are also consistent or similar with various other studies on flowfield about simple geometries. For example, Spazzini et al.[35] identified a maximum unsteadiness in surface shear stress at a location corresponding to $x = 0.7x_r$ downstream of a backward-facing step across a range of Reynolds numbers. Heenan and Morrison[29] observed that the location of maximum unsteadiness in the surface pressure downstream of a backward-facing step resided between $0.8x_r$ and $0.9x_r$. These authors also identified the maximum amplitude of the shear-layer flapping frequency at a location corresponding to $0.75x_r$. As discussed by these authors, this location coincided with the region of maximum pressure recovery in the separation bubble. Similar locations of maximum unsteadiness in the flowfields about simple geometries were also reported in other studies, including those reported by Cherry et al.,[26] Hudy et al.,[25] Driver et al.,[38] and Castro and Haque.[37]

4.3.4 Quarter-Round Geometry

It was shown in Section 4.2.4 that the addition of a quarter-round geometry to the NACA 0012 airfoil reduced the airfoil performance to an extent related to the feature height of the quarter round and dependent on the location of the geometry. However, the maximum unsteadiness present in the flowfield about the airfoil with a quarter-round geometry did not appear to have a direct dependence on changing the feature height or location of the quarter round. The effect of various sized quarter-round geometries on the distribution of σ_{C_p} across the airfoil upper surface is presented in Fig. 4.26. Shown in Fig. 4.26 are the σ_{C_p} distributions for $\alpha = 5°$, with quarter-round geometries of various feature heights placed on the airfoil upper surface at $x/c = 0.02$. From Fig. 4.26 it can be observed that for a fixed angle of attack, the increase in the feature height of the quarter-round geometry causes the chordwise location of maximum unsteadiness (as evaluated by σ_{C_p}) to move downstream. This downstream movement of the location of maximum σ_{C_p} can be expected, as it was shown in Fig. 4.17 that the increase in the feature height of the quarter round also led to a downstream movement of the mean shear-layer reattachment location. While the location of maximum σ_{C_p} tends to move downstream with increased feature height, it can be seen in Fig. 4.26 that the magnitude of the maximum σ_{C_p} remains largely unchanged for a fixed pre-stall angle of attack when the feature height of the quarter-round is changed. The maximum σ_{C_p} values for all of the quarter-round heights in Fig. 4.26 correspond to values within 0.16 ± 0.01. This suggests that the level of flowfield unsteadiness measured in the pressure distribution does not primarily scale by the feature height of the quarter-round geometry, but rather the incidence or projected height of the airfoil model.

As a result, the measured unsteadiness in the airfoil flowfield with the quarter-round geometry will be higher when the airfoil is operating at a higher (pre-stall) angle of attack. This can be observed from the distribution of σ_{C_p} across the airfoil for the various-sized quarter-round geometries at $x/c = 0.02$, which is shown in Fig. 4.27. Since the 1/8 in. quarter round is associated with the highest stall angle of attack ($\alpha_{stall} \approx 8°$) of all of the quarter-round cases tested at $x/c = 0.02$, the highest level of σ_{C_p} in Fig. 4.27 a) – e) is achieved for the 1/8 in. quarter-round height at $x/c = 0.02$ at $\alpha = 8°$, as shown in Fig. 4.27 a). Conversely, of the quarter-round heights tested, the 3/8 in. quarter round had the greatest reduction in stall angle of attack for the airfoil ($\alpha_{stall} \approx 5°$). As a result, the maximum value of σ_{C_p} identified in the flowfield for the 3/8 in. quarter-round case in Fig. 4.27 e) at the stall angle of attack was lower than that identified in the other quarter-round cases. This is shown in Fig. 4.28, where the upper-surface σ_{C_p} distributions are presented at α_{stall} for each of the quarter-round heights placed on the airfoil upper surface at $x/c = 0.02$. From Fig. 4.28, a clear decrease in the maximum values of σ_{C_p} at α_{stall} with increased feature height can be observed.

Some similar effects can be observed when inspecting the distribution of unsteadiness associated with the flowfield of the 1/4 in. quarter-round geometry at various locations across the airfoil upper surface, which is presented in Fig. 4.29 for $\alpha = 5°$. From Fig. 4.29, it can be seen that the value of maximum σ_{C_p} remains relatively constant for a fixed angle of attack as the quarter-round geometry is moved across the leading-edge portion of the airfoil model. This was also observed in Fig. 4.26 when the feature height of the quarter-round geometry at $x/c = 0.02$ was changed at a fixed pre-stall angle of attack.

The upper-surface σ_{C_p} distributions are also provided for various pre-stall angles of attack for the 1/4 in. quarter round located at different chordwise locations in Fig. 4.30. By comparing these σ_{C_p} distributions, it can be observed that the distribution of unsteadiness takes on similar trends as the cases analyzed previously. Namely, the value of maximum σ_{C_p} generally increases and the corresponding location of this maximum value moves downstream with increased angle of attack until α_{stall}. However, by comparing the differences between Fig. 4.30 a) – c), it can be seen that the maximum value of σ_{C_p} achieved prior to stall tends to decrease as the location of the quarter-round geometry is moved downstream. This can be seen by comparing Fig. 4.30 a) at $\alpha = 6°$ and Fig. 4.30 b) at $\alpha = 6°$. When the quarter round is placed at $x/c = 0.02$, the maximum value of σ_{C_p} at $\alpha = 6°$ is 0.17, compared to the maximum value of 0.15 obtained at $\alpha = 6°$ when the quarter round is placed at $x/c = 0.10$. This result is not surprising, as the extent of the unsteadiness is largely driven by the characteristics of the separation bubble. When the quarter-round geometry is moved downstream, at the onset of stall a lower value of maximum σ_{C_p} is achieved as the length of the separated region is smaller.

4.3.5 Validation of Unsteady Reattachment Location

Using the measurements obtained from the hot-film array and the data reduction method outlined in Section 3.6, the unsteady shear-layer reattachment location was identified on the NACA 0012 airfoil model with the leading-edge horn-ice shape at $\alpha = 5°$. In order to ensure that the method for determining the unsteady shear-layer reattachment location developed in this study was consistent with results reported by previous authors, a qualitative and quantitative comparison of the reattachment data from the current study was made with data from the literature. In order to determine the qualitative similarity of the results of the current study to the reattachment data reported in the literature, a comparison of the unsteady reattachment location from the current study is made with the mathematical model of the unsteady reattachment location downstream of a backward-facing step developed by Kiya and Sasaki.[31]

The resulting comparison of the unsteady reattachment location is presented in Fig. 4.31. From Fig. 4.31 a) and as discussed in Section 2.2.1.1.2, according to Kiya and Sasaki[31] the dimensionless unsteady location of shear-layer reattachment can be approximated by superimposing a traveling wave and a standing wave of different frequencies and amplitudes. The standing wave represents the effects of the low-frequency component, and the traveling wave represents the effect of large-scale vortical motion on the movement of the shear-layer reattachment location. In Fig. 4.31 a), the standing wave is represented by the blue dot-dash curve and the traveling wave, which is superimposed on the standing wave, is represented by the red solid curve.

An example of the resulting unsteady shear-layer reattachment location obtained in the current investigation using the hot-film array downstream of the horn-ice shape, for $\alpha = 5°$, is shown in Fig. 4.31 b). In Fig. 4.31 b), the solid red curve was created using a 7-point moving average, and the blue dash-dot curve was created using a 60-point moving average. By comparing Fig. 4.31 b) to Fig. 4.31 a), the results of the current investigation and the results in the literature provide a striking similarity. From Fig. 4.31 b), a similar classification of frequency content can be observed in the results from the current investigation that were also observed in the mathematical model in Fig. 4.31 a). The results of the current investigation reveal similar values of the normalized instantaneous reattachment location, $(x - x_r)/x_r$, for both the low-frequency mode and the regular mode. The largest significant difference between Fig. 4.31 a) and Fig. 4.31 b) is that the ratio of frequencies between the low-frequency mode and the regular mode appear to be different between the current investigation and the model from the literature. This is apparent in Fig. 4.31, where a greater number of oscillations induced by the regular mode across one cycle of the low-frequency mode appear to occur in the current investigation than what occur in the mathematical model.

The resulting unsteady shear-layer reattachment location from the surface-mounted hot-film array measurements also compares favorably to the reattachment location determined from surface oil flow visualization of the NACA 0012 airfoil model with the leading-edge horn-ice shape at $\alpha = 5°$, which was presented in Fig. 4.13. As shown in Fig. 4.13, the time-averaged reattachment location for $\alpha = 5°$ was identified at $x_r/c = 0.48$, and the reattachment zone was estimated to occur from approximately x/c = 0.42 to x/c = 0.53. Similarly, the time-averaged shear-layer reattachment location determined using the hot-film array method in Fig. 4.31 b) was x_r/c = 0.466, and the minimum and maximum instantaneous shear-layer reattachment locations corresponded to x/c = 0.388 and x/c = 0.559, respectively. While the reattachment zone identified using the hot-film array method was larger than that estimated from surface oil flow visualization, as discussed in Section 4.2.3 it can be expected that the reattachment zone determined from the time-averaged image in Fig. 4.13 is more characteristic of a standard deviation of the reattachment location from the mean value, rather than the absolute bounds. Thus, by comparing the results from Fig. 4.31 b) with Fig. 4.13, the time-averaged reattachment location and approximate reattachment zone determined from the hot-film array is qualitatively consistent with that determined from the surface oil flow visualization.

While qualitative comparisons of the reattachment location determined from the hot-film array measurements of the current study can be made to results from the literature for studies of flows about simple geometries as well as results from surface oil flow visualization, a quantitative comparison to iced-airfoil reattachment data is also necessary. Since a limited amount of unsteady reattachment data on iced airfoils are available in the literature, the reattachment data from the current investigation will be quantitatively compared to the results obtained by Jacobs.[23] This prior investigation used PIV to study the flowfield about an iced airfoil, part of which included a statistical analysis of the instantaneous shear-layer reattachment location downstream of the ice shape. These tests were conducted on an NACA 0012 airfoil model with a 2D ice shape similar to the horn-ice shape being studied in the current investigation. All data in this prior study were acquired at $\mathrm{Re} = 0.9 \times 10^6$ and $M = 0.20$.

A schematic of the time-averaged shear-layer reattachment location and reattachment zone is shown in Fig. 4.32 after Jacobs.[23] For comparison, the unsteady shear-layer reattachment location from the current study is presented in Fig. 4.33, which was determined using the hot-film array measurements for the airfoil with the horn-ice shape at $\alpha = 5°$. The reattachment locations reported by Jacobs[23] were determined using the separation bubble stagnation streamlines and separation streamlines calculated from the PIV results. In Fig. 4.32, the average shear-layer reattachment location corresponds to x/c = 0.46 at $\alpha = 5°$. Also in Fig. 4.32 is the reattachment zone downstream of the horn-ice shape, which was calculated as the range of locations containing 98% of all instantaneous shear-layer reattachment locations from all PIV realizations taken at a given angle of attack. By comparing Fig. 4.32 with the unsteady reattachment location results from the current study in Fig. 4.33, the time-averaged shear-layer reattachment location in Fig. 4.33 is consistent with the average reattachment location in Fig. 4.32. However, the outer bounds of the reattachment zone from Jacobs[23] in Fig. 4.32 are somewhat farther from the mean reattachment location than the furthest instantaneous reattachment locations in the current investigation results in Fig. 4.33. A possible reason for this will be explained in the latter portion of this section.

Additional information about the unsteady reattachment process can also be obtained from inspection of the probability density (p) and the cumulative distribution (P) functions of the normalized reattachment location. This statistical comparison between the current study and the results of Jacobs[23] are presented in Fig. 4.34. From Fig. 4.34 a), the probability density function of the current study on the NACA 0012 airfoil with the leading-edge horn ice shape at $\alpha = 5°$ follows the same trends as the probability density function from Jacobs corresponding to $\alpha = 5°$, with one exception. The tails of the probability density function from Jacobs are larger than those from the current study, which also causes the probability density function in the current study to have higher values closer to the mean reattachment location, or $(x - x_r)/x_r = 0$. However, the physical locations on the airfoil surface of the tails in p from Jacobs[23] corresponded in the current study to locations outside of the region covered by the hot-film array. As a result, in the current study the probability density function approaches zero at these locations, since measurements to estimate the shear-layer reattachment location could not be made in those regions. This is also the reason why, in Fig. 4.34 b), the cumulative distribution function of the current entry deviates from the results of Jacobs for $\alpha = 5°$ far from the mean reattachment location. However, for the purposes of this study, the inability to fully capture the tails in the probability density function is of little concern, as reattachment at these locations was so infrequent.

The probability density functions reveal that the reattachment location occurs most often near the mean location, and the probability decreases as the location deviates further from the mean. This is also indicated in the cumulative distribution function, where the slopes of the functions are greatest near the mean reattachment location, and taper off with increased distance from the mean. By comparing the probability density and cumulative distribution function from the current study to those from Jacobs,[23] the current method for estimating the unsteady reattachment location using hot-film array measurements is shown to be consistent with the trends in shear-layer reattachment location determined from PIV.

4.3.6 Iced-Airfoil Flowfield Spectral Content

In addition to estimating the distribution of unsteadiness across the airfoil surface using the calculated σ_{C_p} values, it was also helpful to identify frequency scales associated with the unsteadiness. This was accomplished by analyzing the frequency spectra of the unsteady C_p distribution across the airfoil upper surface. The PSDs of the unsteady C_p measurements were calculated using the methods outlined in Section 3.10.1. Since the frequency content of the quarter-round cases were observed to be similar to the horn-ice case, only results obtained for the horn-ice case will be presented in this section and in the characterization discussed in Sections 4.4–4.6. An example of the frequency scales at select locations across the upper surface is presented in Fig. 4.35 for the airfoil with the horn-ice shape at $\alpha = 5.5°$. In Fig. 4.35, the peaks occurring at 139 Hz at all locations corresponded to the structural mode of the model, and the peaks occurring at multiples of 91 Hz were due to the wind tunnel fan blade passing. These same structural and fan blade passing frequencies were observed by Gurbacki,[6] and were also discussed in Section 3.7. These structural or fan blade frequencies are marked by an arrow in Fig. 4.35 in order to assist in differencing these tunnel-induced frequency peaks from the aerodynamic peaks of interest.

From Fig. 4.35, the oscillations in the airfoil local surface pressure appear to occur across different frequency ranges, depending on the location on the airfoil chord. At $\alpha = 5.5°$, these ranges include a broad-band high-frequency range on the order of 50 Hz to 225 Hz, and narrow-band peaks occurring across a low-frequency range between 5 Hz and 35 Hz. In order to better identify these low-frequency peaks, the PSDs of the unsteady C_p at the same locations in Fig. 4.35 are also shown in Fig. 4.36 across a low-frequency range. As was done for Fig. 4.35, the fan blade and structural frequencies visible in Fig. 4.36 are marked by an arrow.

From Fig. 4.36, it can be seen that across the low-frequency range between 5 Hz and 35 Hz, there are two narrow-band peaks in the C_p PSDs, primarily occurring at locations upstream of the mean reattachment location. In the upstream region of the separation bubble, from $x/c = 0.03$ to $x/c = 0.21$, a narrow-band, low-frequency peak was identified with a maximum amplitude centered at a frequency of 25.2 Hz. An example of this peak in the C_p PSD at x/c = 0.07 is shown in Fig. 4.36 a). This region is also distinctly dominated by low-frequency content, as the amplitude in the C_p PSDs below 50 Hz is markedly higher than that above 50 Hz. Throughout the remainder of the separation bubble, from x/c = 0.21 to x/c = 0.6, the C_p PSDs are also dominated by a second low-frequency peak, centered near 8.7 Hz. Additionally, this region has significantly greater energy in the C_p PSDs above 50 Hz than the upstream section of the separation bubble. Downstream of the mean reattachment location at x/c = 0.63, the amplitudes of these low-frequency peaks were observed to diminish, but were still present. This can be observed in Fig. 4.36 e) and f) for the two peaks below 35 Hz in the PSDs downstream of the mean reattachment location. Additional details, classification, and characterization of these frequency ranges will be discussed in great detail throughout Sections 4.4–4.6.

It is also helpful to observe the distribution of frequency content across the airfoil upper surface relative to the location of shear-layer reattachment. This is shown in the contour map of the C_p distribution PSD presented in Fig. 4.37 for the airfoil with the horn-ice shape at $\alpha = 5.5°$. In Fig. 4.37, the x-axis represents the chordwise location on the upper surface, the y-axis represents the frequency distribution, and the contour represents the amplitude of the PSD. Additionally, the mean reattachment location is represented in Fig. 4.37 as a vertical dashed line. Much like in Fig. 4.35, the structural mode of the model can be seen in Fig. 4.37 by the high-amplitude peak at a frequency of 139 Hz. Additionally, the wind tunnel fan blade passing frequencies corresponded to frequencies at multiples of 91 Hz, including the high-amplitude peaks at 182 Hz and 364 Hz.

The ranges of frequencies of the unsteadiness in the airfoil surface pressure, which were observed in Fig. 4.35, can also be seen in Fig. 4.37. From Fig. 4.37, in the leading-edge region of the airfoil, two narrow-band peaks can be observed, corresponding to frequencies near 10 Hz and 25 Hz. These peaks appear to be present across the entire airfoil upper surface, but are strongest in the region constrained by the leading-edge separation bubble. The peak near 25 Hz has maximum amplitude at the leading edge of the separation bubble at x/c = 0.03, decreases in amplitude with downstream distance, and increases again to reach a maximum in amplitude at x/c = 0.45. The lower-frequency peak near 10 Hz also reaches a maximum in amplitude at x/c = 0.45. The broad-band region of high amplitude across the high-frequency range from 100 Hz to 300 Hz can also be seen in Fig. 4.37. This region of high energy density is visible from approximately x/c = 0.25 to x/c = 0.90, reaching maximum amplitude near x/c = 0.50.

The frequency content presented in Fig. 4.37 can also be compared with the σ_{C_p} values obtained for the airfoil with the horn-ice shape at $\alpha = 5.5°$, presented in Fig. 4.38. By comparing Fig. 4.37 with Fig. 4.38, it is not surprising that the region near $x/c = 0.45$ ($x/x_r = 0.714$) is characterized by the greatest amount of flowfield unsteadiness in the upper surface σ_{C_p} distribution. Near this region, the low-frequency peaks exhibit high amplitudes of energy density. This is consistent with the observations of Heenan and Morrison,[29] where the greatest spectral content at the shear-layer flapping frequency was identified at $x/x_r = 0.75$. Additionally, the high-frequency, broad-band oscillation between 50 Hz and 225 Hz also exhibits high amplitudes of oscillation at this location. It is also interesting to compare the dominant presence of the two different frequency ranges inside and outside of the separation bubble. While the low-frequency peaks appear to have the highest amplitude upstream of x_r/c and diminish downstream of x_r/c, the high-frequency broad-band energy appears to be present both upstream and downstream of x_r/c. As such, the low-frequency fluctuations are most dominant inside the separation bubble, and the higher-frequency fluctuations originate in the separation bubble, but have a dominating effect downstream of the separation bubble. This will be discussed in detail throughout Sections 4.4–4.6.

Similar distributions of frequency content across the iced-airfoil upper surface can also be seen in Fig. 4.39 for $\alpha = 4.5°$, 5°, 6°, and 6.5°. For comparative purposes, the contours in Fig. 4.39 are presented at the same levels as Fig. 4.37. By comparing Fig. 4.37 with Fig. 4.39, it can be seen that an increase in angle of attack, and the associated elongation of the separation bubble, is accompanied with greater amplitudes of energy density in the C_p PSDs. Despite these differences in amplitude of the C_p PSDs with changing angle of attack, the locations of dominant frequency peaks appear to be consistent in regards to their location relative to the mean reattachment location. That is, the low-frequency peaks are consistently dominant across the length of the separation bubble, and the broad-band energy across the higher frequency range originates upstream of the mean reattachment location and is dominant downstream of the mean reattachment location.

While analyzing the distribution of flowfield unsteadiness is useful for setting a framework for better understanding the ice-induced unsteadiness generated on an airfoil, it was also important to perform additional analysis and characterization of the various unsteady modes identified in the spectral content. As discussed in Section 2.2.2, the unsteadiness in an airfoil flowfield can be attributed to various sources or classifications. Sections 4.4–4.6 will be devoted to analyzing the spectral content of the airfoil unsteady C_p distributions and unsteady performance, classifying the modes of unsteadiness, comparing these modes to the literature, and describing additional analysis and results of the ice-induced flowfield unsteadiness.

4.4 Regular Mode of Vortical Motion

One of the sources of unsteadiness present in most separated flows is due to vortical motion in the flowfield, including vortex motion in the shear layer and shedding from a separation bubble. In this section, the frequency content associated with the regular mode will be identified, and the dimensionless scaling and convective characteristics of the regular mode will be reported with an associated comparison to the literature. Also, a visualization of the vortex convection throughout the iced-airfoil flowfield will be presented.

4.4.1 Frequency Scales of Regular Mode

As discussed by Gurbacki,[6] on an iced airfoil the regular mode can be primarily identified in the pressure measurements taken downstream of the mean reattachment location at a given angle of attack. The presence of the regular mode was also discussed by Mabey[2] as typically occurring in the pressure fluctuation spectra near the mean reattachment location downstream of several canonical geometries. Cherry et al.[26] observed that a broad-band range of shedding frequencies appeared to dominate the pressure spectra across a zone beginning at 60% of the bubble length and running downstream of the reattachment zone. Similarly, Spazzini et al.[35] observed the dominance of the regular mode beginning around x/x_r = 0.50, and continuing downstream of the reattachment zone. Driver et al.[38] also observed the regular mode in the spectral content of pressure measurements acquired slightly upstream of the mean reattachment location that persisted downstream of the reattachment zone, and compared the frequency to those observed for vortical structures in free shear layers. Since these authors acquired measurements at higher Reynolds numbers than most other investigations of flows about simple geometries, they were able to conclude that the vortical structures remain present in backward-facing step flows at higher Reynolds numbers.

The regular mode was also observed in the pressure measurements of the current investigation. Following the descriptions of the effects of the regular mode reported in the literature, the broad-band spectral content that was observed in Section 4.3.3 for frequencies primarily above 50 Hz was attributed to the regular mode. The PSDs of C_p at various locations across the airfoil surface are shown in Fig. 4.40 for the airfoil with the horn-ice shape at $\alpha = 5°$. The frequencies of the airfoil model structural modes and fan blade passing are marked in Fig. 4.40 with an arrow. Also included in Fig. 4.40 is the approximate progression of the center frequency of the regular mode across the airfoil chord, which is denoted by a dashed line. In Fig. 4.40, the effects of the regular mode can be observed from the broad-band peak from approximately 50 Hz to 300 Hz. Much like the observations made in other studies in the literature, the regular mode begins to be apparent around $x/c = 0.28$, which corresponds to approximately 60% of the separation bubble length. With increased distance towards the downstream edge of the separation bubble, the amplitude of the regular mode appears to increase. Downstream of the mean reattachment location (x_r), the presence of the low-frequency modes diminishes, making the broad-band frequency range of the regular mode much more apparent. With increased distance downstream of the reattachment location, the amplitude of the regular mode in the C_p PSD tends to decrease.

A careful inspection of Fig. 4.40 also reveals a decrease in the regular mode frequency with increased downstream distance throughout the separation bubble region. For example, at $x/c = 0.36$, the central frequency of the regular mode is approximately 185 Hz. Farther downstream, at $x/c = 0.70$, the central frequency of the regular mode decreases to approximately 165 Hz. A similar effect was observed by Cherry et al.[26] in the pressure spectra downstream of a backward-facing step. These authors attributed the decrease in frequency to changes in the shear-layer structure that occur upstream of the reattachment zone, until a constant shedding frequency is reached. Such a claim could be reinforced by the observations of Troutt et al.[110] who identified that reductions in the frequencies of vortical motion (e.g. via pairing) can occur upstream of reattachment, but tend to be inhibited after shear-layer reattachment occurs. As a result, a constant frequency of the regular mode is reached downstream of the reattachment zone as a constant shedding frequency is reached. This can also be observed in Fig. 4.40, where the central frequency of the regular mode remains unchanged from $x/c = 0.55$ to $x/c = 0.925$.

As discussed by Gurbacki,[6] an increase in airfoil angle of attack was accompanied with a decrease in the bandwidth and the center frequency of the regular mode peak. An example of this is presented in Fig. 4.41, where the PSDs of the airfoil C_p at $x/c = 0.85$ are shown across a range of angles of attack. In Fig. 4.41, the approximate center frequency of the regular mode is denoted by the dashed vertical line. Similar to the observations of Gurbacki,[6] the bandwidth and central frequency of the regular mode spectral peaks are observed to decrease with angle of attack in Fig. 4.41 up to stall. For the post-stall angle-of-attack range of $7° \leq \alpha \leq 9°$, the regular mode spectral peak was observed to retain a similar bandwidth and center frequency as the peak for $\alpha = 6.5°$. For this reason, the C_p PSDs are not shown in Fig. 4.41 for this post-stall angle-of-attack range.

It can also be observed from Fig. 4.41 that the amplitude of the regular mode spectral peak increases with increased angle of attack. This indicates that as the adverse pressure gradient imposed across the separation region increases, and as the separation bubble elongates, the oscillations imposed by vortical motion become more energetic. This is consistent with the observations of Jacobs,[23] where an increase in angle of attack of an airfoil with a horn-ice shape was observed to be associated with a greater density of large-scale vortices present in the flowfield.

It can also be expected that the regular mode would be observed in the hot-film velocity measurements that were acquired in the wake (U_{wake}) of the airfoil upper surface. For example, in addition to observing the regular mode in the pressure spectra across the reattachment zone, Cherry et al.[26] identified the presence of the regular mode in the spectral content of unsteady velocity measurements acquired at the shear-layer edge. Additionally, Kiya and Sasaki[30] identified from the velocity spectra downstream of a blunt flat plate that the upper edge of the shear layer was dominated by large-scale vortex structures characteristic of the regular mode. Similarly, in the current investigation the regular mode was most visible in the hot-film velocity measurements acquired at the upper edge of the wake. In order to show this, a comparison of the spectral content of the airfoil C_p and the spectral content of the velocity at the upper edge of the wake is presented in Fig. 4.42.

In Fig. 4.42, the PSDs for the airfoil C_p at $x/c = 0.85$ and the velocity at the upper edge of the wake at $\alpha = 5°$, 6°, and 7° are shown on the left side, with the corresponding wake profiles shown on the right side. These wake hot-film measurements were acquired approximately 1.17 chord lengths downstream of the airfoil model. The y-location corresponding to the wake velocity PSD is denoted using an open circle symbol on the wake profile. From Fig. 4.42, it can be observed that the frequency content of the regular mode observed in the airfoil C_p

measurements is consistent with that observed in the wake velocity measurements acquired at the upper-wake edge. This consistency includes both the approximate frequency and bandwidth of the regular mode spectral content. For example, in Fig. 4.42 a), at $\alpha = 5°$ both the airfoil C_p PSD and the U_{wake} PSD contain a broad-band range of increased energy from approximately 50 Hz to 300 Hz. With increased angle of attack, this bandwidth was previously shown in Fig. 4.41 to decrease. As a result, when compared to lower angles of attack, at $\alpha = 7°$ both the airfoil C_p PSD and the U_{wake} PSD in Fig. 4.42 c) contain a more narrow-band spectral peak from approximately 40 Hz to 120 Hz.

4.4.2 Strouhal Scaling

As discussed in Section 2.2.1.1.1, the regular mode reported in the literature consistently corresponds to a Strouhal number (based on mean separation bubble length) within the range from $\mathrm{St}_L = 0.5$ to $\mathrm{St}_L = 0.8$. The Strouhal numbers resulting from the current investigation for the airfoil model with the horn-ice shape are shown in Fig. 4.43 as a function of angle of attack. The frequencies used in calculating St_L were the same frequencies that were denoted in the C_p PSDs at $x/c = 0.85$ in Fig. 4.41. For the post-stall angles of attack included in Fig. 4.43, the central frequencies of the regular mode were estimated using the PSDs of the C_p at $x/c = 0.85$ (not shown) and the separation length was assumed to be the airfoil chord. The average value of Strouhal number across the angle-of-attack range shown in Fig. 4.43 is $\mathrm{St}_L = 0.62$.

As discussed by Gurbacki,[6] downstream of the horn-ice shape on an airfoil the regular mode frequency was observed to tend towards a constant Strouhal number when calculated using the separation bubble length (L_r) and freestream velocity. The same can be seen in Fig. 4.43, where the Strouhal number values tend towards $\mathrm{St}_L = 0.6$. This is particularly true for the angle-of-attack range from $\alpha = 4°$ to $\alpha = 7°$. At angles of attack higher than $\alpha = 7°$, the values of St_L begin increasing with increased angle of attack. The reason for this increase can be attributed to the decrease in frequency of the regular mode with increased downstream distance (until reattachment) that was observed in Fig. 4.40. Since the entire flow is separated across the upper surface for $\alpha \geq 7°$, the C_p measurements at $x/c = 0.85$ were acquired within the separated region for this angle-of-attack range. Since the broad-band frequency peak was observed to occur at a slightly higher frequency inside the separation bubble than downstream of reattachment in Fig. 4.40, it can be expected that the frequencies used in calculating St_L at these higher angles of attack are slightly above the shedding frequencies identified in the C_p measurements at $x/c = 0.85$ at the lower angles of attack.

A comparison of the values of Strouhal number for the regular mode from the current study were also made with values reported in the literature. A summary of this comparison is presented in Table 4.2. From Table 4.2, the values of St_L reported in the current study are consistent with those reported in the literature. Most references cite the regular mode as occurring within the range of $0.5 \leq \mathrm{St}_L \leq 0.8$, which is consistent with the range reported by Mabey.[2] The major outliers of the range include the studies by Spazzini et al.[35] and Heenan and Morrison,[29] who reported Strouhal numbers for the regular mode at $\mathrm{St}_L = 1$. It is possible that this difference in St_L reported by these authors could be a consequence of the method used to analyze the spectral content of the acquired measurements. For instance, Spazzini et al.[35] identified the frequency of the regular mode using the normalized spectra of skin friction energy represented by $fE(f)/\tau'^2_{\mathrm{RMS}}$, where E represents the energy spectra of the skin friction measurement. A similar spectral representation was used by Heenan and Morrison.[29] Since this normalized representation of the energy spectra requires multiplying the energy spectra by the frequency, when using this quantity to determine relevant frequency content the higher frequencies will tend to have more influence in the normalized spectra, leading to bias towards higher values of St_L than those reported elsewhere.

The consistency in values of St_L across the various geometries considered in the comparison in Table 4.2 lends credence to the self-similarity of vortex shedding from separation bubbles. Moreover, it appears as though using L_r as the length scale and U_∞ as the velocity scale is appropriate for non-dimensionalizing the regular mode frequency in the current study.

Table 4.2 Comparison of St_L for regular mode determined in the current study with those reported in the literature for separation bubbles generated about various geometries

Author(s)	Geometry	Re	Regular Mode St_L
Current Study	Airfoil w/ 2D Horn-Ice Shape	$\mathrm{Re}_c = 1.8 \times 10^6$	0.6
Gurbacki[6] (2003)	Airfoil w/ 2D and 3D Horn-Ice Shape	$\mathrm{Re}_c = (1.0 \ldots 1.8) \times 10^6$	0.53–0.73
Mabey[2] (1972)	Various (Review)	—	0.5–0.8
Kiya & Sasaki[30] (1983)	2D Blunt Flat Plate	$\mathrm{Re}_{2H} = 2.6 \times 10^4$	0.6
Cherry et al.[26] (1984)	2D Blunt Flat Plate	$\mathrm{Re}_H = 3.2 \times 10^4$	0.7
Kiya et al.[50] (1997)	Blunt Circular Cylinder (Axisymm)	$\mathrm{Re}_d = (0.69 \ldots 2.76) \times 10^5$	0.46
Hudy et al.[25] (2003)	2D Fence	$\mathrm{Re}_{2H} = 2.56 \times 10^4$	0.6–0.9
Driver et al.[38] (1987)	2D Backward-Facing Step	$\mathrm{Re}_H = 3.7 \times 10^4$	0.6
Heenan & Morrison[29] (1998)	2D Backward-Facing Step	$\mathrm{Re}_H = 1.9 \times 10^5$	1
Lee & Sung[111] (2001)	2D Backward-Facing Step	$\mathrm{Re}_H = 3.3 \times 10^4$	0.48
Spazzini et al.[35] (2001)	2D Backward-Facing Step	$\mathrm{Re}_H = (0.35 \ldots 1.6) \times 10^4$	1
Liu et al.[33] (2005)	2D Backward-Facing Step	$\mathrm{Re}_H = 3.3 \times 10^4$	0.54

4.4.3 Convective Characteristics

Using the method outlined in Section 3.10.2, the phase angle distribution of the regular mode was calculated across the airfoil upper surface. Identifying the phase angle distribution at the frequency of the regular mode is useful, as it provides a representation of the progression of the effects of the regular mode on the airfoil surface C_p, beginning at a reference location. The phase spectrum was calculated using the C_p cross-spectra between locations on the airfoil upper surface. In these calculations, the C_p at the $x/c = 0.03$ location was used as a reference, such that the phase angle spectrum was determined between $x/c = 0.03$ and the location of interest. The resulting distributions of phase angles corresponding to the regular mode are shown in Fig. 4.44 for the NACA 0012 airfoil with the leading-edge horn-ice shape. In Fig. 4.44 the phase angles have been unwrapped in order to account for the discontinuity in the phase angle distribution that would otherwise occur upon a completion of an oscillation cycle (i.e. when $\theta > \pi$). From Fig. 4.44, the phase angle distribution is characterized by a progression of increasing phase with downstream distance. This occurs since the oscillations induced by the regular mode at a given frequency are occurring as they are propagated through the flowfield, and thus, are at a different phase of the oscillation at different locations. Since the phase angle distribution is increasing monotonically with increased distance downstream, this indicates that the regular mode (i.e. progression of vortical motion) moves only in the downstream direction.

From Fig. 4.44 a), it can be observed that the relative phase angle at a fixed location tends to decrease with increasing angle of attack. This decrease in magnitude is caused by the decrease in frequency of the regular mode that occurs with increasing length of the separation bubble as α is increased prior to stall. As the frequency of the regular mode decreases with increased angle of attack, the period of the oscillation increases. As a result, for a fixed convection velocity, as the frequency of the oscillation decreases, the oscillation can be convected from the airfoil leading edge to the trailing edge in a shorter number of cycles, resulting in a reduction in the calculated phase. It can be observed in Fig. 4.44 b), however, that upon full separation of the upper surface flowfield, the phase angle distribution collapses towards a single trend, regardless of an increase in angle of attack. The same trend was also observed for $8° \leq \alpha \leq 9°$ (not shown). Since the frequency of the regular mode reached a consistent value, the collapse of the phase angle distributions in Fig. 4.44 b) can be expected.

The phase angle distributions of Fig. 4.44 were also used to determine the distribution of time lag across the airfoil upper surface associated with the regular mode, which is shown in Fig. 4.45. From Fig. 4.45, it can be seen that even though the phase angle distribution varied with angle of attack, the time lag distributions remained relatively consistent with changing angle of attack. The small variation in the time delay distributions that can be observed for a fixed chordwise location is a general increase in time delay with increased angle of attack for $4° \leq \alpha \leq 7°$ and a decrease in time delay with increased angle of attack for $7° \leq \alpha \leq 9°$.

The time delay distributions in Fig. 4.45 are representative of the average amount of time required for a vortex to pass a given location on the airfoil upper surface. Using the slope of the time delay distributions with respect to distance, the convection velocity of the regular mode could be calculated using the method discussed in Section 3.10.2. This convection velocity of the regular mode thus represents the average convection velocity of the vortical structures in the shear layer and shed vortices from the separation bubble. The resulting vortex convection velocities (U_c) are shown in Fig. 4.46. Also shown in Fig. 4.46 is the vortex velocity relative to freestream velocity (U_c/U_∞). Additionally, when shear-layer reattachment occurred on the airfoil surface (i.e. for $\alpha \leq 6°$), the resulting convection velocities when only considering the time delays upstream or downstream of reattachment are also shown in Fig. 4.46. The only exception to this was for $\alpha = 6°$, as there were an insufficient number of time delay locations downstream of x_r to accurately determine U_c downstream of shear-layer reattachment.

As shown in Fig. 4.46, the convection velocities of the vortical structures inside the separated shear layer remained relatively constant near $U_c/U_\infty = 0.45$. This is evident in Fig. 4.46 for the convection velocities reported across $4° \leq \alpha \leq 6°$ when only the time delays upstream of x_r were considered and for $6.5° \leq \alpha \leq 9°$ when the time delays across the full upper surface were considered since the entire airfoil surface was separated. The convection velocities of the vortices shed from the separation bubble were somewhat higher than the convection velocities of the structures in the shear layer. This can be seen in Fig. 4.46 as the reported values of U_c are higher when only the time delays downstream of x_r are considered. Similar observations were also reported by Gurbacki.[6] As may be expected, the convection velocity of the vortices shed from the separation bubble decreases with increased angle of attack from $4° \leq \alpha \leq 5.5°$. This can be attributed to the effect of the increased adverse pressure gradient imposed with increased α.

The convection velocities shown in Fig. 4.46 are also very similar to those reported in the literature. The vortex convection velocities in the literature generally corresponded to a value between $0.5U_\infty$ to $0.6U_\infty$, and are summarized in Table 4.3. The actual value of U_c reported depended, in part, on the location along the model that U_c was being determined. For example, the results of Heenan and Morrison[29] display convection velocities between $0.4U_\infty$ and $0.5U_\infty$ inside the separation bubble, while downstream of reattachment U_c increases to approximately $0.65U_\infty$. These results are highly consistent with the observations made in the current study. Similarly, the convection velocities downstream of the backward-facing step at the higher frequencies discussed in Farabee and Casarella[28] exhibited a range from approximately $0.4U_\infty$ close to the step to $0.7U_\infty$ far enough downstream of x_r that the flow was assumed to reach equilibrium.

Additionally, Cherry et al.[26] identified an average vortex convection velocity of $0.5U_\infty$ near shear-layer reattachment downstream of a backward-facing step using a correlation analysis of pressure sensors. However, these authors also identified a higher vortex convection speed of $0.63U_\infty$ when analyzing the cross-correlations of the surface pressure near the reattachment location and the hot-wire velocity measurements in the separated shear layer. These authors explained that, for the latter case, these higher velocities resulted as the shear layer velocity measurements were more biased towards larger vortical structures. The same would be said for the vortex convection velocities determined downstream of reattachment in Fig. 4.46, which would correspond to larger vortical structures that have completed the pairing and amalgamation processes. Thus, the higher vortex convection rates downstream of reattachment in Fig. 4.46 are consistent with the values reported in Cherry et al.[26] for the convection speeds of large vortical structures.

Table 4.3 Comparison of vortex U_c determined in the current study with those reported in the literature for separation bubbles generated about various geometries

Author(s)	**Geometry**	**Re**	**Vortex Convection (U_c/U_∞)**
Current Study	Airfoil w/ 2D Horn-Ice Shape	$Re_c = 1.8 \times 10^6$	0.4–0.65
Gurbacki[6] (2003)	Airfoil w/ 2D and 3D Horn-Ice Shape	$Re_c = (1.0 \ldots 1.8) \times 10^6$	0.41–0.67
Kiya & Sasaki[30] (1983)	2D Blunt Flat Plate	$Re_{2H} = 2.6 \times 10^4$	0.5
Cherry et al.[26] (1984)	2D Blunt Flat Plate	$Re_H = 3.2 \times 10^4$	0.5–0.63
Kiya et al.[50] (1997)	Blunt Circular Cylinder (Axisymm)	$Re_d = (0.69 \ldots 2.76) \times 10^5$	0.5
Hudy et al.[25] (2003)	2D Fence	$Re_{2H} = 2.56 \times 10^4$	0.57
Farabee & Casarella[28] (1986)	2D Backward-Facing Step	$Re_H = 2.3 \times 10^4$	0.4–0.7
Heenan & Morrison[29] (1998)	2D Backward-Facing Step	$Re_H = 1.9 \times 10^5$	0.4–0.65
Lee & Sung[111] (2001)	2D Backward-Facing Step	$Re_H = 3.3 \times 10^4$	0.6
Liu et al.[33] (2005)	2D Backward-Facing Step	$Re_H = 3.3 \times 10^4$	0.56

Overall, as observed in Fig. 4.46, the vortex convection velocities inside the separation bubble remained constant with changes in the airfoil angle of attack. Conversely, downstream of the reattachment location, the vortex convection velocity in Fig. 4.46 was greater than the convection velocity inside the separation bubble, which was consistent with the results reported by Heenan and Morrison.[29] Additionally, the convection of the vortices shed from the separation bubble exhibited an angle-of-attack dependence, which resulted from the changes in adverse pressure gradient imposed on the shed vortex with changing angle of attack. These observations of the vortex convection characteristics in the current study are consistent with those reported in the literature. However, rather than reporting a specific value of the vortex convection velocity, which was found to be done in most studies, the vortex convection velocities in the current study are classified across a general range. This provided the opportunity to identify changes in the vortex convection characteristics upstream of reattachment, when changes to the structure were continuing to occur, and downstream of reattachment, where the structure of the vortices was established.

4.4.4 Visualization of Vortex Shedding

In order to aid in the understanding of the physical process of the regular mode, the smoke wire flow visualization results are used to display the presence of vortical motion in the shear layer and vortex shedding from the separated region downstream of the horn-ice shape. Select sequential images from the smoke wire flow visualization video that was acquired at $\alpha = 7°$ is presented in Fig. 4.47. Also in Fig. 4.47 are arrows that are used to mark the location of large-scale vortical structures in the shear-layer and being shed into the airfoil wake. While the vortices themselves are not easily seen in Fig. 4.47, their approximate locations can be identified based on the effect of the vortices on the streamlines adjacent to the separated region.

From Fig. 4.47 a), a shed vortex can be observed near the quarter-chord location on the airfoil. It is likely that this structure is actually a set of vortices that underwent a pairing process prior to and upstream of the location denoted in Fig. 4.47 a). In Fig. 4.47 b) – e), this vortex is convected downstream. As discussed in Section 4.4.3, this vortex convects downstream at a rate near $0.5U_\infty$. By Fig. 4.47 f), the vortex is shed into the wake of the airfoil. Since the regular mode is periodic (across a wide bandwidth), in Fig. 4.47 g) another vortex has formed in the shear layer, which will later be convected downstream and shed into the airfoil wake.

4.5 Shear-Layer Flapping

As discussed in Section 2.2.1.1.2, the shear-layer flapping phenomenon is a low-frequency source of unsteadiness associated with separation bubbles that is characterized by a vertical "flapping" motion of the shear layer and a streamwise oscillation of the shear-layer reattachment location. This phenomenon is thought to be inherent to separation bubbles and is typically studied in the flows about various canonical geometries associated with separation bubbles. In this section, the frequency content of shear-layer flapping will be identified and the resulting Strouhal numbers will be compared to those reported in the literature. Additionally, the convective characteristics will be described and compared to observations from studies of flowfields about simple geometries. Finally, a representation of shear-layer flapping in the smoke-flow visualization results will be presented.

4.5.1 Frequency Scales of Shear-Layer Flapping

As described in the literature (see Section 2.2.1.1.2), shear-layer flapping is typically observed at very low frequencies, when compared to the characteristic frequencies of most other flow phenomena. Results from multiple studies in the literature have identified that shear-layer flapping is most prevalent in the leading-edge section of a separation bubble, with little to no discernibility downstream of the mean shear-layer reattachment location.[25,26,29,35] This was, perhaps, best exhibited by Heenan and Morrison.[29] These authors were able to suppress shear-layer flapping downstream of a backward-facing step by using permeable reattachment surface. Upon comparing the pressure spectra of the impermeable and permeable walls, the low-frequency peak that is clearly discernible for the impermeable wall case near the step is no longer visible for the permeable case, leading to a different distribution of dominant frequency content at this location. However, downstream of the mean shear-layer reattachment location, the pressure spectra of the impermeable and permeable wall cases are essentially identical, indicating that the shear-layer flapping that existed for the impermeable wall case did not play a significant role downstream of shear-layer reattachment.

Recalling the C_p PSDs from Fig. 4.35 and Fig. 4.36, two frequency peaks were identified across the low-frequency range (i.e. ≤ 40 Hz). However, in the spectral content of the upstream portion of the separation bubble, an example of which is shown in Fig. 4.36 a), the energy in the C_p signal is dominated by a single low-frequency peak. The center frequency of this peak changed with increasing angle of attack, but was typically observed in the frequency range between 40 Hz and 20 Hz. The presence of such a low-frequency peak can be seen in Fig. 4.48, where the C_p PSDs of the airfoil with the horn-ice shape at $\alpha = 5°$ are shown for the chordwise region covered by the separation bubble. From Fig. 4.48, the effects of shear-layer flapping are visible in the PSDs corresponding to $x/c = 0.03$ and $x/c = 0.105$ at a frequency of 26.8 Hz. Farther downstream in the separation bubble, at $x/c = 0.21$ and $x/c = 0.32$, the effects of the shear-layer flapping mode diminish and are not identifiable at $f = 26.8$ Hz. However, at $x/c = 0.45$, which is very close to the mean shear-layer reattachment location, the effects of shear-layer flapping are again visible at $f = 26.8$ Hz. This reoccurrence of the shear-layer flapping mode can be attributed to the streamwise low-frequency movement of the shear-layer reattachment location induced by the flapping motion. This is consistent with the observations of Heenan and Morrison,[29] where the maximum amplitude of the shear-layer flapping mode was identified at the location corresponding to $x = 0.75x_r$. Downstream of the separation bubble, at $x/c = 0.55$, the effects of the shear-layer flapping mode have substantially diminished.

An example of the shear-layer flapping mode in the airfoil C_p PSDs at $x/c = 0.07$ is also shown in Fig. 4.49 with the estimated center frequency of the peak denoted by a vertical dashed line. This center frequency was estimated by applying a median average filter to smooth the PSDs, applying a local quadratic polynomial fit to sections of a PSD and identifying the frequency with which the maximum amplitude is reached. From Fig. 4.49, the center frequency of the shear-layer flapping mode tended to decrease with increased angle of attack up to $\alpha = 7°$, and the amplitude of the shear-layer flapping peak tended to increase up to stall. For angles of attack higher than $\alpha = 7.5°$ (not shown), the low-frequency range was replaced by a wide-band distribution of high energy levels, and a distinct peak for the shear-layer flapping mode was no longer identifiable.

The effects of the shear-layer flapping phenomenon on the iced-airfoil wake velocities of the airfoil could also be observed downstream of the airfoil upper surface. As the separation bubble underwent a quasi-periodic surface-normal flapping, the streamlines just above the separation bubble would be forced to oscillate with the flapping motion. This motion would then cause the streamlines to sweep across the hot-film probe in the wake downstream of the separation bubble according to the flapping frequency. An example of this is presented in Fig. 4.50, showing the resulting wake velocity spectra along with the corresponding C_p spectra in the upstream portion of the separation bubble. From Fig. 4.50, the center frequencies of the peaks for shear-layer flapping are consistent between the airfoil C_p PSDs and the U_{wake} PSDs. Since the shear-layer flapping phenomenon has been observed to affect the entire separation bubble, its effects in the wake could be seen across the entire upper-surface wake deficit region.

4.5.2 Strouhal Scaling

As discussed in Section 2.2.1.1.2, most results from the literature identify the effects of shear-layer flapping as occurring at a Strouhal number on the order of $\mathrm{St}_h = 0.02$ or $\mathrm{St}_L = 0.1$. It remains unclear which length scale is more appropriate for classifying the Strouhal number, though the projected height length scale will be used for non-dimensionalizing the shear-layer flapping frequency in this investigation. It should be noted that even though the projected height of the airfoil was used in the current study to calculate the Strouhal number of the shear-layer flapping mode, the St_L values obtained in the current study still compare reasonably well with those also reported in the literature. The projected height of the airfoil was also preferred as a length scale over the feature height of the ice shape. This was due in large part to the observations of Hudy et al.,[25] where the Strouhal numbers for shear-layer flapping favorably compared to other results from the literature when the total fence height ($2H$) was used as the relevant length scale, rather than the step height of the fence (h_f). Additionally, by inspecting the low-frequency content of the airfoil with various-sized quarter-round geometries at $x/c = 0.02$ (not shown), the center frequency of shear-layer flapping did not appear to scale directly with a change in the feature height of the quarter round.

The resulting values of St_h corresponding to the shear-layer flapping mode that were obtained in the current investigation are shown in Fig. 4.51. These values were calculated using the central frequencies of the shear-layer flapping mode labeled in Fig. 4.49. From Fig. 4.51, using the projected height of the airfoil as the characteristic length scale of shear-layer flapping, the resulting Strouhal numbers tend towards a constant value of approximately $\mathrm{St}_h = 0.0185$. Interestingly, there does not appear to be an angle-of-attack dependence on St_h in Fig. 4.51, which might be expected since a change in airfoil angle of attack is accompanied with a change in the pressure gradient imposed. This suggests that the frequency of the shear-layer flapping mode is scaled based on a characteristic vertical length of the body bounding the separation bubble, or that the effects of the changing adverse pressure gradient with increased angle of attack are effectively represented by the change in airfoil projected height.

The values of Strouhal numbers of the shear-layer flapping mode were compared with those reported in the literature. A summary of this comparison is presented in Table 4.4. It should be noted that Zaman and Potapczuk[63] defined the iced-airfoil angle of attack differently than the current study. As a result, the angle of attack and St_h reported by these authors have been adapted to fit the definitions of the current study. From Table 4.4, the values of St_h for shear-layer flapping obtained in the current study are consistent with the range of values reported in the literature. This suggests that the low-frequency peak that was identified in the current study with central frequency between 40 Hz and 20 Hz can be attributed to the same shear-layer flapping mechanism observed in separation bubble flowfields about simple geometries.

The values of St_h from the current study are also in agreement with the results by Bragg et al.[21] and the experimental results reported in Zaman and Potapczuk,[63] as shown in

Table 4.4. However, it is important to clarify why certain other studies on unsteadiness in clean or iced airfoil flows are not included in Table 4.4. While certain other studies reported the presence of low-frequency modes in an airfoil flowfield, it is unlikely that these low-frequency modes were a direct effect of shear-layer flapping. This presumption was made mainly due to the fact that the Strouhal numbers for these low-frequency modes reported in these studies are less than half of what might be expected from the studies reported on flows about simple geometries. Indeed, this inconsistency was discussed by Gurbacki,[6] as the Strouhal numbers of a low-frequency mode in the flowfield of an iced airfoil were inconsistent with those reported for shear-layer flapping in flowfields about simple geometries, despite attempting numerous alternative scaling factors. As a result, while it is unlikely that the low-frequency mode identified in these studies was shear-layer flapping, it could have easily been due to an instability that was introduced to the flowfield as a result of shear-layer flapping indirectly. Additional discussion and characterization of this low-frequency mode will be made in Section 4.6.

It is also conjectured that the oscillations occurring in the current study with $St_h = 0.0185$ are likely due to shear-layer flapping for numerous reasons. In addition to having a Strouhal number that is consistent with the literature, the characteristics of this mode of unsteadiness in the flowfield are consistent with those attributed to shear-layer flapping in the literature. For example, as discussed in Section 4.5.1, the upstream portion of a separation bubble has been commonly reported as being the location where shear-layer flapping is most dominant in the spectral content of acquired measurements. Since the same unsteady mode frequency was identified in the hot-film wake measurements downstream of the iced-airfoil upper surface, it is likely that this same shear-layer flapping mode could be identified in similar measurements reported in the literature. This is the case for the results reported by Bragg et al.[21] and in the experimental results portion of Zaman and Potapczuk.[63] Both studies identified a mode of unsteadiness at a low frequency in the spectral content of hot-wire measurements taken downstream of the separation bubble produced by a simulated leading-edge ice shape. Due to the similarity in the quantities being measured and the consistency in St_h values reported, it is likely that the unsteady modes observed by Bragg et al.[21] and reported in the experimental portion of Zaman and Potapczuk[63] are representative of the same shear-layer flapping mode reported in the current study. For this reason, results from these studies are included in Table 4.4.

Table 4.4 Comparison of St_h of shear-layer flapping determined in the current study with those reported in the literature for separation bubbles generated about various geometries

Author(s)	Geometry	Re	Shear-Layer Flapping St_h
Current Study	Airfoil w/ 2D Horn-Ice Shape	$Re_c = 1.8 \times 10^6$	0.0185
Zaman & Potapczuk[63] [Experimental Results] (1989)	Airfoil w/ 2D Glaze Ice	$Re_c = (0.75\ldots1.25) \times 10^5$	0.0153
Bragg et al.[21] (1992)	Airfoil w/ 2D Glaze Ice	$Re_c = 1.5 \times 10^6$	0.0185
Kiya & Sasaki[30] (1983)	2D Blunt Flat Plate	$Re_{2H} = 2.6 \times 10^4$	0.012
Cherry et al.[26] (1984)	2D Blunt Flat Plate	$Re_H = 3.2 \times 10^4$	< 0.025
Hudy et al.[25] (2003)	2D Fence	$Re_{2H} = 2.56 \times 10^4$	0.02
Driver et al.[38] (1987)	2D Backward-Facing Step	$Re_H = 3.7 \times 10^4$	0.033
Heenan & Morrison[29] (1998)	2D Backward-Facing Step	$Re_H = 1.9 \times 10^5$	0.018
Spazzini et al.[35] (2001)	2D Backward-Facing Step	$Re_H = (0.35\ldots1.6) \times 10^4$	0.014–0.018
Lee & Sung[32] (2002)	2D Backward-Facing Step	$Re_H = 3.3 \times 10^4$	0.015
Chun et al.[27] (2004)	2D Backward-Facing Step	$Re_H = 3.3 \times 10^4$	0.025
Liu et al.[33] (2005)	2D Backward-Facing Step	$Re_H = 3.3 \times 10^4$	0.02

4.5.3 Phase Angle Characteristics

In order to further aid in the comparison with the literature, the phase angle distribution characteristics of the shear-layer flapping mode were determined using the methods discussed in Section 3.10.2. Like in Section 4.4.3, the C_p at the $x/c = 0.03$ location on the upper surface was used as the reference for determining the phase angle distributions. The phase angle distributions of the shear-layer flapping mode are shown in Fig. 4.52 for airfoil with the leading-edge horn-ice shape across the angle-of-attack range from $\alpha = 5°$ to $\alpha = 7°$. From Fig. 4.52 a), the phase angle distribution is characterized by a region of decreasing phase angle with downstream distance near the airfoil leading edge, which is indicative of an upstream convection of the shear-layer flapping mode in this region. Further downstream, an increase in phase angle is encountered, transitioning to a positive downstream progression of the phase angle across the aft portion of the airfoil, as evident by the increase in phase angle with downstream distance across this region.

The phase angle distributions are also presented in Fig. 4.52 b) with respect to the chordwise direction, normalized by the mean shear-layer reattachment location. As shown in Fig. 4.52 b), the location at which the slope in phase angle transitions from negative to positive corresponds to approximately 30% of the length of the separation bubble (or, in the case of a fully-separated upper surface, 30% of the airfoil chord). Also from Fig. 4.52 b), the phase distribution appears to be consistent across the length of the separation bubble between the angles of attack presented. This indicates that, while the frequency of the regular mode changes with angle of attack, the progression of the shear-layer flapping mode exhibits a phase angle distribution of the oscillation that is characteristic of the separation bubble region. In fact, at the location of shear-layer reattachment ($(x - x_r)/x_r = 0$), the phase angle distribution for all angles of attack tend toward a value of π, with the exception of $\alpha = 6.5°$ and $\alpha = 7°$ where shear-layer reattachment does not occur on the airfoil. This phase angle of π would correspond to one half of a full oscillation cycle of the shear-layer flapping mode. This can also be seen in the results of Hudy et al.,[25] though these authors did not comment on this observation.

The phase angle distribution in Fig. 4.52 bears a semblance to the phase angle distribution for shear-layer flapping presented by Hudy et al.[25] in several other ways as well. In order to aid in this comparison, the phase angle distribution from Hudy et al.[25] is also included in Fig. 4.52 b). For example, both studies present a negative slope in phase angle in the leading-edge portion of the separation bubble, which transitions to a positive slope between $(x - x_r)/x_r = -0.7$ to $(x - x_r)/x_r = -0.6$ ($0.3x_r$ to $0.4x_r$). For the lower angles of attack included in Fig. 4.52 (e.g. $\alpha = 5°$), the change in phase angle slope from negative to positive occurs more gradually than for the higher angles of attack (e.g. $\alpha = 7°$). Rather than observing a continuous increase in phase angle associated with this slope change, Hudy et al.[25] observed a discontinuous increase in phase angle by a factor of π near $x = 0.5x_r$, which can be seen in Fig. 4.52 b). These authors related this sudden increase in phase distribution to the standing-wave character of the shear-layer flapping mode.

Indeed, by considering the shear-layer flapping mode as a standing wave, the slight difference in location of the phase increase of π (and the slope change of the phase angle between the upstream and downstream portions of the separation bubble) between the current study and Hudy et al.[25] can be described by the difference in pressure distribution of the geometries. For example, the normalized pressure coefficient (C_p*) distribution was calculated for the angle-of-attack range included in Fig. 4.52 using the relation,

$$C_p{}^* = \frac{C_p - C_{p,\min}}{1 - C_{p,\min}} \tag{4.1}$$

where $C_{p,\min}$ represents the minimum pressure coefficient inside the separation bubble. A comparison was then made of the resulting normalized pressure coefficient distributions from the current study and Hudy et al.,[25] as shown in Fig. 4.53.

As described by Hudy et al.,[25] the change in phase angle by π would be expected to occur at the location of $C_p^* = 0$. If, for example, the separation bubble were to elongate due to the effects of shear-layer flapping, the pressure upstream of the $C_p^* = 0$ location would tend to increase, and the pressure downstream of $C_p^* = 0$ would tend to decrease. The opposite would be true if the separation bubble was shrinking. Since the effects of shear-layer flapping on the surface pressure would have opposite sign across the location of $C_p^* = 0$, it can be expected that this would be accompanied with a shift in phase by a factor of π. Since the location of $C_p^* = 0$ in the current study is slightly further upstream in the separation bubble from that of Hudy et al.,[25] the change in slope of the phase angle distribution changes from negative to positive slightly farther upstream in the current study, as evident in Fig. 4.52.

While the time delay distributions could be calculated from the phase angle distributions in Fig. 4.52, they are not shown here. Due to the reversal in convection direction of the shear-layer flapping mode near $x/x_r = 0.35$, the convection velocity of the shear-layer flapping mode could not be reliably determined using only a select few locations in a least-squares fit of the phase angle distribution upstream or downstream of $x/x_r = 0.35$.

4.5.4 Visualization of Shear-Layer Flapping

In order to provide a visible representation of shear-layer flapping in the iced-airfoil flowfield, results from the fog generator smoke flow visualizations are presented in Fig. 4.54. In Fig. 4.54, the estimated edge of the separation region is indicated by a blue line, which traced the upper edge of the smoke entrained into the separation region. The visualization results from the fog generator were used over the smoke wire, as the fog generator method was able to produce a greater amount of smoke that was entrained into the separation region. Observing the smoke inside the separation region allowed the separation boundary to be more clearly identified than from the streamlines in the flowfield produced by the smoke wire technique.

Starting in Fig. 4.54 a), the shear-layer flapping mode is in the enlarged state, where the vertical displacement of the shear layer is farthest from the surface. Next, a large-scale shedding event occurs and the separated shear layer begins to move towards the surface. This is visible in

Fig. 4.54 b), where the large-scale separation can be seen over the trailing-edge portion of the airfoil. Such a large-scale bubble shedding event was described by Kiya and Sasaki[30] as being characteristic of shear-layer flapping. However, a distinction should be made that this large-scale shedding event is not the same as the large-scale vortex shedding behavior of the regular mode. The separated shear layer continues to move towards the surface of the airfoil in Fig. 4.54 c). Next, the separation region begins to increase again in size, and the separated shear layer begins to move away from the airfoil surface. This is visible in Fig. 4.54 d) – f). After the shear layer reaches its maximum displacement from the surface of the airfoil (shown in Fig. 4.54 f)), it again undergoes a large-scale ejection of the separation region, which can be seen in Fig. 4.54 g). After this event, the separated shear layer again begins moving towards the airfoil surface, as shown in Fig. 4.54 h).

By estimating the frequency of the shear-layer flapping mode in the smoke flow visualization results in Fig. 4.54 it can be seen that the frequency of this oscillation is consistent with the shear-layer flapping mode identified in the surface pressure and wake measurements. For example, one full cycle of the shear-layer flapping mode was imaged across a period of 0.167 seconds (i.e. Fig. 4.54 a) – f)). This corresponds to a frequency of 6 Hz. Since the fog generator smoke flow visualization was conducted at $Re = 0.5 \times 10^6$, it can be expected that the frequency of the oscillation identified in the flow visualization will be lower than those observed in the measurements acquired at $Re = 1.8 \times 10^6$. By directly scaling the 6 Hz frequency with velocity from $Re = 0.5 \times 10^6$ to $Re = 1.8 \times 10^6$, the expected frequency at the higher Reynolds number would be 21.6 Hz. This frequency is consistent with the frequency peak of the shear-layer flapping mode identified in Fig. 4.49. As a result, it is likely that the oscillation observed in the flow visualization results in Fig. 4.54 at $Re = 0.5 \times 10^6$ is the same shear-layer flapping oscillation that was identified in the measurements about the airfoil surface pressure and upper surface wake velocity at $Re = 1.8 \times 10^6$.

4.6 Low-Frequency Mode

The final source of unsteadiness that will be discussed that can appear in an iced-airfoil flowfield is a low-frequency mode characterized by an oscillation of the global airfoil flowfield. As discussed in Section 2.2.2.1, this low-frequency mode has also been observed in the flowfields about certain clean airfoils prior to stall. These oscillations are typically associated with airfoils that exhibit a thin-airfoil stall type or a combination thin-airfoil and trailing-edge stall type. The oscillation is thought to be a result of a self-sustained stalling and unstalling of the airfoil due to the bursting and reformation of the leading-edge separation bubble.[61] In this section, the frequency scales of the low-frequency mode in the measurements of the current study will be identified. Using these frequency scales, the resulting Strouhal numbers will be compared to those found in the literature. A brief overview of the convective characteristics of this mode will also be discussed, and a physical representation of the low-frequency mode will be presented in the flow visualization results.

4.6.1 Frequency Scales of Low-Frequency Mode

As discussed by Zaman et al.,[56] the unsteady forces that are produced on the airfoil due to this low-frequency mode can be quite large. For this reason, the low-frequency mode has been readily identified in the airfoil lift coefficient measurements reported in the literature.[56,58,61] Again recalling the C_p PSDs from Fig. 4.35 and Fig. 4.36, there were two frequency peaks identified across the low-frequency range of $f \leq 40$ Hz. While the frequency peak occurring between the range of 20 Hz and 40 Hz was identified as being associated with shear-layer flapping, it is believed that the other low-frequency peak, having center frequency near 10 Hz, is associated with the low-frequency mode.

In order to better observe the effects of the low-frequency mode, the PSDs of the unsteady airfoil performance coefficients are presented in Fig. 4.55 and Fig. 4.56 across the angle-of-attack range near stall. From Fig. 4.55, a low-frequency peak in the airfoil performance PSDs can be observed with a center frequency near 10 Hz for $5° \leq \alpha \leq 7°$. The center frequency of this low-frequency peak does not appear to change significantly with changing angle of attack, though the amplitude of the peak is observed to increase with increasing angle of attack until static stall. While this low-frequency peak is most pronounced in the C_l PSDs in Fig. 4.55 a), it can also be clearly seen in the C_m and C_h PSDs in Fig. 4.55 b) and c), respectively. In addition, the effects of shear-layer flapping can also be observed in the C_m and C_h PSDs in Fig. 4.55 b) and c), as evident by the peaks within the frequency range between 20 Hz and 40 Hz. The center frequencies of these shear-layer flapping peaks are the same as those reported in Section 4.5.1.

As the angle of attack is increased beyond static stall, the peak associated with the low-frequency mode becomes suppressed. This can be seen in Fig. 4.56, where the peak of the low-frequency mode becomes increasingly obscured with increased angle of attack past static stall. Instead, in the airfoil C_l the low-frequency peaks identified in the PSDs in Fig. 4.56 a) are replaced by a general distribution of high-amplitude content across $f \leq 10$ Hz. This was also discussed by Broeren,[58] where the breakdown of the low-frequency peak was consistently observed near the stalling angle of attack for an airfoil. The PSDs of C_m and C_h also exhibit a smoothing of the low-frequency peak, along with a decrease in amplitude of the low-frequency content, for angles of attack above static stall. Since the low-frequency mode has been thought to be related to a quasi-periodic stalling and unstalling of the airfoil, it can be expected that the low-frequency mode will cease occurring with such structured periodicity after static stall.

The peak detection routine discussed in Section 4.5.1, which was used to estimate the center frequency of the shear-layer flapping mode, was also used on the PSDs of the airfoil performance coefficients in order to estimate the center frequency of the low-frequency mode. The resulting frequencies are tabulated in Table 4.5 for each of the three airfoil performance coefficients for the angle-of-attack range from $\alpha = 4.5°$ to $\alpha = 7.5°$. Also in Table 4.5 is the average frequency between these performance coefficients. From Table 4.5, the central frequencies identified from the airfoil performance PSDs were consistent between performance coefficients at most angles of attack. The only exception to this is $\alpha = 5.5°$, where the central frequency extracted from the C_l PSD was approximately 1.3 Hz higher than those extracted from C_m and C_h. As in Table 4.5, and discussed previously, the central frequency of the peak for the low-frequency mode was not observed to change significantly with changing angle of attack. While the central frequency of the shear-layer flapping mode was observed in Section 4.5.1 to occur across the frequency range from $f = 20$ Hz to $f = 40$ Hz, it can be observed here that the shear-layer flapping frequency peak cannot simply be a harmonic of the peak of the low-frequency mode. Rather, the frequencies of these modes of unsteadiness appear to be linearly independent from one-another, though more complex (i.e. nonlinear) interactions or dependence between these modes may exist.

Table 4.5 Central frequencies of low-frequency mode peaks in airfoil performance coefficient PSDs and average value

α	C_l Freq (Hz)	C_m Freq (Hz)	C_h Freq(Hz)	Avg Freq (Hz)
4.5°	9.61	9.90	9.83	9.78
5°	9.39	9.30	9.39	9.36
5.5°	9.00	7.59	7.79	8.13
6°	8.61	7.89	8.10	8.20
6.5°	8.49	8.79	8.79	8.69
7°	9.69	9.69	9.60	9.66
7.5°	9.90	10.11	9.84	9.95

Since the low-frequency mode has a global effect on the entire airfoil flowfield, it can be expected that its effects could be observed in the flowfield off of the airfoil body as well. Indeed, the low-frequency mode was observed in off-surface measurements reported in the literature. For example, the low-frequency mode was identified in hot-wire measurements taken in the flowfield of a clean LRN(1)-1007 by Zaman et al.[56] and Bragg et al.,[5,55] and was also captured in the LDV measurements of Broeren and Bragg.[57] Similarly, the low-frequency mode was shown to have a global effect in the LES results of Almutairi and AlQadi,[61] even into the outer potential flow region away from the airfoil surface. These authors identified that the low-frequency oscillation had an unsteady effect on the circulation about the entire airfoil. Due to this global effect, in the current investigation the low-frequency mode was identified in the hot-film measurements acquired in the region outside of the airfoil wake downstream of the airfoil model. An example of this is shown in Fig. 4.57.

From Fig. 4.57, a low-frequency peak on the order of 10 Hz is visible in both the C_l PSDs and the U PSDs with a consistent center frequency. While in Fig. 4.57 the PSDs for U were calculated using the hot-film measurements acquired below the wake of the lower surface, it should also be noted that similar peaks were also identified in the PSDs of U from the hot-film measurements acquired above the upper surface wake. However, the PSDs of U acquired in the lower surface wake tail were accompanied with a slightly lower noise floor across the low-frequency range, which is why they are shown here.

While the low-frequency mode can be identified in the flow velocity outside of the airfoil wake in Fig. 4.57, it should be noted that it is not observed in the wake velocity PSDs downstream of the airfoil upper surface in Fig. 4.50. However, by comparing the amplitudes of the PSDs in Fig. 4.57 and Fig. 4.50, it can be seen that the amplitudes in the wake of the airfoil are much greater in magnitude than those in the freestream, outside of the airfoil wake. As a result, the low-frequency mode is not observed in the airfoil wake, as the other modes of unsteadiness were dominant over the low-frequency mode within the viscous-dominated wake region. In contrast, the low-frequency mode is identified in the potential flow region outside of the airfoil wake, making it much easier to identify the low-frequency mode within this region. Similarly, the shear-layer flapping mode that was identified in the upper surface wake of the iced airfoil in Fig. 4.50 is not observed in the flow velocity PSDs outside of the wake in Fig. 4.57. This indicates that the effect of the shear-layer flapping mode on the airfoil wake is constrained within the region downstream of the airfoil upper surface, and the effects do not permeate out of the viscous-dominated wake region into the inviscid, outer potential flow region.

It should be stressed that this low-frequency mode is not attributed to any structural modes of the airfoil model installation, nor is it due to any instabilities induced by the wind tunnel fan. The frequencies of the structural modes and fan blade passing were discussed in Section 3.7, and were identified as occurring at frequencies much higher than those observed for the low-frequency mode. Additionally, by inspecting the PSDs of C_l and U at a lower angle of attack than those shown in Fig. 4.55 and Fig. 4.57, it was observed that the low-frequency mode was not present in these measurements. An example of this is shown in Fig. 4.58 for the PSDs of C_l at $\alpha = 3°$ and U outside of the airfoil wake at $\alpha = 0°$. These two cases were selected, as they represented the lowest angles of attack at which a large numbers of samples were acquired for the corresponding measurements. From Fig. 4.58, there are no identifiable frequency peaks in the low-frequency ranges of the PSDs. It would be expected that if the low-frequency mode were instead caused by a structural mode or wind tunnel fan instability, it would also manifest at these lower angles of attack.

Furthermore, it is not believed that this low-frequency phenomenon was produced artificially by the wind tunnel environment. Since this phenomenon has also been observed in computational results of the near-stall flowfield for an airfoil exhibiting a thin-airfoil stall type (e.g. Almutairi and AlQadi,[61] Sandham[62]), and similar results for the low-frequency mode were produced without wind tunnel wall boundary conditions

4.6.2 Strouhal Scaling

Since the Strouhal number of the low-frequency mode has typically been calculated in the literature using the projected airfoil height as the characteristic length scale and the freestream velocity as the characteristic velocity scale, the same non-dimensionalization will be utilized in the current study. The values of St_h obtained using the center frequencies of the low-frequency mode shown in Table 4.5 are presented in Fig. 4.59. Since the center frequencies in Table 4.5 were so consistent between the airfoil performance coefficients, the resulting values of St_h are also consistent between performance coefficients in Fig. 4.59. From Fig. 4.59, the values of St_h obtained in the current study ranged from approximately 0.005 to 0.010. As well, the values of St_h in Fig. 4.59 exhibit a clear angle-of-attack dependence, as the value of St_h appears to increase with increasing α. Such a behavior was also discussed in length by various authors in the literature.[5,6,58,112] Across the angle-of-attack range from $\alpha = 5.5°$ to $\alpha = 7.5°$, this increase in St_h appears to progress linearly with respect to α. It is worth noting that due to the dependence of St_h on angle of attack, it is possible that there is a more appropriate characteristic length scale or characteristic velocity scale that could more effectively characterize the low-frequency mode, as was also suggested by Gurbacki.[6]

In order to provide a comparison of the low-frequency mode Strouhal numbers obtained in the current study to the literature, the St_h values reported from several investigations on low-frequency oscillations about clean and iced airfoils are presented in Fig. 4.60, along with the St_h values calculated using the average in the frequencies between performance coefficients from Table 4.5. In Fig. 4.60, the authors and geometry corresponding to each study are referenced in the legend. As noted in Section 4.5.2, the values of α and St_h from Zaman and Potapczuk[63] have been adapted to fit the definition of α of the current study. From Fig. 4.60, the St_h values for the low-frequency mode reported in the current study fall within a range that is consistent with those reported in the literature. Since the Strouhal number of the low-frequency mode was observed to increase with respect to α, the values of St_h from the current study are significantly lower than some of those reported for clean airfoils at much higher angles of attack. However, the values of St_h from the current study are in agreement with results from other studies performed on an NACA 0012 with a leading-edge ice shape across a similar angle-of-attack range. Furthermore, the results from the current study are within the range of St_h that would be expected from an extrapolation of the results reported for clean airfoils to a lower angle-of-attack range.

A few clarifications should also be made about the comparison to the other studies that were conducted about an iced NACA 0012 airfoil. As discussed in Section 4.5.2, the results of Bragg et al.[21] and the experimental results reported by Zaman and Potapczuk[63] were likely the product of shear-layer flapping. Conversely, the results of Gurbacki[6] and the computational results reported by Zaman and Potapczuk[63] identified low-frequency peaks in spectral content of the lift coefficient of an iced airfoil, which would be representative of an oscillation of the global airfoil flowfield and airfoil circulation. Since similar oscillations of the airfoil performance coefficients were identified in the current study, and due to the favorable comparison of the values of St_h reported in these studies to those of the low-frequency mode reported elsewhere, it is likely that the oscillations observed by Gurbacki[6] and in the computational results of Zaman and Potapczuk[63] were due to a similar low-frequency mode. Additionally, these authors made comparisons to clean-airfoil low-frequency oscillations, similar to what is presented in Fig. 4.60.

4.6.3 Convective Characteristics

Using the same method that was used in Sections 4.4.3 and 4.5.3 to analyze the C_p phase angle distributions at the regular mode and the shear-layer flapping mode, respectively, the relative phase progression of the low-frequency mode across the airfoil upper surface was also studied. The resulting phase angle distributions of the low-frequency mode are presented in Fig. 4.61. Like for the shear-layer flapping case, the phase angle distribution of the low-frequency mode is presented as a function of chordwise location in Fig. 4.61 a), as well as the x-location normalized by the time-averaged reattachment location in Fig. 4.61 b). From Fig. 4.61 a), the phase angle of the low-frequency mode appears to progress across the airfoil upper surface in a nonlinear fashion. Also, the phase angle distribution appears to vary significantly with angle of attack. For example, at a fixed chordwise location downstream of $x/c = 0.20$, the phase angle appears to decrease with increasing angle of attack.

However, upon normalizing the x-location in the phase angle distribution by the time-averaged reattachment location, the angle-of-attack dependence of the phase angle distribution is eliminated. This can be seen in Fig. 4.61 b), where the phase angle distributions for all of the included angles of attack collapse towards a single trend. This trend includes the nonlinear progression of the phase angle across the airfoil upper surface that was observed in Fig. 4.61 a). As such, the phase angle distributions in Fig. 4.61 b) appear to have a different slope in region upstream of $x = 0.5x_r$ than the region downstream of $x = 0.5x_r$. A similar trend was observed by Gurbacki,[6] where a distinct difference in slope of the phase angle distribution and resulting convection velocity was identified between a "forward" and "aft" portion of the airfoil upper surface.

The phase angle of the low-frequency mode was also observed in Fig. 4.61 b) to tend towards π at $x = x_r$ across the various angles of attack included in Fig. 4.61. A similar trend was identified for the shear-layer flapping mode in Section 4.5.3. Also in Fig. 4.61 b), a negligible change in phase angle appears to occur across the region upstream of $x = 0.20x_r$. This indicates that across this region, the absolute phases of the oscillations in pressure at the low-frequency mode were all the same. It should be noted that this was not an artifact of using incomparable signals during processing, as high levels of coherence were observed between C_p measurements at the low-frequency mode. This region of the separation bubble was upstream of the minimum pressure location in the separation bubble (i.e. $C_p^* = 0$) shown in Fig. 4.53, and was associated with a favorable pressure gradient. An additional description of the phase and convective properties of the low-frequency mode will be presented in Section 4.8.4.

Using the phase angle distributions in Fig. 4.61, the time delay distributions of the low-frequency mode were also calculated. The resulting time delay distributions are presented in Fig. 4.62. From Fig. 4.62 a), the same trends that were observed in the phase angle distribution in Fig. 4.61 a) are also observed in Fig. 4.62 a). When observing the time delay distributions as a function with the x-location normalized by the time-averaged reattachment location, a similar trend of a difference in slope in time delay across $x = 0.5x_r$ can be observed, as was seen in Fig. 4.61 b). However, as the angle of attack is increased from $\alpha = 5°$ to $\alpha = 7.5°$, this difference in slope across the $x = 0.5x_r$ location appears to decrease. As a result, at $\alpha = 7.5°$ the time delay distribution progresses more linearly across the entire airfoil upper surface than it did at $\alpha = 5°$.

With this difference in slope in the time delay distributions across $x = 0.5x_r$ in mind, the convection velocity of the low-frequency mode can be calculated in various regions across the airfoil upper surface. The resulting average convection velocities across the upper-surface region downstream of $0.2x_r$, as well as upstream and downstream of $x = 0.5x_r$ are presented in Fig. 4.63. It should be noted that the velocities in Fig. 4.63 were calculated using only the C_p locations downstream of $x/c = 0.20$. From Fig. 4.63, the average convection velocity across the upper surface upstream of $x = 0.5x_r$ appears to be slower than that downstream of $x = 0.5x_r$. The difference in average convection velocity across $x = 0.5x_r$, however, appears to be reduced with increasing angle of attack, up to $\alpha = 7.5°$. This is due to the slopes of the time delay distribution upstream and downstream of $x = 0.5x_r$ becoming more consistent at higher angles of attack, as discussed earlier. Additionally, the average convection velocity across the upper surface tended to decrease from $\alpha = 5°$ to $\alpha = 6°$, but remained constant for $\alpha \geq 6°$.

Gurbacki[6] reported a range of convection velocities for the low-frequency mode, ranging from $0.04U_\infty$ to $0.24U_\infty$. A range of convection velocities was provided, as the convection velocity of the low-frequency mode was observed to vary depending on airfoil angle of attack and location on the airfoil upper surface. The range of convection velocities in Fig. 4.63 are similar, ranging from $0.02U_\infty$ to $0.18U_\infty$. Additionally, Gurbacki[6] identified that the low-frequency convection velocities in the forward region (i.e. upstream) of the airfoil were consistently lower than the convection velocities in the aft region (i.e. downstream) of the airfoil. The same trend can be identified in the low-frequency convection velocities reported in the current study in Fig. 4.63. Finally, the average convection velocity of the low-frequency mode reported by Gurbacki[6] corresponded to $0.10U_\infty$. Similarly, the overall average convection velocity of the low-frequency mode for the current study was $0.11U_\infty$.

4.6.4 Visualization of the Low-Frequency Mode

Evidence of the low-frequency mode was identified in the smoke wire flow visualization that was performed on the iced NACA 0012 airfoil model. Since the low-frequency mode represented an oscillation about the total airfoil circulation, its effects could be observed by a periodic deflection of the smoke streamlines. As the circulation of the airfoil changed, the velocity it induced in the flowfield was also changed accordingly. This was, perhaps, most easily observed at the leading edge of the airfoil, where the low-frequency mode led to an oscillation of the stagnation point location across the airfoil lower surface. For example, at a positive angle of attack when the circulation of the airfoil was at a local maximum, the velocity induced at the leading edge of the airfoil would cause the stagnation point to move further downstream on the airfoil lower surface. As the circulation was then reduced and reached a local minimum, the reduction in circulation would cause the stagnation streamline to move farther upstream on the airfoil lower surface.

This effect is shown in Fig. 4.64, which displays select sequential frames of the smoke wire flow visualization video. In order to assist in showing this movement of the stagnation point, the three streamlines which run closest to the stagnation at the airfoil leading edge are traced in green, red, and blue. These colored tracings represent the same smoke wire traces in all images. In Fig. 4.64, the left row of images displays the entire streamwise length of the flowfield captured in the flow visualization, and the right row of images displays the leading-edge region of the flowfield. Starting in Fig. 4.64 a), the highlighted streamlines all flow above the ice shape and over the airfoil model. At this instance, the lift coefficient of the iced airfoil would be at a local maximum, as the circulation-induced vertical upwash on the highlighted streamlines is largest. As time passes the airfoil circulation decreases, causing the highlighted streamlines to be deflected in the direction towards the airfoil lower surface. In Fig. 4.64 b) the lower (blue) highlighted streamline is swept downward due to reductions in the upwash induced by the airfoil circulation. As the airfoil circulation is further decreased in Fig. 4.64 c), the middle (red) highlighted streamline is also swept downward due to reductions in the upwash induced by the airfoil circulation. In Fig. 4.64 d), the airfoil circulation has reached a local minimum, and all three highlighted streamlines experience a local minimum in upwash induced by the airfoil circulation. As time passes further, the airfoil circulation increases and the opposite effect occurs, as can be seen in Fig. 4.64 e) and f).

By inspecting the period of an entire oscillation cycle in the flow visualization results, the frequency of the oscillation is determined to be consistent with what would be expected from the Strouhal scaling in Section 4.6.2. For example, in Fig. 4.64, one oscillation occurs over approximately 2 seconds, corresponding to a frequency of about 0.5 Hz. Since the smoke wire flow visualization was conducted at $\mathrm{Re} = 0.1 \times 10^6$, if this frequency were to be scaled directly with velocity, at $\mathrm{Re} = 1.8 \times 10^6$ it would correspond to a frequency of 9 Hz. By comparing this approximate frequency with the low-frequency mode at $\alpha = 7°$ in Table 4.5, it can be expected that the low-frequency oscillations being measured at $\mathrm{Re} = 1.8 \times 10^6$ and visualized at $\mathrm{Re} = 0.1 \times 10^6$ represent the same mode of unsteadiness.

4.7 Summary of Unsteady Modes

4.7.1 Comparison of Shear-Layer Flapping Mode and Low-Frequency Mode

As discussed in Sections 4.4–4.6, the flowfield about the iced airfoil exhibits three distinct modes of unsteadiness. While the regular mode has been commonly reported in the literature, it would seem that no distinction has been previously made between the shear-layer flapping mode and the low-frequency mode. Since both of these modes of unsteadiness occur at such low frequencies, it is likely that they have incidentally been thought to be the same. Additionally, since the shear-layer flapping mode occurs at a frequency that is somewhat close to a multiple of that for the low-frequency mode, it would be easy to confuse the shear-layer flapping peak as a harmonic of the low-frequency mode. However, it has been confirmed that the frequencies of the shear-layer flapping mode and low-frequency mode are not harmonics, as the shear-layer flapping frequency is not a direct multiple of the low-frequency mode. Additionally, the center frequency of the shear-layer flapping mode was observed to change with changing airfoil angle of attack, while the changes in center frequency of the low-frequency mode with angle of attack were insignificant in comparison. The small changes that did occur in the frequency of the low-frequency mode were much less than any scaled difference in frequency of the shear-layer flapping mode.

By comparing the Strouhal number values from the current study to those reported in the literature for each of the two phenomena separately, it was also shown that the scaling of each mode independently compares to results reported in the literature for two different phenomena. While it is possible that the shear-layer flapping mode and the low-frequency mode are linked by some interaction at these different frequencies, they are manifested in the airfoil flowfield differently. As a result, the different modes appeared in measurements acquired at different locations in the airfoil flowfield, which is summarized in the following section.

4.7.2 Locations of Unsteady Modes

A summary of the locations where each different unsteady mode was identified is presented in Fig. 4.65. From Fig. 4.65, the regular mode was most easily identified in the aft portion of the separation bubble, downstream of the mean shear-layer reattachment location, and in the upper boundary of the upper surface wake. As the vortices in the shear layer upstream of reattachment followed the streamline that curved back to the airfoil surface, the influence of the vortices could be measured by the local surface pressure. After the separated shear layer reattached to the surface, the vortices were shed downstream and could then be identified by their effect on the local surface pressure as they passed over the surface, as well as in the upper boundary of the iced-airfoil wake.

Also in Fig. 4.65, the effect of shear-layer flapping was identified to be dominant in the region just downstream of the ice shape, which is a characteristic that has been consistently observed in the literature. The effects of shear-layer flapping were also observed across the region of the airfoil surface covered by the separation bubble, and in the wake downstream of the iced-airfoil upper surface. Since the shear-layer flapping mode would cause the streamlines across the airfoil upper surface to be quasi-periodically deflected with the flapping motion, this motion can be observed across the entire upper surface wake region.

Finally, in Fig. 4.65 the low-frequency mode can be thought of as a quasi-periodic oscillation of the airfoil circulation. As a result, its effects are similar to what would occur for a vortex of oscillating circulation strength in a freestream potential flow. As a result, the effects of the low-frequency mode were most prominently identified when integrating the pressure distribution about the entire airfoil surface, and were observed in the region outside of the wake downstream of the iced airfoil. Similarly, in the smoke flow visualization results, the low-frequency mode was observed to deflect the streamlines upstream of the airfoil model, and acted to cause the stagnation point on the airfoil surface to move across the airfoil lower surface, as discussed in Section 4.6.4. While not shown here, the low-frequency mode was also observed in the spectral content of the C_p distribution on the airfoil lower surface. These traits are indicative of the circulation oscillation effects previously described.

4.7.3 Effect of Reynolds Number on Unsteady Modes

In order to assess the effect of reducing the freestream velocity on the frequencies of the unsteady modes, the NACA 0012 airfoil with the horn-ice shape was also tested at a reduced Reynolds number of $\mathrm{Re} = 0.5 \times 10^6$. It was shown by Gurbacki[6] that the frequencies of the unsteady modes scaled directly proportional to the freestream velocity when the Reynolds number was reduced from $\mathrm{Re} = 1.8 \times 10^6$ to $\mathrm{Re} = 1.0 \times 10^6$. However, since the smoke flow visualization was conducted at reduced Reynolds numbers of Re = 0.5×10^6 and Re = 0.1×10^6, it was also important to ensure that the expected direct relationship between the frequency of the unsteady modes and the freestream velocity was preserved at much lower Reynolds numbers. As a result, measurements from the surface-integrated unsteady pressure transducers were also acquired at Re = 0.5×10^6 for the NACA 0012 airfoil with the horn-ice shape. While an attempt was made to acquire similar measurements at Re = 0.1×10^6, the test instrumentation was not sensitive enough to acquire significant results at this reduced speed.

The three unsteady modes associated with the iced-airfoil flowfield were also observed in the measurements acquired at Re = 0.5×10^6. The spectral content of the acquired measurements at the reduced Reynolds number of Re = 0.5×10^6 and the full Reynolds number of Re = 1.8×10^6 are compared for each of the three unsteady modes in the PSDs in Fig. 4.66, Fig. 4.67, and Fig. 4.68 at $\alpha = 6°$. Additional comparison of the central frequencies of these unsteady modes with the change in freestream velocity is summarized in Table 4.6 and also described below. The regular mode was visible in the spectral content of the airfoil C_p at $x/c = 0.85$ for both Reynolds numbers, as shown in Fig. 4.66. As discussed in Section 4.4.1, the central frequency of the regular mode peak at Re = 1.8×10^6 was estimated to be 95 Hz. From Fig. 4.66 a), the central frequency of the regular mode peak at Re = 0.5×10^6 is approximately 26.6 Hz. The freestream velocity of the full Reynolds number was approximately 3.64 times that of the reduced Reynolds number. By comparing the central frequencies of the regular mode in Fig. 4.66, the frequency at the full Reynolds number is 3.57 times that of the reduced Reynolds number. This indicates that the frequency of the regular mode scales directly proportional with the freestream velocity, even through the low speeds for Re = 0.5×10^6.

The shear-layer flapping mode was also identified at both Re = 0.5×10^6 and Re = 1.8×10^6 in the spectral content of the airfoil C_p at $x/c = 0.03$, as shown in Fig. 4.67. From Fig. 4.67 a), the central frequency of the shear-layer flapping mode at the reduced Reynolds number is approximately 6.6 Hz. Indeed, this frequency is also very close to the frequency qualitatively estimated from the flow visualization results discussed in Section 4.5.4. As discussed in Section 4.5.1, the central frequency of the shear-layer flapping mode was 23.7 Hz for Re = 1.8×10^6 and $\alpha = 6°$. Thus, the central frequency of the shear-layer flapping mode at the full Reynolds number is 3.59 times that of the reduced Reynolds number. Like for the regular mode, it would appear as though the frequency of the shear-layer flapping mode indeed scales directly proportional with the freestream velocity, through the low speeds at $\mathrm{Re} = 0.5 \times 10^6$ for the current study.

The final unsteady mode in the iced-airfoil flowfield that was compared at the different Reynolds numbers is the low-frequency mode. The comparison of the PSDs of C_l at $\alpha = 6°$ for $\mathrm{Re} = 0.5 \times 10^6$ and $\mathrm{Re} = 1.8 \times 10^6$ is shown in Fig. 4.68. As discussed in Section 4.6.1, the central frequency of the low-frequency mode at $\mathrm{Re} = 1.8 \times 10^6$ and $\alpha = 6°$ was identified at 8.2 Hz. From Fig. 4.68 a), the central frequency of the low-frequency mode at $\mathrm{Re} = 0.5 \times 10^6$ can be observed at 2.3 Hz. Using these frequencies, the central frequency of the low-frequency mode at the full Reynolds number was 3.57 times that of the central frequency at the reduced Reynolds number. This indicates that the low-frequency mode is also likely scaled directly proportional to the freestream velocity, at least up until the freestream velocity at $\mathrm{Re} = 0.5 \times 10^6$ of the current study.

Table 4.6 Summary of frequencies of unsteady modes for NACA 0012 at $\alpha = 6°$ between $\mathrm{Re} = 1.8 \times 10^6$ and $\mathrm{Re} = 0.5 \times 10^6$

	$\mathrm{Re} = 1.8 \times 10^6$	$\mathrm{Re} = 0.5 \times 10^6$	Ratio
U_∞ (ft/sec)	199.21	54.75	3.64
$f_{Regular\ Mode}$ (Hz)	95	26.6	3.57
$f_{Shear\text{-}Layer\ Flapping\ Mode}$ (Hz)	23.70	6.6	3.59
$f_{Low\text{-}Frequency\ Mode}$ (Hz)	8.20	2.3	3.57

4.8 Shear-Layer Reattachment and Surface Flowfield Effects of Low-Frequency Mode

In order to characterize the modes of unsteadiness involved in separation bubble flows, the effect of the regular mode and shear-layer flapping mode have been intensely studied in the flowfields about canonical geometries. This includes the effects that these modes have on the movement of the shear-layer reattachment location and local surface pressure and velocity. For example, as discussed in Section 2.2.1.2, Lee and Sung[32] identified a sawtooth profile in the reattachment location that occurred as a result of periodic large-scale vortex passing. As a vortex would pass the over the reattachment surface, the upstream velocity induced at the wall by the vortex caused a retreating of the instantaneous shear-layer reattachment location. These authors also identified a quasi-periodic oscillation in the shear-layer reattachment location due to shear-layer flapping, and also characterized the time-dependent relationship between the unsteady shear-layer reattachment location and local surface pressure due to the shear-layer flapping mode.

However, since the low-frequency mode has not been identified in flows about canonical geometries, it would appear as though this mode of unsteadiness is unique to lift-generating aerodynamic bodies with separation bubbles. While the presence and effect of the low-frequency mode on the lift performance of airfoils was studied in great detail by Broeren,[58] and the convection characteristics of the low-frequency mode on an iced airfoil was reported by Gurbacki,[6] the effects of the low-frequency mode on the unsteady location of shear-layer reattachment has not been distinguished. For this reason, it is useful to identify the time-dependent relationship of the reattachment location and the airfoil surface flowfield at the low-frequency mode.

The unsteady shear-layer reattachment location was determined for the NACA 0012 airfoil with the horn-ice shape at $\alpha = 5°$ using the method outlined in Section 3.6. As discussed in Section 4.3.5, the resulting shear-layer reattachment location compared well with the PIV-derived mean reattachment location and the reattachment statistics of Jacobs.[23] An example of the low-frequency component of the shear-layer reattachment location is presented in Fig. 4.69. From Fig. 4.69, the effect of the low-frequency mode on the shear-layer reattachment location is represented by a quasi-periodic oscillation of the reattachment location about the time-averaged shear-layer reattachment location. The frequency scales of this oscillation and the time-dependent relationship between the shear-layer reattachment location and the airfoil surface flowfield at the low-frequency mode will be discussed in the following subsections. Since the low-frequency mode represents a global oscillation in the airfoil circulation, the primary comparison will be made between the unsteady shear-layer reattachment and iced-airfoil lift coefficient. Additional insight will also be provided by also analyzing the time-dependent relationship between the shear-layer reattachment location and the unsteady surface pressure distribution.

4.8.1 Comparison of Frequency Scales

At $\alpha = 5°$, the PSD functions of the reattachment location and iced-airfoil lift coefficient were calculated. The resulting PSDs for the unsteady shear-layer reattachment location and the unsteady airfoil C_l are shown in Fig. 4.70. As shown in Fig. 4.70, the PSDs for the shear-layer reattachment location and the unsteady airfoil C_l reveal consistent peaks in low-frequency spectral content. The central frequency of the spectral peak for the shear-layer reattachment location was determined using the peak detection routine discussed in Sections 4.5.1 and 4.6.1. The resulting central frequency of the low-frequency mode in the shear-layer reattachment location corresponded to 9.35 Hz, as shown in Fig. 4.70 a). This value is comparable to the peak in C_l at 9.39 Hz, as reported in Section 4.6.1 and as shown in Fig. 4.70 b). This indicates that at $\alpha = 5°$, the dominant oscillations in the reattaching shear layer and the iced-airfoil lift coefficient occur at the same frequency. Since Fig. 4.70 reveals similarities in frequency content between x_r and C_l, additional understanding of the low-frequency mode can be gained by investigating the relationship between the movement in the shear-layer reattachment location and the airfoil lift coefficient at the shared low frequency of unsteadiness.

4.8.2 Time-Dependent Relationship

Since the low-frequency mode has been identified as not being strictly periodic,[6] using the entire time history to calculate the cross-correlation function between the reattachment location and the unsteady iced-airfoil lift coefficient in order to identify their time-dependent relationship may result in small to negligible levels of correlation between signals. The quasi-periodicity of the low-frequency mode would cause the local maxima and local minima in the signals being correlated to inconsistently correspond to one-another across the same time lag, τ. As a result, it is desirable to instead perform an analysis on the average time-dependent relationship between the unsteady shear-layer reattachment location and unsteady iced-airfoil C_l corresponding to the low-frequency mode. In order to achieve this, the conditional averaging scheme outlined in Section 3.10.3 was used. As discussed in Section 3.10.3, the end of the shrinking phase of the shear-layer reattachment location was used to prescribe which segments of time were used in the conditional averaging scheme. Since the measurements in the unsteady surface pressure were time-resolved with the unsteady shear-layer reattachment location, the conditionally-averaged unsteady C_p and lift coefficient were determined using measurements at the same time instances that were used in the conditional average of the unsteady shear-layer reattachment location.

In order to determine the time-dependent relationship between the shear-layer reattachment location and the unsteady iced-airfoil lift coefficient corresponding to the low-frequency mode, the cross-correlation coefficient was computed between x_r and C_l. The computed cross-correlation coefficient of the conditionally-averaged signals is shown in Fig. 4.71. From Fig. 4.71, significant levels of correlation exist between the conditionally-averaged reattachment location and iced-airfoil lift coefficient at regular time lag intervals corresponding to the oscillation cycle of the low-frequency mode. For example, the cross-correlation coefficient in Fig. 4.71 displays positive peaks at $\tau = -0.034$ sec and $\tau = 0.074$ sec. The time between these peaks is 0.108 seconds, which is approximately one full cycle of the 9.39 Hz low-frequency mode oscillation.

The relationship between the reattachment location and the iced-airfoil lift coefficient can also be characterized by observing the sign and corresponding time lags of local extrema in the cross-correlation coefficient. For example, using the same peaks mentioned previously in Fig. 4.71, the positive peak nearest zero time lag corresponds to $\tau = -0.034$ sec, which is close to one-quarter of the oscillation cycle for the low-frequency mode. The cross-correlation coefficient also crosses near the origin at $\tau = 0$ sec, and reaches another positive peak at a positive time lag near three-quarters of a cycle of the low-frequency mode at $\tau = 0.074$ sec. This suggests the possibility of a phase relationship of approximately $\pi/2$ between the separation bubble length and the lift coefficient, which will be confirmed in Section 4.8.3.

For the peak in the cross-correlation coefficient at $\tau = -0.034$ sec and $\rho = 0.356$, the value of the cross-correlation coefficient is positive, but the time lag is negative. This would indicate that prior to a local maximum in length of the separation bubble, there tends to be a maximum in lift coefficient. Similarly, prior to a local minimum in the length of the separation bubble, there tends to be a minimum in lift coefficient. From an aerodynamics perspective, this type of behavior would be expected, as a higher circulation effect of the airfoil would cause the length of the separation bubble to increase. However, shortly after $\tau = 0$ sec, the first extremum in the cross-correlation coefficient is reached at $\tau = 0.0245$ sec and $\rho = -0.348$. This would indicate that a local minimum in lift coefficient tends to be preceded by a local maximum in separation bubble length, or a local maximum in lift coefficient tends to be preceded by a local minimum in separation bubble length. Since correlation does not indicate causation, it is not possible to determine here whether the unsteadiness in the shear-layer reattachment location or the iced-airfoil lift coefficient serves as a source of these oscillations.

In order to further understand how the airfoil lift coefficient can lead the movement of the reattachment location, the cross-correlation coefficients between the conditionally-averaged reattachment location and upper surface C_p were also calculated. The resulting correlation coefficients are provided in the contour of Fig. 4.72. From Fig. 4.72, it can be seen that at $\tau = 0$ sec, the reattachment location exhibits strong levels of positive correlation with the C_p at the airfoil leading edge. Thus, at one given time instance, if the separation bubble is large, the leading-edge pressure tends to be high, and if the separation bubble is small, the leading-edge pressure tends to be low. This observation is to be expected, and has been frequently observed in a time-averaged sense in the literature.[18]

From the cross-correlation coefficients shown in Fig. 4.72, it appears as though the oscillations in C_p have convective qualities, as indicated by the downstream movement of the regions of high or low correlation coefficient with time. However, this downstream convection is only observed downstream of $x/c = 0.15$. Upstream of $x/c = 0.15$, the relative maxima in the cross-correlation coefficients appear to occur at the same time lags, indicating that the effects of the low-frequency mode occur at approximately the same time instance across this region. It is unknown whether these effects are then propagated downstream, or if the low-frequency mode effects are propagated upstream from the region downstream of $x/c = 0.15$, and the effect on the local pressure simply has opposite sign across this $x/c = 0.15$ location, leading to a reversal in the sign of the cross-correlation coefficient.

Regardless, the cause of the airfoil lift coefficient leading the reattachment location can be determined by observing the region of strong anti-correlation near $x/c = 0.20$ and $\tau = -0.03$ sec. This location corresponds to the beginning of the pressure recovery region on the airfoil surface, as observed in the iced-airfoil C_p distribution in Fig. 4.14. Since the correlation coefficient is negative near $x/c = 0.20$, this would indicate that prior to a local maximum in the length of the separation bubble, there would tend to be a local minimum in pressure within this region, and hence contribute to a local maximum in lift coefficient. Similarly, prior to a local minimum in the length of the separation bubble, there would tend to be a local maximum in pressure within this region, contributing to a local minimum in lift coefficient. While it is fairly common for the leading-edge suction peak to be dominant in the lift generation in an airfoil flowfield, a long separation bubble on an airfoil tends to decrease the influence of this suction peak and create long stretches of constant pressure on the airfoil surface.[18] As a result, in this case the instance in time when maximum lift is achieved is not when the leading-edge pressure is lowest, but rather when the plateau in the airfoil C_p along the separation bubble length is associated with the lowest pressure. This then explains how the observations from the cross-correlation coefficient between x_r and C_l in Fig. 4.71 and the observations from the cross-correlation coefficients between x_r and C_p in Fig. 4.72 are related.

4.8.3 Phase Angle Relationship

Based on the observations from the cross-correlation coefficients in Fig. 4.71, a more detailed investigation on the phase relationship between the reattachment location and lift coefficient was performed. Since the cross-correlation coefficient between x_r and C_l tended to cross near the origin, switching signs after crossing $\tau = 0$ sec, and since the low-frequency mode was observed at a consistent frequency in the PSDs of the reattachment location and the iced-airfoil lift coefficient in Fig. 4.70, this suggests the existence of a phase relationship between the separation bubble length and the iced-airfoil lift coefficient at the low-frequency mode. In order to better understand this phase relationship, the relative signal phase distributions in the cross-spectra between the reattachment location and iced-airfoil lift coefficient was calculated. It should be mentioned that the full record lengths of the reattachment location and lift coefficient signals were used to calculate this phase spectrum.

The resulting relative phase distribution, as a function of frequency, is shown in Fig. 4.73. From Fig. 4.73, at a frequency of 9.59 Hz, C_l does appear to lead the phase of the reattachment location by $\pi/2$. The phase relationship comparison was made at a frequency of 9.59 Hz, as it is the frequency nearest the common low-frequency mode observed in x_r and the iced-airfoil performance using the frequency resolution of Fig. 4.73. This observation is consistent with the cross-correlation coefficient shown in Fig. 4.71.

4.8.4 Spectral Content Across Time

The analysis performed insofar on the low-frequency mode in the iced-airfoil flowfield reveal consistency in the frequency content of the reattachment location and the airfoil lift coefficient, as well as a phase relationship between the separation bubble length and the airfoil lift coefficient. However, additional understanding of the low-frequency mode that operates in the iced-airfoil flowfield and reattachment location can be obtained by observing changes in spectral content over time. These changes in the spectral content over time were identified using the wavelet transform of the conditionally-averaged signals. As discussed in Section 3.10.5, the Morlet wavelet was used to calculate the continuous wavelet transform (CWT) of the conditionally-averaged reattachment location and iced-airfoil lift coefficient. The resulting wavelet transforms of these conditionally-averaged signals are presented in Fig. 4.74. In Fig. 4.74, the time instances where the maximum CWT amplitude is reached at a frequency of 9.5 Hz are marked using black square symbols. This frequency was the closest to that of the low-frequency mode included in the 0.5 Hz frequency resolution of the CWTs presented in Fig. 4.74. From Fig. 4.74, as expected, the high concentrations of energy in the signals correspond to the same low-frequency mode, as was the case in Fig. 4.70.

However, it is interesting to note that the concentration of energy at the low-frequency mode is not constant across time. Instead, a region of high-amplitude activity on the order of 9.5 Hz can be observed in both of the wavelet transforms in Fig. 4.74 near $t = 0$ sec, that then decreases in magnitude farther from $t = 0$ sec. This concentration of energy at the low-frequency mode can be expected, as the purpose of the conditional average was to focus the signal analysis on one average low-frequency oscillation cycle. As seen in Fig. 4.74 a), the wavelet transform of the conditionally-averaged shear-layer reattachment location produces a high-amplitude output at $t = 0$ sec. Since this region of high energy at the low-frequency mode is centered at $t = 0$ in the wavelet transform of x_r, it suggests that the conditional averaging scheme that was used in this investigation correctly centers the signals being averaged about a reference center in the low-frequency mode in the reattachment location. Due to the quasi-periodicity of the low-frequency mode, outside of one oscillation cycle the low-frequency mode is suppressed by the averaging process, which is evident by the reductions in CWT amplitude outside of $t = \pm 0.10$ sec.

Additionally, from Fig. 4.74 b) the CWT of the conditionally-averaged lift coefficient also exhibits a maximum amplitude at $t = 0$ sec. While the cross-correlation coefficient between x_r and C_l shown in Fig. 4.71 displayed nearly zero correlation between x_r and C_l at $\tau = 0$ sec, the time corresponding to the highest level of spectral content at 9.5 Hz was the same between the reattachment location and C_l. This consistency in the time at which the maximum CWT amplitude is observed in the C_l and x_r wavelet transforms is to be expected, as the CWT determines the magnitude of oscillations at a given frequency. These regions of high spectral activity observed in the CWT of C_l and x_r are contrasted with the time lags of maximum cross-correlation coefficient, which determines the time-dependent relationship between two signals by comparing relative magnitudes of the signals across various time lags. As noted in Section 4.8.2, the value of the cross-correlation coefficient between x_r and C_l at $\tau = 0$ sec was approximately zero. It is possible that the oscillations at a given frequency can be strongest in x_r and C_l at the same instance in time, even if this does not correspond to the instance in time of an absolute extremum in a signal. Since the instance where the maximum CWT at the low-frequency mode is reached is consistent between x_r and C_l, this suggests that there is an interaction between the movement of the shear-layer reattachment location and the change in the airfoil circulation at the low-frequency mode.

The relationship between the propagation of the low-frequency mode through the upper surface C_p and the movement of the shear-layer reattachment location can be further studied using the wavelet transform of the unsteady C_p signals from the surface-integrated pressure transducers. By performing a wavelet transform on each of these conditionally-averaged C_p signals and extracting the variations in amplitude at the low-frequency mode at 9.5 Hz, changes in the energy content of the low-frequency mode throughout the surface pressure flowfield can be observed as a function of time. Again, the frequency of 9.5 Hz was extracted as this was the closest frequency to the low-frequency mode within the frequency resolution of the CWTs. Using the same conditional averaging scheme discussed earlier, the average progression of the low-frequency mode through the upper surface C_p can be identified in response to an oscillation of the shear-layer reattachment location at the low-frequency mode. The resulting wavelet-based progression of the low-frequency mode through the airfoil C_p is shown in Fig. 4.75.

In Fig. 4.75, it is important to recall that, like in Fig. 4.74 a), the low-frequency mode in the shear-layer reattachment location is fixed near $t = 0$ seconds. With this in mind, it can be seen from Fig. 4.75 that the low-frequency mode in the reattachment location acts at an instance in time that is consistent with the low-frequency mode in the iced-airfoil upper surface C_p. The regions of highest amplitude in the C_p wavelet transform at the low-frequency mode also appear to be limited to the region covered by the average separation bubble length. Also included with Fig. 4.75 is the time delay distribution for $\alpha = 5°$, which was calculated using the phase distributions in C_p discussed in Section 4.6.3. However, in Fig. 4.75 the time delays upstream of $x/c = 0.15$ were calculated with a phase shifted by a factor of π in order to account for the natural phase shift that would occur with a reversal in sign of the oscillation in C_p across $x/c = 0.18$, as described below.

As the low-frequency mode affects the local surface C_p, the sign of the oscillation would change between the region upstream of $x/c = 0.18$ to the region downstream of $x/c = 0.18$. Since the low-frequency mode can be thought of as an oscillation in the airfoil circulation, its effects are similar to what would occur with a small increase or decrease in the airfoil angle of attack. An example of this is shown in Fig. 4.76, where the time-averaged C_p distributions for the iced airfoil are presented for $\alpha = 5°$, along with $\alpha = 5° \pm 0.5°$. If, for example, the airfoil angle of attack was slightly increased, it can be expected that the C_p about the airfoil leading edge would slightly increase, and the C_p within the pressure recovery region would slightly decrease. Thus, the reversal in sign of the effects on C_p across the $x/c = 0.18$ location would be associated with a reversal in phase, shifting the relative phase distribution by a factor of π.

As shown in Fig. 4.75, the time delays calculated using the relative phase distribution in C_p appear to follow the progression of the high-amplitude content of the low-frequency mode calculated using the CWT. It is interesting to note how the high-amplitude content at the low-frequency mode appears to be present in Fig. 4.75 near $x/c = 0.18$ prior to $t = 0$ sec, and then be convected downstream. This suggests that the low-frequency oscillations in the airfoil C_p begin near this location. Also, the consistency between the shifted time delays upstream of $x/c = 0.15$ with the CWT of C_p at the low-frequency mode suggests that the low-frequency mode indeed has an effect on the airfoil C_p upstream of $x/c = 0.18$ that is of opposite sign than the effect that the oscillation has on the airfoil C_p downstream of $x/c = 0.18$. Since the effect of a change in airfoil circulation would have an opposite effect on the surface pressure across the $x/c = 0.18$ location, and since this also corresponds to the location where the low-frequency mode appeared to originate in the C_p CWT, it is possible that the low-frequency mode mechanism could be related to the difference in stretching and compression tendencies of the separation bubble depending on a change in the surface pressure, similar to that discussed by Kiya and Sasaki.[31] However, additional investigation is required into these observations to determine their implications, which has been reserved for future work.

It can also be observed in Fig. 4.75 that after accounting for the phase reversal in the pressure measurements across $x/c = 0.18$, the time delay at the mean shear-layer reattachment location is the same as the time delay across the region upstream of $x/c = 0.18$. This is due to the observation that was made in Section 4.6.3, where it was identified that the characteristic phase angle at the reattachment location for the low-frequency mode was approximately π. This observation is consistent with the self-sustaining mechanism of the low-frequency mode introduced by Almutairi and AlQadi.[61] These authors identified that after bubble bursting occurred on an airfoil, acoustic waves produced by the wake of the separated region were propagated upstream, excited the flow at the location of separation, which then led to a reduction in the length of the separation region. This mechanism represented a self-sustaining oscillation at the low-frequency mode. In the current study, the low-frequency mode was not present in the region upstream of $x/c = 0.18$ until the low-frequency mode propagated downstream and reached the shear-layer reattachment location. This could possibly be due to a similar effect as that discussed by Almutairi and AlQadi,[61] where the instabilities related to the low-frequency mode are not seen by the upstream portion of the flowfield until they are propagated upstream from the shear-layer reattachment location.

4.8.5 Summary of Oscillation Cycle at Low-Frequency Mode

With the $\pi/2$ phase relationship between the shear-layer reattachment location and the iced-airfoil lift coefficient known, the low-frequency oscillation can be explained according to the following description, and by using schematic presented in Fig. 4.77. When the airfoil C_l increases and reaches a local maximum, it is also associated with an increase in the strength of the airfoil circulation. The increase in airfoil circulation acts to move the stagnation point farther downstream on the lower surface of the airfoil, as represented in Fig. 4.77 a). This increase in airfoil circulation induces an effect similar to what would occur with a small increase in the airfoil angle of attack, including a decrease in the minimum airfoil C_p and increase in the adverse pressure gradient across the airfoil upper surface. These effects lead to an elongation of the separation bubble, which is represented in Fig. 4.77 b). This increase in the separation bubble length acts to disrupt the airfoil flowfield by decambering the airfoil, leading to effects on the airfoil pressure distribution similar to that of the long bubble described by Tani.[18] This disruption increases the pressure on the airfoil upper surface, which causes the airfoil C_l to decrease. This decrease in C_l is associated with a decrease in the circulation of the airfoil, which causes the stagnation point to move farther upstream on the lower surface of the airfoil, as represented in Fig. 4.77 c). The decrease in the airfoil circulation also induces effects similar to what would be observed with a small decrease in the airfoil angle of attack, including an increase in the minimum airfoil C_p and a reduction of the adverse pressure gradient on the airfoil upper surface. These effects lead to a shrinking of the separation bubble, as represented in Fig. 4.77 d). The movement of the stagnation point according to the low-frequency mode in the leading-edge region of the iced airfoil due to changes in the airfoil circulation was indicated by the deflection of the streamlines upstream of the airfoil model in the smoke flow visualization results reported in Section 4.6.4.

4.9 Prediction of Ice-Induced Airfoil Stall Based on Unsteady Hinge Moment

Using the improved understanding of unsteady modes present in the flowfield of an airfoil with a leading-edge horn-ice shape, significant improvements were made to the predictive capabilities of the hinge-moment-based airfoil stall prediction system. As described in Section 2.4.1, it was discovered that the hinge moment unsteadiness induced by a leading-edge horn-ice shape was markedly greater prior to stall than other forms of leading-edge contaminants on an airfoil. With an improved knowledge of the characteristics of the modes of unsteadiness present in the iced-airfoil flowfield, it was possible to develop a hinge-moment-based airfoil stall prediction method that distinguished the unsteadiness induced by a horn-ice shape from that associated with other contamination configurations. This system used the wavelet transform of the unsteady hinge moment coefficient to identify a horn-ice-induced stall, such that the correct evaluation of hinge moment unsteadiness could be used to predict the angle-of-attack margin to airfoil stall.

4.9.1 Wavelet-Based Prediction Algorithm

As discussed in Section 3.10.5, the wavelet transform of a signal provides an evaluation of the signal frequency content as a function of time. An example of the CWT of C_h for the iced and clean airfoil at an angle of attack 0.5° prior to stall is presented in Fig. 4.78. From Fig. 4.78 a), the effect of the low-frequency mode can be observed in the CWT of the iced airfoil by the regions of high amplitude within the low-frequency range from 6 Hz to 10 Hz. Across this low-frequency range, discrete regions of particularly high-amplitude spectral content can be observed. These regions occur regularly, approximately every 0.5 seconds. In contrast, the

CWT of the clean airfoil C_h in Fig. 4.78 b) is not characterized by any significant levels of unsteadiness across the low-frequency range. For comparative purposes, the contour in Fig. 4.78 b) is presented with the same contour scaling as Fig. 4.78 a). The regions of high-amplitude unsteadiness across the low-frequency range in Fig. 4.78 a) are unique to the iced-airfoil case prior to stall. As a result, the presence of this low-frequency content in the CWT can be used to distinguish the ice-induced stall case from the clean airfoil stall.

Since the low-frequency mode is accompanied with a distinct time-dependent signature in the CWT of C_h, like in Fig. 4.78 a), the intermittency of the high-amplitude content in the hinge moment CWT can be used to distinguish a stall induced by a horn-ice shape from a clean or tripped airfoil stall. The intermittency was used to determine what portion of the total time history the CWT of C_h exceeded a given threshold across a prescribed bandwidth. The intermittency was calculated using,

$$\gamma_{CWT} = \sum_{i=1}^{N} \frac{I(t_i)}{N} \qquad I(t_i) = \begin{cases} 0, & \max[CWT(t_i)] \le CWT_{crit} \\ 1, & \max[CWT(t_i)] > CWT_{crit} \end{cases} \tag{4.2}$$

where γ_{CWT} represents the intermittency factor, I is the intermittency function, $\max[CWT(t)]$ is the maximum wavelet transform amplitude at a given time across the prescribed bandwidth, and CWT_{crit} is the amplitude threshold of the wavelet transform.

Since the CWTs of C_h for the clean and tripped airfoil configurations did not have any significant variations in amplitude across time, the amplitude threshold could be set to a value above the amplitudes present in the C_h CWTs of the clean and tripped cases. As a result, the regular occurrence of the high-amplitude content in the CWT of C_h for the horn-ice case would exceed the prescribed threshold and contribute to the intermittency calculation, while the CWTs of C_h for the clean and tripped airfoil cases would not. The resulting intermittency factor can then be used in conjunction with a hinge-moment-based stall prediction system (e.g. from Ansell et al.[7]) in order to identify whether an increase in hinge-moment unsteadiness is due to an impending leading-edge or trailing-edge stall type of the airfoil, or if it is due to the unsteady modes induced by a leading-edge horn-ice shape.

4.9.2 Prediction Results

The wavelet-based prediction system described in the previous section was used in an example in the current study. The hinge moment measurements of the clean, tripped, and horn-ice shape configurations in the current study were used to calculate the corresponding intermittency factors. In an example, the intermittency factors were calculated across a frequency bandwidth from 4 Hz to 12 Hz, with a prescribed CWT amplitude threshold of -35 dB. The resulting intermittency factors that were calculated for each airfoil configuration are shown in Fig. 4.79. From Fig. 4.79, the intermittency factor for the horn-ice case has a clear, steep increase at an angle of attack several degrees prior to stall. Conversely, the clean and tripped configurations are characterized by low levels of intermittency until the stall angle of attack is reached. As a result, the level of γ_{CWT} effectively identifies the signature of the hinge moment unsteadiness that is present for the horn-ice case, but not present in the clean or tripped case prior to stall.

As discussed by Ansell et al.,[78] the use of a hinge-moment-based stall prediction system for a horn-ice case on an NACA 23012 airfoil produced results that were inconsistent with all of the other contamination configurations tested. This was demonstrated in Section 2.4.1 with the results presented in Fig. 2.6, after Ansell et al.[78] Using this example, for an angle-of-attack margin of $(\alpha - \alpha_{stall}) = -2°$, the hinge-moment-based stall prediction for all contamination configurations on the NACA 23012 airfoil would be consistent, with the exception of the horn-ice case. With an $\alpha - \alpha_{stall}$ margin setting of 2°, the horn-ice case would trigger a warning at an estimated 1°–1.5° prematurely, between $\alpha - \alpha_{stall} = -3°$ and $\alpha - \alpha_{stall} = -3.5°$. However, by using the detector function outputs of Ansell et al.[7] and the intermittency factors presented in Fig. 4.79, the premature stall prediction could be identified by also applying a threshold in γ_{CWT}. For example, a threshold of $\gamma_{CWT} = 0.15$ is indicated in Fig. 4.79 by a horizontal dashed line. By linearly interpolating the points of γ_{CWT} included in Fig. 4.79, this line is crossed for the horn-ice case at $\alpha - \alpha_{stall} = -3.82°$. Conversely, for the clean and tripped configurations, all points of γ_{CWT} lie below the $\gamma_{CWT} = 0.15$ threshold until $\alpha - \alpha_{stall} = 0°$ is reached.

Thus, when a stall warning is triggered at $\alpha - \alpha_{stall} = -2°$ by the detector function system of Ansell et al.,[7] the value of γ_{CWT} can be checked before a stall warning is provided. If γ_{CWT} remains below a given threshold at this angle of attack (e.g. $\gamma_{CWT} = 0.15$), then the impending stall is not being induced by the effects of a leading-edge horn-ice shape. However, if the detector function system produces a stall warning corresponding to an $\alpha - \alpha_{stall}$ margin of 2°, but γ_{CWT} is above a given threshold (e.g. $\gamma_{CWT} = 0.15$), then the stall warning is premature and the detector function logic is modified to raise the detector function threshold to that for the horn-ice case. In this case, the hinge-moment unsteadiness is correlated to the specific signature of the low-frequency mode present in the wavelet transform through γ_{CWT}, and is used to identify the influence of the ice shape on the hinge-moment unsteadiness characteristics. Additionally, the threshold in γ_{CWT} is reached before the detector function threshold set for an $\alpha - \alpha_{stall}$ margin of 2°, which would minimize the chance of a premature stall warning being provided. As a result, the intermittency observed in the low-frequency range of the hinge moment wavelet transform can be used to adapt the prior method for stall prediction to more accurately predict the thin-airfoil-type stall produced with the addition of a horn-ice shape on an airfoil.

4.10 Chapter 4 Figures

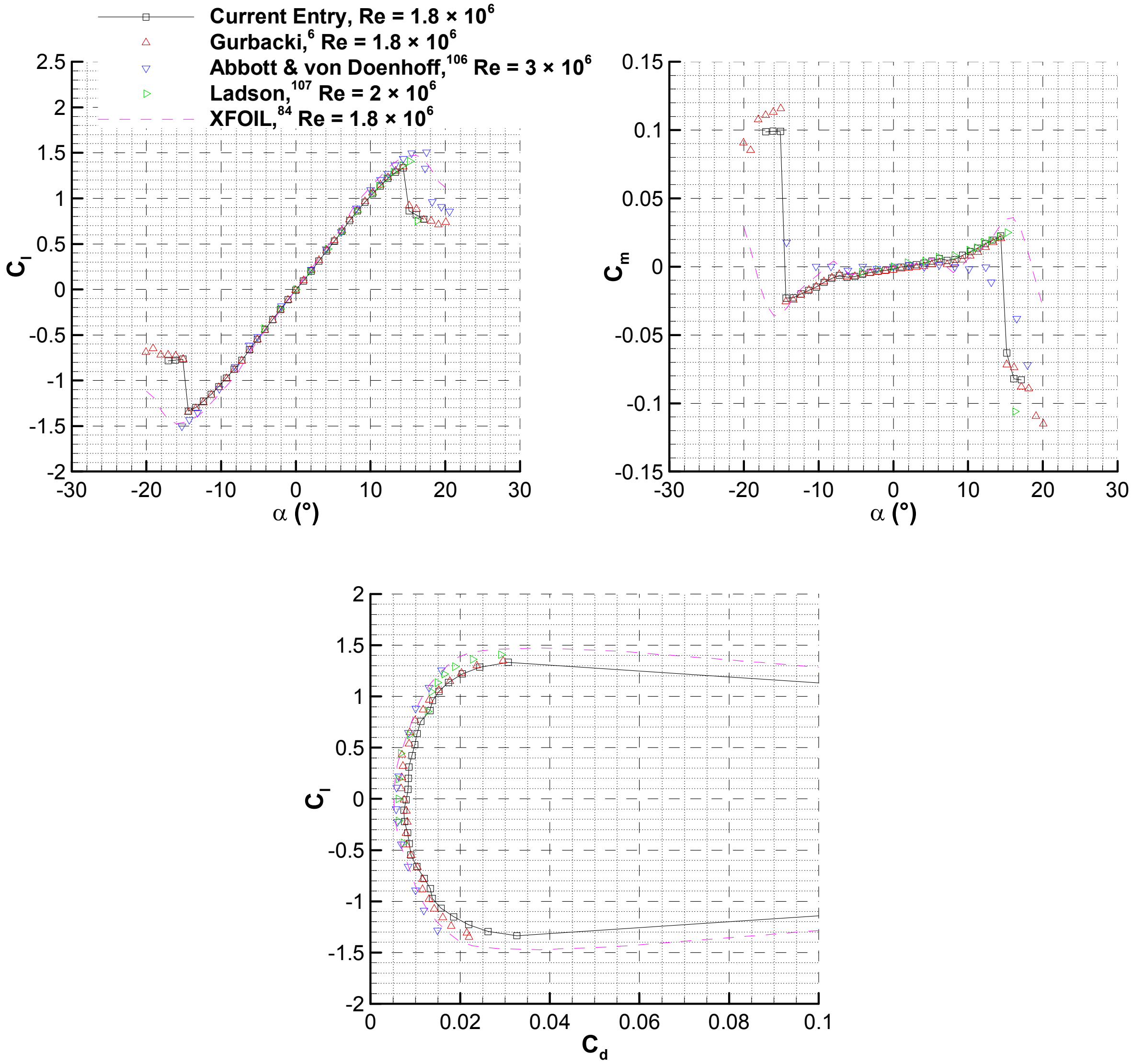

Fig. 4.1 Comparison of NACA 0012 airfoil data from the current investigation to performance results reported in the literature.

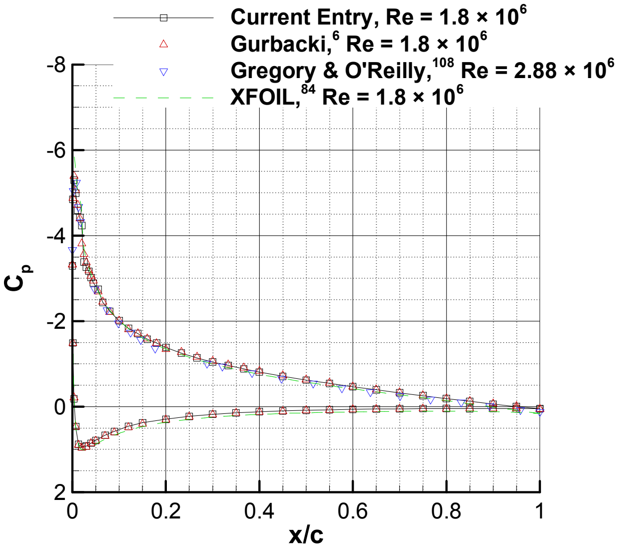

Fig. 4.2 Comparison of NACA 0012 airfoil C_p distribution from the current investigation to those reported in the literature, all data corresponds to $\alpha = 10°$.

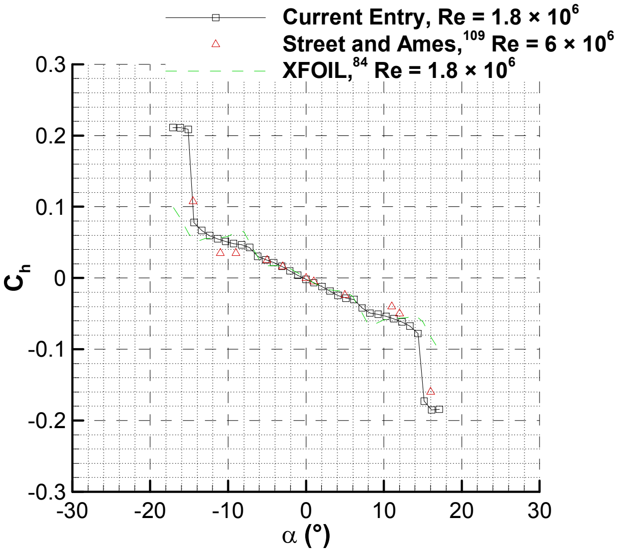

Fig. 4.3 Comparison of NACA 0012 airfoil C_h for 30%-chord flap from the current investigation to similar hinge moment results reported in the literature.

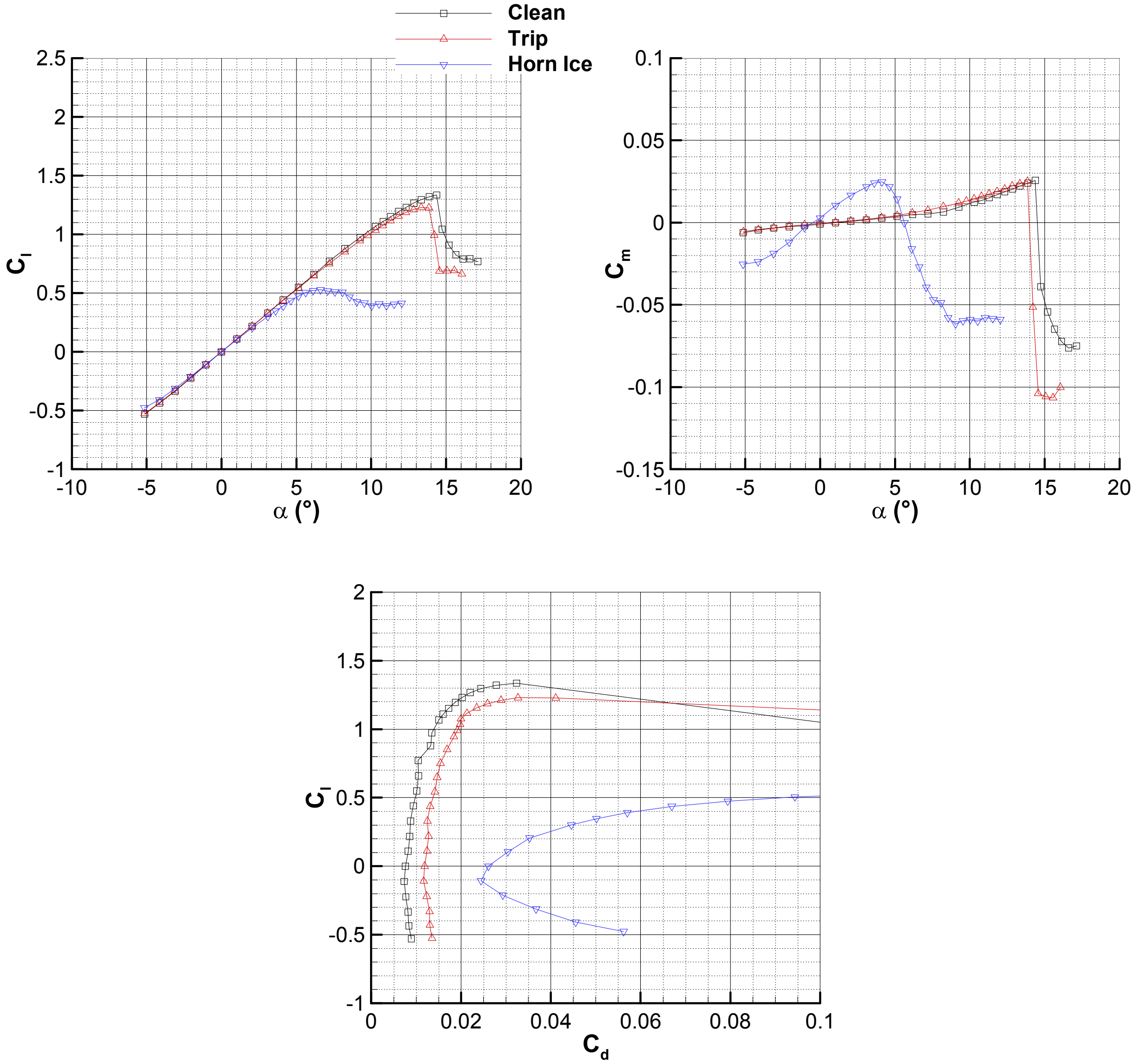

Fig. 4.4 Performance of NACA 0012 airfoil in clean, tripped, and horn-ice configurations.

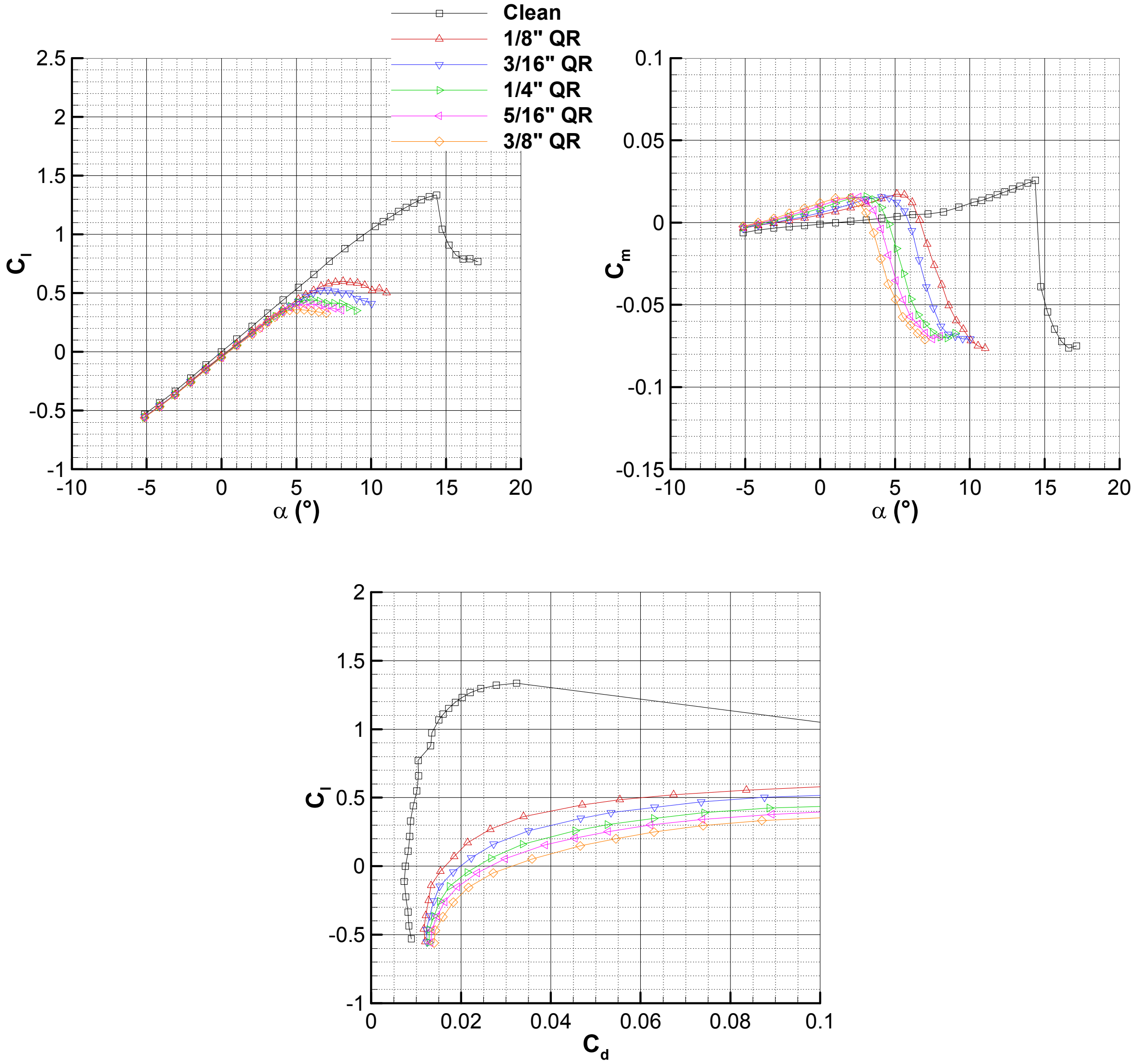

Fig. 4.5 Performance of NACA 0012 airfoil with various sized quarter-round geometries placed at *x*/*c* = 0.02 on the airfoil model upper surface.

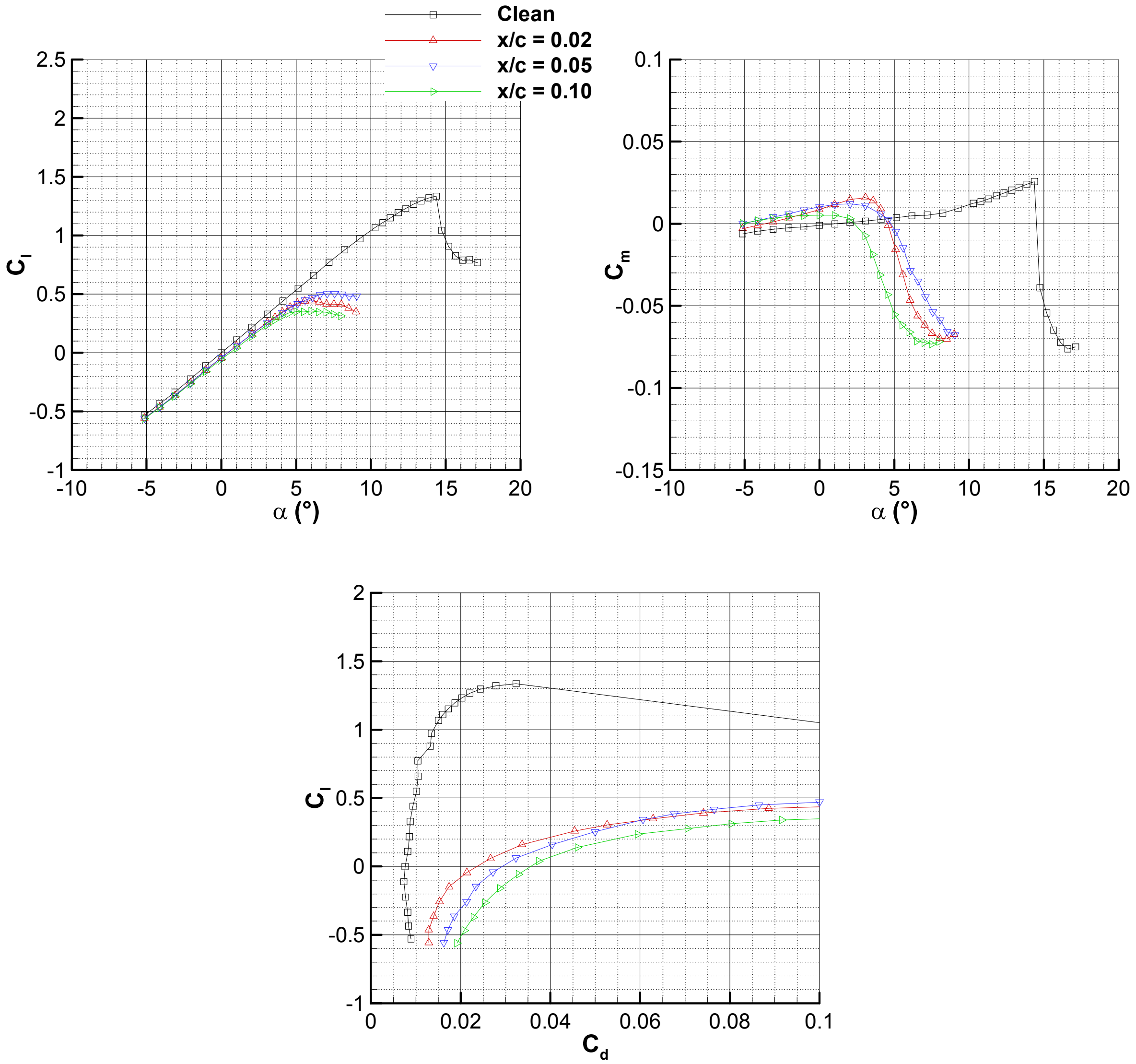

Fig. 4.6 Performance of NACA 0012 airfoil with 1/4 in. quarter-round geometry placed at various locations on airfoil model upper surface.

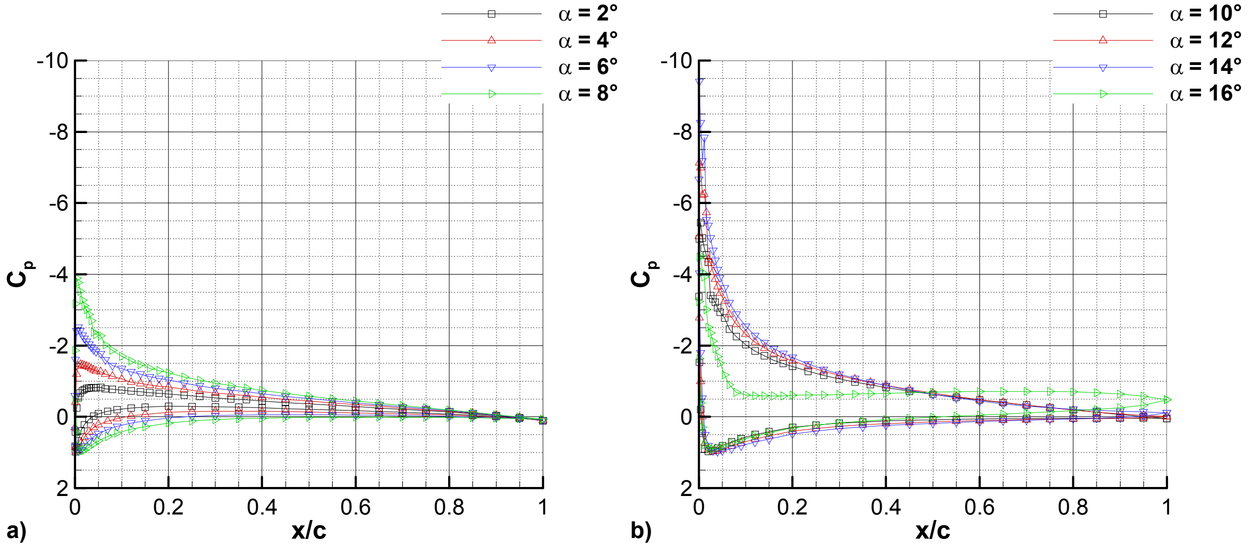

Fig. 4.7 Clean NACA 0012 airfoil C_p distributions: a) angle-of-attack range from $\alpha = 2°$ to $\alpha = 8°$, b) angle-of-attack range from $\alpha = 10°$ to $\alpha = 16°$.

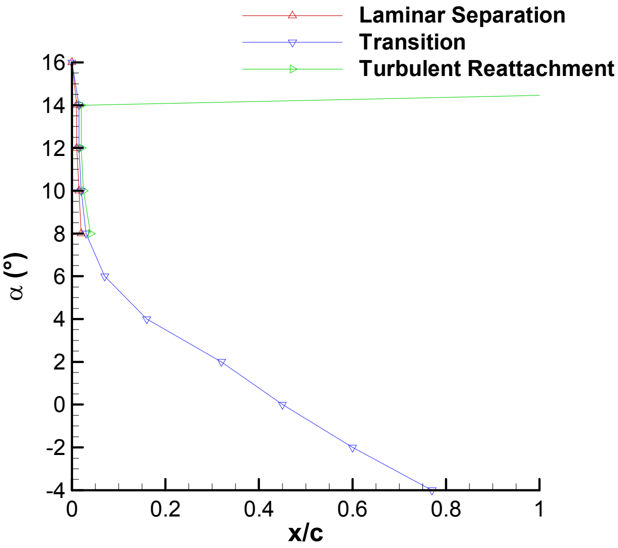

Fig. 4.8 Summary of surface oil flow visualization results for clean NACA 0012.

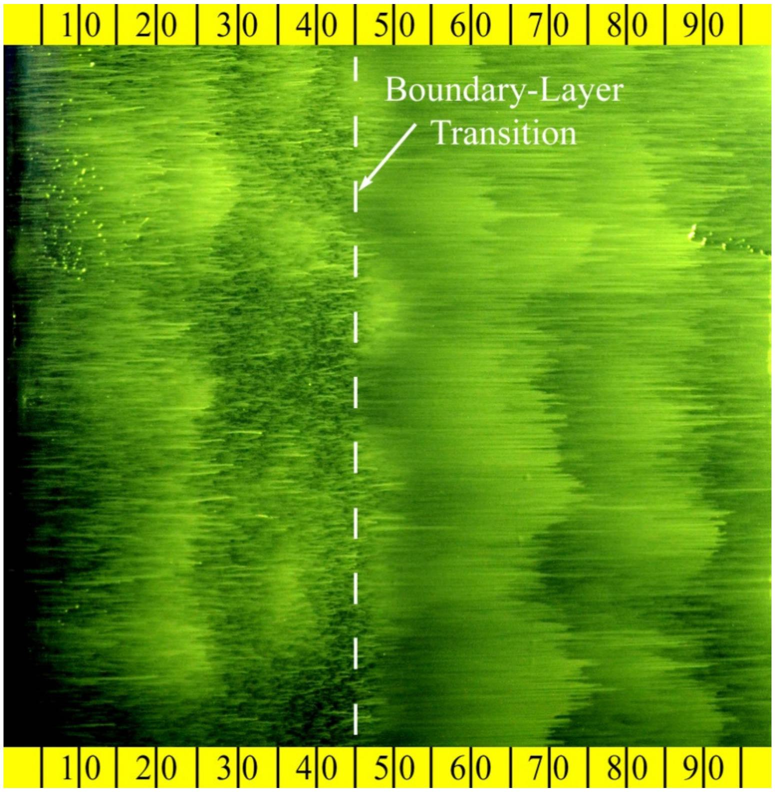

Fig. 4.9 Surface oil flow visualization image for clean NACA 0012 airfoil at $\alpha = 0°$.

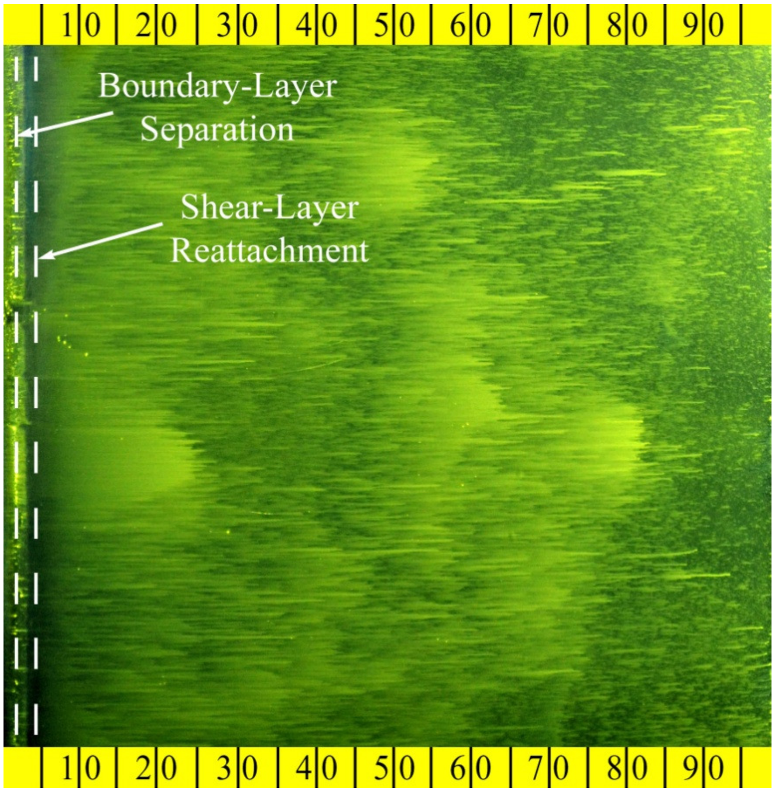

Fig. 4.10 Surface oil flow visualization image for clean NACA 0012 airfoil at $\alpha = 8°$.

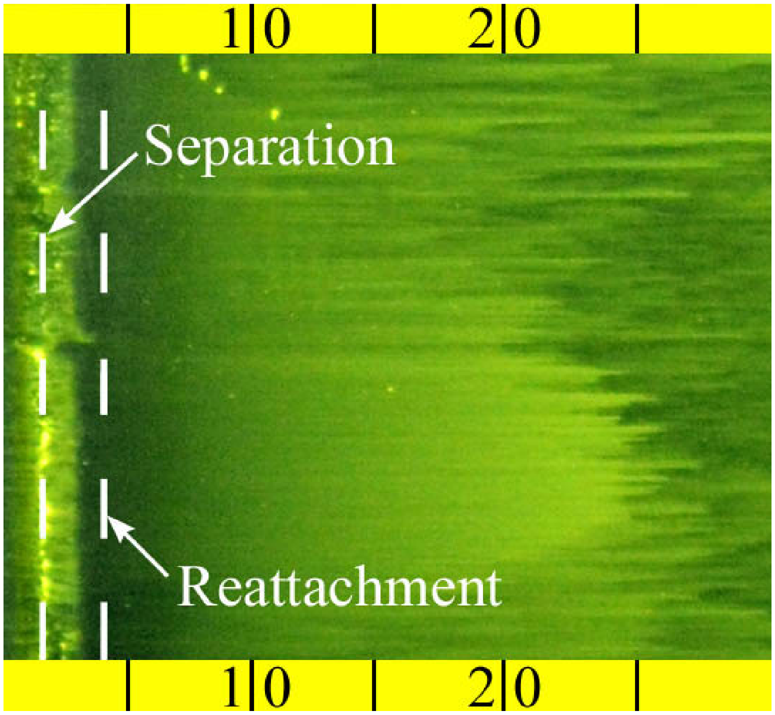

Fig. 4.11 Close view of surface oil flow visualization showing leading-edge separation bubble on clean NACA 0012 airfoil at $\alpha = 8°$.

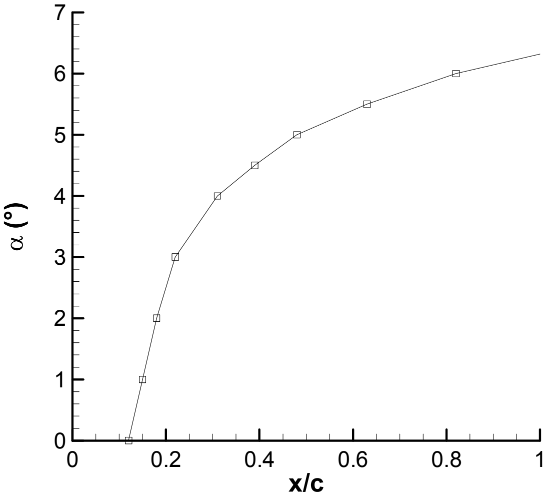

Fig. 4.12 Time-averaged location of shear-layer reattachment for 0° ≤ α ≤ α_{stall}, determined from surface oil flow visualization for NACA 0012 airfoil with leading-edge horn-ice shape (k/c = 0.0202).

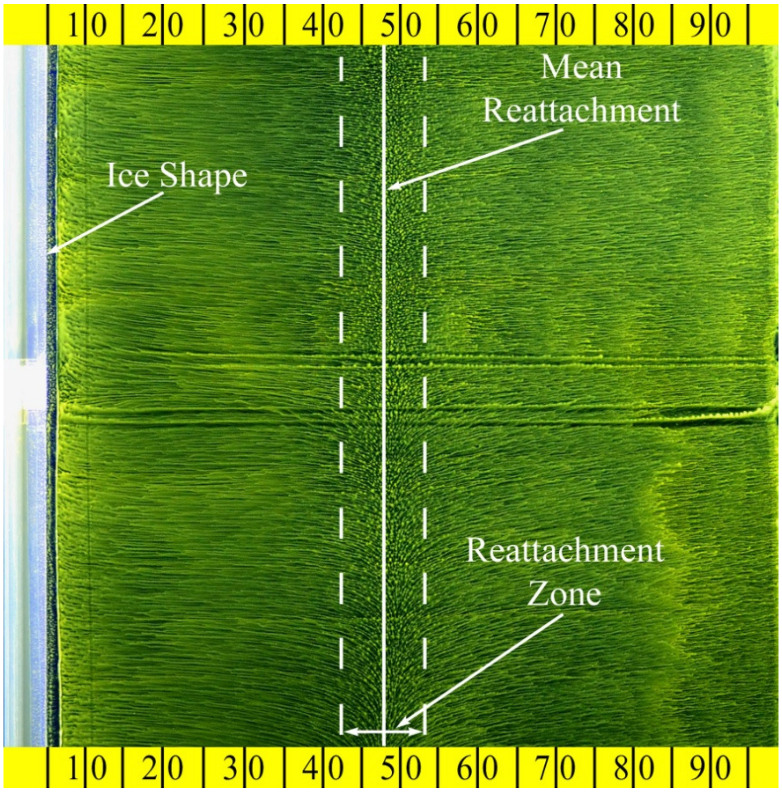

Fig. 4.13 Surface oil flow visualization image of horn-ice case at α = 5°.

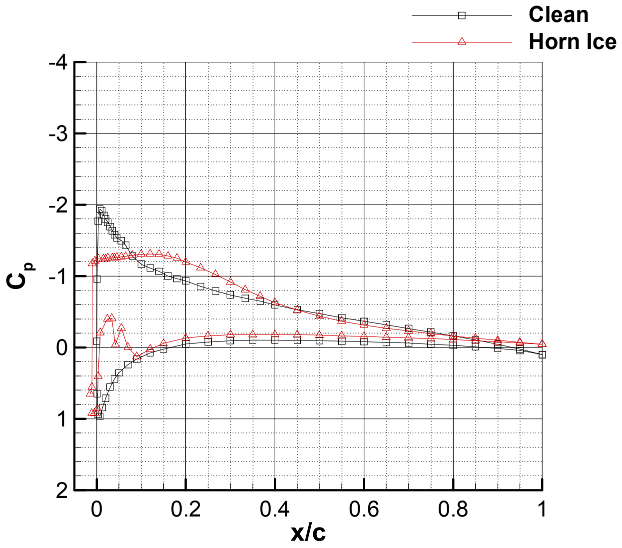

Fig. 4.14 NACA 0012 airfoil C_p distribution at $\alpha = 5°$ for clean and horn-ice cases.

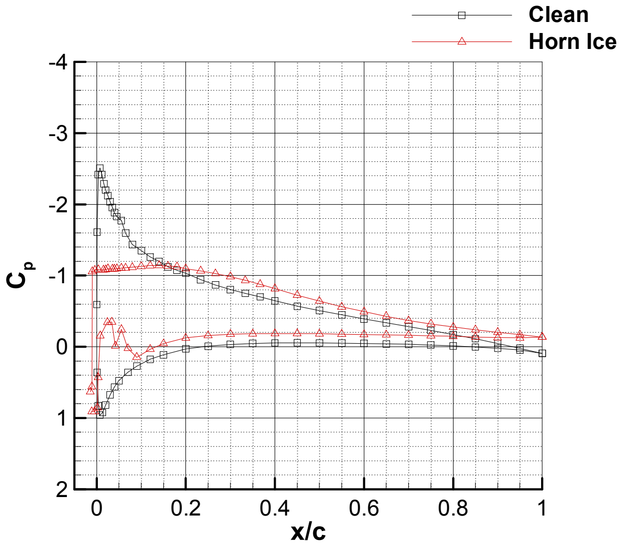

Fig. 4.15 NACA 0012 airfoil C_p distribution at $\alpha = 6°$ for clean and horn-ice cases.

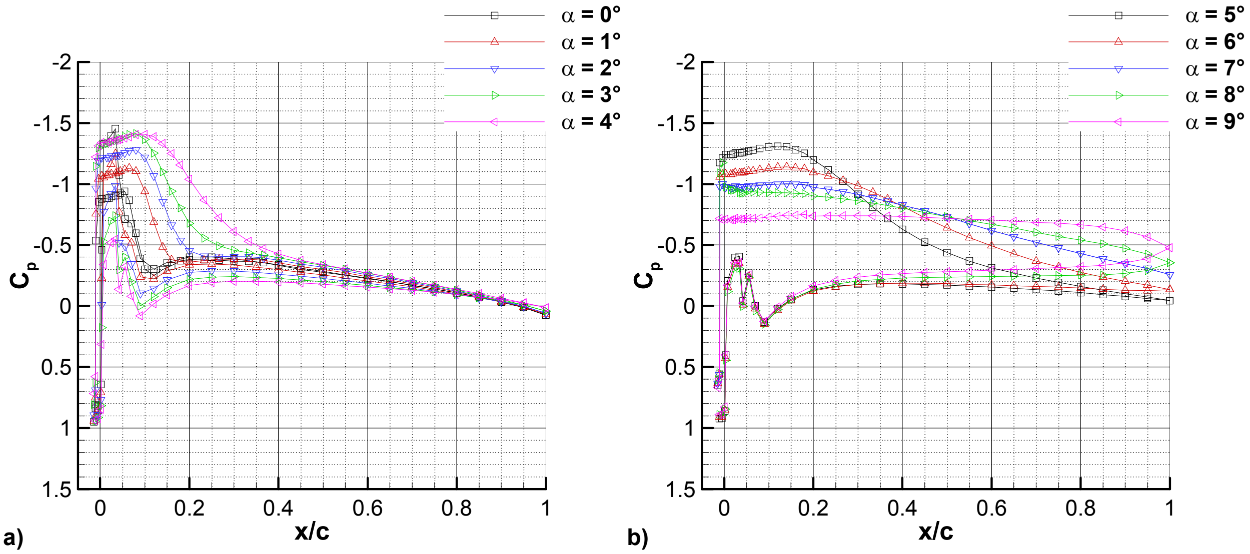

Fig. 4.16 C_p distributions for NACA 0012 airfoil with leading-edge horn-ice shape: a) angle-of-attack range from $\alpha = 0°$ to $\alpha = 4°$, b) angle-of-attack range from $\alpha = 5°$ to $\alpha = 9°$.

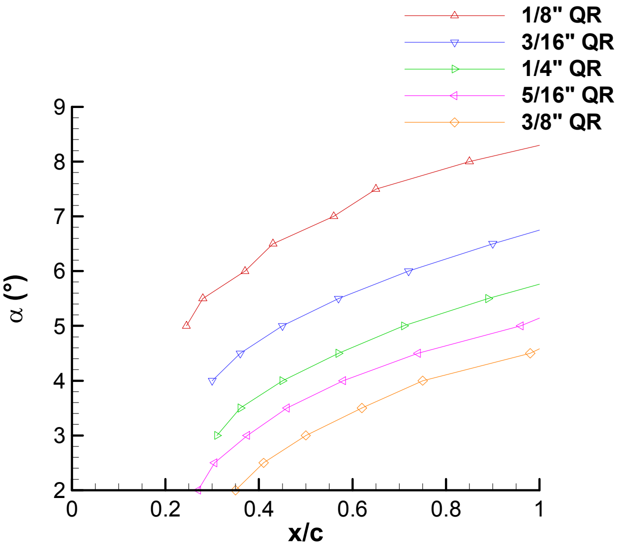

Fig. 4.17 Time-averaged shear-layer reattachment location determined from surface oil flow visualization for NACA 0012 airfoil with various sized quarter-round geometries placed at $x/c = 0.02$ on the airfoil model upper surface.

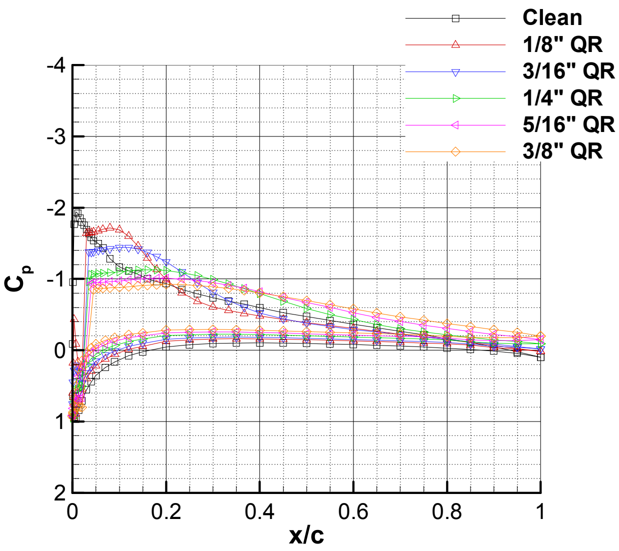

Fig. 4.18 NACA 0012 airfoil C_p distribution at $\alpha = 5°$ for clean case and with various sized quarter-round geometries placed at $x/c = 0.02$ on the airfoil model upper surface.

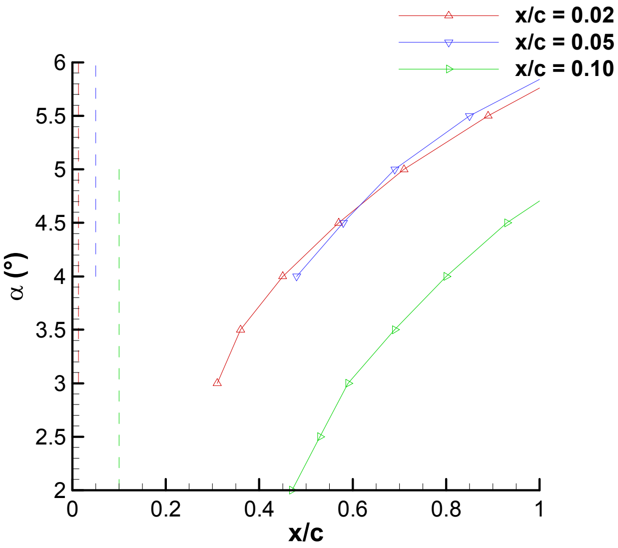

Fig. 4.19 Time-averaged shear-layer reattachment location determined from surface oil flow visualization for NACA 0012 airfoil with 1/4 in. quarter-round geometry placed at various locations on airfoil model upper surface; chordwise location of the tip of the 1/4 in. quarter-round geometry (assumed separation location) shown for each case with vertical dashed line in color corresponding to figure legend.

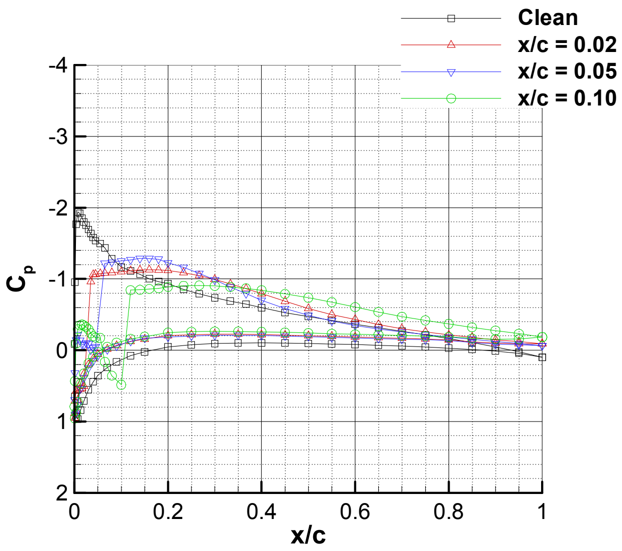

Fig. 4.20 NACA 0012 airfoil C_p distribution at $\alpha = 5°$ for clean case and with 1/4 in. quarter-round geometry placed at various locations on airfoil model upper surface.

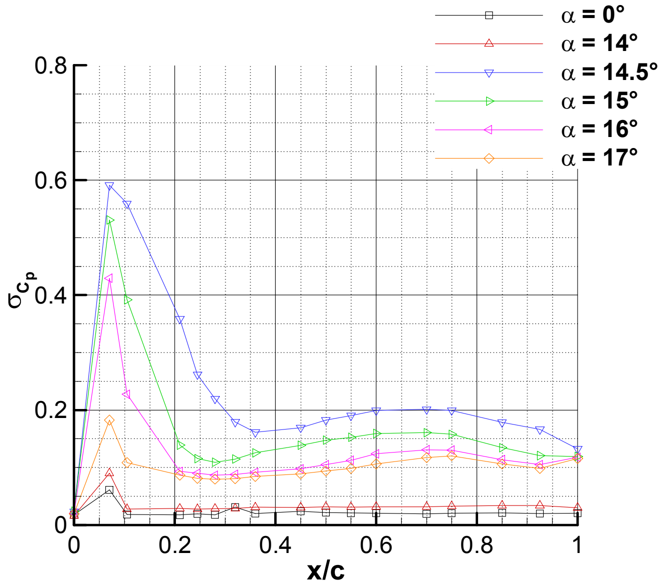

Fig. 4.21 Clean NACA 0012 airfoil upper surface σ_{C_p} distribution.

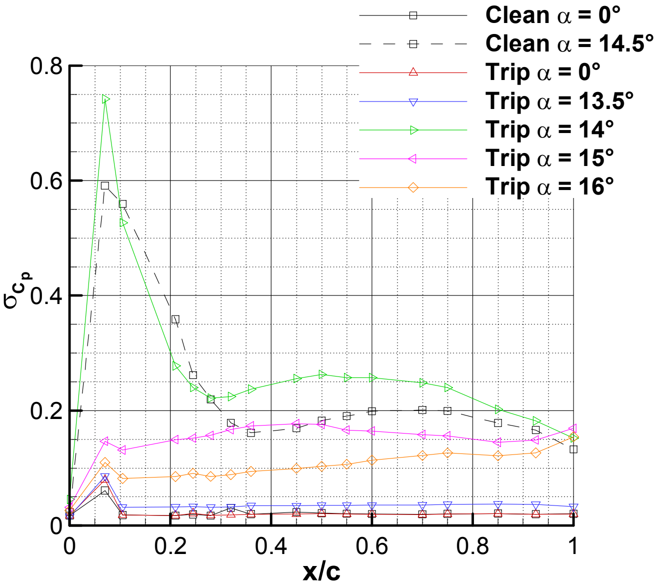

Fig. 4.22 Upper surface σ_{C_p} distributions for NACA 0012 airfoil with boundary-layer trips.

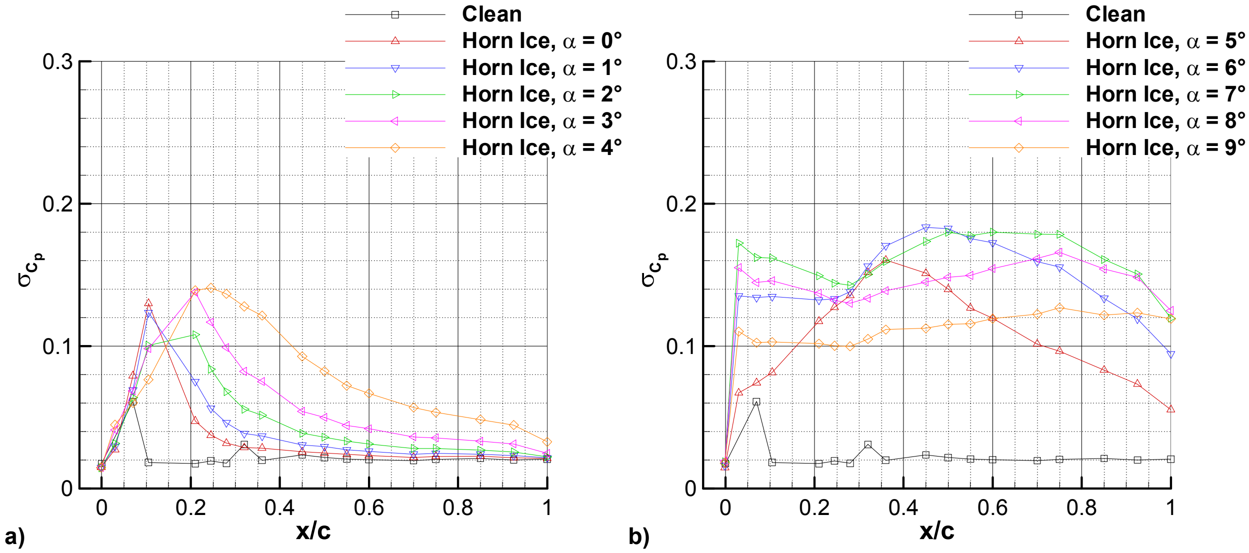

Fig. 4.23 Upper surface σ_{C_p} distributions for NACA 0012 airfoil with horn-ice shape (clean airfoil σ_{C_p} distribution at $\alpha = 0°$ provided for reference), angle-of-attack range from: a) $\alpha = 0°$ to $\alpha = 4°$, b) $\alpha = 5°$ to $\alpha = 9°$.

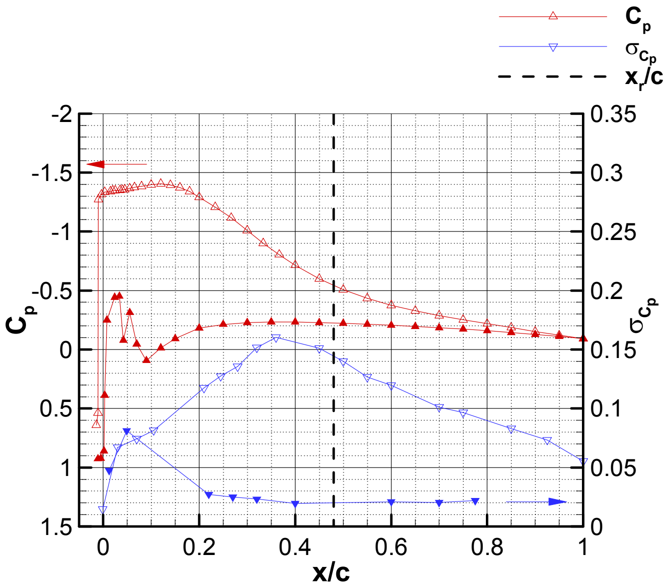

Fig. 4.24 Distribution of C_p and σ_{C_p} for horn-ice case at $\alpha = 5°$, with time-averaged shear-layer reattachment location on upper surface; lower surface marked by filled symbols.

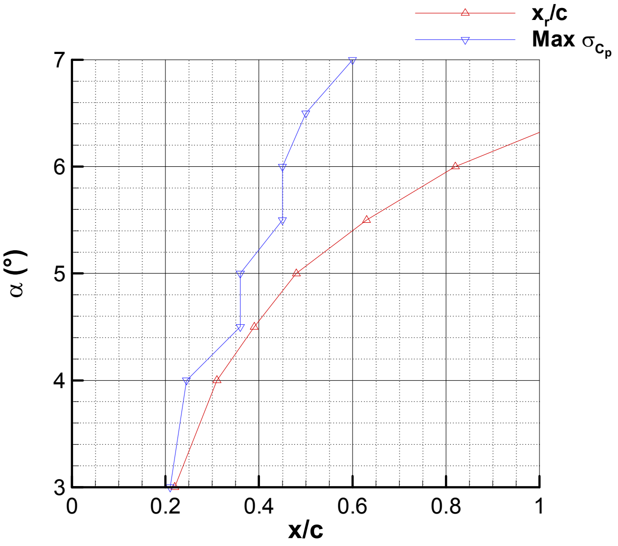

Fig. 4.25 Comparison of chordwise location of mean reattachment on airfoil upper surface and maximum σ_{C_p} for NACA 0012 airfoil with leading-edge horn-ice shape across for an angle-of-attack range near stall.

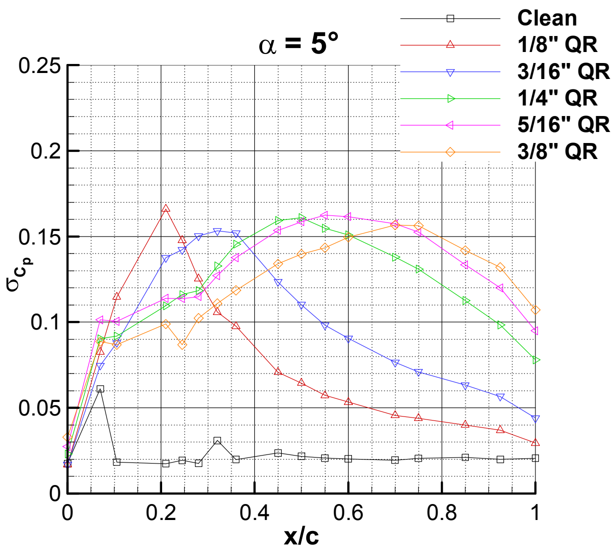

Fig. 4.26 Upper surface σ_{C_p} distributions for NACA 0012 airfoil with quarter-round geometry place at x/c = 0.02 on upper surface (clean airfoil σ_{C_p} distribution at α = 0° provided for reference) at α = 5°.

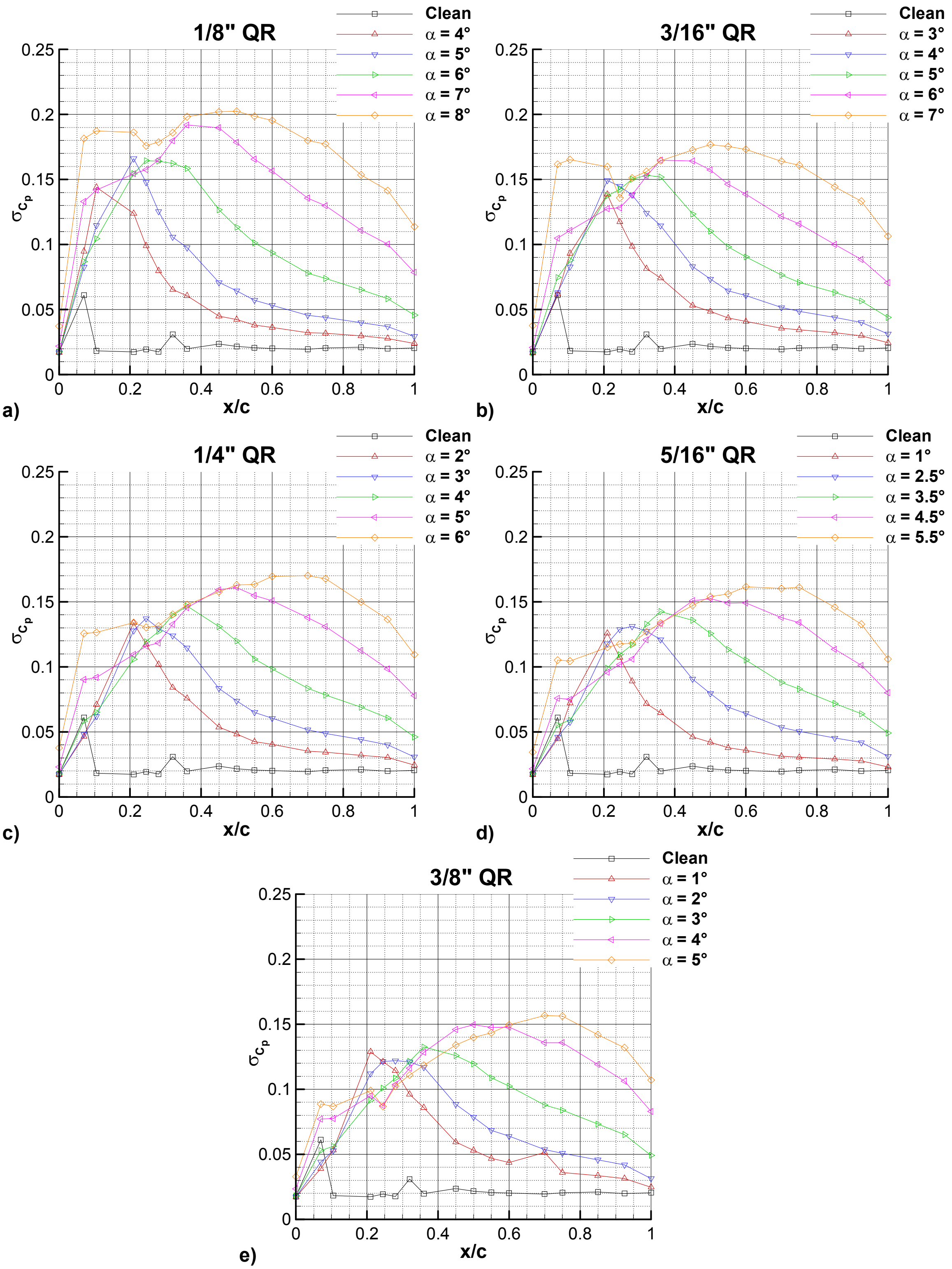

Fig. 4.27 Upper surface σ_{C_p} distributions for NACA 0012 airfoil with quarter-round geometry place at *x*/*c* = 0.02 on upper surface (clean airfoil σ_{C_p} distribution at α = 0° provided for reference): a) 1/8 in. quarter round, b) 3/16 in. quarter round, c) 1/4 in. quarter round, d) 5/16 in. quarter round, e) 3/8 in. quarter round.

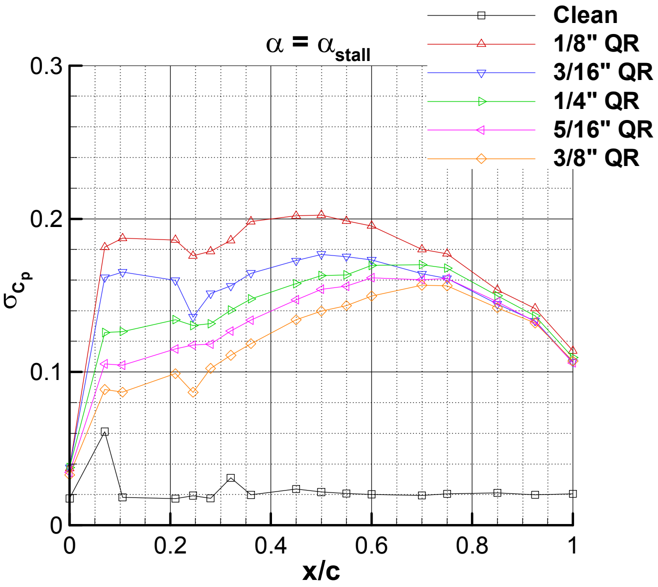

Fig. 4.28 Upper surface σ_{C_p} distributions at α_{stall} for NACA 0012 airfoil with quarter-round geometry placed at x/c = 0.02 on upper surface (clean airfoil σ_{C_p} distribution at α = 0° provided for reference).

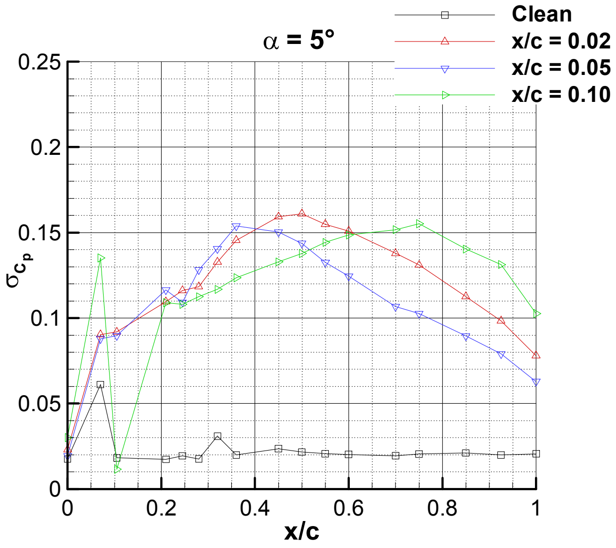

Fig. 4.29 Upper surface σ_{C_p} distributions for NACA 0012 airfoil with 1/4 in. quarter-round geometry place at various locations on upper surface (clean airfoil σ_{C_p} distribution at α = 0° provided for reference) at α = 5°.

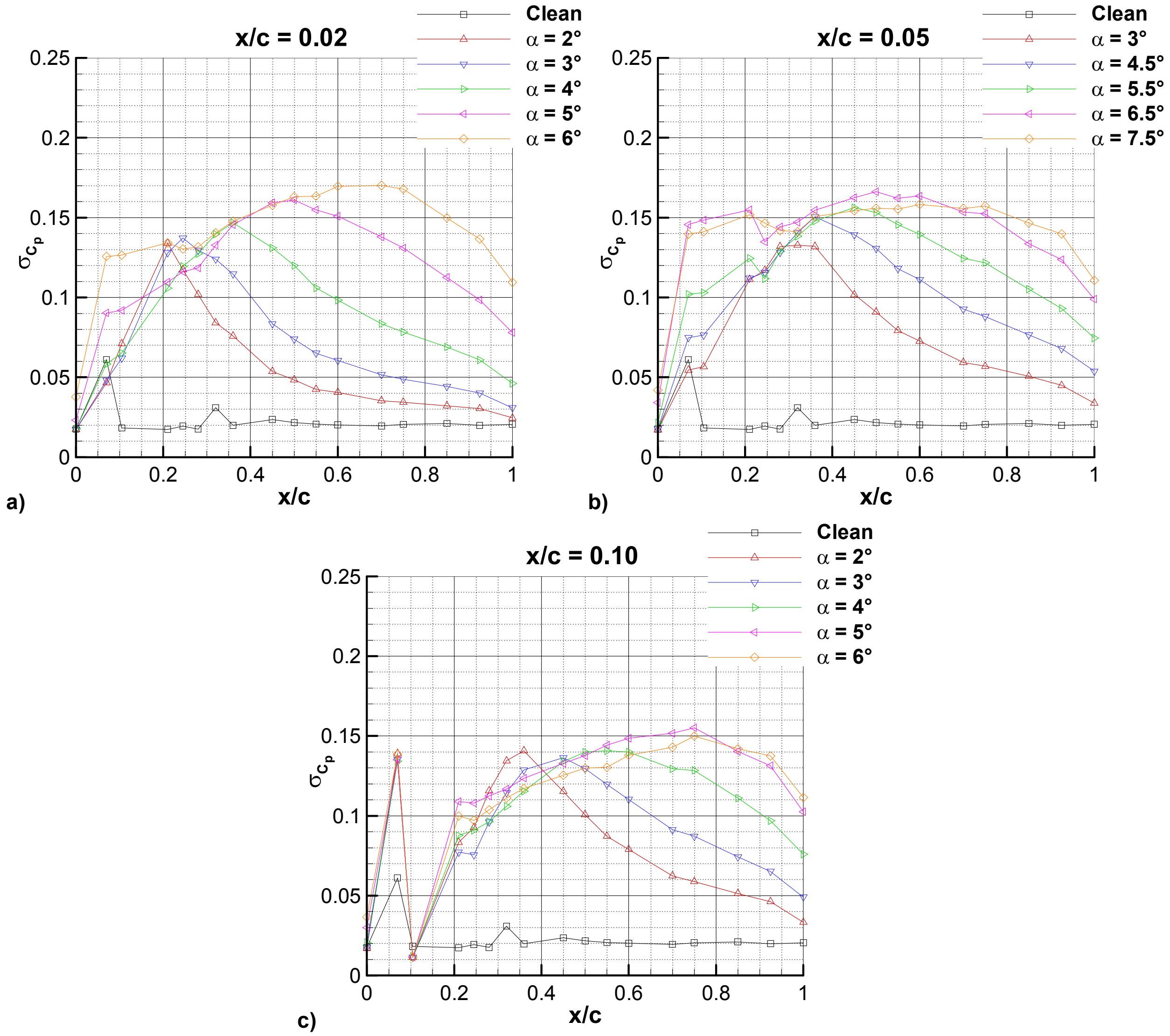

Fig. 4.30 Upper surface σ_{C_p} distributions for NACA 0012 airfoil with 1/4 in. quarter-round geometry place at various locations on upper surface (clean airfoil σ_{C_p} distribution at $\alpha = 0°$ provided for reference): a) quarter round at $x/c = 0.02$, b) quarter round at $x/c = 0.05$, c) quarter round at $x/c = 0.10$.

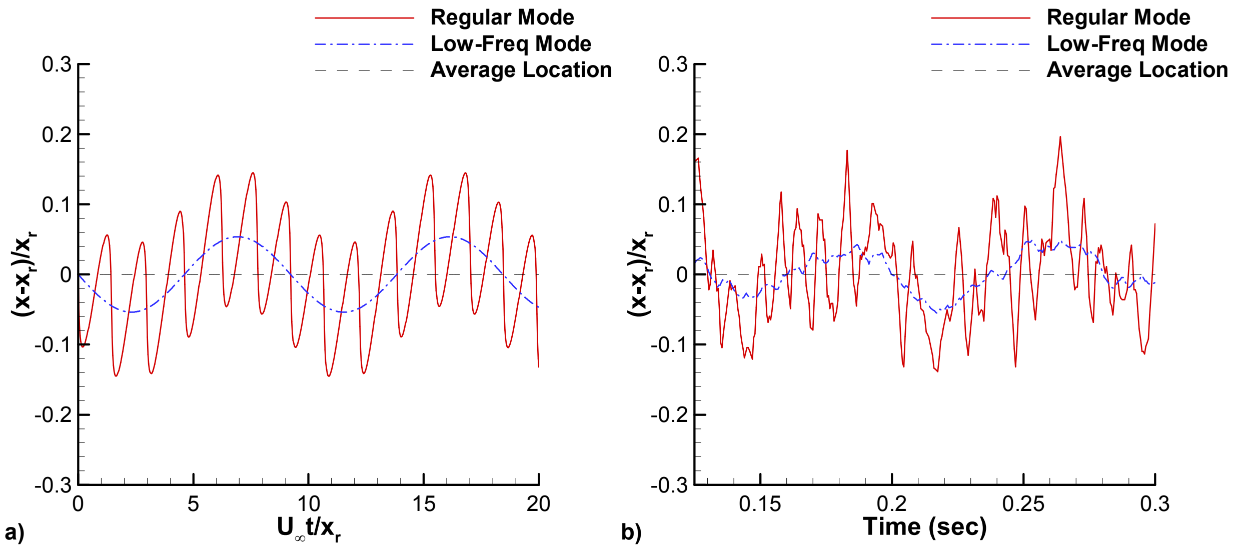

Fig. 4.31 Comparison of unsteady shear-layer reattachment location: a) reproduced using the model of Kiya and Sasaki[31] downstream of backward-facing step, b) determined using hot-film array in current investigation for NACA 0012 airfoil with horn-ice shape at $\alpha = 5°$.

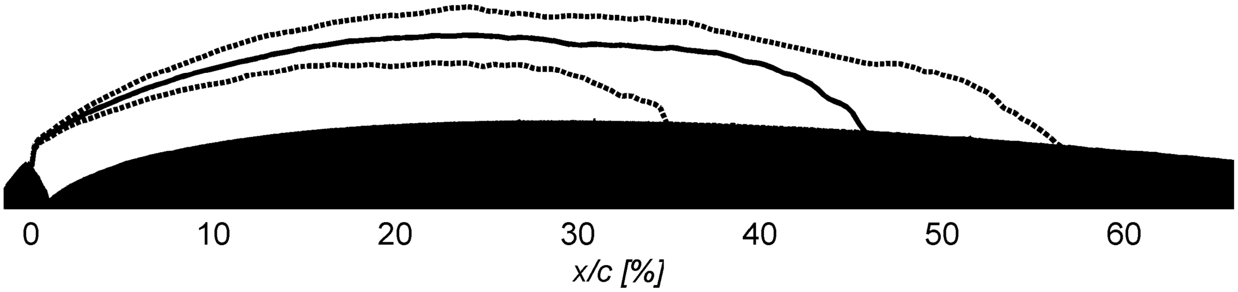

Fig. 4.32 Average shear-layer reattachment location and reattachment zone for NACA 0012 airfoil with horn-ice shape at $\alpha = 5°$, from the PIV results of Jacobs.[23]

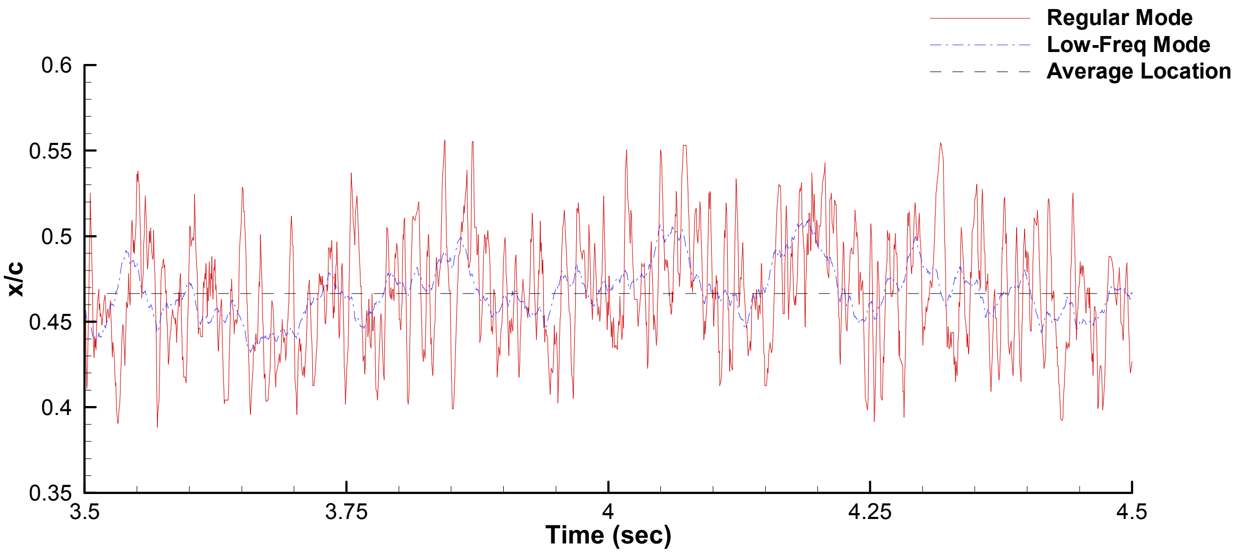

Fig. 4.33 Unsteady shear-layer reattachment location determined using hot-film array for NACA 0012 airfoil with horn-ice shape at α = 5°.

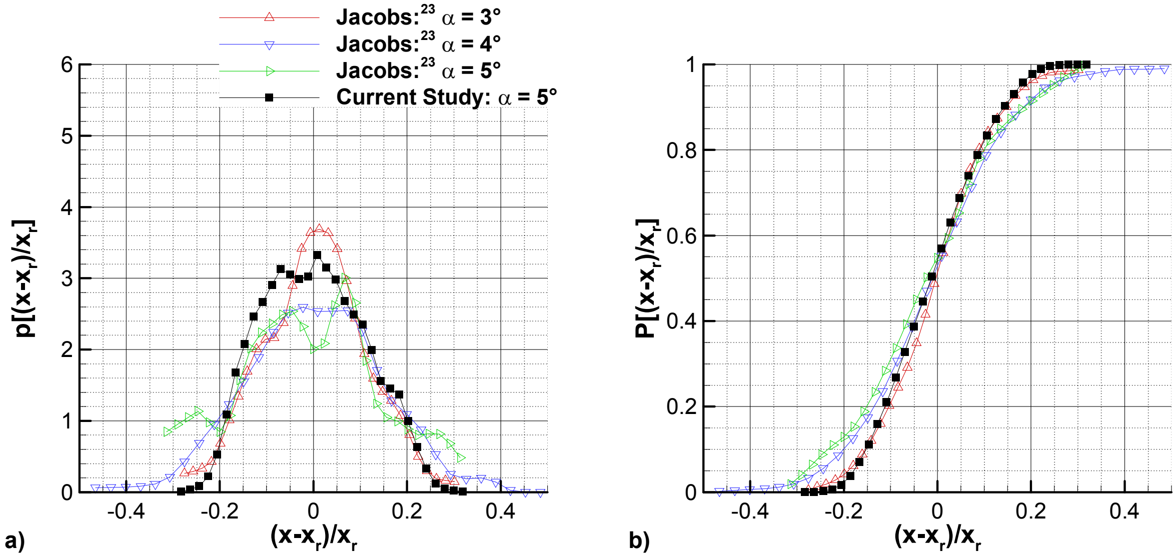

Fig. 4.34 a) Probability density (*p*) and b) cumulative distribution (*P*) functions of the normalized unsteady reattachment location on an NACA 0012 airfoil downstream of a horn-ice shape; comparisons provided after Jacobs.[23]

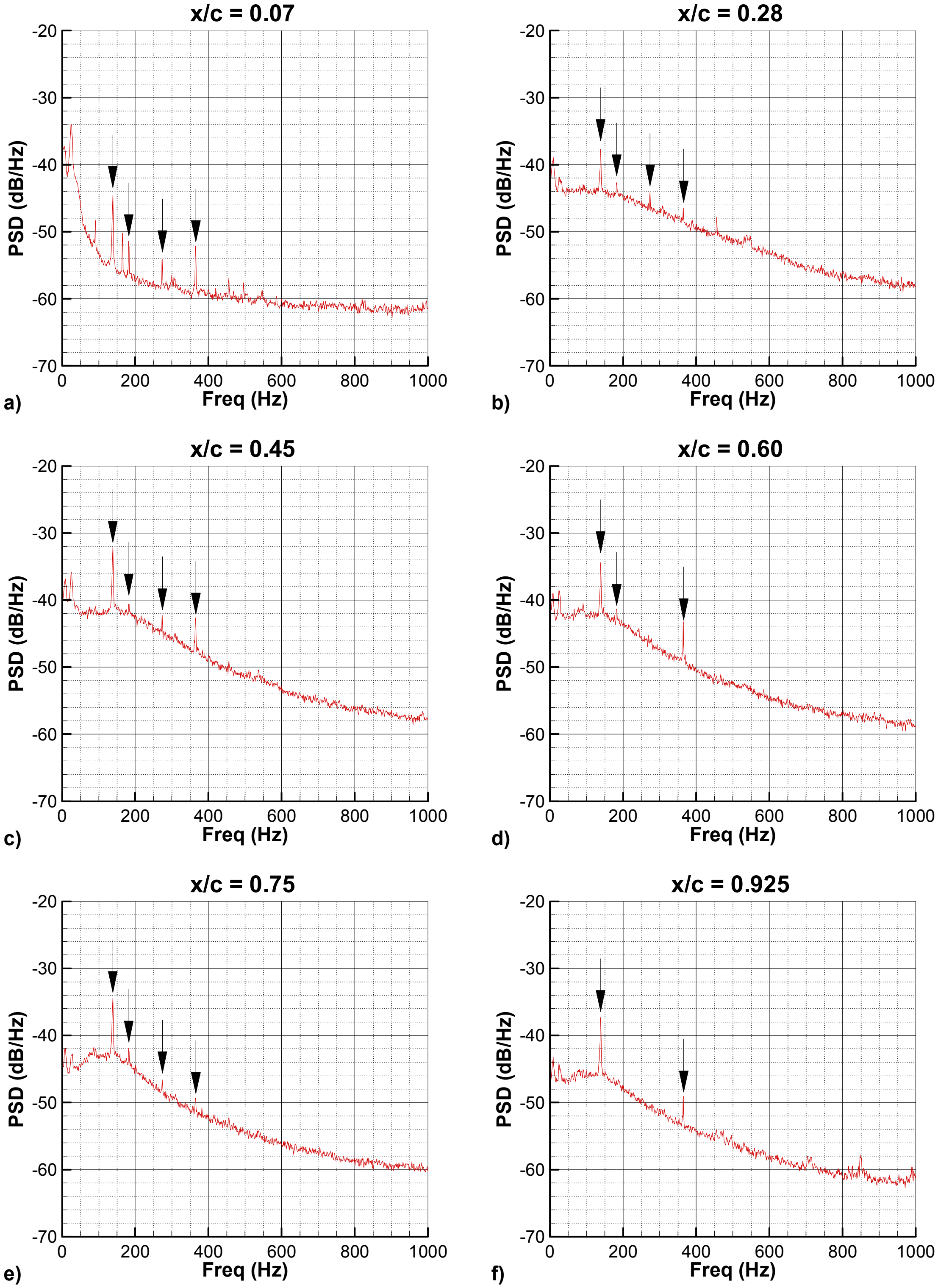

Fig. 4.35 PSD of unsteady upper surface C_p for airfoil with horn-ice shape at $\alpha = 5.5°$, frequency resolution of 1 Hz, fan blade and structural frequencies marked by arrows: a) $x/c = 0.07$, b) $x/c = 0.28$, c) $x/c = 0.45$, d) $x/c = 0.60$, e) $x/c = 0.75$, f) $x/c = 0.925$.

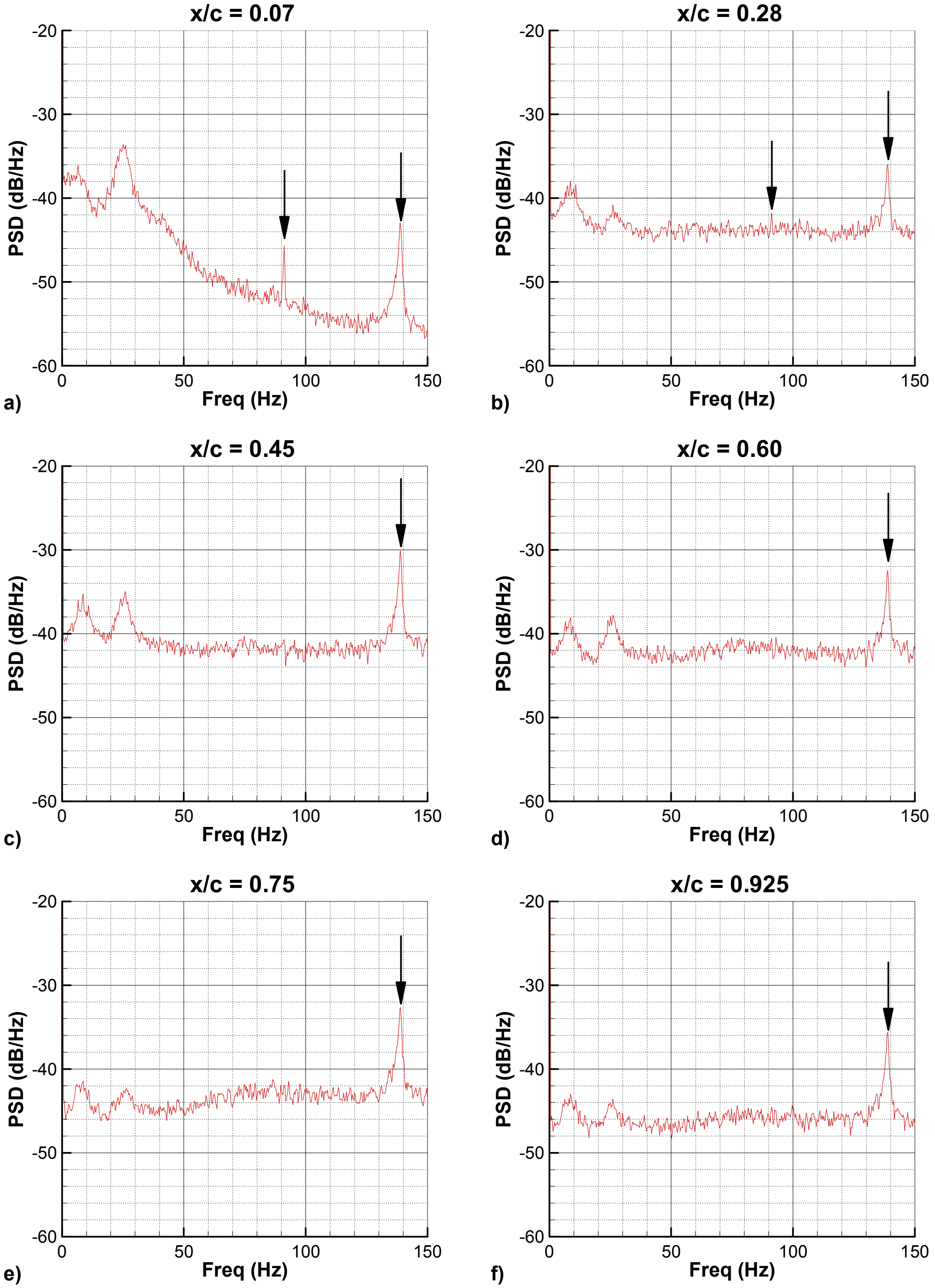

Fig. 4.36 PSD of unsteady upper surface C_p for airfoil with horn-ice shape at $\alpha = 5.5°$, low-frequency region shown with frequency resolution of 0.3 Hz, fan blade and structural frequencies marked by arrows: a) $x/c = 0.07$, b) $x/c = 0.28$, c) $x/c = 0.45$, d) $x/c = 0.60$, e) $x/c = 0.75$, f) $x/c = 0.925$.

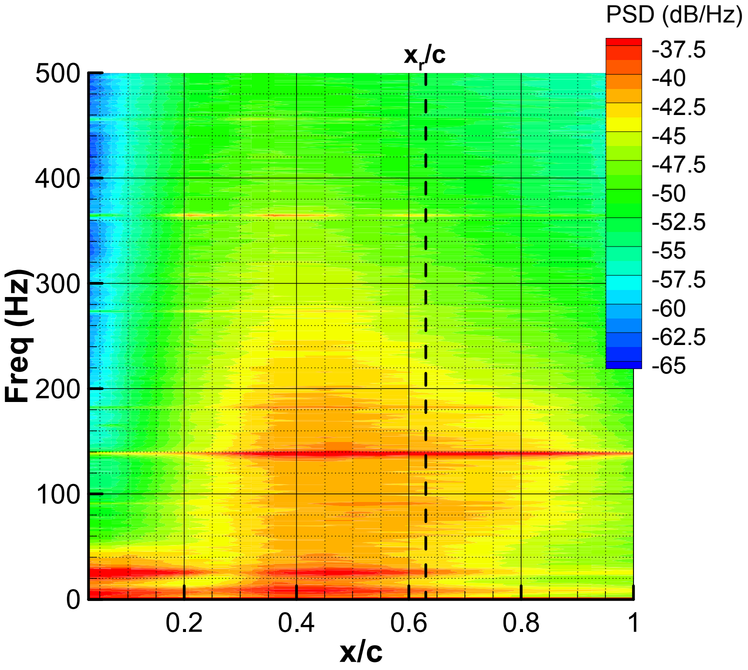

Fig. 4.37 Contour map for PSD of unsteady upper surface C_p across airfoil with horn-ice shape at α = 5.5°, with mean shear-layer reattachment location marked with dotted line.

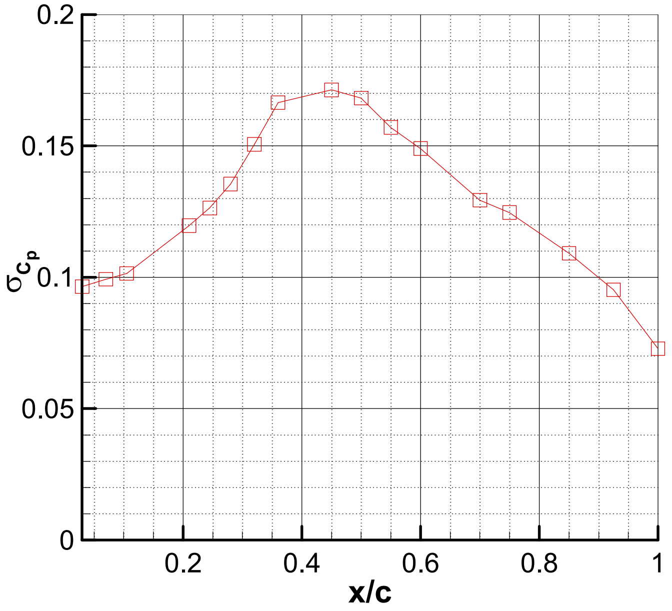

Fig. 4.38 Upper surface σ_{C_p} distribution for airfoil with horn-ice shape at α = 5.5°.

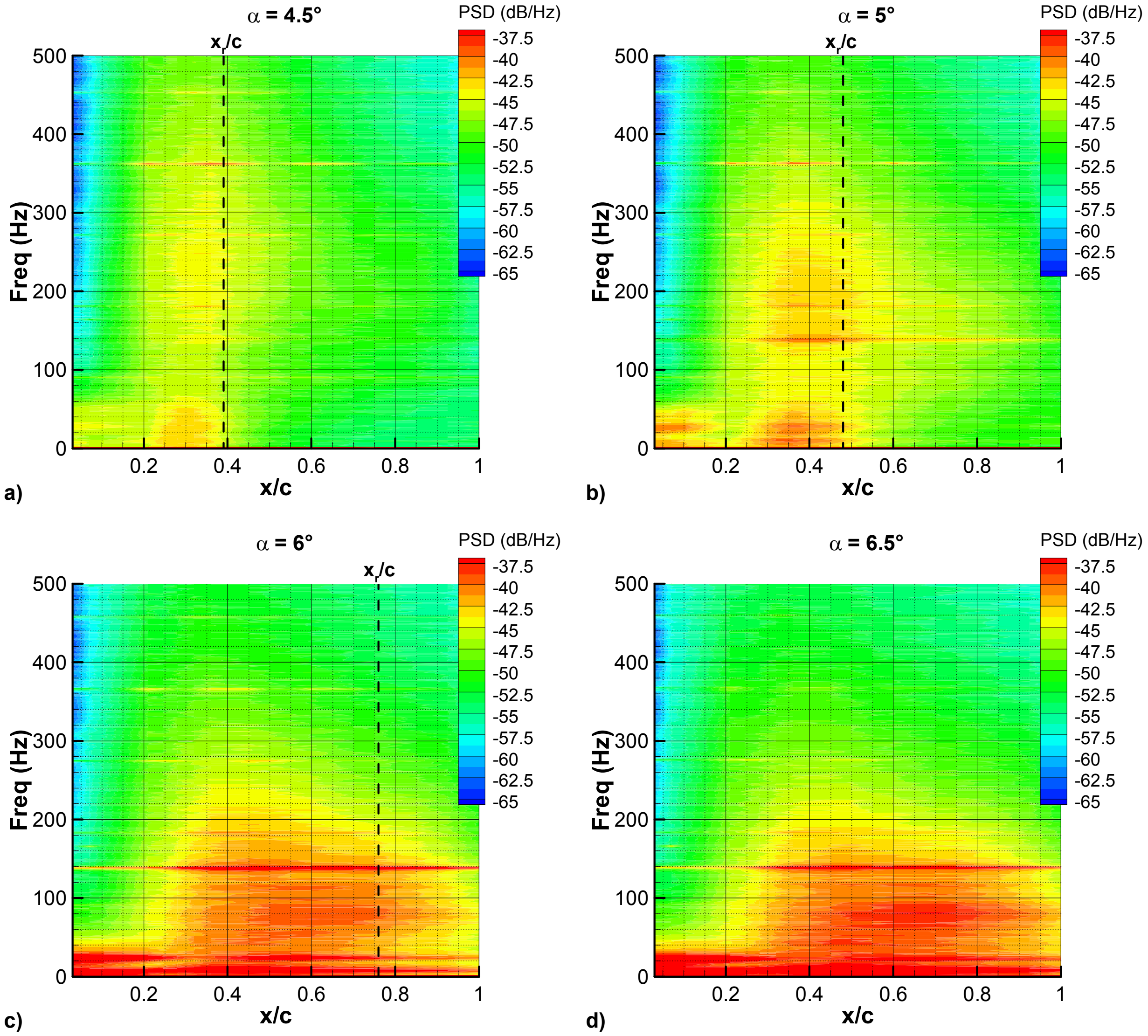

Fig. 4.39 Contour map for PSD of unsteady upper surface C_p across airfoil with horn-ice shape, with mean shear-layer reattachment location marked with dotted line: a) α = 4.5°, b) α = 5°, c) α = 6°, and d) α = 6.5°.

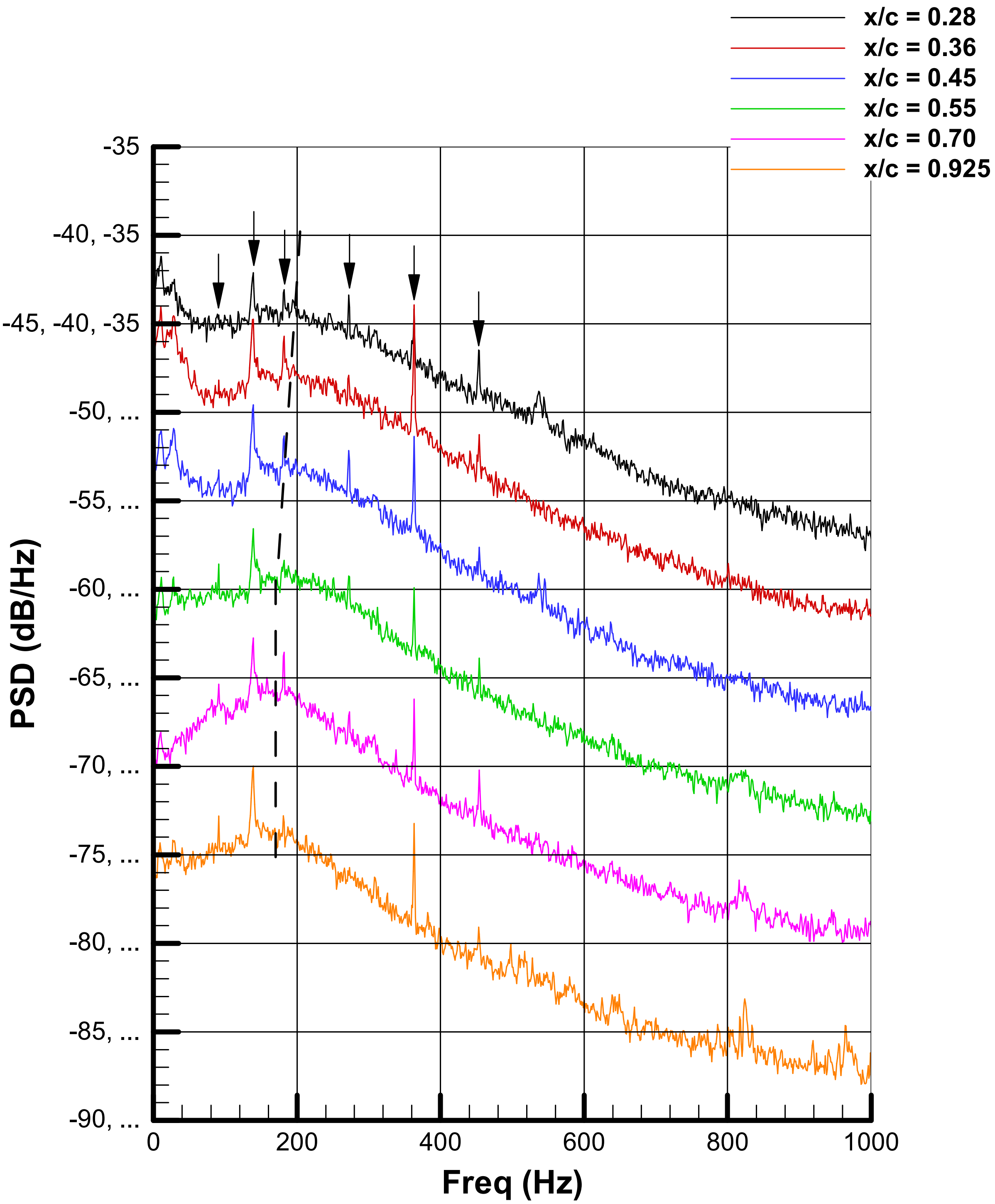

Fig. 4.40 PSDs of C_p for NACA 0012 airfoil with horn-ice shape at α = 5°, frequency resolution of 1 Hz, fan blade and structural frequencies marked by arrows, -5 dB increment in plotted PSD amplitude, approximate progression of the center frequency for regular mode denoted by dashed line.

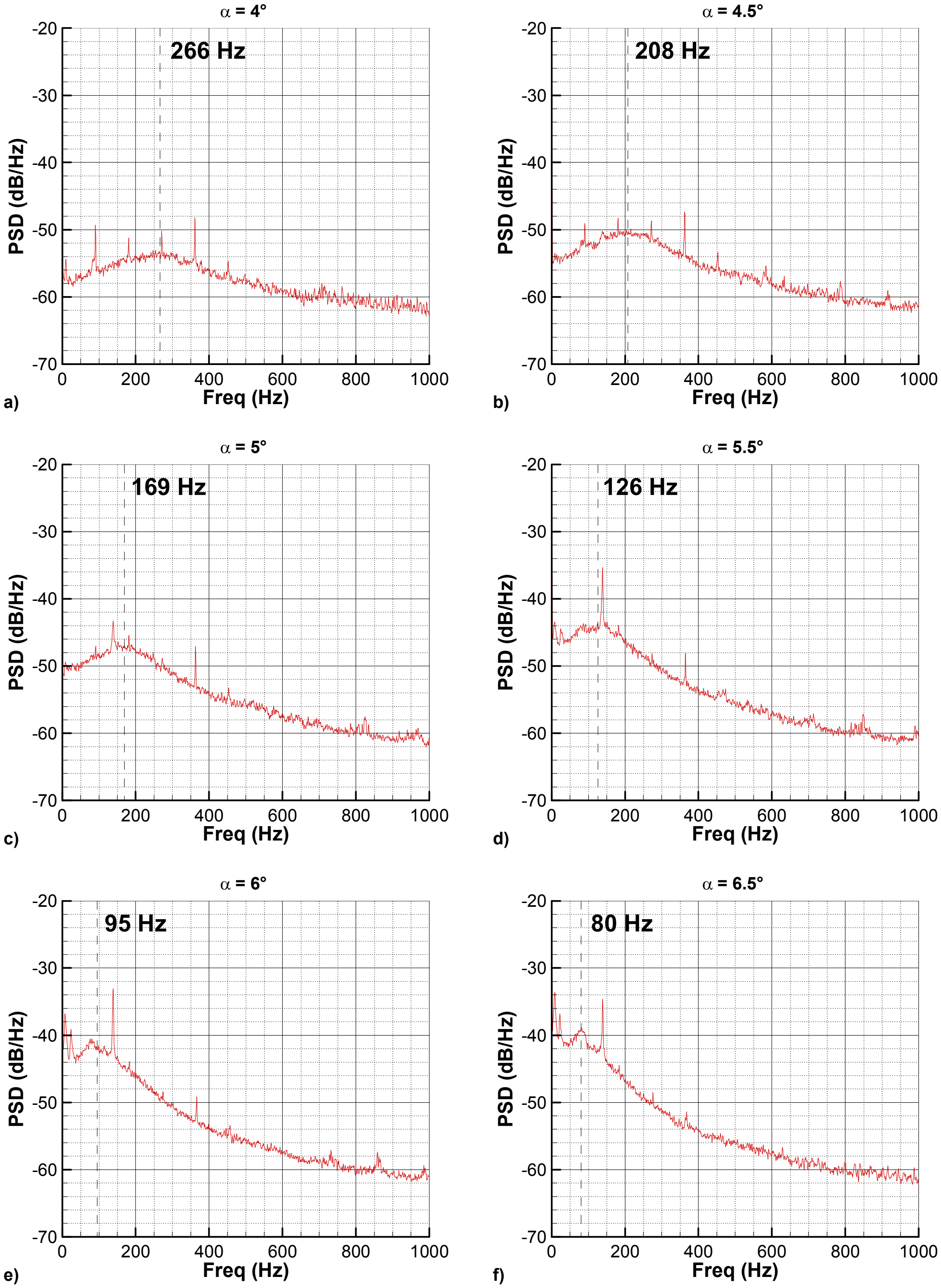

Fig. 4.41 PSD of airfoil C_p at x/c = 0.85 with estimated regular mode center frequency denoted by vertical dashed line: a) α = 4°, b) α = 4.5°, c) α = 5°, d) α = 5.5°, e) α = 6°, f) α = 6.5°.

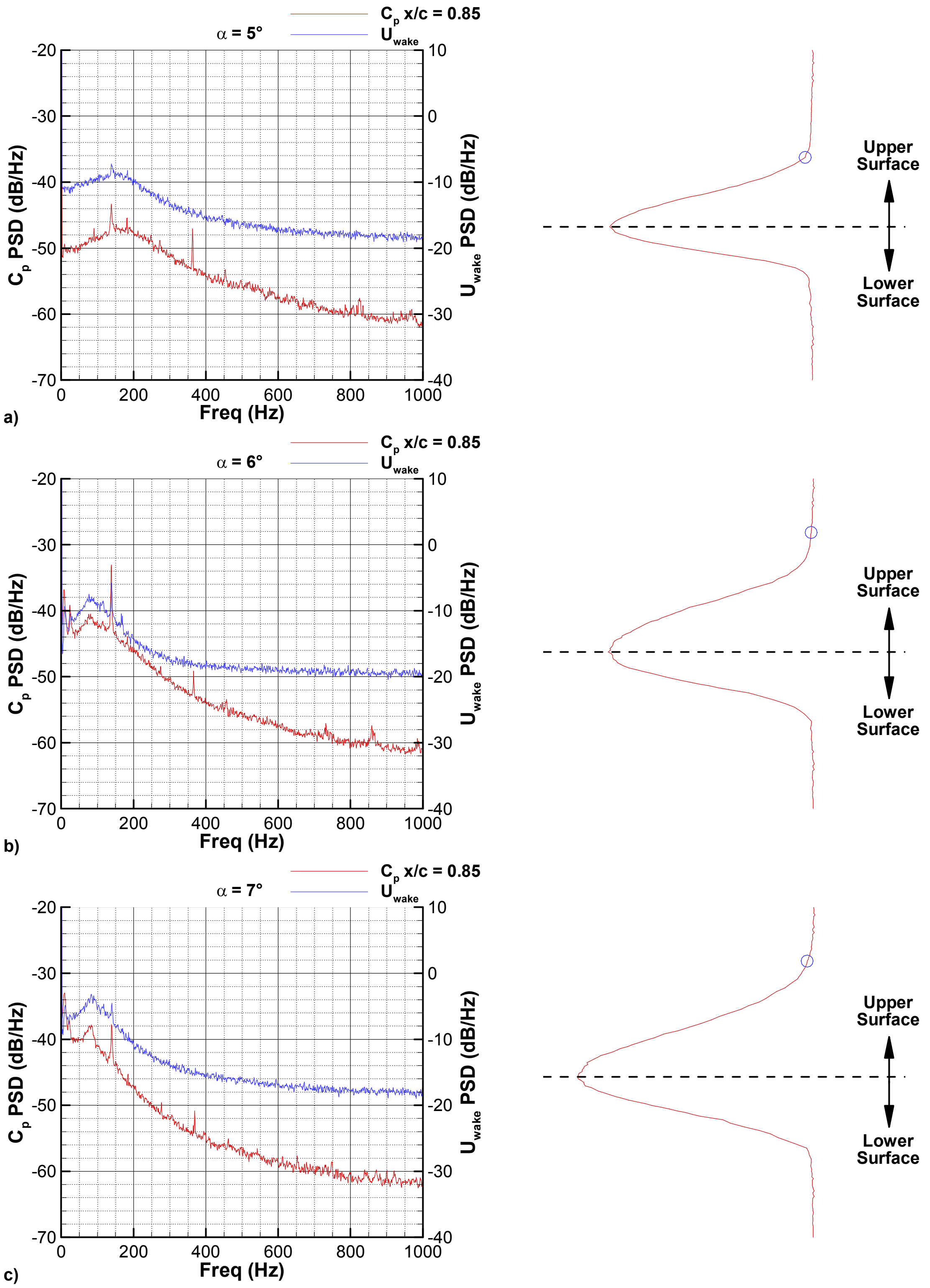

Fig. 4.42 (Left) PSDs showing regular mode spectral peak in airfoil C_p at x/c = 0.85 and U_{wake} at upper-wake edge, (right) wake profile with open circle symbol representing y-location of U_{wake} PSD: a) α = 5°, b) α = 6°, c) α = 7°.

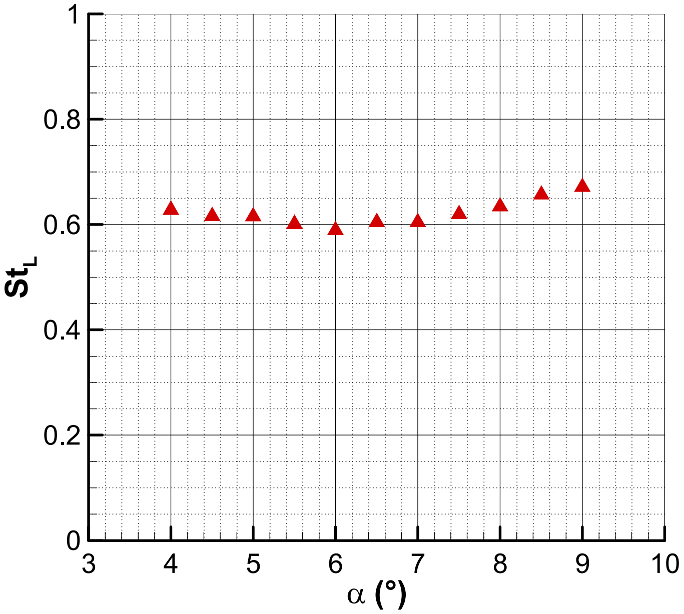

Fig. 4.43 Strouhal number of regular mode for NACA 0012 airfoil with horn-ice shape; St$_L$ calculated using regular mode center frequency peaks from PSD of C_p at $x/c = 0.85$.

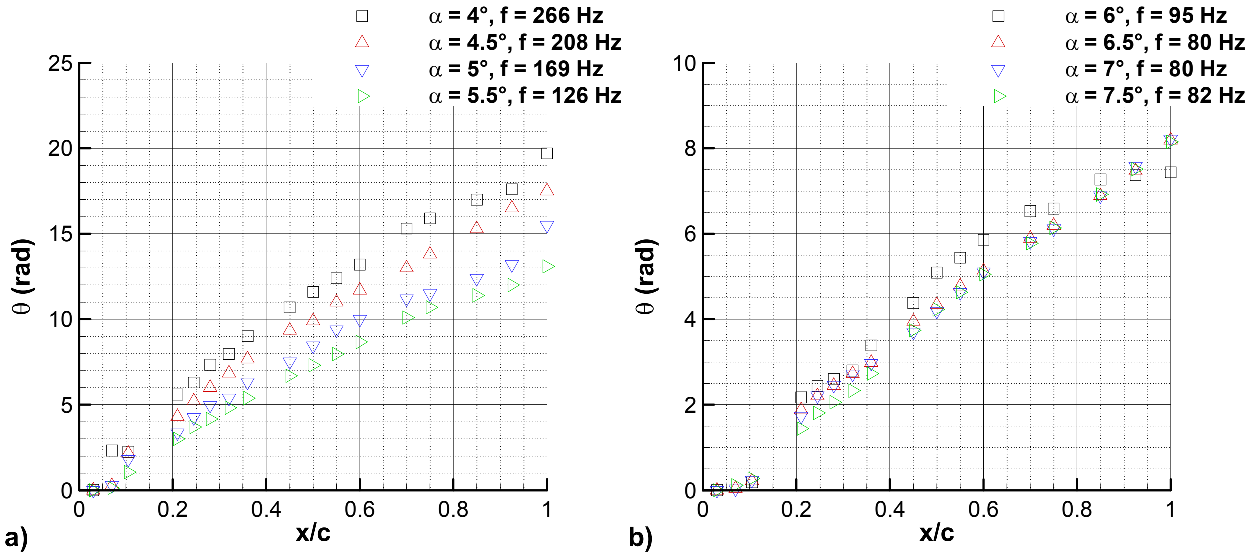

Fig. 4.44 Phase angle distributions for regular mode on NACA 0012 with leading-edge horn-ice shape: a) $\alpha = 4°$ to $\alpha = 5.5°$, b) $\alpha = 6°$ to $\alpha = 7.5°$.

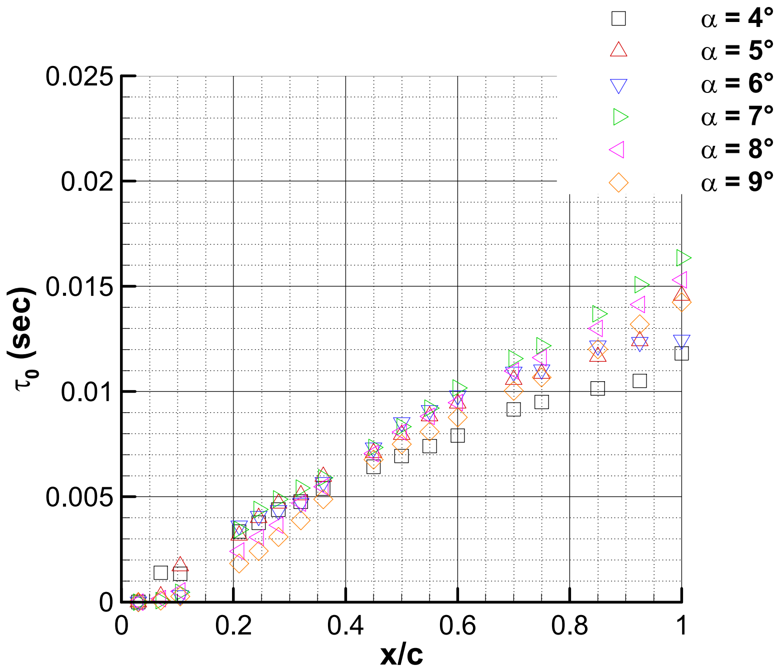

Fig. 4.45 Time delay distributions for regular mode on NACA 0012 with leading-edge horn-ice shape.

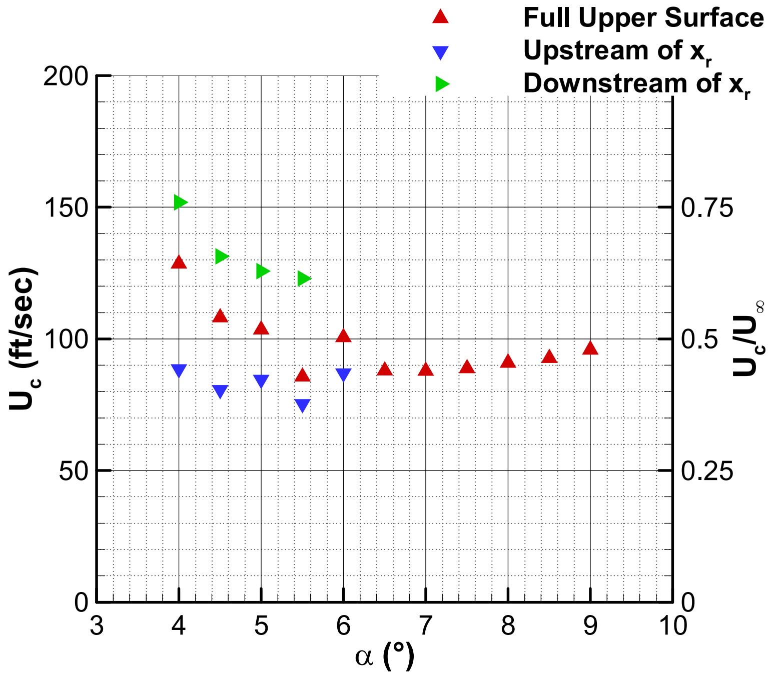

Fig. 4.46 Average vortex convection velocity across airfoil upper surface; for angles of attack with shear-layer reattachment on surface ($\alpha \leq 6°$), convection velocities upstream and downstream of reattachment also shown.

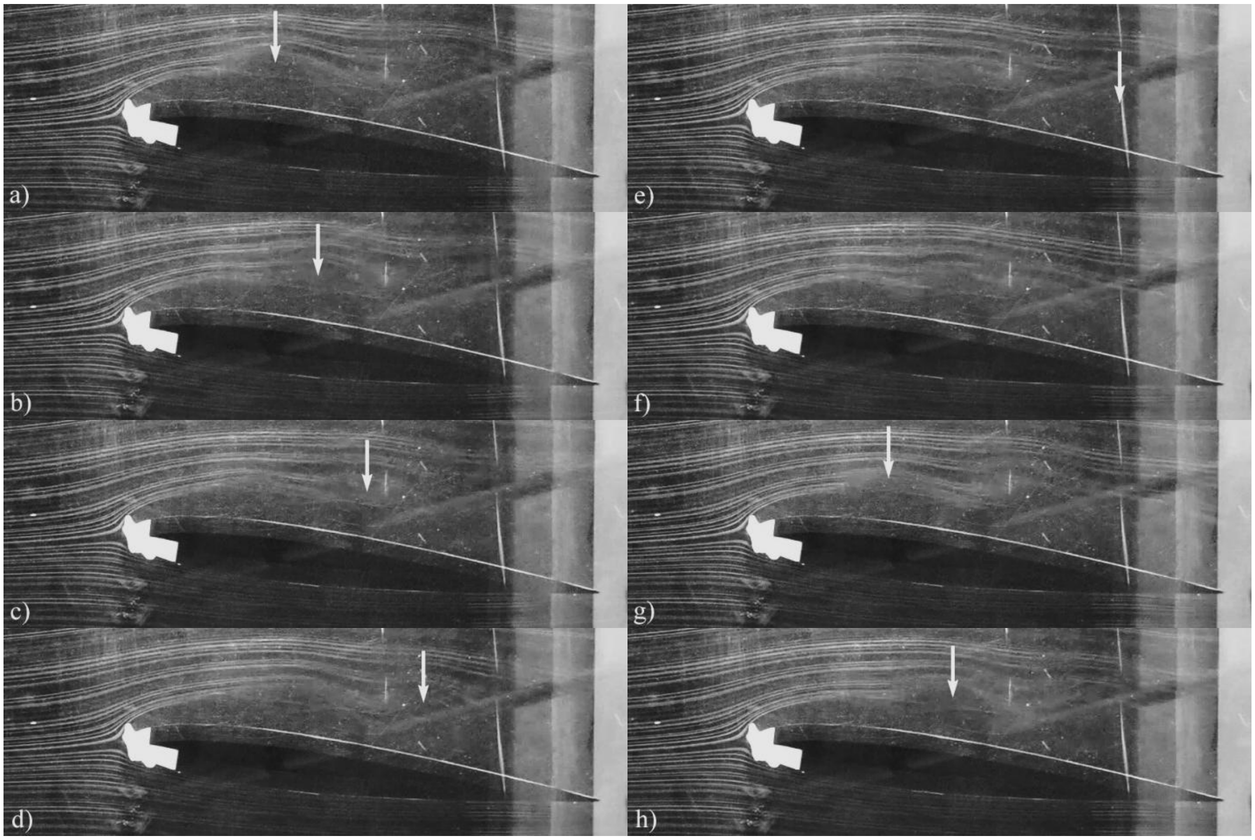

Fig. 4.47 Smoke wire flow visualization of NACA 0012 airfoil with horn-ice shape at $\alpha = 7°$, location of large-scale vortices indicated using white arrows: a) $t = 0$ sec, b) $t = 0.033$ sec, c) $t = 0.067$ sec, d) $t = 0.10$ sec, e) $t = 0.133$ sec, f) $t = 0.167$ sec, g) $t = 0.20$ sec, h) $t = 0.233$ sec.

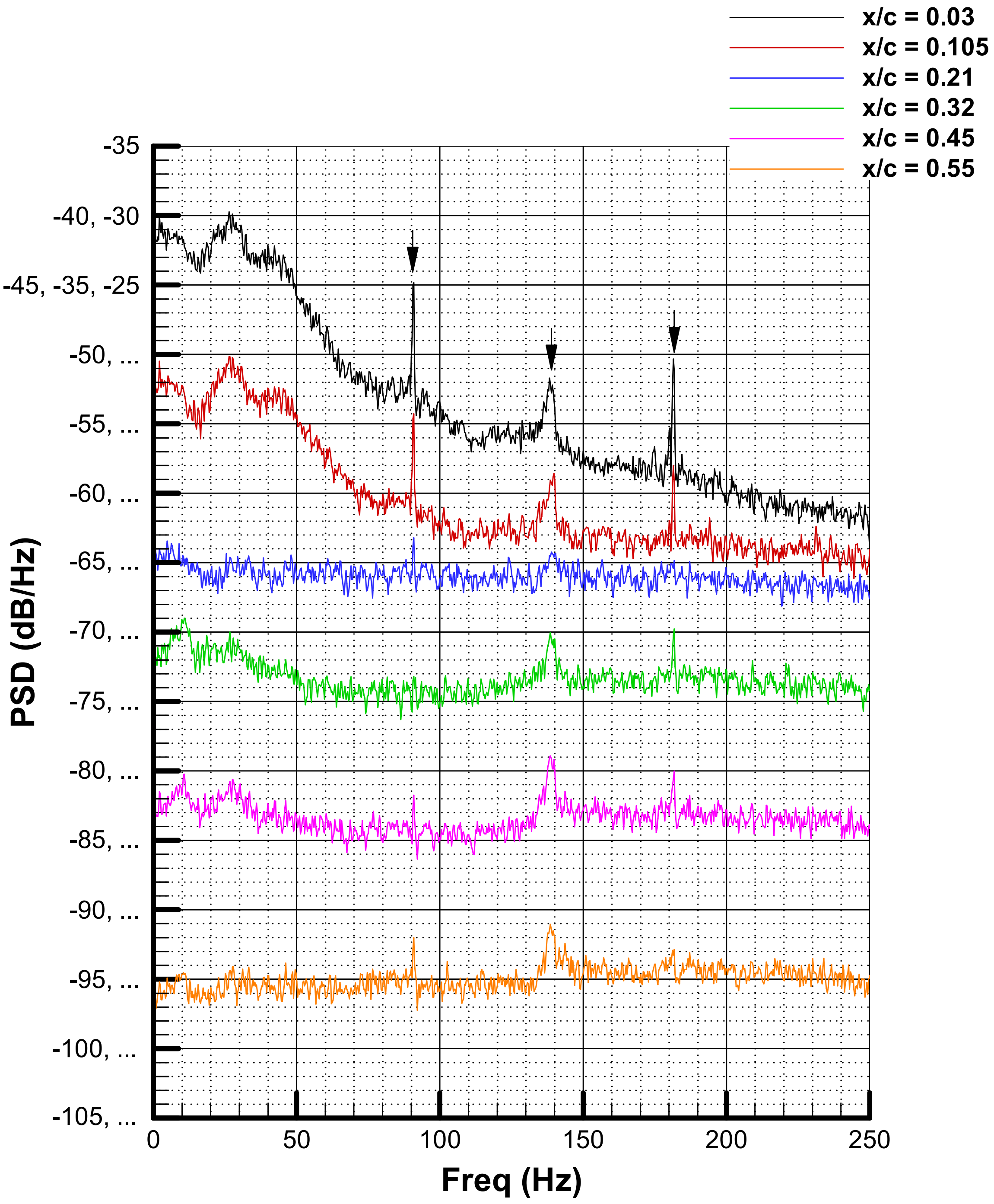

Fig. 4.48 PSDs of C_p for NACA 0012 airfoil with horn-ice shape at α = 5°, frequency resolution of 0.3 Hz, fan blade and structural frequencies marked by arrows, -10 dB increment in plotted PSD amplitude.

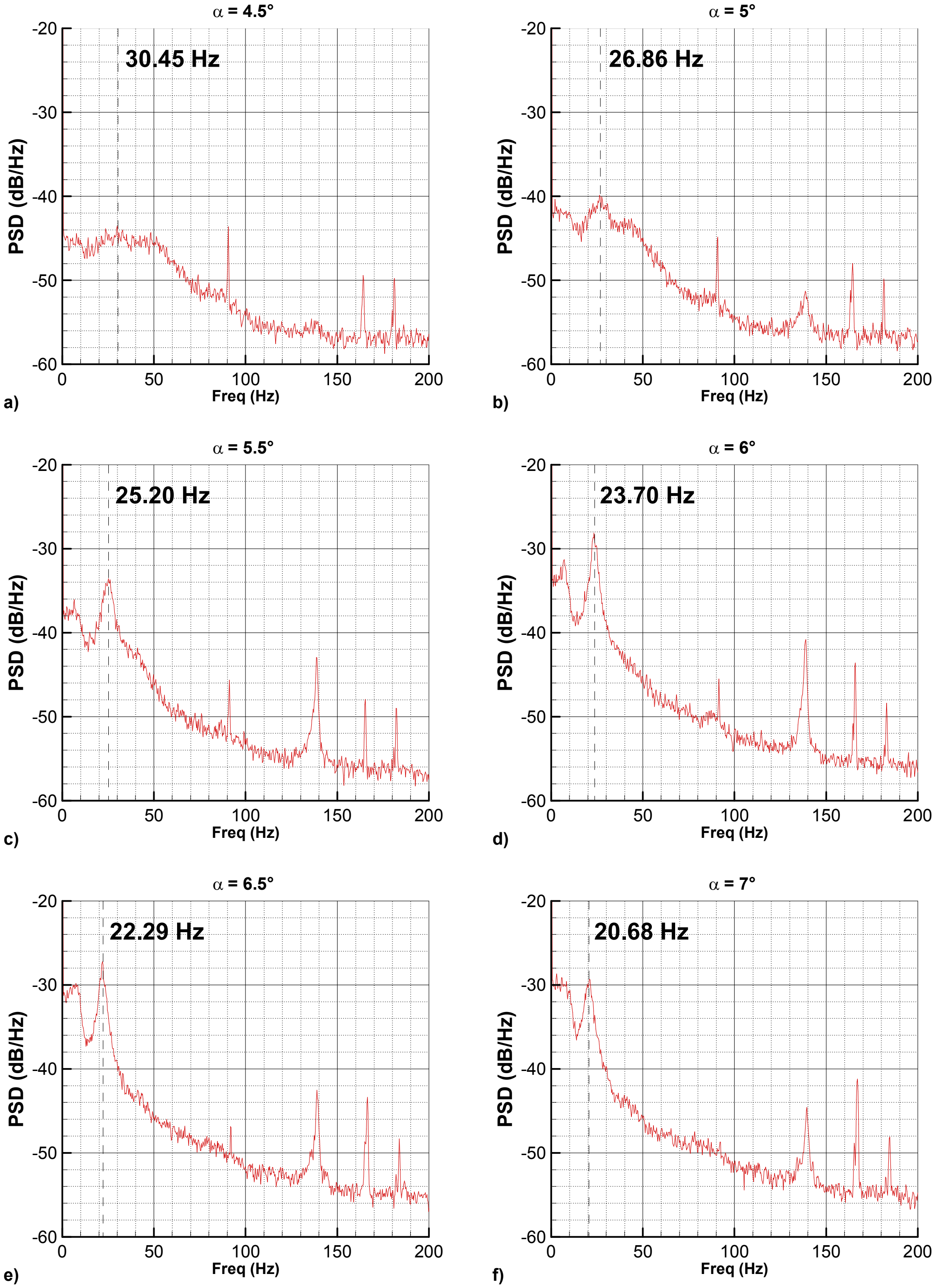

Fig. 4.49 PSD of airfoil C_p at x/c = 0.07 with estimated shear-layer flapping mode center frequency denoted by vertical dashed line: a) α = 4°, b) α = 4.5°, c) α = 5°, d) α = 5.5°, e) α = 6°, f) α = 6.5°.

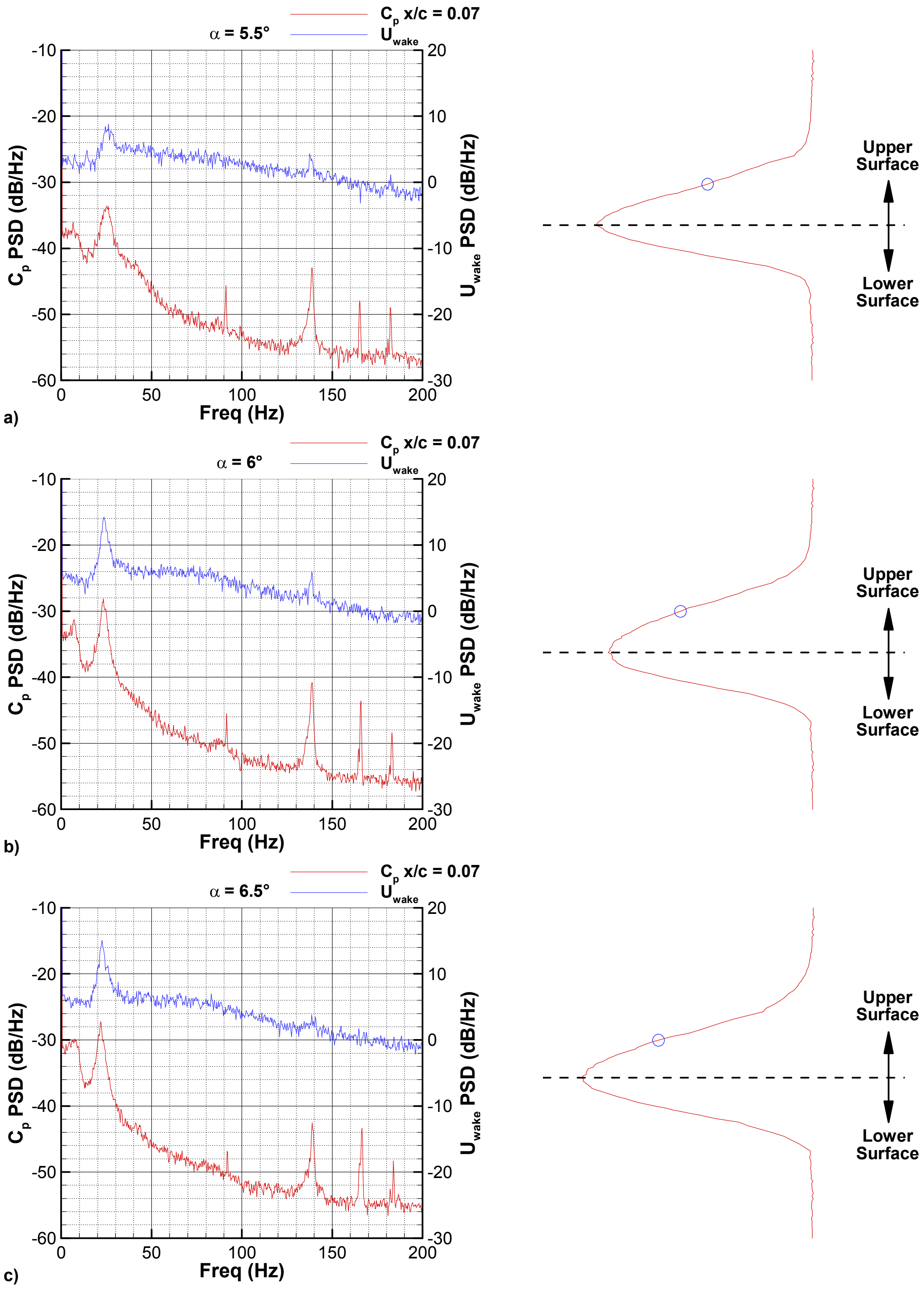

Fig. 4.50 (Left) PSDs showing shear-layer flapping mode spectral peak in airfoil C_p at x/c = 0.07 and U_{wake} across upper surface, (right) wake profile with open circle symbol representing y-location of U_{wake} PSD: a) $\alpha = 5.5°$, b) $\alpha = 6°$, c) $\alpha = 6.5°$.

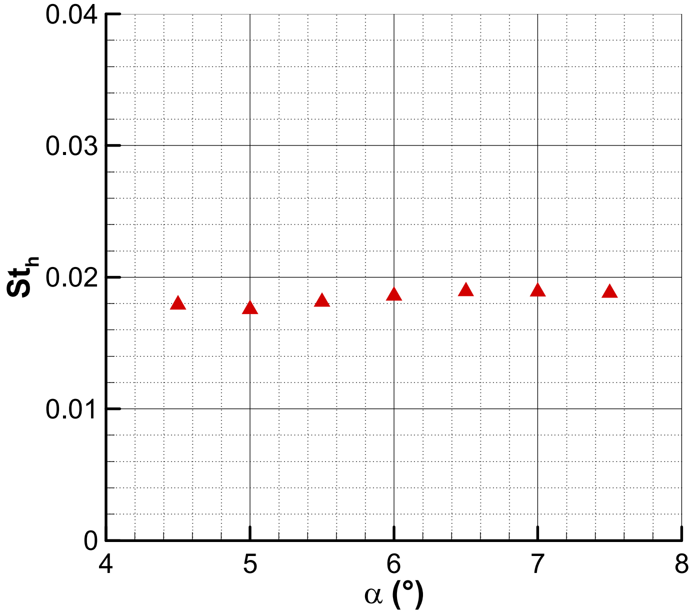

Fig. 4.51 Strouhal number of shear-layer flapping for NACA 0012 airfoil with horn-ice shape.

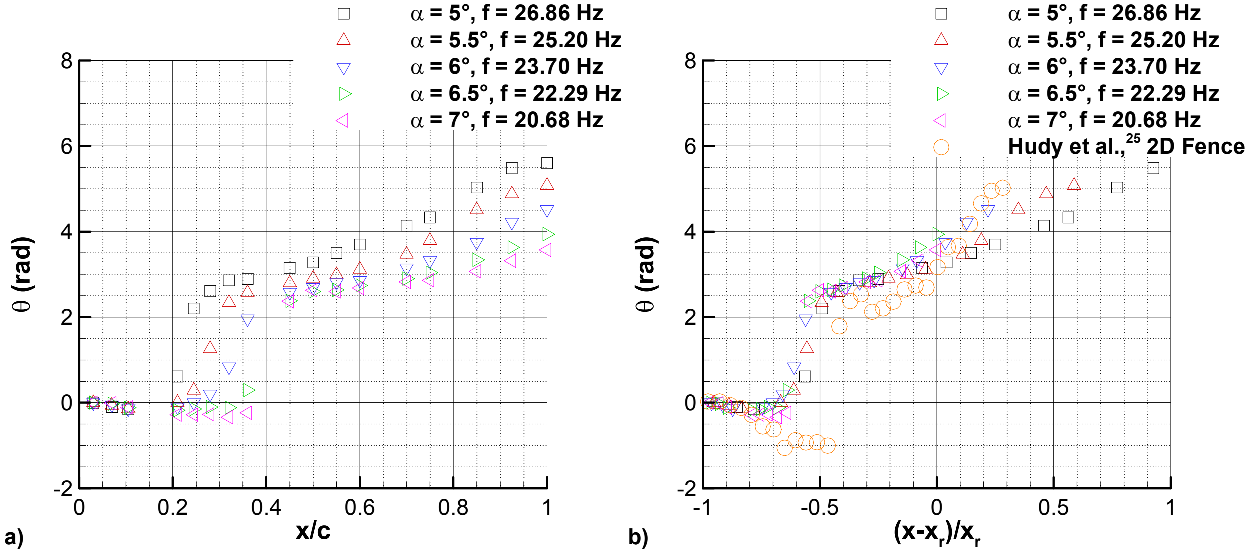

Fig. 4.52 Phase angle distributions for shear-layer flapping mode on NACA 0012 with leading-edge horn-ice shape: a) distribution across airfoil chord, b) distribution across streamwise distance normalized by separation bubble length.

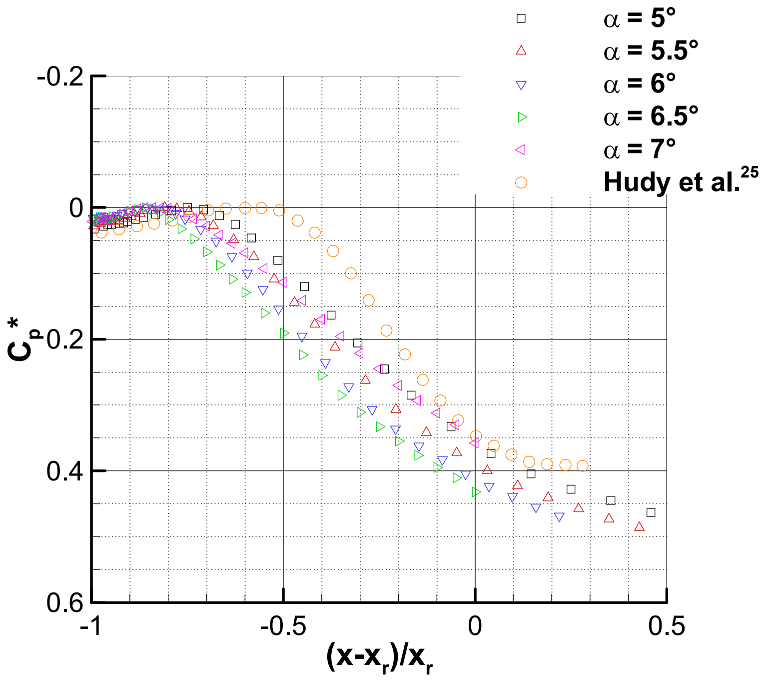

Fig. 4.53 Comparison of C_p* distributions between current study and Hudy et al.[25]

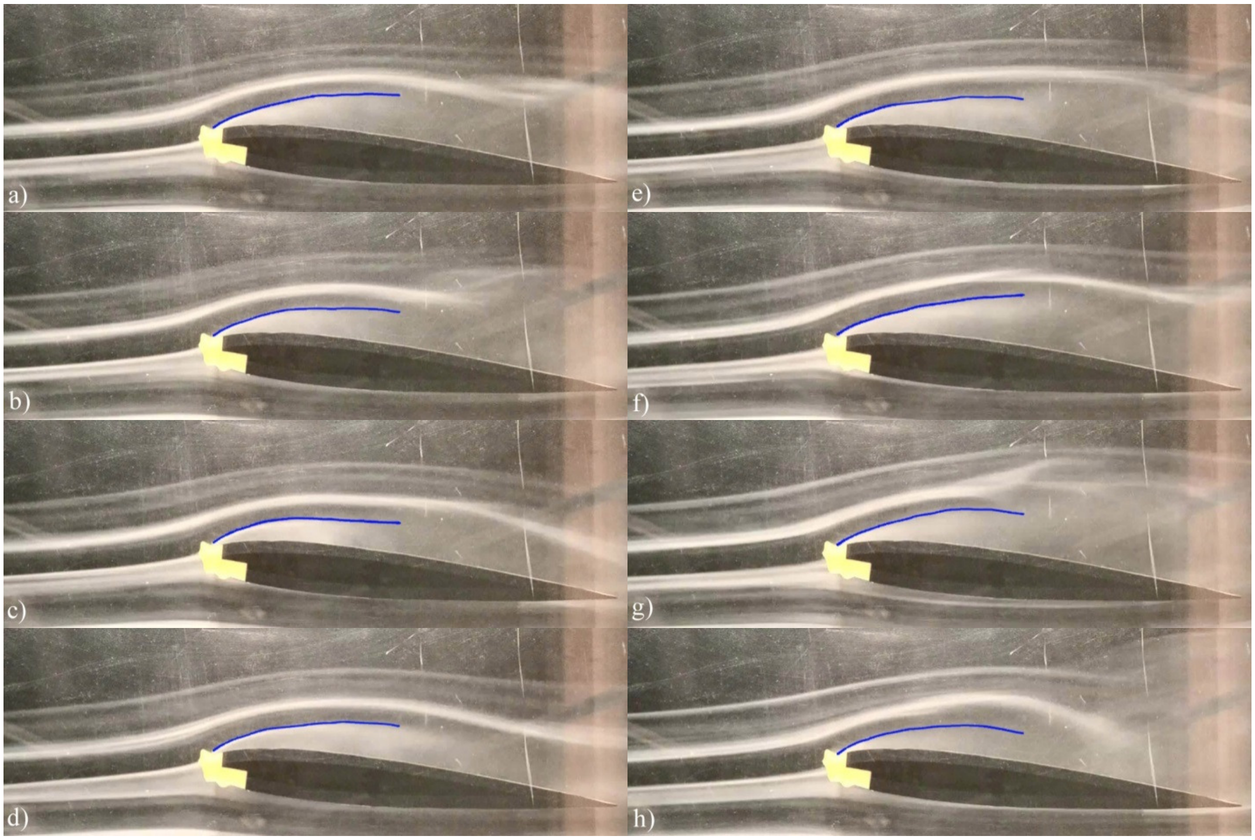

Fig. 4.54 Smoke flow visualization of NACA 0012 airfoil with horn-ice shape at α = 7°, approximate boundary of separation region indicated by blue line: a) t = 0 sec, b) t = 0.033 sec, c) t = 0.067 sec, d) t = 0.10 sec, e) t = 0.133 sec, f) t = 0.167 sec, g) t = 0.20 sec, h) t = 0.233 sec.

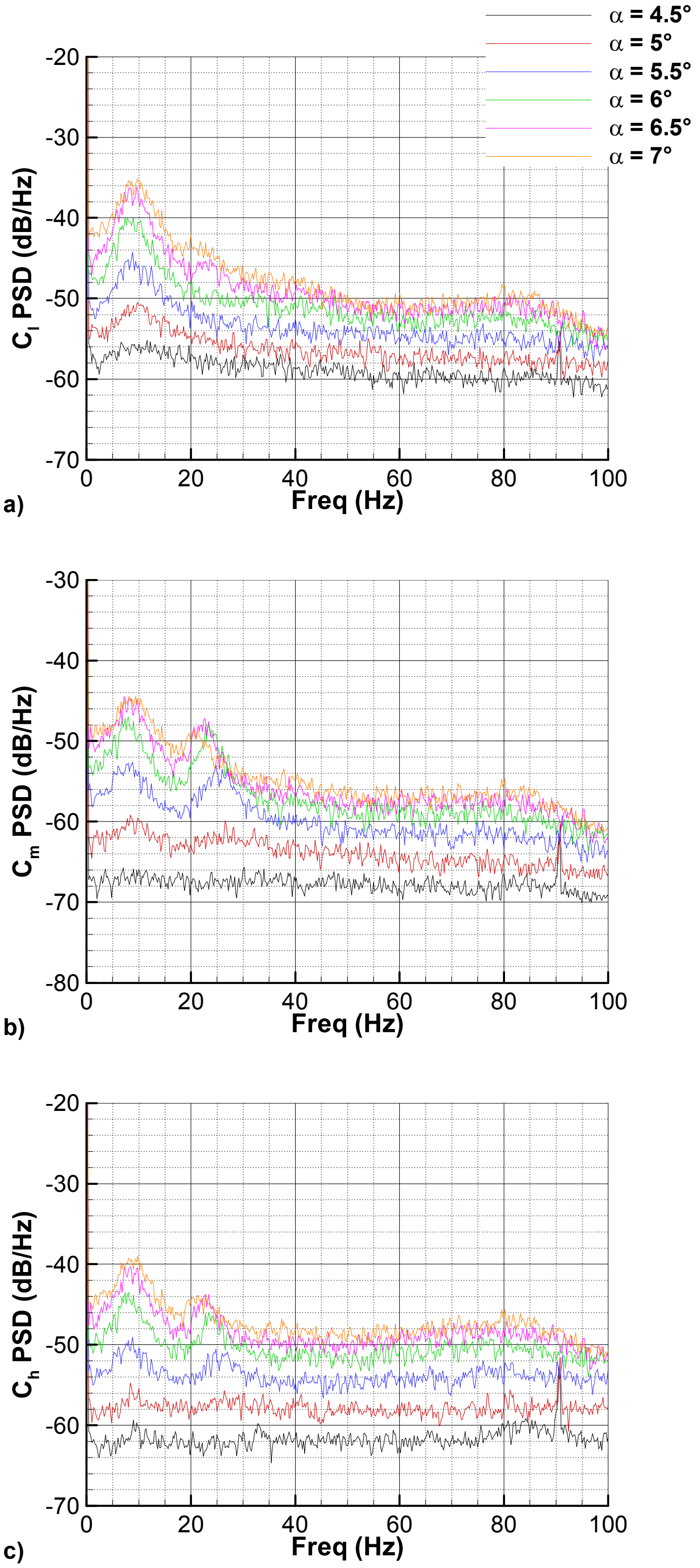

Fig. 4.55 Airfoil performance PSDs for NACA 0012 airfoil with horn-ice shape, frequency resolution of 0.2 Hz, angle-of-attack range of 4.5° ≤ α ≤ 7°: a) C_l PSD, b) C_m PSD, c) C_h PSD.

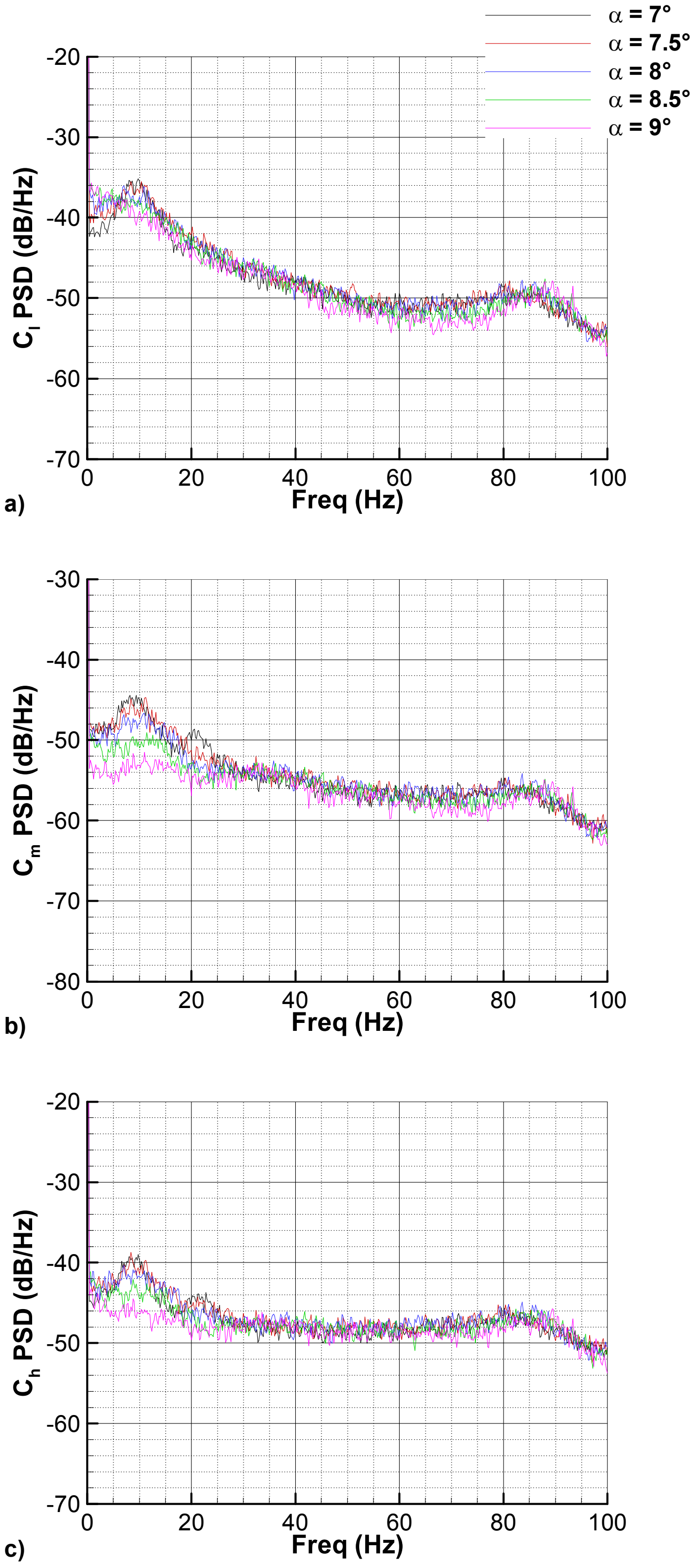

Fig. 4.56 Airfoil performance PSDs for NACA 0012 airfoil with horn-ice shape, frequency resolution of 0.2 Hz, angle-of-attack range of 7° ≤ α ≤ 9°: a) C_l PSD, b) C_m PSD, c) C_h PSD

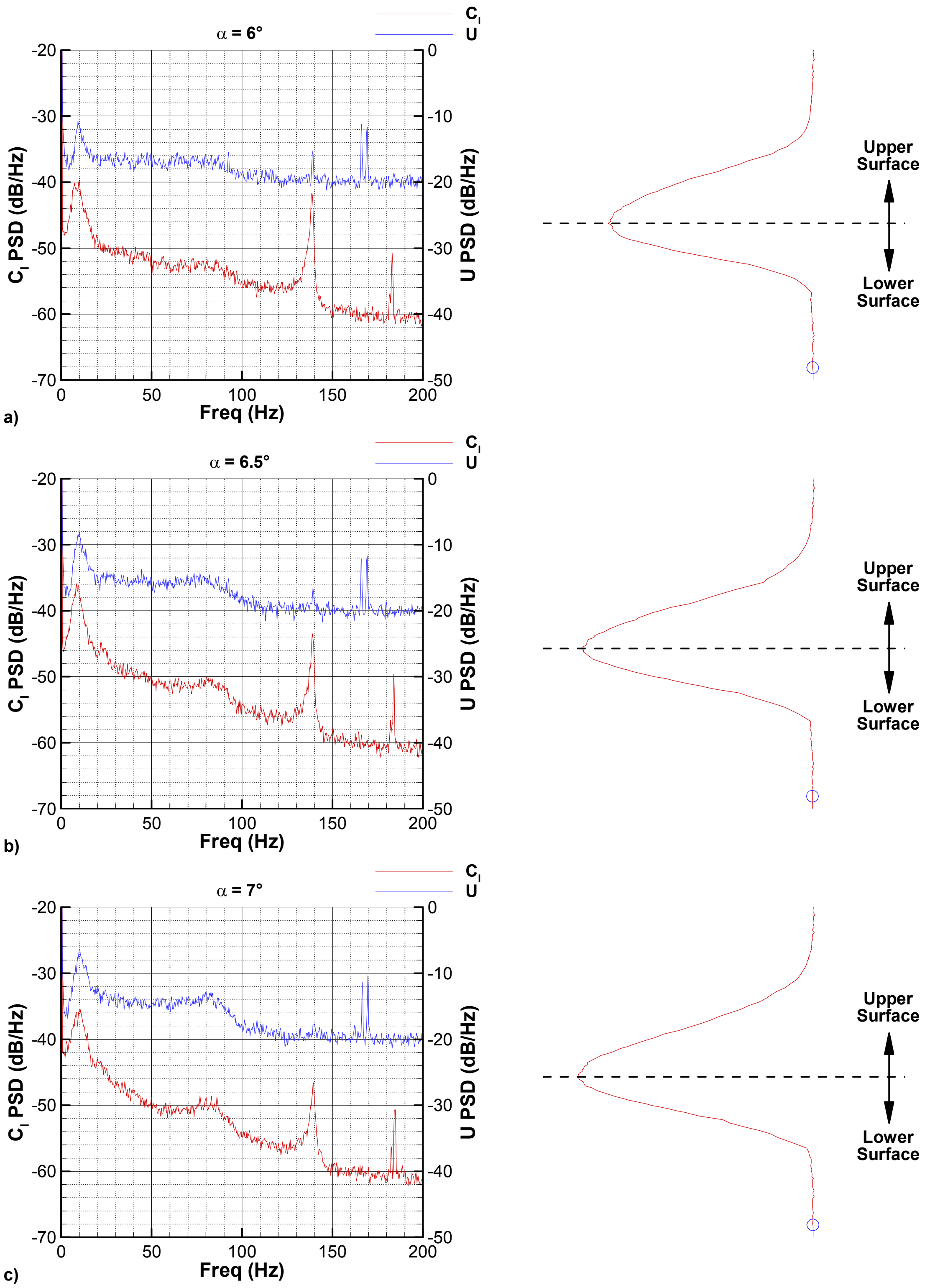

Fig. 4.57 (Left) PSDs showing low-frequency mode spectral peak in airfoil C_l and U outside of wake, (right) wake profile with open circle symbol representing y-location of U PSD: a) $\alpha = 6°$, b) $\alpha = 6.5°$, c) $\alpha = 7°$.

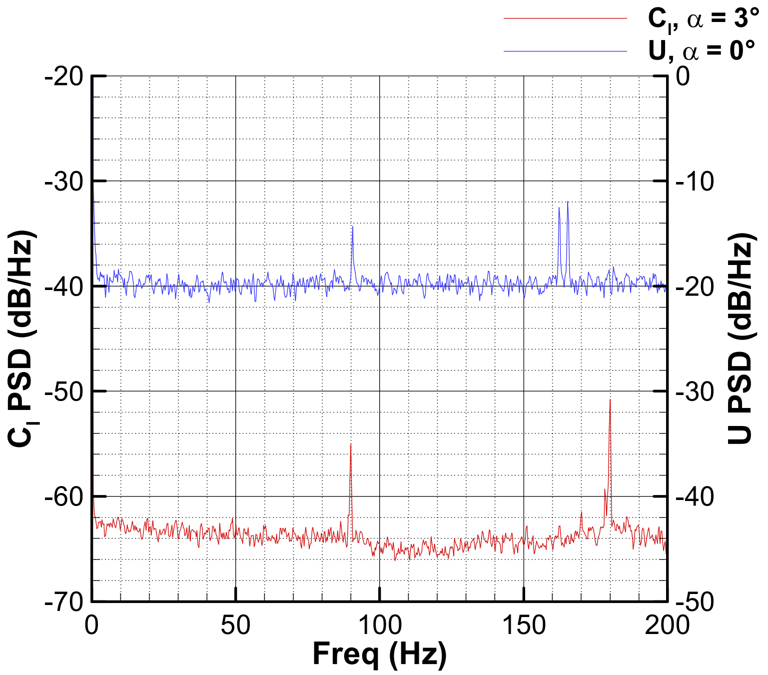

Fig. 4.58 PSDs of C_l at $\alpha = 3°$ and U at $\alpha = 0°$ for NACA 0012 airfoil with horn-ice shape.

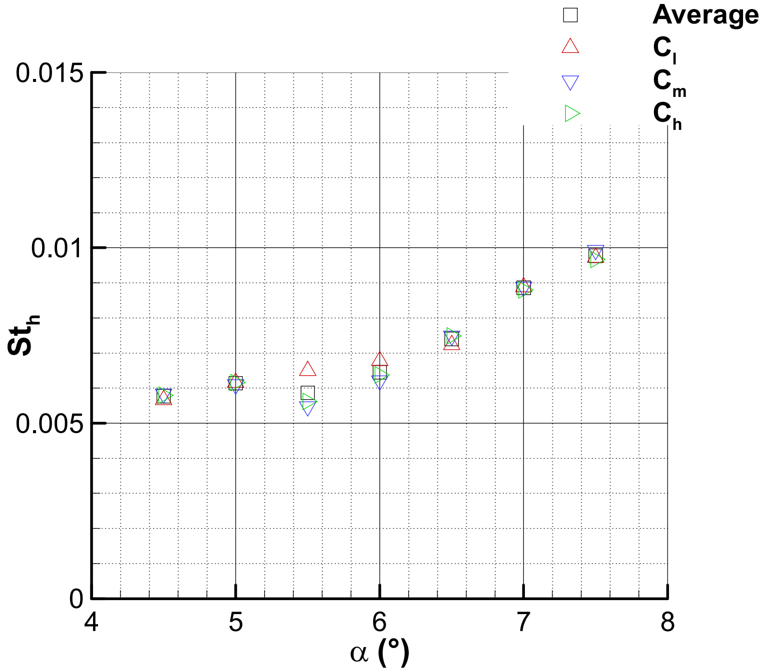

Fig. 4.59 Strouhal number of low-frequency mode for NACA 0012 airfoil with horn-ice shape, St$_h$ values determined using frequencies from Table 4.5.

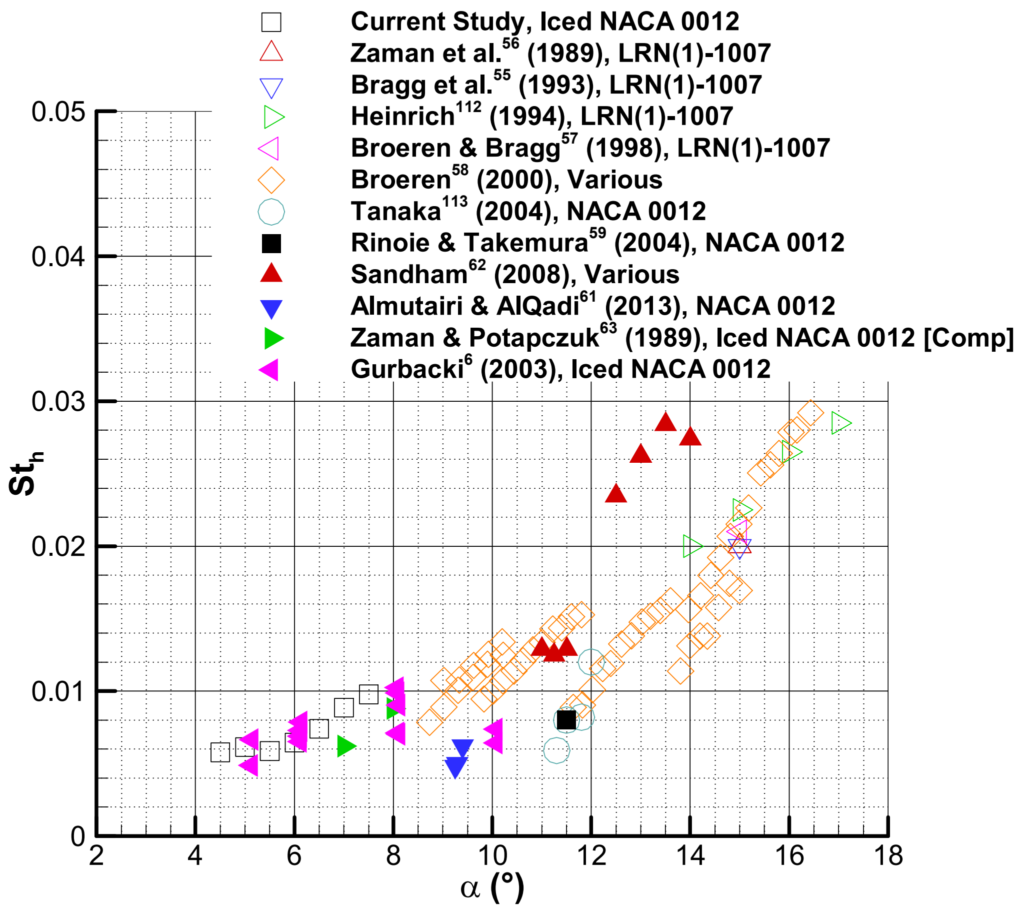

Fig. 4.60 Comparison of St_h for the low-frequency mode with results from the literature.

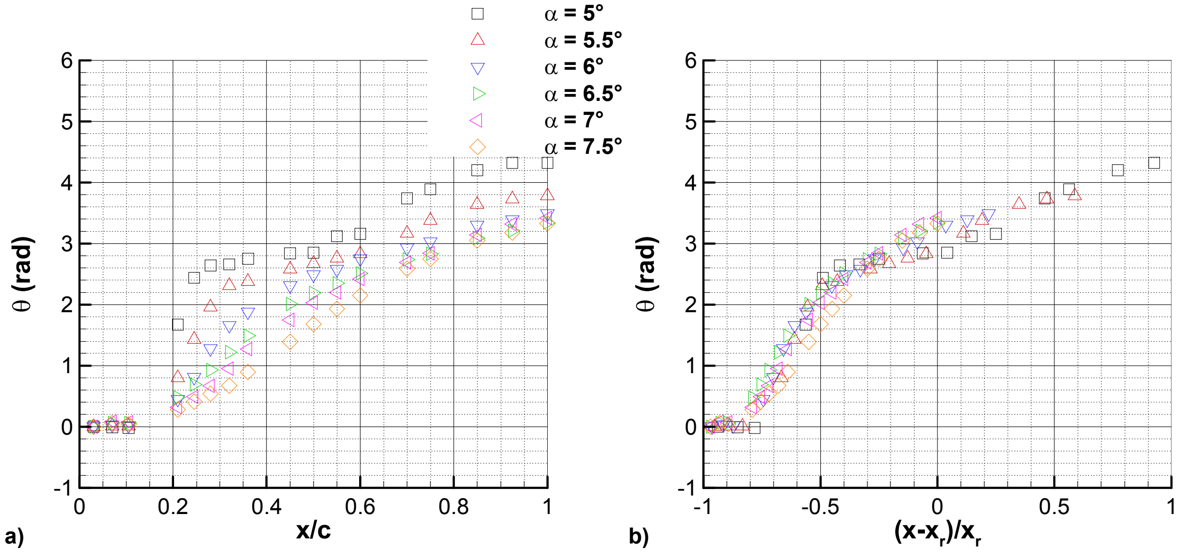

Fig. 4.61 Phase angle distributions for low-frequency mode on NACA 0012 with leading-edge horn-ice shape: a) distribution across airfoil chord, b) distribution across streamwise distance normalized by separation bubble length.

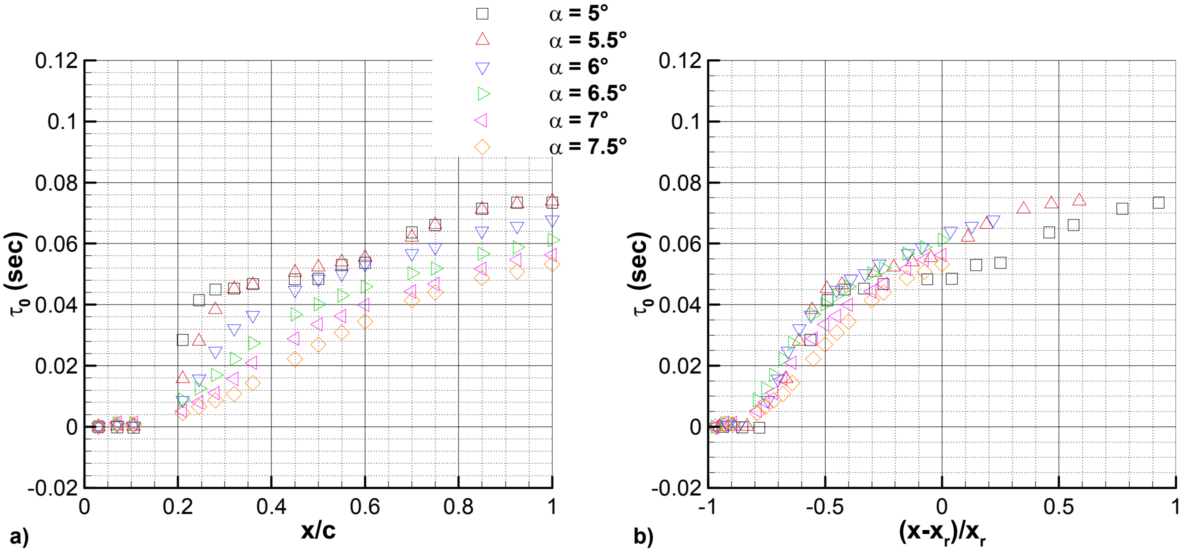

Fig. 4.62 Time delay distributions for low-frequency mode on NACA 0012 with leading-edge horn-ice shape: a) distribution across airfoil chord, b) distribution across streamwise distance normalized by separation bubble length.

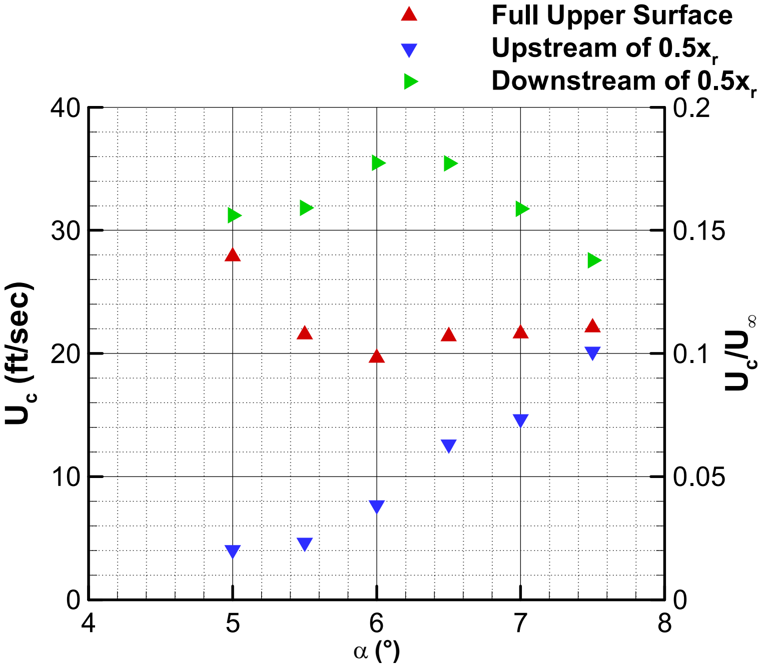

Fig. 4.63 Average convection velocities of low-frequency mode across airfoil upper surface.

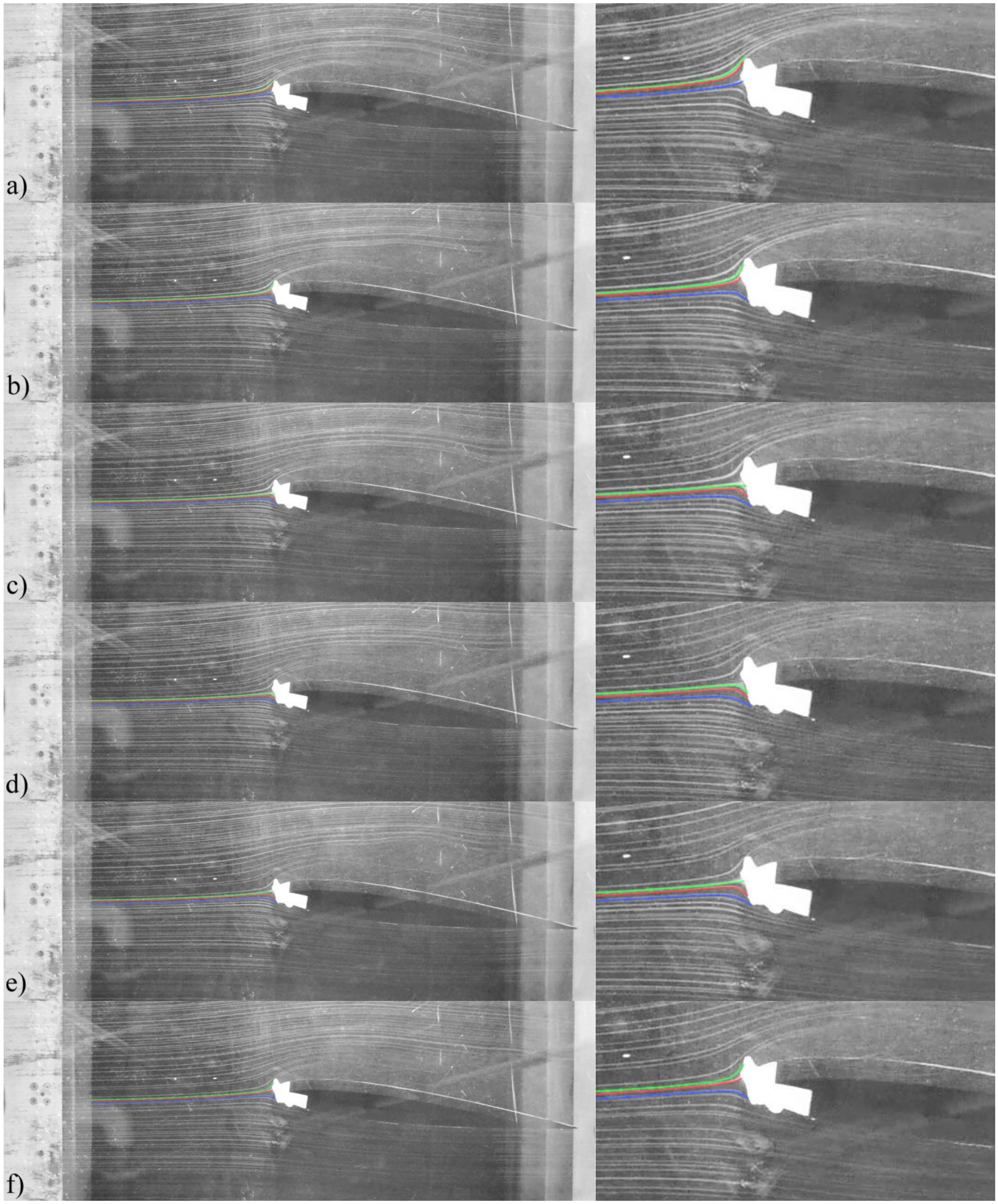

Fig. 4.64 Smoke wire flow visualization of NACA 0012 airfoil with horn-ice shape at $\alpha = 7°$ showing low-frequency mode, (left) full airfoil off-surface flowfield, (right) leading-edge region, leading-edge streamlines highlighted in green, red, and blue: a) $t = 0$ sec, b) $t = 0.4$ sec, c) $t = 0.8$ sec, d) $t = 1.2$ sec, e) $t = 1.6$ sec, f) $t = 2.0$ sec.

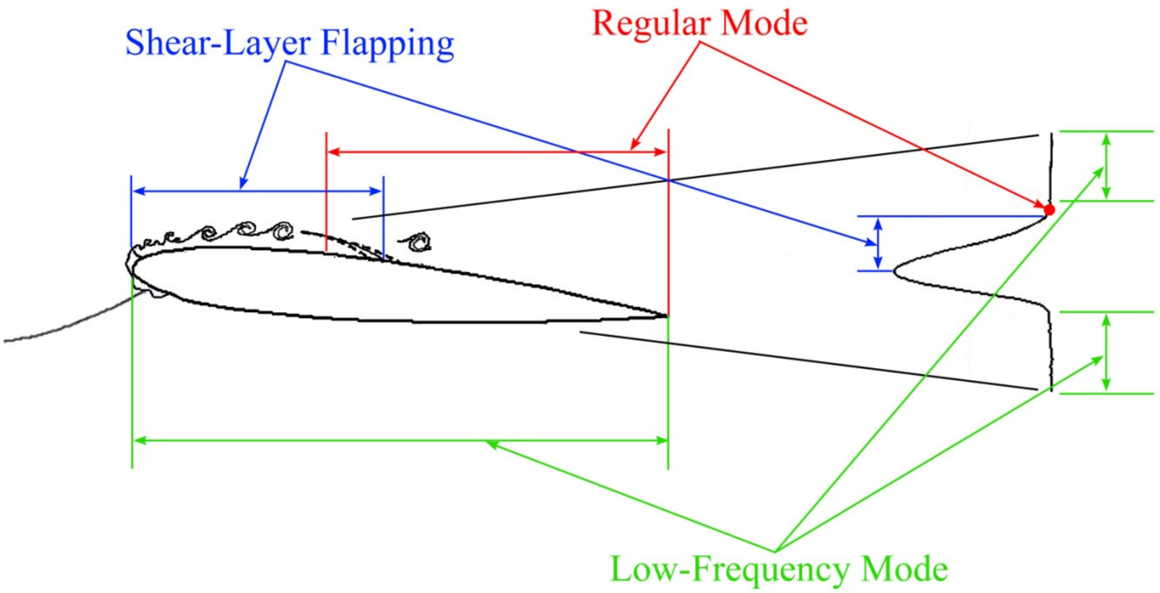

Fig. 4.65 Summary of locations where unsteady modes were identified in the iced-airfoil flowfield.

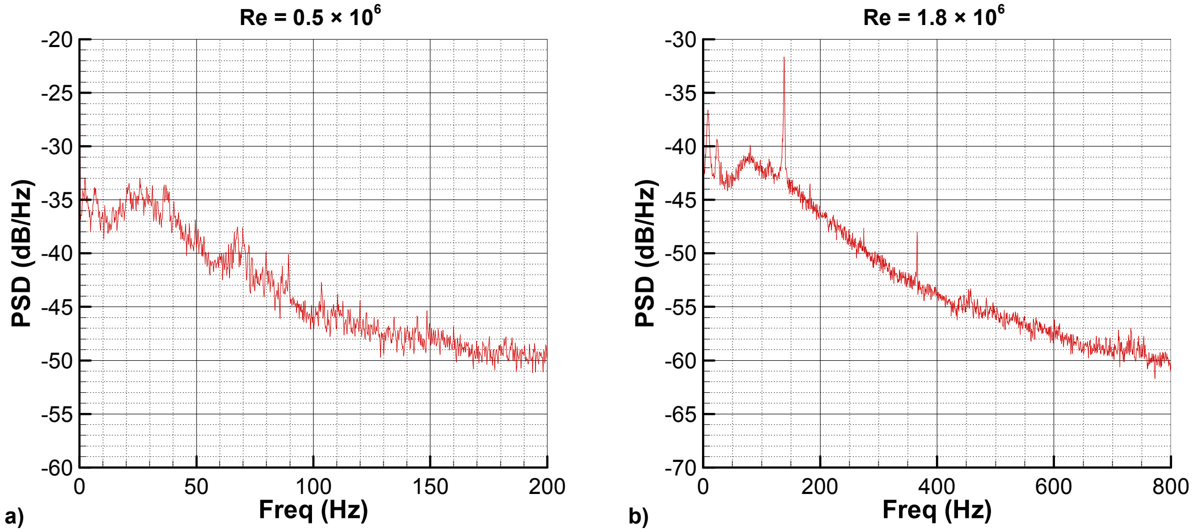

Fig. 4.66 PSDs of C_p at $x/c = 0.85$ on NACA 0012 airfoil with horn-ice shape at $\alpha = 6°$: a) Re = 0.5×10^6, b) Re = 1.8×10^6.

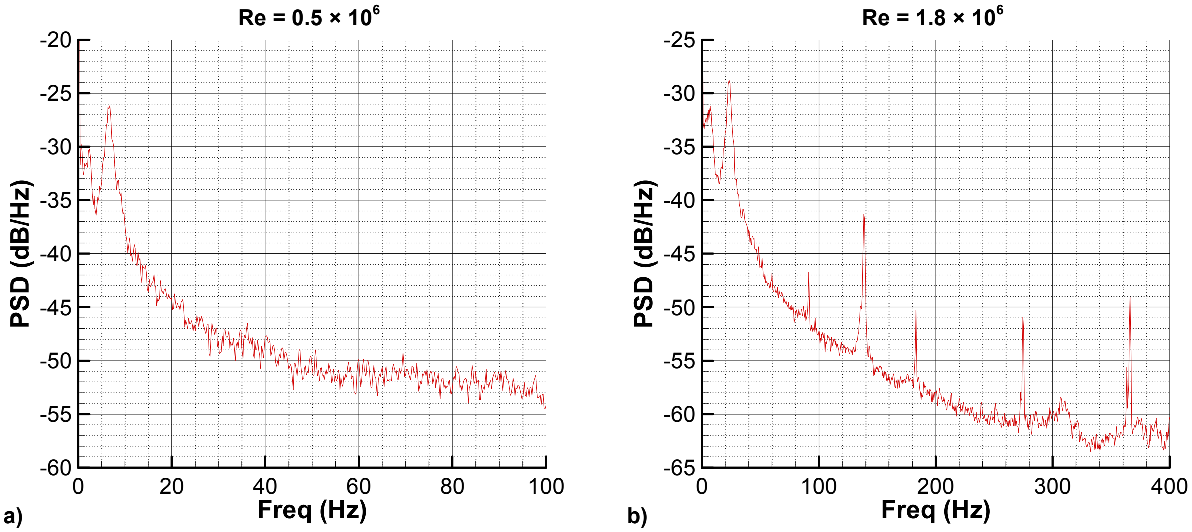

Fig. 4.67 PSDs of C_p at $x/c = 0.03$ on NACA 0012 airfoil with horn-ice shape at $\alpha = 6°$: a) Re = 0.5×10^6, b) Re = 1.8×10^6.

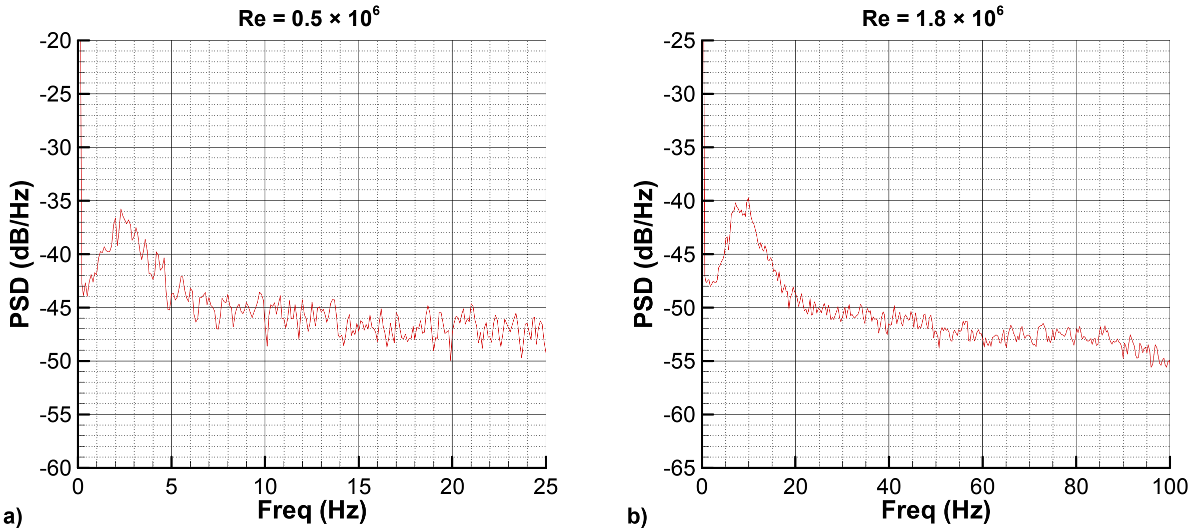

Fig. 4.68 PSDs of C_l of NACA 0012 airfoil with horn-ice shape at α = 6°: a) Re = 0.5×10^6, b) Re = 1.8×10^6.

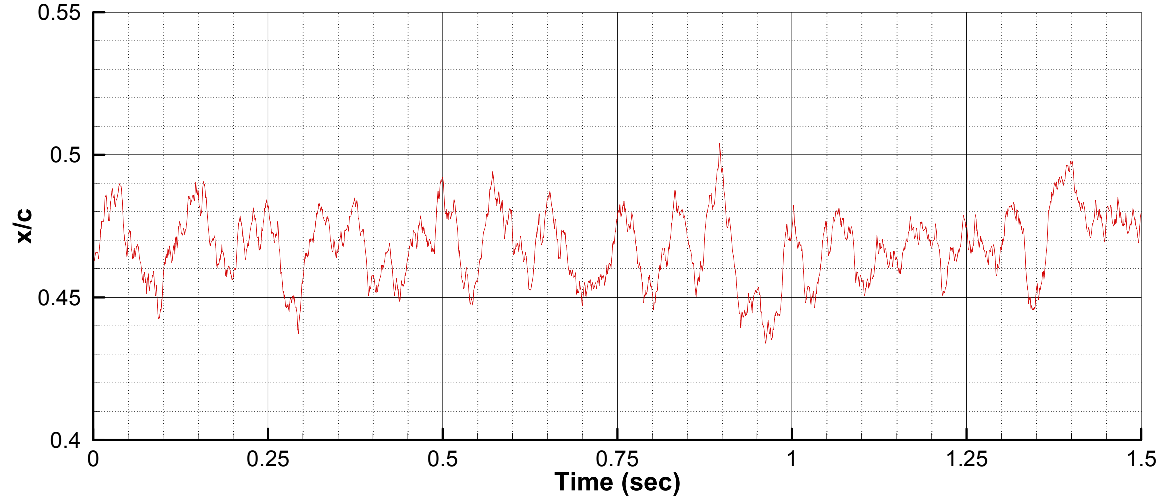

Fig. 4.69 Low-frequency mode component of shear-layer reattachment location for NACA 0012 airfoil with horn-ice shape at $\alpha = 5°$.

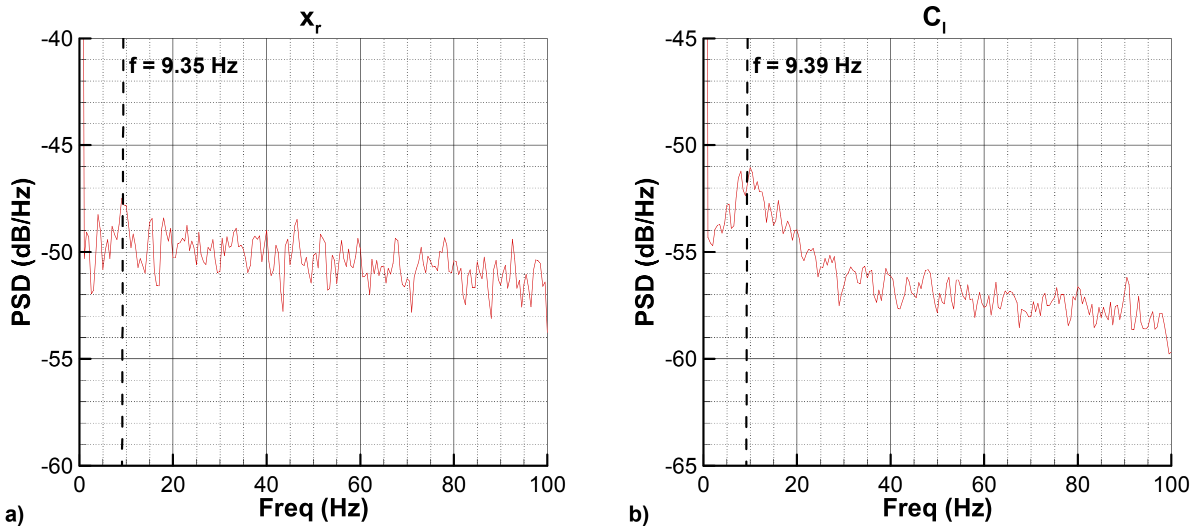

Fig. 4.70 PSDs for NACA 0012 with horn-ice shape at $\alpha = 5°$: a) reattachment location, b) C_l.

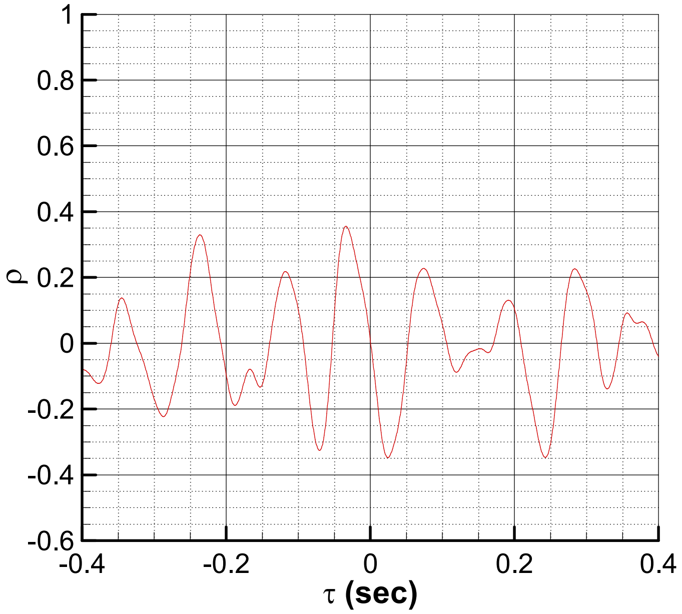

Fig. 4.71 Cross-correlation coefficient of conditionally-averaged shear-layer reattachment location and iced-airfoil lift coefficient.

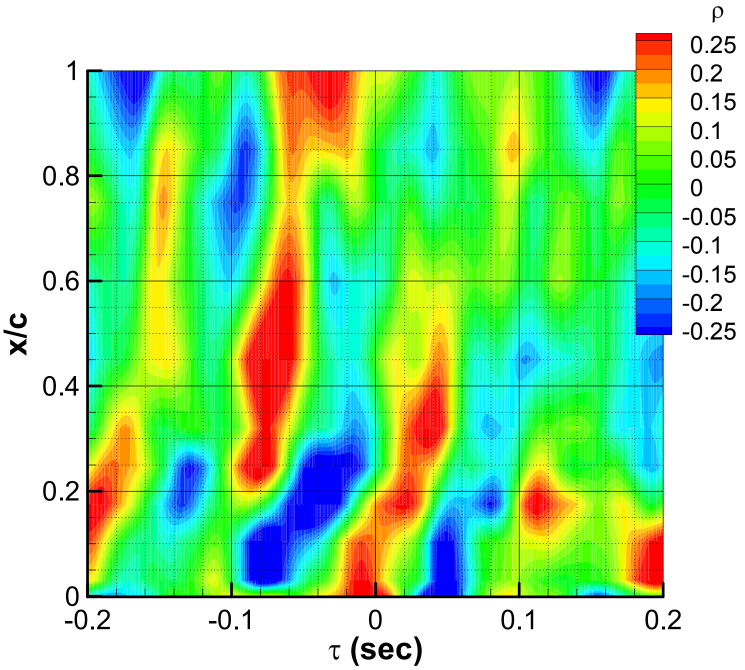

Fig. 4.72 Cross-correlation coefficients of conditionally-averaged shear-layer reattachment location and upper surface airfoil C_p.

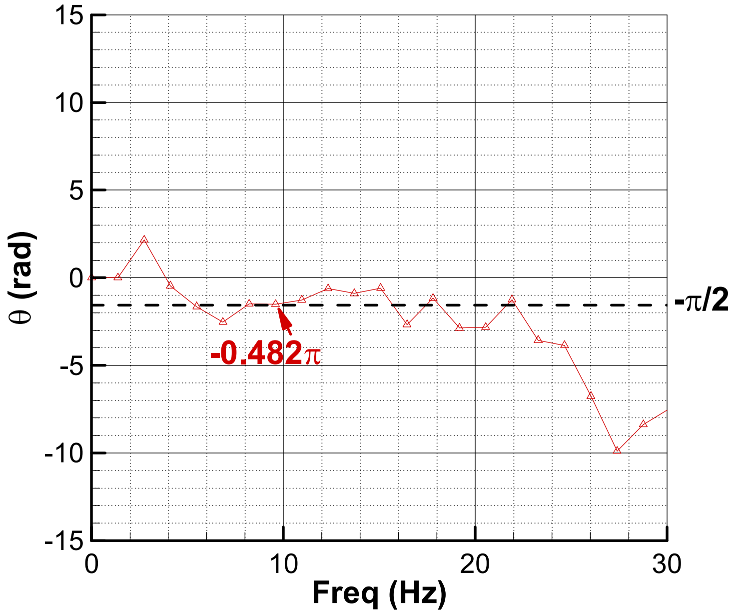

Fig. 4.73 Phase relationship between shear-layer reattachment location and iced-airfoil lift coefficient across low-frequency range, α = 5°.

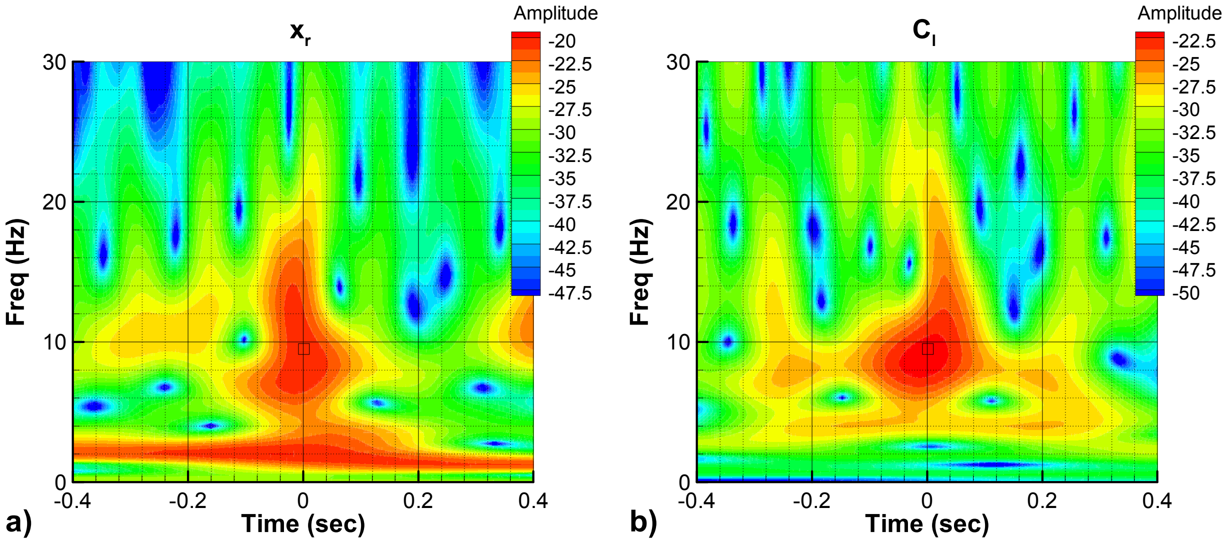

Fig. 4.74 Continuous Morlet wavelet transform, α = 5°: a) Shear-layer reattachment location, b) C_l; maximum amplitude at 9.5 Hz marked with square symbol.

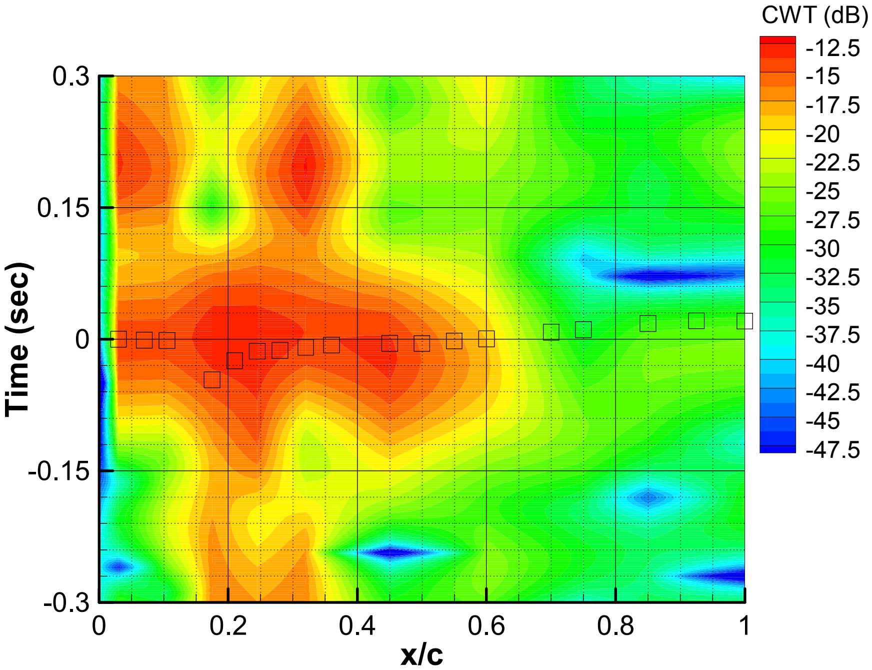

Fig. 4.75 Propagation of low-frequency mode (f = 9.5 Hz) in conditionally-averaged airfoil C_p determined using wavelet transform, with average low-frequency mode time delays.

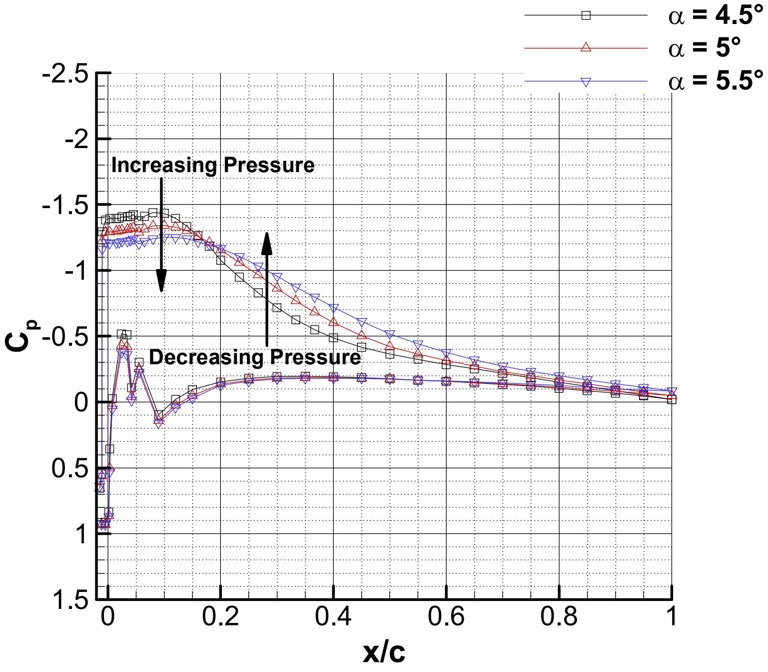

Fig. 4.76 Iced-airfoil time-averaged C_p for α = 5° and small increase or decrease in angle of attack.

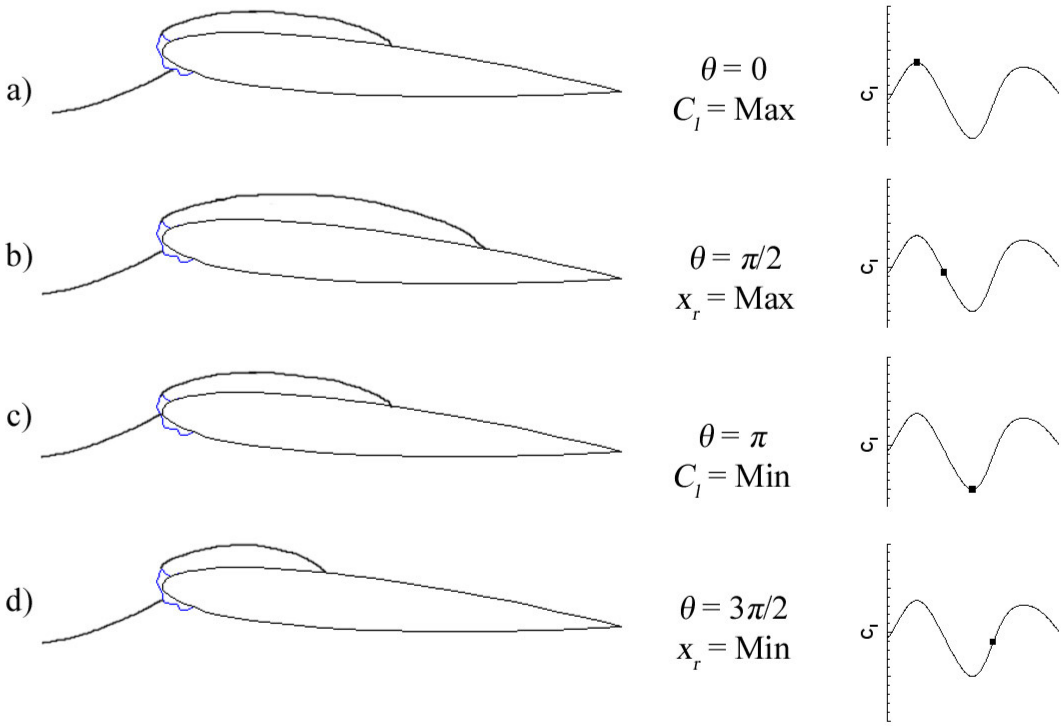

Fig. 4.77 Schematic of low-frequency oscillation cycle.

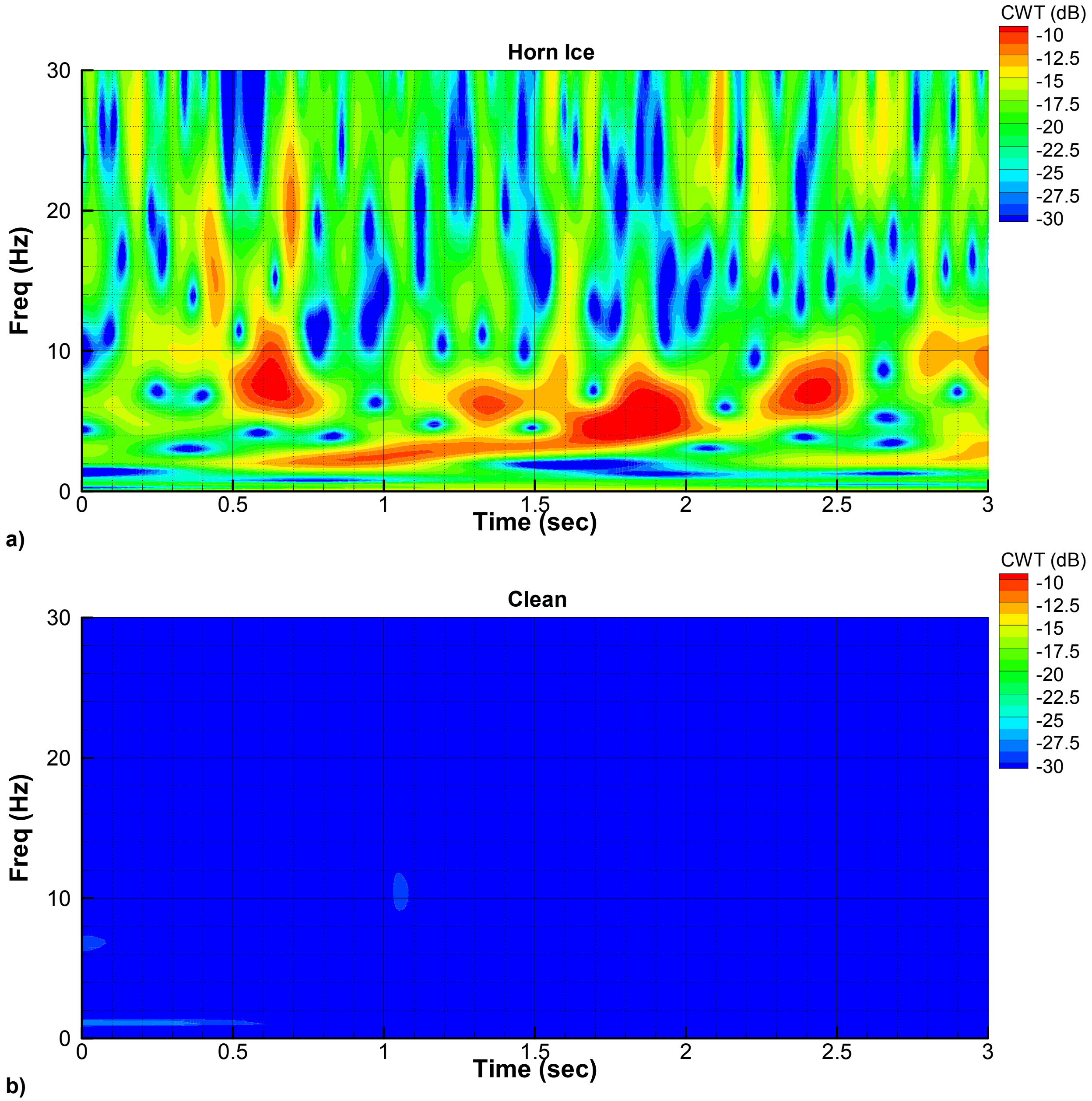

Fig. 4.78 Continuous wavelet transform (CWT) of C_h for airfoil at $\alpha - \alpha_{stall}$ = -0.5°: a) horn-ice configuration (α = 6°), b) clean configuration (α = 13.5°).

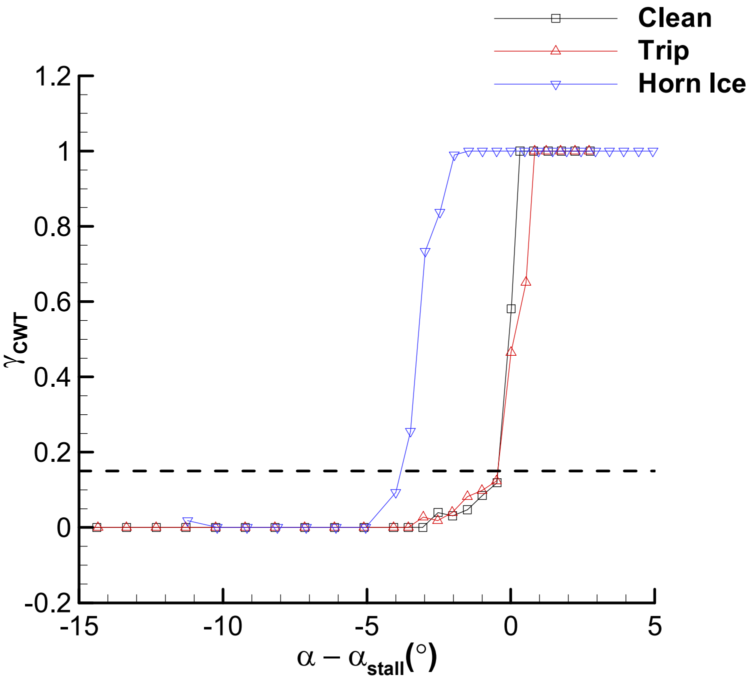

Fig. 4.79 Comparison of intermittency factor of wavelet transform amplitude as a function of $\alpha - \alpha_{stall}$ for clean, trip, and horn-ice airfoil configurations.

Chapter 5

Summary, Conclusions, and Recommendations

This chapter provides an overview of the current study. It includes a brief description of the experiments performed, summarizes key findings, and provides suggestions for future work.

5.1 Summary

An experimental study was conducted at the University of Illinois at Urbana–Champaign in order to understand the unsteady aerodynamic effects of a leading-edge horn-ice shape. Of particular interest was the characterization of unsteady modes present in the iced-airfoil flowfield. In order to complete the goals and objectives of this study, an NACA 0012 airfoil model was tested extensively in a subsonic wind tunnel. Both time-averaged and time-dependent measurements were acquired in order to determine the steady and unsteady airfoil performance and related flowfield effects. In addition to acquiring measurements for the clean NACA 0012 airfoil, the model was also tested in a tripped configuration and an array of simulated leading-edge icing configurations.

The unsteadiness present in the airfoil flowfield was determined using measurements of the unsteady airfoil surface pressure distribution and acquired wake velocity measurements. Relevant frequency scales at various locations across the airfoil surface were identified. It was discovered that three distinct modes of unsteadiness were present in the iced-airfoil flowfield.

These modes of unsteadiness included a regular mode of vortical motion, a shear-layer flapping mode, and a low-frequency mode. The regular mode was identified as the product of the vortical motion in the shear layer and vortex pairing and shedding process from the separation bubble. The shear-layer flapping mode was identified at a low frequency, and was recognized as having a dimensionless frequency similar to those reported in fundamental studies investigating the separation bubbles generated in flows about simple geometries. The low-frequency mode was identified as being similar to those reported elsewhere on iced airfoils or clean airfoils with a thin-airfoil stall type prior to static airfoil stall. This low-frequency mode is characterized by a quasi-periodic oscillation of the airfoil circulation and is present globally in the airfoil flowfield. The effect of changing the Reynolds number of the flow on the frequencies present in the flowfield was also identified.

Since the previous understanding of the low-frequency mode in iced-airfoil flowfields has been limited, additional investigation was conducted in order to characterize the low-frequency mode and its effect on the unsteady airfoil performance, surface pressure distribution, and separation bubble shear-layer reattachment location. A new method was developed for identifying the near-instantaneous shear-layer reattachment location using a surface-mounted hot-film array, and it was used extensively to characterize the low-frequency mode. From the improved understanding of the low-frequency mode that was gained throughout this investigation, a modification to an existing hinge-moment-based airfoil stall prediction system was suggested. This modification provided a new addition to the stall prediction system, which improved the predictive capabilities of the hinge-moment-based stall prediction method. Using this addition, the prediction of an impending stall due to the effects of a leading-edge horn-ice shape could be isolated from other contaminant-induced effects. Additionally, problematic issues of the previous hinge-moment-based system producing premature stall predictions for a horn-ice configuration were resolved.

5.2 Results and Conclusions

The relevant findings of the current investigation are summarized in the following subsections.

5.2.1 Iced-Airfoil Flowfield Effects

- Prior to stall, the amount of unsteadiness present in the flowfield about an airfoil with a leading-edge ice shape is much greater than that associated with a clean or tripped airfoil configuration.
- The maximum amount of unsteadiness in the iced-airfoil flowfield consistently resided upstream of the mean shear-layer reattachment location. In the current study, the average location of maximum flowfield unsteadiness was identified at $0.79x_r$.
- For a given iced-airfoil configuration, the flowfield unsteadiness was observed to increase with angle of attack until stall and decrease as the angle of attack was increased past stall.
- The maximum amount of unsteadiness across the flowfield was observed to be a function of airfoil angle of attack. For a fixed angle of attack, consistent levels of maximum unsteadiness were observed as changes in the ice shape feature height or location were made.
- Three primary modes of unsteadiness were observed in the airfoil surface pressure measurements. All three modes were identified in the measurements that were acquired at $\text{Re} = 1.8 \times 10^6$. One was observed across a broad-band, high-frequency range on the order of 50 Hz to 225 Hz, one was observed across a narrow-band low-frequency range between 20 Hz and 35 Hz, and the last was observed across a narrow-band low-frequency range between 5 Hz and 10 Hz.
- The unsteady modes occurring at low frequencies were observed to be most dominant inside the region bound by the separation bubble, and the unsteadiness induced by the higher frequencies were observed just upstream of reattachment as well as across the airfoil surface downstream of the reattachment location.
- The frequencies of the three primary unsteady modes were observed to scale directly proportionally with freestream velocity.

5.2.2 Regular Mode

- The regular mode was attributed to flowfield unsteadiness due to vortical motion in the separated shear layer and vortex pairing and shedding from the separation bubble. This mode was identified in the region just upstream of the mean reattachment location and in the region downstream of reattachment. The presence of the regular mode was also identified in the velocity measurements at the upper edge of the wake of the iced airfoil.

- The frequency content of the regular mode appeared as an increase in energy across a broad band of frequencies. The bandwidth and center frequency of the increased energy was observed to decrease with increased angle of attack to stall (or, with increased separation bubble length). The center frequency of the regular mode was observed to slightly decrease with downstream distance through the separation bubble until the mean reattachment location. Downstream of reattachment, the frequency of the regular mode remained constant.
- The Strouhal number for the regular mode was calculated by non-dimensionalizing the center frequency using the length of the separation bubble and the freestream velocity. The resulting Strouhal numbers consistently corresponded to $\mathrm{St}_L = 0.60$, which compared well with those presented in the literature for studies of flows about simple geometries and iced airfoils.
- The vortex convection velocities across the airfoil surface were calculated. Upstream of the mean reattachment location, the convection velocity was approximately $0.45U_\infty$ and was independent of angle of attack. The vortex convection velocity was higher downstream of reattachment and tended to decrease with increasing angle of attack. These results were similar to those reported elsewhere in the literature for flows about simple geometries and iced airfoils.

5.2.3 Shear-Layer Flapping

- The effects of shear-layer flapping were observed across a narrow-band, low-frequency range. The center frequency of the shear-layer flapping mode typically occurred between 20 Hz and 30 Hz. The center frequency was also observed to decrease with increasing angle of attack.
- The shear-layer flapping mode was most dominant in the frequency spectra of the pressure measurements at the location just downstream of the ice shape. Spectral content of the shear-layer flapping mode was constrained to the length of the separation bubble and was not clearly evident downstream of the time-averaged reattachment location. The

presence of the shear-layer flapping mode was also identified in the velocity measurements across the wake of the upper surface of the iced airfoil.

- The Strouhal number of the shear-layer flapping mode was calculated by non-dimensionalizing the flapping frequency using the projected height of the airfoil and the freestream velocity. The resulting Strouhal numbers consistently corresponded to a value of $\mathrm{St}_h = 0.0185$, which was consistent with similar values reported in the literature.
- The progression of the shear-layer flapping mode across the airfoil surface was characterized by observing the phase angle distributions of the flapping frequency. A reversal in phase angle progression was identified on the airfoil at a location corresponding to $0.35x_r$. This location was also consistent with the location of minimum pressure in the airfoil C_p distribution.
- The phase angle distributions of the shear-layer flapping mode from the current study were similar to those reported elsewhere in the literature, with small variations correlating to differences in the pressure distribution of the separation bubble.

5.2.4 Low-Frequency Mode

- The low-frequency mode was identified across a narrow-band, low-frequency range. The center frequency of this low-frequency mode was identified between 8 Hz and 10 Hz and did not significantly change with changing airfoil angle of attack. This frequency range was not associated with any natural frequencies of the airfoil model structure or fan blade passing frequencies of the wind tunnel.
- The effects of the low-frequency mode were most clearly identified in the spectral content of the unsteady airfoil performance coefficients, as the low-frequency mode was best characterized by a global change in the airfoil circulation. The low-frequency mode was also identified in the velocity measurements taken downstream of the airfoil model outside of the airfoil wake.
- The Strouhal number of the low-frequency mode was calculated by non-dimensionalizing the frequency of the low-frequency mode using the airfoil projected height and the freestream velocity. The resulting height-based Strouhal number values appeared to have an angle-of-attack dependence. However, a comparison of the St_h values for the low-frequency mode was made with those reported in the literature for clean and iced airfoils

prior to stall, and the values of St_h from the current study were within the range that would be expected from these prior studies.

- The low-frequency mode was observed to convect downstream in the region downstream of $0.20x_r$. Upstream of this location, the phase angle of the low-frequency mode did not significantly change with distance.
- The slope of the phase progression was markedly different between the regions upstream and downstream of $0.50x_r$. The convection velocity of the low-frequency mode was greater in the region downstream of $0.50x_r$ than it was upstream. However, with increased angle of attack up to stall, the phase angle became more linear and the convection velocity across the entire upper surface collapsed to $0.11U_\infty$. The convection velocities of the low-frequency mode from the current study also favorably compared with those reported in the literature for flows about an iced airfoil.
- The unsteady changes to the airfoil circulation due to the low-frequency mode were observed in smoke wire flow visualization results. A distinct unsteady deflection of the streamlines just upstream of the airfoil was observed due to unsteady changes in the circulation-induced upwash produced by the airfoil.

5.2.5 Flowfield Characterization of Low-Frequency Mode

- The low-frequency mode was identified in the spectral content of the shear-layer reattachment location at $\alpha = 5°$. The corresponding frequency was consistent with that observed for the low-frequency mode in the airfoil lift coefficient.
- A $\pi/2$ phase relationship was identified between the unsteady shear-layer reattachment location and the lift coefficient at the low-frequency mode, where the lift coefficient leads the reattachment location. As the lift coefficient increased, the increased circulation of the airfoil led to an elongation of the separation bubble. This increased bubble length further disrupted the airfoil flowfield through a decambering effect, causing the lift coefficient to decrease. The accompanying decrease in the airfoil circulation led the separation bubble to shrink. As the length of the separation bubble decreased, the lift coefficient increased, which restarted the low-frequency oscillation cycle.
- The pressure at the airfoil leading edge was directly correlated to the separation bubble length. As the reattachment location moved downstream, the pressure at the leading edge

of the airfoil tended to increase. Conversely, as the reattachment location moved upstream, the pressure at the leading edge tended to decrease. This time-dependent relationship is similar to what occurs in the time-averaged sense with a change in separation bubble length (e.g. due to changing angle of attack).

- The effects of the low-frequency mode on the surface pressure displayed convective qualities, as the correlation exhibited between the reattachment location and the airfoil C_p tended to move downstream with increasing time.

5.2.6 Iced-Airfoil Stall Prediction Using Hinge Moment Measurements

- The low-frequency mode was identified in the wavelet transform of the hinge moment coefficient as having regularly-spaced discrete regions of high amplitude content across a range of low frequencies. This characteristic of the low-frequency mode was not observed in the wavelet transform of the hinge moment coefficient for the clean or tripped airfoil configurations.
- The signature of the low-frequency mode in the iced-airfoil hinge moment coefficient wavelet transform was used to adapt the existing hinge-moment-based stall prediction method to more appropriately handle the horn-ice configuration. Using an intermittency-based function of the hinge moment wavelet transform, the presence of the effects induced by the horn-ice shape could be identified and the horn-ice-induced stall case could be isolated from the other contamination configurations. This difference could be detected prior to a premature stall warning being issued, increasing the effectiveness of the hinge-moment-based stall prediction system for airfoils.

5.3 Recommendations

While the results from this investigation provided a much greater understanding of the unsteady modes present in the flowfield about an airfoil with a leading-edge horn-ice shape, several additional questions arose which merit additional investigation. These topics are provided as recommendations for future research:

- While the Strouhal numbers calculated for the regular mode and the shear-layer flapping mode were observed to collapse towards a value that was independent of airfoil incidence, the Strouhal numbers that were calculated for the low-frequency mode did not.

Since it is likely that there exists a self-similarity solution of the low-frequency mode in the flowfield of an airfoil with a separation bubble, additional investigation should be conducted into identifying more appropriate length scales and velocity scales in calculating the Strouhal number. By properly selecting the most relevant length scales in this non-dimensionalization, additional insight would be gained into how the low-frequency mode is produced and assist in identifying the instability mechanism. Since identifying relevant length and velocity scales could require specific measurements about the boundary-layer and separation-bubble flowfield (e.g. boundary-layer thickness, shear-layer velocity, momentum thickness, or velocity in recirculation region of bubble), this may be best pursued using PIV measurements or computational methods.

- While not discussed in this study, high levels of flowfield unsteadiness were identified in the leading-edge region of the clean airfoil just after the stall angle of attack was exceeded. This flowfield unsteadiness was observed to decrease with increased incidence past the stall angle of attack. It is the belief of the current author that this unsteadiness is caused by a leading-edge vortex that forms on the airfoil just past stall. A much greater understanding of this unsteadiness could be obtained by observing the flowfield dynamics using some form of non-intrusive velocimetry method and by correlating those observations to detailed measurements acquired on the surface.
- In this study, a method for determining the unsteady shear-layer reattachment location on a surface using measurements from a surface-mounted hot-film array was introduced. Since use of this technique would be useful for other studies outside of the scope of the current study, additional development of this technique would be valuable. Notably, a sampling system with greater maximum simultaneous sample rate capabilities could be used to expand the capabilities of this method. As a result, the correlation coefficients used in reducing the unsteady shear-layer reattachment location could be calculated without any overlap between correlation windows, and the resulting instantaneous reattachment location would be less susceptible to spurious data points. A similar effect could also be achieved for studies conducted at lower subsonic speeds, as this would correspondingly lower the frequencies of most unsteady modes. Additionally, more involved signal processing methods could be used to more precisely determine the location between adjacent sensors where the instantaneous reattachment location occurs.

For example, the time lag value where the maximum anti-correlation is observed in the short-time correlation window could be used as an indicator to determine the approximate location of the instantaneous reattachment location in the region bound between two adjacent sensors.

- While the hinge-moment-based stall prediction system for airfoils has been improved to account for the increased hinge-moment unsteadiness that is exhibited by the horn-ice case, additional investigation is necessary to advance this technique to the next stage of development. While this method was shown to also be effective when implemented on a 3D wing system,[77] there are several issues that remain unresolved. For example, the effects of gust loading on the efficacy of this method remain unknown. Further study in this technology could take the form of performing a flight test on a full-scale aircraft, or a remote flight test on a sub-scale aircraft, with an instrumented control surface to provide a real-time evaluation of the hinge-moment-based stall prediction method.
- In the phase angle spectra of the airfoil C_p distributions, at the time-averaged location of shear-layer reattachment the phase angle corresponding to the shear-layer flapping mode and the low-frequency mode both tended towards π. Since the quasi-periodic enlargement and shrinkage of the separation bubble would have an opposite effect on the local surface pressure in the upstream portion of the separation bubble than it would in the downstream section, this would induce a phase reversal in the phase angle spectra at the location of the sign reversal. As discussed in Section 4.8.4, this would indicate that the effects of the low-frequency mode occur at both the upstream section of the separation bubble and the reattachment location at nearly the same instance in time. This shared instance at which the low-frequency mode is observed in the surface pressure could indicate that the effects of the low-frequency mode are fed to the upstream portion of the separation bubble whenever they reach the shear-layer reattachment location. Additional investigation would be helpful to identify if this observation is coincidental, inconsequential, or significant towards explaining the low-frequency mode. In order to identify the acoustic wave patterns that could provide this proposed feedback system of the low-frequency mode, this problem would best be approached using computational methods or a carefully-designed experiment.

References

[1] Bragg, M.B., Broeren, A.P., and Blumenthal, L.A., "Iced-Airfoil Aerodynamics," *Progress in Aerospace Sciences*, Vol. 41, 2005, pp. 323–362.

[2] Mabey, D.G., "Analysis and Correlation of Data on Pressure Fluctuations in Separated Flow," *Journal of Aircraft*, Vol. 9, No. 9, 1972, pp. 642–645.

[3] Eaton, J.K., and Johnston, J.P., "Low-frequency Unsteadyness of a Reattaching Turbulent Shear Layer," *Turbulent Shear Flows 3*, edited by L.J.S. Bradbury, F. Durst, B.E. Launder, F.W. Schmidt, and J.H. Whitelaw, Springer-Verlag, New York, 1982, pp. 162–170.

[4] Zaman, K.B.M.Q., Bar-Sever, A., and Mangalam, S.M., "Effect of Acoustic Excitation on the Flow over a Low-Re Airfoil," *Journal of Fluid Mechanics*, Vol. 182, 1987, pp. 127–148.

[5] Bragg, M.B., Heinrich, D.C., Balow, F.A., and Zaman, K.B.M.Q., "Flow Oscillation over an Airfoil Near Stall," *AIAA Journal*, Vol. 34, No. 1, 1996, pp. 199–201.

[6] Gurbacki, H.M., "Ice-Induced Unsteady Flowfield Effects on Airfoil Performance," Ph.D. Dissertation, University of Illinois at Urbana–Champaign, Urbana, IL, 2003.

[7] Ansell, P.J., Bragg, M.B., and Kerho, M.F., "Stall Warning Using Flap Hinge Moment Measurements," *Journal of Aircraft*, Vol. 48, No. 5, 2011, pp. 1822–1824.

[8] Kim, H.S. and Bragg, M.B., "Effects of Leading-Edge Ice Accretion Geometry on Airfoil Performance," AIAA Paper 99-3150, *17th Applied Aerodynamics Conference*, Norfolk, VA, 1999.

[9] McCullough, G.B. and Gault, D.E., "Examples of Three Representative Types of Airfoil-Section Stall at Low-Speed," NACA TN 2502, 1951.

[10] Papadakis, M., Alansatan, S., and Seltmann, M., "Experimental Study of Simulated Ice Shapes on a NACA 0011 Airfoil," AIAA Paper 99-0096, *37th AIAA Aerospace Sciences Meeting and Exhibit*, Reno, NV, 1999.

[11] Lee, S. and Bragg, M.B., "Experimental Investigation of Simulated Large-Droplet Ice Shapes on Airfoil Aerodynamics," *Journal of Aircraft*, Vol. 36, No. 5, 1999, pp. 844–850.

[12] Busch, G.T., Broeren, A.P., and Bragg, M.B., "Aerodynamic Simulation of a Horn-Ice Accretion on a Subscale Model," *Journal of Aircraft*, Vol. 45, No. 2, 2008, pp. 604–613.

[13] Broeren, A.P., Bragg, M.B., Addy, H.E., Lee, S., Moens, F., and Guffond, D., "Effect of High-Fidelity Ice-Accretion Simulations on Full-Scale Airfoil Performance," *Journal of Aircraft*, Vol. 47, No. 1, 2010, pp. 240–254.

[14] Bragg, M.B., "Experimental Aerodynamic Characteristics of an NACA 0012 Airfoil with Simulated Glaze Ice," *Journal of Aircraft*, Vol. 25, No. 9, 1988, pp. 849–854.

[15] Bragg, M.B., Broeren, A.P., Addy, H., Potapczuk, M., Guffond, D., and Montreuil, E., "Airfoil Ice-Accretion Aerodynamics Simulation," AIAA Paper 2007-85, *45th AIAA Aerospace Sciences Meeting and Exhibit*, Reno, NV, 2007.

[16] Wright, W.B., "User's Manual for the NASA Glenn Ice Accretion Code LEWICE Version 3.0," available on the NASA LEWICE 3.0 release CD, Apr. 2003.

[17] Wright, W.B., Gent, R.W., and Guffond, D., "DRA/NASA/ONERA Collaboration on Icing Research, Part II – Prediction of Airfoil Ice Accretion," NASA Contractor Report 202249, May 1997.

[18] Tani, I., "Low-Speed Flows Involving Bubble Separations," *Progress in Aerospace Sciences*, Vol. 5, 1964, pp. 70–103.

[19] Roberts, W.B., "Calculation of Laminar Separation Bubbles and Their Effect on Airfoil Performance," *AIAA Journal*, Vol. 18, No. 1, 1980, pp. 25–31.

[20] Gurbacki, H.M. and Bragg, M.B., "Unsteady Aerodynamic Measurements on an Iced Airfoil," AIAA Paper 2002-0241, *40th AIAA Aerospace Sciences Meeting & Exhibit*, Reno, NV, 2002.

[21] Bragg, M.B., Khodadoust, A., and Spring, S.A., "Measurements in a Leading-Edge Separation Bubble due to a Simulated Airfoil Ice Accretion," *AIAA Journal*, Vol. 30, No. 6, 1992, pp. 1462–1467.

[22] Broeren, A.P., Bragg, M.B., and Addy, H.E., "Flowfield Measurements About an Airfoil with Leading-Edge Ice Shapes," *Journal of Aircraft*, Vol. 43, No. 4, 2006, pp. 1226–1234.

[23] Jacobs, "Iced Airfoil Separation Bubble Measurements by Particle Image Velocimetry," Ph.D. Dissertation, University of Illinois at Urbana–Champaign, Urbana, IL, 2007.

[24] Jacobs, J.J. and Bragg, M.B., "Two- and Three-Dimensional Iced Airfoil Separation Bubble Measurements by Particle Image Velocimetry," AIAA Paper 2007-88, *45th Aerospace Sciences Meeting & Exhibit*, Reno, NV, 2007.

[25] Hudy, L.M., Naguib, A.M., and Humphreys, W.M., "Wall-Pressure-Array Measurements Beneath a Separating/Reattaching Flow Region," *Physics of Fluids*, Vol. 15, No. 3, 2003, pp. 706–717.

[26] Cherry, N.J., Hiller, R., and Latour, M.E.M.P., "Unsteady Measurements in a Separated and Reattaching Flow," *Journal of Fluid Mechanics*, Vol. 144, 1984, pp. 13–46.

[27] Chun, S., Liu, Y.Z., and Sung, H.J., "Wall Pressure Fluctuations of a Turbulent Separated and Reattaching Flow Affected by an Unsteady Wake," *Experiments in Fluids*, Vol. 37, 2004, pp. 531–546.

[28] Farabee, T.M. and Casarella, M.J., "Measurements of Fluctuating Wall Pressure for Separated/Reattached Boundary Layer Flows," *Journal of Vibration, Acoustics, Stress, and Reliability in Design*, Vol. 108, 1986, pp. 301–307.

[29] Heenan, A.F. and Morrison, J.F., "Passive Control of Pressure Fluctuations Generated by Separated Flow," *AIAA Journal*, Vol. 36, No. 6, 1998, pp. 1014–1022.

[30] Kiya, M. and Sasaki, K., "Structure of a Turbulent Separation Bubble," *Journal of Fluid Mechanics*, Vol. 137, 1983, pp. 83–113.

[31] Kiya, M. and Sasaki, K., "Structure of Large-Scale Vortices and Unsteady Reverse Flow in the Reattaching Zone of a Turbulent Separation Bubble," *Journal of Fluid Mechanics*, Vol. 154, 1985, pp. 463–491.

[32] Lee, I. and Sung, H.J., "Multiple-Arrayed Pressure Measurement for Investigation of the Unsteady Flow Structure of a Reattaching Shear Layer," *Journal of Fluid Mechanics*, Vol. 463, 2002, pp. 377–402.

[33] Liu, Y.Z., Kang, W., and Sung, H.J., "Assessment of the Organization of a Turbulent Separated and Reattaching Flow by Measuring Wall Pressure Fluctuations," *Experiments in Fluids*, Vol. 38, 2005, pp. 485–493.

[34] Tihon, J., Legrand, J., and Legentilhomme, P., "Near-Wall Investigation of Backward-Facing Step Flows," *Experiments in Fluids*, Vol. 31, 2001, pp. 484–493.

[35] Spazzini, P.G., Iuso, G., Onorato, M., Zurlo, N., and Di Cicca, G.M., "Unsteady Behavior of Backward-Facing Step Flow," *Experiments in Fluids*, Vol. 30, 2001, pp. 551–561.

[36] Devenport, W.J. and Sutton, E.P., "Near-Wall Behavior of Separated and Reattaching Flows," *AIAA Journal*, Vol. 29, No. 1, 1991, pp. 25–31.

[37] Castro, I.P. and Haque, A., "The Structure of a Shear Layer Bounding a Separation Region," *Journal of Fluid Mechanics*, Vol. 179, 1987, pp. 439–468.

[38] Driver, D.M., Seegmiller, H.L., and Marvin, J.G., "Time-Dependent Behavior of a Reattaching Shear Layer," *AIAA Journal*, Vol. 25, No. 7, 1987, pp. 914–919.

[39] Castro, I.P. and Haque, A., "The Structure of a Shear Layer Bounding a Separation Region. Part 2. Effects of Free-Stream Turbulence," *Journal of Fluid Mechanics*, Vol. 192, 1988, pp. 577–595.

[40] Abbott, D.E. and Kline, S.J., "Experimental Investigation of Subsonic Turbulent Flow Over Single and Double Backward Facing Steps," *Journal of Fluids Engineering*, Vol. 84, No. 3, 1962, pp. 317–325.

[41] Kostas, J., Soria, J., and Chong, M.S., "Particle Image Velocimetry Measurements of a Backward-Facing Step Flow," *Experiments in Fluids*, Vol. 33, 2002, pp. 838–853.

[42] Sohn, J.L., “Evaluation of FIDAP on Some Classical Laminar and Turbulent Benchmarks,” *International Journal for Numerical Methods in Fluids*, Vol. 8, 1988, pp. 1469–1490.

[43] Ghia, K.N., Osswald, G.A., and Ghia, U., “Analysis of Incompressible Massively Separated Viscous Flows Using Unsteady Navier-Stokes Equations,” *International Journal for Numerical Methods in Fluids*, Vol. 9, 1989, pp. 1025–1050.

[44] Yang, Z. and Voke, P.R., “Large-Eddy Simulation of Boundary-Layer Separation and Transition at a Change of Surface Curvature,” *Journal of Fluid Mechanics*, Vol. 439, 2001, pp. 305–333.

[45] Schäfer, F., Breuer, M., and Durst, F., “The Dynamics of the Transitional Flow over a Backward-Facing Step,” *Journal of Fluid Mechanics*, Vol. 623, 2009, pp. 85–119.

[46] Suksangpanomrung, A., Djilali, N., and Moinat, P., “Large-Eddy Simulation of Separated Flow Over a Bluff Rectangular Plate,” *International Journal of Heat and Fluid Flow*, Vol. 21, 2000, pp. 655–663.

[47] Le, H., Moin, P., and Kim, J., “Direct Numerical Simulation of Turbulent Flow Over a Backward-Facing Step,” *Journal of Fluid Mechanics*, Vol. 330, 1997, pp. 349–374.

[48] Deck, S. and Thorigny, P., “Unsteadiness of an Axisymmetric Separating-Reattaching Flow: Numerical Investigation,” *Physics of Fluids*, Vol. 19, 065103, 2007, 065103.

[49] Sigurdson, L.W., “The Structure and Control of a Turbulent Reattaching Flow,” *Journal of Fluid Mechanics*, Vol. 298, 1995, pp. 139–165.

[50] Kiya, M.S., Shimizu, M., and Mochizuki, O., “Sinusoidal Forcing of a Turbulent Separation Bubble,” *Journal of Fluid Mechanics*, Vol. 342, 1997, pp. 119–139.

[51] Kim, J., Kline, S.J., and Johnston, J.P., “Investigation of a Reattaching Turbulent Shear Layer: Flow Over a Backward-Facing Step,” *Journal of Fluids Engineering*, Vol. 102, No. 3, 1980, pp. 302–308.

[52] Eaton, J.K., “Turbulent Flow Reattachment: An Experimental Study of the Flow and Structure Behind a Backward-Facing Step,” Ph.D. Dissertation, Stanford University, Stanford, CA, 1980.

[53] Huang, H.T. and Fiedler, H.E., “A DPIV Study of a Starting Flow Downstream of a Backward-Facing Step,” *Experiments in Fluids*, Vol. 23, 1997, pp. 395–404.

[54] Burgmann, S. and Schröder, W., “Investigation of the Vortex Induced Unsteadiness of a Separation Bubble via Time-Resolved and Scanning PIV Measurements,” *Journal of Experimental Fluids*, Vol. 45, 2008, pp. 675–691.

[55] Bragg, M.B., Heinrich, D.C., and Khodadoust, A., “Low-Frequency Flow Oscillation over Airfoils near Stall,” *AIAA Journal*, Vol. 31, No. 7, 1993, pp. 1341–1343.

[56] Zaman, K.B.M.Q., McKinzie, D.J., and Rumsey, C.L., "A Natural Low Frequency Oscillation of the Flow over an Airfoil Near Stalling Conditions," *Journal of Fluid Mechanics*, Vol. 202, 1989 pp. 403–442.

[57] Broeren, A.P. and Bragg, M.B., "Flowfield Measurements over an Airfoil During Natural Low-Frequency Oscillations Near Stall," *AIAA Journal*, Vol. 37, No. 1, 1998, pp. 130–132.

[58] Broeren, A.P., "An Experimental Study of Unsteady Flow over Airfoils Near Stall," Ph.D. Dissertation, Department of Mechanical and Industrial Engineering, University of Illinois, Urbana, IL 2000.

[59] Rinoie, K. and Takemura, N., "Oscillating Behavior of Laminar Separation Bubble Formed on an Aerofoil Near Stall," *Aeronautical Journal*, Vol. 108, No. 1081, 2004, pp. 153–163.

[60] Gaster, M., "The Structure and Behavior of Laminar Separation Bubbles," Aeronautical Research Council R&M 3595, 1967.

[61] Almutairi, J.H. and AlQadi, I.M., "Large-Eddy Simulation of Natural Low-Frequency Oscillations of Separating-Reattaching Flow Near Stall Conditions," *AIAA Journal*, Vol. 51, No. 4, 2013, pp. 981–991.

[62] Sandham, N.D., "Transitional Separation Bubbles and Unsteady Aspects of Aerofoil Stall," *Aeronautical Journal*, Vol. 112, No. 1133, 2008, pp. 395–404.

[63] Zaman, K.B.M.Q. and Potapczuk, M.G., "The Low Frequency Oscillation in the Flow Over a NACA 0012 Airfoil with an 'Iced' Leading Edge," *Low Reynolds Number Aerodynamics*, edited by T.J. Mueller, Springer-Verlag, New York, 1989, pp. 271–282.

[64] Olson, S.D., and Thomas, F.O., "Quantitative Detection of Turbulent Reattachment Using a Surface Mounted Hot-Film Array," *Experiments in Fluids*, Vol. 37, 2004, pp. 75–79.

[65] Mangalam, A.S., and Moes, T.R., "Real-Time Unsteady Loads Measurements Using Hot-Film Sensors," NASA TM 2004-212854, 2004.

[66] Stack, J.P., Mangalam, S.M., and Kalburgi, V., "The Phase Reversal Phenomenon at Flow Separation and Reattachment," AIAA Paper 88-0408, *AIAA 26th Aerospace Sciences Meeting*, Reno, NV, Jan. 1988.

[67] Lee, T., and Mateescu, D., "Experimental and Numerical Investigation of 2-D Backward-Facing Step Flow," *Journal of Fluids and Structures*, Vol. 12, 1998, pp. 703–716.

[68] Stack, J.P., Mangalam, S.M., and Berry, S.A., "A Unique Measurement Technique to Study Laminar-Separation Bubble Characteristics on an Airfoil," AIAA Paper 87-1271, *AIAA 19th Fluid Dynamics, Plasma Dynamics, and Lasers Conference*, Honolulu, HI, June 1987.

[69] Fedele, J., private communication, 15 June 2011.

[70] Maris, J.M., “Method of Predicting the Approaching Stall of an Aircraft Wing,” U.S. Patent 4,435,695, issued Mar. 6, 1984.

[71] Maris, J.M., “Airfoil Performance Monitor,” U.S. Patent Application Publication US 2011/0285550 A1, Nov. 24, 2011.

[72] Myers, T.T., Klyde, D.H., and Magdaleno, R.E., “The Dynamic Icing Detection System (DIDS),” AIAA Paper 2000-0364, *AIAA 38th Aerospace Sciences Meeting and Exhibit*, Reno, NV, Jan. 2000.

[73] Gingras, D.R., Barnhart, B., Ranaudo, R., Ratvasky, T.P., and Morelli, E., “Envelope Protection for In-Flight Ice Contamination,” AIAA Paper 2009-1458, *47th AIAA Aerospace Sciences Meeting and Exhibit*, Orlando, FL, Jan. 2009.

[74] Gurbacki, H.M. and Bragg, M.B., “Sensing Aircraft Icing Effects by Unsteady Flap Hinge-Moment Measurement,” *Journal of Aircraft,* Vol. 38, No. 3, 2001 pp. 575–577.

[75] “Aircraft Surface Contamination Sensing System Using Control Surface Hinge Moment Measurements,” M.B. Bragg and H. M. Gurbacki, patent # 6,140,942, Oct. 31, 2000.

[76] Bragg, M.B., Basar, T., Perkins, W.R., Selig, M.S., Voulgaris, P.G., Melody, J.W., and Sarter, N.B., “Smart Icing Systems for Aircraft Icing Safety,” AIAA Paper 2002-0813, *AIAA Aerospace Sciences Meeting & Exhibit*, Reno, NV, Jan. 2002.

[77] Ansell, P.J., Kerho, M.F., and Bragg, M.B., “Envelope Protection for Contaminant-Induced Adverse Aerodynamics on a Wing Using Flap Hinge Moment Measurements,” AIAA Paper 2013-2654, *31st AIAA Applied Aerodynamics Conference*, San Diego, CA, June 2013.

[78] Ansell, P.J., Bragg, M.B., and Kerho, M.F., “Envelope Protection System for Iced Airfoils Using Flap Hinge Moment,” 11ICE-0025/2011-38-0066, *SAE 2011 International Conference on Aircraft and Engine Icing and Ground Deicing*, Chicago, IL, June, 2011.

[79] Busch, G., Broeren, A.P., and Bragg, M.B., “Aerodynamic Fidelity of Sub-scale Two-Dimensional Ice Accretion Simulations,” AIAA Paper 2008-7062, *26th AIAA Applied Aerodynamics Conference*, Honolulu, HI, Aug. 2008.

[80] Broeren, A. P., Whalen, E. A., Busch, G. T., and Bragg, M. B., “Aerodynamic Simulation of Runback Ice Accretion,” AIAA Paper 2009-4261, *1st AIAA Atmospheric and Space Environments Conference*, San Antonio, TX, June 2009.

[81] Lu, B. and Bragg M.B., “Airfoil Drag Measurement with Simulated Leading-Edge Ice Using the Wake Survey Method,” AIAA Paper 2003-1094, *41st Aerospace Sciences Meeting and Exhibit,* Reno, NV, Jan. 2003.

[82] Braslow, A.L. and Knox, E.C., “Simplified Method for Determination of Critical Height of Distributed Roughness Particles for Boundary-Layer Transition at Mach Numbers from 0 to 5,” NACA TN 4363, 1958.

[83] Schlichting, H., *Boundary-Layer Theory*, McGraw-Hill Book Company, New York, 1979.

[84] Drela, M., XFOIL, Software Package, Ver. 6.97, Cambridge, MA, 2008. Available from http://web.mit.edu/drela/Public/web/xfoil/

[85] Anderson, J.D., *Introduction to Flight*. McGraw-Hill Book Company, New York, 2007.

[86] Jones, B. M., "Measurement of Profile Drag by the Pitot-Traverse Method," Tech. Rep. 1688, Aeronautical Research Council R&M, 1936.

[87] Lee, S., "Effects of Supercooled Large Droplet Icing on Airfoil Aerodynamics," Ph.D. Dissertation, University of Illinois at Urbana–Champaign, Urbana, IL, 2001.

[88] Senflex Multi-Element Surface Hot-Film Sensors: General Information and Catalog of Standard Arrays, Tao of Systems Integration, Inc., Hampton, VA.

[89] Fingerson, L.M. and Freymuth, P., Thermal Anemometers, in Goldstein, R.J., *Fluid Mechanics Measurements*, 2nd ed., Washington DC, Taylor & Francis, 1996, Chapter 3.

[90] Bruun, H.H., *Hot-Wire Anemometry: Principles and Signal Analysis*, Oxford University Press, New York, 1995.

[91] Strang, G., and Nguyen, T., *Wavelets and Filter Banks*, 2nd ed., Wellesley, MA: Wellesley-Cambridge Press, 1997, Chapter 1.

[92] Ansell, P.J., "Flight Envelope Protection Using Flap Hinge Moment Measurement," M.S. Thesis, University of Illinois at Urbana–Champaign, Urbana, IL, 2010.

[93] Busch, G.T., "Experimental Study of Full-Scale Iced-Airfoil Aerodynamic Performance Using Sub-Scale Simulations," Ph.D. Dissertation, University of Illinois at Urbana–Champaign, Urbana, IL, 2009.

[94] Barlow, J.B., Rae, W.H. Jr. and Pope, A., *Low-Speed Wind Tunnel Testing*, 3rd Edition, John Wiley & Sons, Inc., New York, 1999.

[95] Tropea, C., Yarin, A.L., and Foss, J.F., *Springer Handbook of Experimental Fluid Mechanics*, Springer-Verlag, Berlin, 2007.

[96] Spring, S.A., An Experimental Mapping of the Flow Field Behind a Glaze Ice Shape on a NACA 0012 Airfoil, M.S. Thesis, The Ohio State University, Columbus, OH, 1987.

[97] Bendat, J.S. and Piersol, A.G., *Random Data: Analysis and Measurement Procedures*, 3rd Edition, John Wiley & Sons, Inc., New York, 2000.

[98] Piersol, A.G., "Time Delay Estimation Using Phase Data," *IEEE Transactions on Acoustics, Speech, and Signal Processing*, Vol. ASSP-29, No. 3, 1981, pp. 471–477.

[99] Teolis, A., *Computational Signal Processing with Wavelets*, Birkhauser, Boston, 1998.

[100] Torrence, C. and Compo, G.P., "A Practical Guide to Wavelet Analysis," *Bulletin of the American Meteorological Society*, Vol. 79, No. 1, 1998, pp. 61–78.

[101] Kline, S.J. and McClintock, F.A., "Describing Uncertainties in Single-Sample Experiments," *Mechanical Engineering*, Vol. 75, No. 1, 1953, pp. 3–8.

[102] Moffat, R.J., "Describing the Uncertainties in Experimental Results," *Experimental and Thermal Fluid Sciences*, Vol. 1, No. 1, 1988, pp. 3–17.

[103] Coleman, H.W. and Steel, W.G., *Experimentation and Uncertainty Analysis for Engineers*, Wiley-Interscience, New York, 1989.

[104] Whalen, E.A., "Aerodynamics of Runback Ice Accretions," Ph.D. Dissertation, University of Illinois at Urbana–Champaign, Urbana, IL, 2007.

[105] Lemonis, G. and Dracos, T., "A New Calibration and Data Reduction Method for Turbulence Measurement by Multihotwire Probes," *Experiments in Fluids*, Vol. 18, 1995, pp. 319–328.

[106] Abbott, I.H. and von Doenhoff, A.E., *Theory of Wing Sections*, Dover Press, New York 1959.

[107] Ladson, C.L., "Effects of Independent Variation of Mach and Reynolds Numbers on the Low-Speed Aerodynamic Characteristics of the NACA 0012 Airfoil Section," NASA TM 4074, 1988.

[108] Gregory, N. and O'Reilly, C.L., "Low-Speed Aerodynamic Characteristics of NACA 0012 Aerofoil Section, including the Effects of Upper-Surface Roughness Simulating Hoar Frost," Aeronautical Research Council R&M 3726, 1970.

[109] Street, W.G. and Ames, M.B., "Pressure-Distribution Investigation of an N.A.C.A. 0009 Airfoil with a 50-Percent-Chord Plain Flap and Three Tabs," NACA TN 734, 1939.

[110] Troutt, T.R., Scheelke, B., and Norman, T.R., "Organized Structures in a Reattaching Separated Flow Field," *Journal of Fluid Mechanics*, Vol. 143, 1984, pp. 413–427.

[111] Lee, I. and Sung, H.J., "Characteristics of Wall Pressure Fluctuations in Separated and Reattaching Flows Over a Backward Facing Step. Part I: Time-Mean Statistics and Cross-Spectral Analyses," *Experiments in Fluids*, Vol. 30, 2001, pp. 262–272.

[112] Heinrich, D.C., "An Experimental Investigation of a Low Frequency Flow Oscillation Over a Low Reynolds Number Airfoil Near Stall," M.S. Thesis, University of Illinois at Urbana–Champaign, Urbana, IL, 1994.

[113] Tanaka, H., "Flow Visualization and PIV Measurements of Laminar Separation Bubble Oscillating at Low Frequency on an Airfoil Near Stall," *24th International Congress of the Aeronautical Sciences*, 2004.